UNIVERSITÁ DI PISA
DOTTORATO DI RICERCA IN INGEGNERIA DELL'INFORMAZIONE

INCREASING THE AUTONOMY OF UNDERWATER VEHICLES OPERATIONS: LONG-ENDURANCE AND PRECISE NAVIGATION PERSPECTIVES

DOCTORAL THESIS

Author
T.V. (AN) Vincenzo Manzari

Tutor (s)
Prof. Andrea Caiti, Prof. Marco Luise, C.F. (AN) Mirko Stifani

Reviewer (s)
Prof. Benedetto Allotta, Dr. Andrea Munafó

The Coordinator of the PhD Program
Prof. Marco Luise

Pisa, May 2019

Cycle XXXI

"Scientific results cannot be used efficiently by soldiers
who have no understanding of them,
and scientists cannot produce results useful for warfare
without an understanding of the operations."
Dr. Theodore von Kármán - former President of AGARD of NATO

Summary

AUV (Autonomous Underwater Vehicle) technology began its development in the 1970s. Since then, improvements in energy efficiency, sensors technology, and computational power have fostered their wide application. As a result, many complex missions that were originally accomplished with towed sensors or manned vehicles are being automated at different levels. AUV designs include torpedo-shapes, gliders, and hovering capable vehicles, and their sizes range from human-portable to hundreds of tons. AUVs are now used for a variety of tasks, including oceanographic surveys, mine countermeasure, anti-submarine warfare, and bathymetric data collection in marine environments from rivers to open oceans. In particular, vehicle endurance is important and crucial because it affects the working duration and mission completion. Research in augmenting AUV persistence has burst in the last ten years, and several techniques address this issue. Among them, environmental energy harvesting is the most promising method. Moreover, AUV accurate localization and navigation are essential to reliably determine its position and to ensure the correct georeferentiation of the senses data for critical applications.

The thesis develops these two perspectives of AUVs operations: long-endurance and precise navigation. First, a unique prototype, called WAVE (Wave-powered Autonomous Vehicle for marine Exploration), for both energy harvesting from the wave motion and low consumption propulsion, is experimentally characterized. Second, an easily deployable Underwater Test Range (UTR) for verification and validation (V&V) of AUVs autonomous navigation skills is presented. These developed capabilities are validated through extensive field demonstrations thanks to SEALab joint applied research laboratory on heterogeneous and autonomous marine systems. It was established in 2015 as a result of an agreement between the Naval Support and Experimentation Center (CSSN) of the Italian Navy and the Interuniversity Research Center of Integrated Systems for Marine Environment (ISME), of which the University of Pisa is a co-founder.

The WAVE module, installed on the modular, torpedo-shaped, hybrid glider/AUV Fòlaga, undergoes an extensive experimental campaign in a towing tank equipped with a wave generator. During the three days of experimentation, a considerable quantity

of data related to different recreated sea conditions and WAVE module configurations was collected. From the energetic characterization of the proposed system in terms of average generated power, the most effective configuration of the WAVE module for the battery charging was identified. Preliminary data processing allowed a first tuning of the designed system dynamical model and the simulative results of the expected performance of WAVE under typical Mediterranean sea conditions not tested in the towing tank are presented in this thesis. More tests with various WAVE module configurations are ongoing to enable deeper analysis and better fitting of the modelling parameters in order to be able to test innovative wing profiles in more complex wave scenarios.

A first experimental assessment of the UTR demonstrates the conceived system based on bearing-only sensors, which is capable of precisely tracking an Autonomous Surface Vehicle (ASV) equipped with Differential GPS as position ground truth. With roots in previous simulative results, estimation of target trajectory is performed via non-linear Kalman Filtering (KF) approaches: both Extended and Unscented KF versions have been implemented and compared. Results show how the proposed methodology performs in a real marine scenario with challenging conditions due to shallow waters and magnetically noisy environment. Future steps will aim to enhance the tracking performance using moving sensor platforms to optimize the UTR topology and implementing a distributed approach with mixed bearing-range measurements.

The results reported in this work show how AUV can be useful in not traditional and complex scenarios. In the imminent future, AUVs will be increasingly used in long-term, long-range, deep-water missions, operating without the support of a ship-based acoustic positioning system. This will require both precise navigation systems, independent of external aids, and an effective energy system that properly combines the primary batteries of the vehicle with environmental energy sources.

Sommario

La tecnologia degli AUV (*Autonomous Underwater Vehicle* - Veicoli autonomi subacquei) ha iniziato a svilupparsi negli anni '70 e da allora i miglioramenti nell'efficienza energetica, nella tecnologia dei sensori e nella potenza di calcolo ne hanno favorito l'impiego in vari ambiti. Di conseguenza, molte missioni complesse - originariamente realizzate con sensori trainati o mezzi con operatori - sono state automatizzate a diversi livelli. Le tipologie di AUV comprendono veicoli siluriformi, *glider* (alianti marini) e veicoli con capacità di *hovering*, con dimensioni che vanno dal *man-portable* (peso inferiore ai 30 kg) sino alle centinaia di tonnellate di peso. Gli AUV sono ormai utilizzati per una varietà di compiti, tra cui rilievi oceanografici, contromisure mine, guerra anti sottomarino (ASW, *Anti Submarine Warfare*) e raccolta di dati batimetrici in ambienti che spaziano dai fiumi agli oceani.

In particolare, l'*endurance* del veicolo (intesa come capacità energetica totale) è cruciale perché influenza la durata massima in operazione e quindi il completamento della missione stessa. La ricerca sull'aumento della persistenza degli AUV è esplosa negli ultimi dieci anni e diverse tecniche affrontano questo problema. Tra queste, l'utilizzo dell'energia ambientale è il metodo più promettente. Inoltre, la localizzazione e la navigazione accurate sono essenziali per un AUV per determinare in modo affidabile la sua posizione e garantire la corretta georeferenziazione dei dati raccolti, particolarmente in applicazioni critiche.

La tesi sviluppa queste due prospettive delle operazioni con AUV: *long-endurance* e precisione della navigazione. Innanzitutto, un prototipo unico al mondo per il recupero energetico dal moto ondoso e propulsione a basso consumo di un AUV, denominato WAVE (*Wave-powered Autonomous Vehicle for marine Exploration* - Veicolo autonomo alimentato dal moto ondoso per l'esplorazione marina), è stato caratterizzato sperimentalmente. In secondo luogo, viene presentato un *Underwater Test Range* (UTR), con caratteristiche di facile dispiegabilità, per la verifica e la validazione (*Verification & Validation*) delle abilità di navigazione autonoma di AUV.

Queste capacità sviluppate sono convalidate attraverso ampie dimostrazioni sul campo, svolte grazie al laboratorio di ricerca applicata congiunto *"SEALab"* sui sistemi marini eterogenei autonomi. Tale laboratorio è stato istituito nel 2015 come risultato di

un accordo di collaborazione tra il Centro di Supporto e Sperimentazione Navale (CSSN) della Marina Militare Italiana e il Centro Interuniversitario di Ricerca sui Sistemi Integrati per l'Ambiente Marino (ISME), di cui l'Università di Pisa è co-fondatrice.

Il modulo WAVE, installato sul glider/AUV Fòlaga, è stato protagonista di una vasta campagna sperimentale svolta nella vasca navale del CNR (Consiglio Nazionale delle Ricerche) a Roma, equipaggiata di un generatore di onde. Durante i tre giorni di sperimentazione, è stata raccolta una notevole quantità di dati relativi alle diverse condizioni del mare e alle configurazioni del modulo WAVE. Dalla caratterizzazione energetica del sistema proposto in termini di potenza media generata, è stata identificata la configurazione più efficace del modulo WAVE per la ricarica energetica. L'elaborazione preliminare dei dati ha consentito una prima messa a punto del modello dinamico di sistema progettato, i cui risultati simulativi delle prestazioni di WAVE in condizioni tipiche del Mar Mediterraneo, non testate in vasca navale, sono presentati nel lavoro di tesi. Sono in corso ulteriori test con varie configurazioni di WAVE per consentire un'analisi più approfondita e un migliore *fitting* dei parametri di modellazione al fine di poter testare profili alari innovativi in scenari d'onda più complessi.

Una prima valutazione sperimentale dell'UTR dimostra che il sistema concepito, basato su sensori passivi *bearing-only*, è in grado di tracciare con precisione un Veicolo di Superficie Autonomo (ASV, *Autonomous Surface Vehicle*) dotato di GPS differenziale come *ground-truth*. Sulle base di precedenti studi in simulazione, la stima della traiettoria del target viene eseguita tramite approcci non lineari di *Kalman Filtering* (KF): sono state implementate e confrontate entrambe le versioni KF *Extended* e *Unscented*. I risultati sperimentali mostrano come la rete di tracciamento proposta riesca a localizzare correttamente il target (cooperativo) anche in uno scenario marino con condizioni elettroacustiche non ottimali a causa della bassa profondità, del rumore antropico tipico di una zona portuale, e di un ambiente magneticamente rumoroso. Le fasi future di ricerca e sviluppo mireranno a migliorare le prestazioni di tracciamento utilizzando piattaforme mobili in grado di ottimizzare la topologia dell'UTR e implementare un approccio distribuito con misurazioni di *range* integrate opportunamente con quelle di *bearing*.

I risultati ottenuti dimostrano ancora una volta il potenziale inespresso che risiede nella più ampia tecnologia degli AUV. Nell'imminente futuro, gli AUV saranno sempre più utilizzati in missioni in acque profonde, di lunga durata e a lungo raggio, dovendo operare senza il supporto di un sistema di posizionamento acustico gestito da una nave madre. Ciò richiederà sia sistemi di navigazione precisi, indipendenti da riferimenti esterni, sia un sistema energetico efficace che combini opportunamente le batterie primarie del veicolo con fonti energetiche ambientali.

List of publications

International Journals

1. Costanzi, R., Fenucci, D., Manzari, V., Caiti, A., & Petroccia, R. (2018). Towards an autonomous underwater vehicles test range: At-sea experimentation of bearing-only tracking algorithms. Annual Reviews in Control. https:// doi.org/ 10.1016/ j.arcontrol.2018.10.007

International Conferences/Workshops with Peer Review

1. Fenucci, D., Caffaz, A., Costanzi, R., Fontanesi, E., Manzari, V., Sani, L., ... and Caiti, A. (2016, September). WAVE: A wave energy recovery module for long endurance gliders and AUVs. *In OCEANS 2016 MTS/IEEE Monterey*. (pp. 1-5). IEEE.

2. Costanzi, R., Fenucci, D., Manzari, V. and Caiti, A. (2016, September). Bearing-only AUV tracking performance: The effect of uncertainty in underwater nodes position. *In OCEANS 2016 MTS/IEEE Monterey*. (pp. 1-6). IEEE.

3. Costanzi, R., Fenucci, D., Manzari, V. and Caiti, A. (2017, July). Bearing-only AUV tracking performance: Unscented Kalman Filter estimation against uncertainty in underwater nodes position. *in IFAC World Congress 2017 Toulouse*. (Vol. 50, pp. 13674-13679).

4. Costanzi, R., Fenucci, D., Manzari, V., Micheli M, Morlando L., Natale D., Stifani M., Tesei A., and Caiti, A. (2018, June). At-Sea NATO Operational Experimentation with Interoperable Underwater Assets Using Different Robotic Middlewares. *In Technology and Science for the Ships of the Future: Proceedings of NAV 2018: 19th International Conference on Ship & Maritime Research*. (p. 194). IOS Press.

5. Caiti, A., Costanzi, R., Fenucci, D., Manzari, V., Caffaz A., and Stifani M. (2018, October). Wave module for hybrid oceanographic autonomous underwater vehicle – prototype experimental validation and characterisation. *In International Ship Control Systems Symposium (iSCSS), Glasgow, Scotland (UK)*.

6. Costanzi, R., Gasparri, A., Pacienza, F., Pollini, L., Caiti, A., Manzari, V., ... and Romanelli, A. (2019, June). Visual acquisition system for georeferenced monitoring and reconstruction of the sea bottom using audio for data synchronisation. *In OCEANS 2019 MTS/IEEE Marseille*. (accepted for publication). IEEE.

7. Terracciano, D., Costanzi, R., Guerrini, P., Manzari, V., ... and Caiti, A. (2019, June). Bearing estimation in very shallow waters with an AUV mounted Acoustic Vector Sensor. *In OCEANS 2019 MTS/IEEE Marseille*. (accepted for publication). IEEE.

List of Abbreviations

A

AHRS	Attitude Heading Reference System. 6, 154
ASV	Autonomous Surface Vehicle. 14
ASW	Anti-Submarine Warfare. 16, 60
AUV	Autonomous Underwater Vehicle. 1, 13, 14, 28, 36, 116
AUVSI	Association for Unmanned Vehicle Systems International. 3

B

BOT	Bearing-only tracking. 128, 157

C

CMRE	Centre for Maritime Research Experimentation. 24, 60, 152
CNR-INSEAN	Italian National Research Council - National Institute for Studies and Experiences of Naval Architecture. 37, 65
CoB	Center of Buoyancy. 93
CoG	Center of Gravity. 81, 93
CRLB	Cramer-Rao Lower Bound. 138
CSSN	Naval Support and Experimentation Center – *Centro di Supporto e Sperimentazione Navale*, in Italian – of the Italian Navy. 7
CTD	Conductivity–Depth–Temperature. 31, 40

D

DoA	Direction of Arrival. 117, 136, 156
DVL	Doppler Velocity Log. 31, 116, 156

E

EKF	Extended Kalman Filter. 8, 121, 140, 143
F	
FIM	Fisher Information Matrix. 138, 143
FOG	Fiber-Optic Gyroscope. 5, 116
G	
GPS	Global Positioning System. 3, 5, 116
H	
HIL	Hardware-In-the-Loop. 44
I	
IMM	Interacting Multiple Model. 127, 134
IMU	Inertial Measurement Unit. 6, 156
INS	Inertial Navigation System. 5
ISME	Interuniversity Research Center of Integrated Systems for Marine Environment. 7
ISR	Intelligence, Surveillance, and Reconnaissance. 1
K	
KF	Kalman Filter. 10, 121
L	
LARS	Launch And Recovery System. 18
LBL	Long BaseLine. 6
LOON	Littoral Ocean Observatory Network. 152
M	
MAC	Medium Access Control. 9, 162
MCM	Mine Countermeasures. 16, 19
MOOS-IvP	Mission Oriented Operating Suite – Interval Programming. 60
MSE	Mean Squared Error. 144
N	
NACA	National Advisory Committee for Aeronautics. 91
NED	North-East-Down. 82, 137, 148
NiMH	Nickel-Metal Hydrate. 63
NURC	NATO Undersea Research Centre. 24
P	
PDF	Probability Density Function. 134
PF	Particle Filter. 121

R

RMSE	Root Mean Squared Error. 150
ROS	Robotic Operating System. 42
ROV	Remotely Operated Vehicle. 2, 14, 19
RSSI	Received Signal Strength Indication. 117

S

SAR	Search And Rescue. 13
SNR	Signal to Noise Ratio. 134
SUA	Sensor Uncertainty Area. 140, 145

T

TDoA	Time Difference of Arrival. 117, 128
TMS	Tether Management System. 17
ToA	Time of Arrival. 117, 128

U

UAV	Unmanned Aerial Vehicle. 6
UKF	Unscented Kalman Filter. 8, 121, 143
UMV	Unmanned Maritime Vehicle. 1, 28
USBL	Ultra-Short BaseLine. 6, 128, 136, 152
USV	Unmanned Surface Vehicle. 6, 14
UTR	Underwater Test Range. 6, 10, 116, 135, 152
UUV	Unmanned Underwater Vehicle. 14, 19, 128
UWSN	Underwater Wireless Sensor Networks. 117

V

V&V	Verification and Validation. 6, 116, 135

W

WAVE	Wave-powered Autonomous Vehicle for marine Exploration. 7, 10, 35, 65, 80
WECS	Wave Energy Conversion System. 5
WMCS	WAVE Mission Control System. 40
WSN	Wireless Sensor Networks. 117

Contents

CHAPTER 1

Introduction

This thesis presents two prototype systems for enhancing the autonomy of Autonomous Underwater Vehicle (AUV) operations, specifically for long-term missions which require extreme navigation and endurance capabilities. In particular, the fundamental vision of this Thesis is aimed at evaluating the applicability in real scenarios of the proposed methods to increase the endurance of an AUV by exploiting the wave energy and to accurately assess its navigation performance. This work further provides a synergistic simulative-experimental analysis for understanding how design choices at different development levels affect the overall performance achievable by the envisioned systems.

1.1 The general picture: motivating problems and existing limitations

The trend of going towards unmanned systems for *dangerous, dull and dirty* tasks has in the last decade started to include the maritime domain, which is distinguished by specific challenges that make underwater robotics very different from air and land robotics. The maritime domain is hard since the sea is a hostile environment where Unmanned Maritime Vehicles (UMVs) could operate in (the comparison with space-type operations is not a far-fetched one). UMV employment in the field of persistent Intelligence, Surveillance, and Reconnaissance (ISR) tasks can support a wide range of maritime operations, particularly in the coastal environment where a multitude of threats converge to create a high risk operating scenario. To name a few examples of key operational tasks, UMVs can conduct ISR of threatened choke points for surface threats or mines, conduct persistent monitoring of known transit routes employed by terrorists, pirates or drug smugglers, as well as conduct harbor surveys after natural disasters. Since knowing your adversary is an essential strategic and tactical require-

ment, most missions in modern warfare are centered on collecting and processing as much information about the opponent and the environment as possible [183]. Even though these missions diversify in scope and requirements, they all focus on collecting and exploiting information about the environment, with the purpose of minimizing the uncertainty regarding the enemy's location, behavior, intentions, and courses of action. Either as a primary sensor/weapon system or as a key enabler to other capabilities, UMVs have the potential to transform the future planning and execution of these core missions. In line with the foreseen threats of the current and future operating environment, the operational use of UMVs underpins the successful completion of the above tasks, while reducing risk and costs to conventional naval forces. If judiciously developed and employed, UMVs will transform the nature of maritime operations.

Nevertheless, UMVs would really contribute to naval needs only if their *autonomy* increases significantly. Indeed, the ability to operate independently for extended periods creates a force multiplier that allows manned systems to extend their reach and focus on more complex tasks. Costs may be reduced when sensors or weapons are operated from the smaller infrastructure of an UMV rather than entirely from manned platforms. Although there is not one standard definition for the term autonomy, there is a common understanding of the properties that an autonomous system should have. Autonomous systems are systems that develop, for themselves, the laws and strategies by which they choose and control their behavior [194]. To be autonomous, a system must have the ability to operate without human intervention while at the same time it optimizes its behavior in a goal-directed manner in unforeseen situations (*i.e.* in a given situation, the autonomous system finds the optimal solution). This ability is a significant improvement compared with the capabilities of automatic systems that are fully pre-programmed and act predictably independent of the situation, even if an autonomous system takes its decisions based on a set of rules and/or limitations. For unmanned systems to express their potential, they must be able to achieve a highly autonomous state of behavior and interaction with their surroundings, understanding and adapting to their environment, collaborating with other autonomous systems.

Marine robotics has been an important branch of robotics since its beginning in the early 1970s [226], and nowadays the world's commercial fleet consisted of almost 100000 vessels [159]. In particular, fully autonomous robotic systems are envisioned to be able to operate completely independent of humans, using a variety of sensors and communication systems to assess the situation and make decisions and changes during operation [162]. If unmanned vehicles were able to navigate safely to their destination even in the event of adverse weather conditions and in the presence of high ship traffic, it is expected to have a remarkable reduction in shipping costs with lower risk of losing human lives at sea. Under the sea surface, the use of Remotely Operated Vehicles (ROVs) and Autonomous Underwater Vehicles (AUVs) is rapidly increasing for pipeline surveys, cable maintenance and other inspection and intervention work on underwater structures, in addition to fields such as marine biology, environmental monitoring, seafloor mapping, oceanography and military use (See Chapter 2 for a review of UMV).

In general, from a state-of-the-art analysis, it can be stated that five research macrotrends are currently aiming at improving the autonomy of AUV operations:

1. Command, control and communication systems (C3S) suitable for complex mis-

sions: the technological trend of the last decades has made small, relatively low-cost AUVs a reality. Then, the available systems spread from those employed for acoustic surveillance for military applications to smaller, less powerful but longer endurance, oceanographic sensing units that can stay at sea for prolonged periods of time [72, 215] and to multi-purpose, mission-oriented assets. Nowadays, when multiple underwater robots are available, the typical approach is still mainly centralized, which means that gliders or AUVs communicate, possibly when on the surface, their known location and measurements to a unique C3S which fuses all this information together and sends back new waypoints or tracklines [78].

2. Interoperability between heterogeneous assets, both manned and unmanned. Other barriers to the diffusion and deployment of underwater robotic nodes are the lack of generally accepted standards, which undermines the interoperability of systems [83]. Even if using software middleware (*e.g.* MOOS-IvP or ROS [130]) is becoming common in the robotics community to ease the software module integration, much has to be undertaken in payload interface and hardware standardization.

3. Correct georeferencing of the collected data for effective data processing. In order to achieve *true* autonomy, an AUV must be able to navigate accurately and reliably in the underwater domain. This is especially applicable to survey missions. If a representation of the environment is constructed by combining local sensor measurements with vehicle and orientation estimates, then the overall consistency and accuracy will depend on the characteristics of the navigation. Geo-referenced positioning is usually needed, however standard tools such as Global Positioning System (GPS) radio-frequency signals are blocked by seawater and cannot be received directly by a submerged vehicle [7, 178].

4. Energy capacity on board the vehicle in order to carry out long-term missions. In fact, as the autonomy of AUVs increases, the energy efficiency of the vehicles becomes a key issue. So far progress in endurance has been linked to progress in electrical batteries; new generation batteries allow for more energy storage while at the same time reducing size and weight [214]. However, this is not yet enough to guarantee mission times of more than few days at the very best. The example of the glider actuation system shows that clever, focused design may allow a much higher jump in efficiency [90]. Environmental energy harvesting is the most promising way to improve UMVs endurance. For instance, the group led by Blidberg at Association for Unmanned Vehicle Systems Internationals (AUVSIs) has pioneered the investigation on solar-powered AUV with solar panels accumulating energy when the vehicle is at the surface [26]. The recent WaveGlider vehicle is a surface autonomous vehicle that exploits wave motion to produce a net horizontal movement in the desired direction [140, 217].

5. Finally, reliable autonomous behavior and precise autonomous navigation are required. In fact, most autonomous systems rely on radio or spread spectrum communications and global positioning above water. Actually, such signals propagate only short distances underwater, while acoustic-based sensors and communications perform better. The latter still suffer from many shortcomings such as small

bandwidth, low data rate, high latency, and variable sound speed. The harsh and unstructured nature of the underwater environment causes significant challenges for underwater autonomous systems. However, with recent advances, this field is progressing at an unprecedented rate [166].

All these scientific and technological challenges are highly interconnected with each other to increase the autonomy of a vehicle. The last two perspectives are approached, analyzed and enhanced in this thesis. The overall envisioned goal for achieving greater autonomy in robotic vehicles is to enable longer missions without the need for human intervention. This ability would further allow for longer range missions, enabling exploration of more remote environments.

Generally speaking, the techniques about power supply for UMVs own unique advantages and drawbacks [214]. For instance, there are still many batteries with insufficient energy density, limited numbers of cycles before failure and a poor shelf life. They cannot provide enough power for extended duration, *i.e.* beyond 2-3 days. Some batteries are desirable with much higher energy density, such as lithium series cells and semi-fuel cells, but they are not cost-effective in scientific research. As an example, Spray Glider powered by lithium primary cells needs about $2850 in refueling, quintuples the cost of Slocum powered by alkaline cells [180]. Not least important, batteries with harmful chemical substances may cause environment pollutions, like lead-acid cells.

On the contrary, environmental energy is quite a novel way to power underwater vehicles. Solar energy, ocean thermal energy, and wave energy are huge, clean and renewable sources, with both advantages and limitations. Solar energy is quite feasible for UMVs power supply with limitations due to the daylight-restricted conversion of solar energy into electrical energy. In addition, the amount of solar energy available on the ocean surface varies significantly with areas, seasons and weather, which is caused by solar radiation distribution. Moreover, solar panels installation require large space on the vehicle also because the conversion efficiencies available are among $10 - 12\%$. It is worth to note that heat is accumulated in water due to sunshine. The temperature and heat vary a lot in different depths, *e.g.* in tropical areas, the temperature of seawater ranges from $29\,^{\circ}$C to $4\,^{\circ}$C where the depth is about $500 - 1000$ m [155]. This difference implies the creation ocean's temperature gradient, from which ocean thermal energy is generated. Albeit ocean thermal energy is derived from solar energy, it is more reliable and predictably available at all hours. In the early 90s, Stommel has envisioned an underwater glider propelled by environmental energy [198]. Several underwater vehicles powered by thermal energy were then designed and developed, such as Slocum Thermal Glider. However, the limitation is that the temperature gradient is not available globally, *i.e.* only in tropic and semi-tropic areas. That is because the temperature difference it needs must be greater than $10\,^{\circ}$C between surface and depth [215]. Therefore, the vehicle powered by thermal energy can only be used between 35° south latitude and 35° north latitude. Wave energy is more promising than solar energy and ocean thermal energy mainly because it is not restricted by time or places. However, harvesting wave energy is quite a difficult process, because it is dispersive and random *i.e.* the conversion efficiency is quite low due to energy loss, which is caused during energy delivery stages. In addition, it has to be highlighted that the vehicle might encounter areas with no waves, and this would constrain its operation as shown in some of the experimental

tests presented in Section 3.3. First, it is necessary to simplify the conversion process and minimize energy loss to improve efficiency.

A new research trend looks at environmental energy conversion devices installed on underwater vehicles. This way, when floating on the surface, the device can absorb environmental energy and convert it into electrical power. Solar panels can be installed on the surface of the vehicle while mini Wave Energy Conversion System (WECS) can be installed within the vehicle. This way, combining battery techniques, electrical power generated can be exploited by UMVs. Part I of the thesis investigates this approach, proposing a novel payload for both energy harvesting from the wave motion and low energy propulsion, to be integrated on a generic, modular, torpedo-shaped AUV. Finally, by applying ocean thermal energy, a heat engine can also change the vehicle buoyancy to drive an underwater vehicle.

Even if an UMV could be able to navigate for months, long-range missions are challenging for robotic systems because the application of the vast majority of navigation methods in an underwater environment presents a different set of sensor limitations and localization challenges than their terrestrial counterparts. Electromagnetic signals commonly used for above-surface navigation are rapidly absorbed in water. As a result, one of the most widely used terrestrial positioning systems, GPS, is inaccessible underwater. In addition, the rapid absorption of light underwater limits the use of vision-based systems, requiring underwater vehicles to carry a light source and operate in close proximity (within a few meters) of imaged objects. This limited utility of electromagnetic waves underwater has led to the widespread use of acoustic signals for underwater navigation. In turn, they exhibit a steep trade-off in achievable accuracy with operational range due to signal absorption and highly non-linear and variable sound speed profile. Aside from these challenges, the underwater environment presents some sensing advantages over terrestrial environments which leads to a somewhat different set of localization challenges. For example, the smooth and predictable variation of pressure underwater allows for highly accurate pressure depth measurements compared with pressure-based altitude sensing in air. This way, the underwater localization problem can be often restricted to a planar problem.

Moreover, underwater dead reckoning systems exploit velocity and/or acceleration measurements to estimate the vehicle's state vector over time. Because these measurements are inherently noisy, their integration results in an accumulation of error over time known as drift. An Inertial Navigation System (INS) refers to a system that uses some combination of the measurements and sensors reported in Table 1.1 along with filtering algorithms to estimate the inertial dynamics of the vehicle in all six degrees of freedom. Higher performing INS systems generally use very accurate accelerometers and gyroscopes, typically Fiber-Optic Gyroscope (FOG), and incorporate software for optimal sensor fusion. The packaging of these sensors in a single, well-calibrated unit further improves performance by significantly reducing the potential for alignment errors between the various sensors. Combining these high performance INS systems with well-designed trajectories has resulted in navigation accuracies as high as 0.01% DT (total accumulated translational error as a percentage of Distance Traveled). Even with these low drift rates, a highly accurate INS does not solve the problem of underwater robotic navigation. The longer range missions desired for these vehicles, up to thousands of kilometers, would result in a navigation error unacceptable for critical mis-

Table 1.1: *Commonly used underwater vehicle navigation sensors. Notice that an Inertial Measurement Unit (IMU) refers to an instrument package with both accelerometer and gyroscopes, with improved accuracy due to the reduced alignment errors between them. An Attitude Heading Reference System (AHRS) incorporates also magnetometers to provide attitude and attitude rate estimates through optimal filtering.*

Instrument	Measured Variable
Pressure Depth	Depth
Magnetic Compass	Magnetic heading
Gyroscopes	Body angular rate
Accelerometers	Body acceleration
IMU	Body angular rate and acceleration
AHRS	Attitude
DVL	Body velocity

sions and applications even when highly accurate systems are employed. Furthermore, highly accurate INS systems can be prohibitively expensive (a high-end marine-grade INS can cost over 1 million dollars).

For successful long range and/or sensor-limited navigation, dead reckoning systems must be supplemented by an aiding sensor which can bound navigation error growth through direct measurements of position (and possibly orientation). Acoustic-aided navigation uses sonar to measure range and potentially bearing to transponders at known locations. The most common forms of underwater acoustic positioning include Long BaseLine (LBL), Ultra-Short BaseLine (USBL), and Homing systems. The reliance upon deployed beacons in both LBL and homing systems results in a limited operating range (less than $10\,\text{km}$), unacceptable for very long range missions. In addition, the high cost typically associated with deploying and calibrating these systems limits their usability for lower-cost systems. USBL provides a lower-cost alternative but they are typically very noisy, with accuracies on the order of tens of meters. In addition, long ranges limit the utility of external sensor systems, such as locally deployed navigation aids.

Experimental validation of the described navigational methods is often reported, but a systematic assessment of the vehicle navigation accuracy is difficult to obtain in many cases because of the lack of a reliable ground-truth and, in general, of testing standardization and facilities. Currently, there are no comprehensive methods to evaluate vehicle navigation accuracy, neither testing arenas to certify AUVs skills. With this motivation, the second part of this thesis deals with the design, implementation, and testing of an easily deployable Underwater Test Range (UTR) for Verification and Validation (V&V) of AUVs autonomous navigation performance. The UTR design for performance prediction provides a mechanism for assessing the ability of an AUV to fulfill long-range mission performance requirements under such constrained environment. The UTR methods and analysis tools developed in this thesis are generally applicable to any UMV.

To summarize the general picture, the primary application of interest to this broad research work is the validation of AUV autonomous navigation for very long-term missions, aiming at a highly persistent AUV, which can remain on-task in the face of weather that would abort the operations of an Unmanned Aerial Vehicle (UAV) or Un-

manned Surface Vehicle (USV), simply by submerging to a calmer depth or switching to a *loiter* mode, exploiting environmental energy for recharging and/or navigating.

The focus on this particular application was motivated in large part by the collaboration in this research between the Naval Support and Experimentation Center – *Centro di Supporto e Sperimentazione Navale*, in Italian – of the Italian Navy (CSSN) and the Interuniversity Research Center of Integrated Systems for Marine Environment (ISME), called *SEALab* (Autonomous Heterogeneous Systems Laboratory – *Laboratorio sui Sistemi Eterogenei Autonomi*, in Italian). It is an applied research laboratory established in 2015, with the main goal of jointly develop and manage research and experimentation activities of common interest in the field of heterogeneous and autonomous marine systems with dual-use purposes, as well as the relative modeling and simulation framework. This collaboration enables both Centres to have mutual access to experimental and logistic facilities, including the free usage of the reserved marine area for experimental trials in La Spezia (Italy) gulf. Furthermore, this collaboration strongly favors a fast transfer of ISME research activities to engineering personnel of the Italian Navy on one side, and it provides valuable operational feedback to ISME during the developmental stages on the other. The *SEALab* collaboration framework enabled the algorithms and methods presented in this thesis to be developed and demonstrated on real systems in the field.

1.2 Goal of the Thesis and Main Contributions

This thesis addresses the outlined limitations by providing two new capabilities for enhanced autonomy in underwater vehicle operations: (1) a prototype to be integrated in an AUV, designed to powerfully extend the vehicle endurance both by exploiting environmental energy sources (wave motion and solar energy) and by making it capable of combining three different types of underwater missions (wavegliding, underwater gliding, and conventional navigation with propeller and engines), and (2) design, analysis and experimental evaluation of an underwater tracking system based on bearing-only sensors, with non-linear Kalman filtering approach, for the validation of AUV navigation systems.

The development of these new capabilities resulted in several important contributions to the field of autonomy in AUV operations:

1. *First-ever successful AUV payload design, implementation, and testing for exploiting wave energy.*

   The Wave-powered Autonomous Vehicle for marine Exploration (WAVE) project is presented in the thesis, which aims to further develop the technology for autonomous long-term marine exploration and surveillance by exploiting energy from environmental renewable sources, *i.e.* solar and wave energy, as potentially unlimited power supply. In particular, the design and the prototypal realization of a hybrid oceanographic glider/AUV with battery recharging capabilities from the wave motion were considered within the project. The presented results offer the possibility to define in a much more targeted way the field of use of the module, as well as several guidelines to improve its efficiency. It is worth to note that the energy recovery system of the WAVE module is currently *unique* in the world;

the WAVE prototype is, in fact, the first experimental example of an autonomous underwater vehicle capable of energy recovery from wave motion.

2. *Comparative analysis of the experimental performance of the WAVE module.*

   The developed wave energy harvesting system was experimentally demonstrated and characterized. Energy harvesting performance in a controlled environment with several configurations of the WAVE module was described. For all the performed tests, generated electric power was indirectly computed from measurements of current and voltage. This procedure allowed a qualitatively understanding of the effect on the generated electric power due to wing shape and mounting configuration (position, direction, and angle), and to module buoyancy and position. This analysis identified new performance factors crucial to successful wave energy harvesting with the proposed prototype.

3. *A modeling and simulation framework for understanding the WAVE performance variation with respect to different parameters.*

   The collected experimental results constitute a solid reference database for a critical tuning of the dynamic model of the system characterized during the first phase of the project, thanks to the comparison of simulative and experimental data. This way, the overall simulator was validated and it gives confidence in the simulative predictions carried out. The combination of the experimental and calibrated simulative results will allow a further analysis on the achievable performance in terms of both expected wave energy harvesting capability and also wave-gliding navigation skills with respect to the vehicle consumption.

4. *Design of an Underwater Test Range for the validation of autonomous underwater navigation capabilities.*

   A comprehensive method to evaluate vehicle navigation performance in an appropriate marine test range was studied and implemented. The UTR main concepts, design choices, and theoretical formulation are given to have an exhaustive overview of the problem. The inevitable effect of uncertainty in the knowledge of sensor positions on tracking performance is accurately described. The impact of the mismatch between ideal and actual sensors location is illustrated with extensive simulations.

5. *Application and related improvements obtainable through non-linear Kalman Filters: the Extended Kalman Filter (EKF) and the Unscented Kalman Filter (UKF).*

   A contribution of this work involves developing estimation algorithms for the 2D bearings-only target localization problem. In particular, an EKF and an UKF are designed for many tracking scenarios. The resulting performance of the filtering algorithms shows that these methods can be used to track stationary and moving targets. Furthermore, the effectiveness of the UKF in bearing-only target localization in presence of unknown sensors position is shown through a precise comparison with the EKF performance. Comprehensive simulative analysis, considering a bearing measurements noise variance consistent with previous authors experience, confirm the improvement obtainable using UKF instead of EKF in estimating the position of a cooperative target. Our evaluations indicate that an UKF-based filter

offers better performance than EKF in both ideal and realistic assumptions on a localization network.

6. *In-field implementation and testing of the envisioned underwater test range.*

   A first experimental assessment of a tracking system for underwater vehicles based on bearing-only sensors was made. Data processing included an initial phase of system calibration and sensors characterization. Results of this step are an essential base for the further carried out analysis and for the future of this research activity.

   The experimental campaign provided several ideas for improvements along the research path towards the described vision perspective. In particular, following steps will aim to extend the UTR using moving sensor platforms that can operate in deeper water and implement an optimal geometry control for tracking performance maximization. A distributed approach exploiting range measurements between USBL sensors and the AUV under test could further ameliorate the UTR performance, by turn involving the study of proper Medium Access Control (MAC) policy to ensure the sharing of the acoustic channel without collisions between the different sensors.

As the following chapters will show, the methods and prototypes developed in this thesis provide previously non-existent solutions to the problem of long-endurance and autonomous navigation assessment in underwater vehicle operations. The improvement of endurance with environmental energy harvesting along with the in-depth analysis of underwater autonomous navigation validation developed in this thesis theoretically enables several mission types not possible with existing vehicles, *e.g.* long-range navigation in silent mode reaching hostile scenarios.

Finally, after the description of the research antecedents and motivation, the goal of this thesis is stated. The general purpose is summarized as:

> The improvement of the hardware and software of an autonomous underwater vehicle in order to be fully operational in autonomous mode for long-range and long-term missions, with high precision in navigation and in the consequent georeferencing of data. Methods have been found that could take advantage of the great availability of environmental energy present in the marine environment, both solar and wave energy, present even in rough weather. In order to be sure that in critical missions, *e.g.* ISR in enemy areas or exfiltration of hostages, underwater navigation performances are highly reliable, precise tracking algorithms of an AUV have been implemented and tested at sea for navigation performance validation.

1.3 Thesis organization

The general research path of this thesis is pervaded by a holistic approach towards AUV operations autonomy. Consequently, several bridgings are made between different topics throughout the text. Nevertheless, the state-of-the-art of the two main perspectives addressed is necessary to the reader for the sake of understanding the potential of the proposed solutions. To perform this, the thesis is divided into two parts of four chapters each.

This first part of the thesis deals with the study, development, and testing of a novel system for both energy harvesting from the wave motion and low consumption propulsion, to be integrated on a generic, modular, torpedo-shaped AUV. In Chapter 2, unmanned maritime vehicles classification is reviewed and a description of the vehicle used for the research is carried out. Chapter 3 then presents the concept, the modeling and the prototype developed in the project WAVE, an Italian National Research Projects of Military interest (PNRM) concluded in October 2017. Chapter 4 describes the experimental data analysis where energy recovery performance is reported and discussed, providing insight into the effectiveness of the WAVE prototype. In order to extend the characterization, Chapter 5 depicts the dynamic model of the system implemented during the first phase of the project and its critical tuning after the experimental campaign. Finally, the simulative predictions of the recharging and wave gliding capability conclude the first part of the thesis, suggesting directions for future work related to this topic.

The second part of the thesis is dedicated to the design, implementation, and testing of an UTR for autonomous navigation validation. Chapter 6 reviews state-of-the-art underwater localization and tracking technologies, defining a taxonomy to classify the different methods. In Chapter 7, the UTR theoretical problem formulation is presented, providing the modeling of both the cooperative target and the observations adopted in the Kalman Filters (KFs) implemented. In addition, the approach to investigate the effect of perturbated sensor positions on filters performance is described, along with the UTR network architecture and optimal sensor placement algorithm. The simulative results are reported and compared in Chapter 8. Finally, Chapter 9 reports the overall experimental set-up and at-sea trials, emphasizing the involved autonomous assets and the algorithm implementation. Future envisioned extensions are planned, like optimal control strategy of moving sensor platform and distributed tracking approach, falling in the broader design of an UTR with enhanced capabilities.

Part I

Wave energy harvesting for long-endurance AUV

Research in the sea and oceans is a timeless challenging area of science due to its complexity and its global importance. It comprises several disciplines and involves many technological tools for effective exploration of the vast blue economic resources, monitoring of the oceans for understanding the changing climate patterns, marine pollution monitoring, military applications and Search And Rescue (SAR) tasks. As response to these needs, unmanned vehicles were developed beginning in the 50's decade. These vehicles were designed first for military operations (as mine counter measures, anti-submarine warfare and rapid environmental assessment), and later their development was extended to industry and scientific surveys. In fact, the ability of unmanned vehicles to operate autonomously of a host deployment vessel along with scientific payloads including geophysical, geochemical, sea floor imaging and oceanographic instruments enables them to be effective in carrying out exploration in remote and challenging environments, from the world's deepest hydrothermal vents to beneath the Polar ice shelves, and making them well suitable for applications in the areas of oceanographic research, defence, offshore industries, search and rescue activities and policy sectors [51, 210, 219].

With its broad capabilities, the global AUV market - which was about US$ 0.3 billion in 2017 - is forecasted to reach US$ 1.2 billion in 2023 and the global AUV fleet is projected to reach 825 units in 2018, a 42% increase compared to 2014 [154, 207, 216]. Indeed, long range AUVs capable of travelling thousands of kilometres over a period of weeks to months before needing to be recovered are currently receiving significant interest to enable end-users to carry out increased and continuous spatio-temporal tasks without the need for a dedicated deployment vessel.

CHAPTER 2

Overview of unmanned maritime vehicles and the Folaga AUV

2.1 Unmanned Maritime Vehicles

Figure 2.1 shows the most accepted general classification of UMVs, recently formalised by European Defence Agency (EDA) in the framework of Unmanned Maritime Systems - Standardisation Technologies (UMS-ST) and Safety and Regulations for European UMS (SARUMS) projects. The first main division is between USVs and Unmanned Underwater Vehicles (UUVs). USVs include two different types of Autonomous Surface Vehicles (ASVs), which can be propelled or use the waves energy for propulsion (Wave glider [140]). ROVs, which are generally tethered, and AUVs, which may have different levels of autonomy, are considered UUVs. The AUVs can be subclassified as propelled AUVs, underwater gliders and biomimetic AUVs. Each vehicle class can ensure different temporal and spatial resolution, and can cover various extension of operative area with their own movement type and source of energy for its propulsion. Short descriptions of each UMV class are provided in the next sections to highlight their characteristics and capabilities in different marine environments.

2.1.1 Autonomous Surface Vehicles

Autonomous Surface Vehicles are vehicles that operate at or near the sea surface with no operators on board, although it may have the capability of being manned for testing, troubleshooting or when required for a manned mission. Depending on practical applications, ASVs may come in a variety of appearances and functionalities. However, some basic elements must be included in every vehicle (Figure 2.2). ASVs are generally self-propelled, but there is a unique vehicle called Wave Glider [140] which

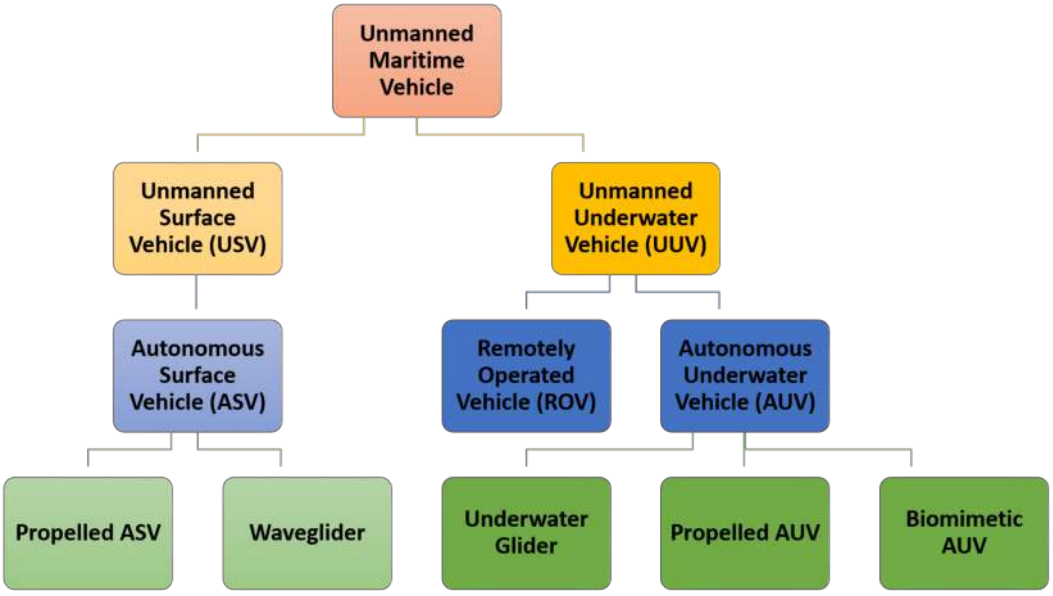

Figure 2.1: *High-level Unmanned Maritime Vehicles classification.*

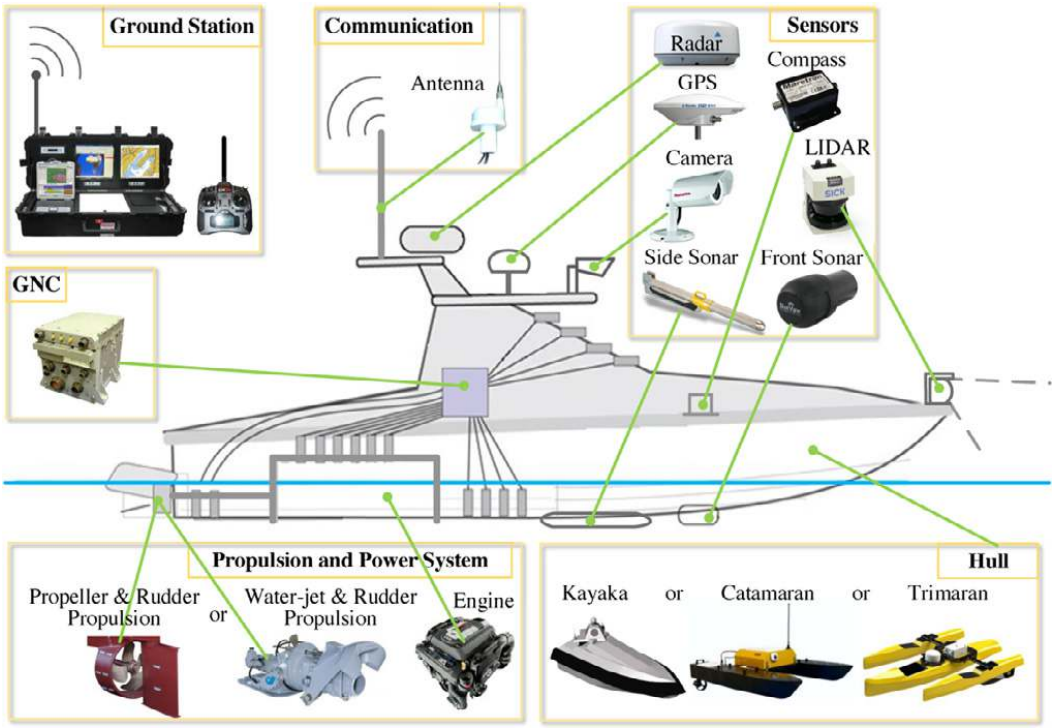

Figure 2.2: *Fundamental architecture of a typical ASV. From [134].*

uses ocean wave energy for platform propulsion, so it has the robustness for extended mission durations through many weather conditions.

They are valuable in lowering the costs and improving the efficiency with respect to operating oceanographic vessels at sea [12, 18, 136]. In fact, conventional oceanographic missions require a large crew and are costly to carry out, while they typically consist of routine operations that could in principle be performed by ASVs capable of automatically acquiring and transmitting data to the on-shore control station. In the future, the use of multiple autonomous surface vessels will enable scientists to perform their data analysis while following remotely the execution of missions at sea from their laboratories. Moreover, this may give them the opportunity to change the ongoing mission in order to perfectly fit the phenomena under study.

From military application point of view, ASVs are tactical systems capable of different missions: for example Mine Countermeasures (MCM), Anti-Submarine Warfare (ASW), Maritime Security (MS) and Maritime Interdiction Operations (MIO) Support [157, 165]. ASVs have the ability to continuously communicate with suitably-equipped surface, air and underwater assets. Mission requirements and currently available technologies result in USVs having varying levels of autonomy.

Despite their growing capabilities, two areas can be identified as mainly defective [220]:

1. Intelligence: the ASV must be able to operate independently of constant operator supervision, navigating safely to complete its task. The USVs must be able to detect environment, identify targets, avoid obstacles, autonomously plan and change paths. One of the more difficult issues related to autonomy is operating in a highly dynamic environment with other vehicles operated by humans and respecting the International Regulations for Preventing Collisions at Sea, known as COLREGS [2, 124].

2. Navigation stability and ASV control: ASV is expected to perform its task even in rough sea conditions. Therefore, stability and anti-capsizing are big issues for ASVs. The ASV GNC (Guidance, Navigation and Control) system should be able to stabilize the hull to prevent excessive deck motion or capsizing and determine the optimal course and speed for the given wave, wind, and current environment. In the worst case scenario, the vehicle may get upside down, so a device for recovering the vehicle back to normal is essential. On the other side, increasingly fast ASVs require new hull forms to take full advantage of the fact that the vehicle is unmanned.

A detailed state of the art, with an overview of the main developed prototype ASVs and their basic design issues, can be found in [22, 134, 139, 148].

2.1.2 Remotely Operated Vehicles

Under the sea surface, the use of Remotely Operated Vehicles (ROVs) is rapidly increasing for widespread applications such as pipeline surveys, cable maintenance and other inspection and intervention tasks on underwater structures, in addition to fields such as marine biology, environmental monitoring, seafloor mapping, oceanography and military use [15, 49]. ROVs are tethered to, powered by and operated from a surface vessel, implying high operation costs and requiring experienced human operator.

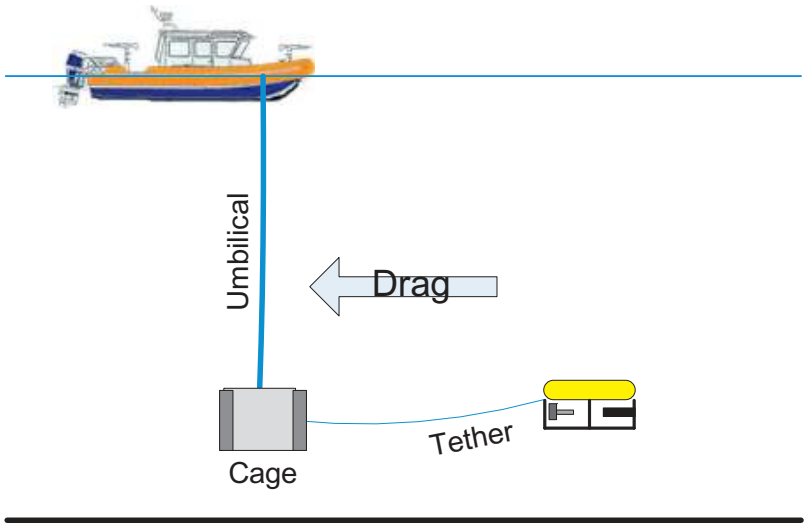

Figure 2.3: *Cage deployed ROV. In essence, the TMS can be part of a cage or top hat deployment system while most operators refer to it as the entire system of cage deployment, tether management, vehicle protection, and junction point for the surface-to-vehicle link. Technically, the TMS is the tether-handling machinery only. Image from [49].*

Tethered robot means all the control systems and the energy transmission are supplied through a cable (also called umbilical) from the ship from which it is operated. The length of the tether changes with the working depth of the ROV, which can be up to 6000 m deep. This fact makes ROVs inherently not fully autonomous. However, the power supply through the wire entails a bigger endurance for the vehicle, providing it with the power to use up to 8 thrusters in order to obtain an extremely precise position and attitude, and to use one or two robotic arms in order to perform manipulation tasks. For this reasons, ROVs rarely have hydrodynamic shapes while typically present a symmetrical design, generally with a rectangular aspect.

ROVs for very deep applications use a Tether Management System (TMS). Within the ROV industry, there is no general agreement on the exact definition of a TMS. Technically [49], the TMS is the subsea tether-handling mechanism (only) allowing the soft flying tether to be payed out or taken up from the junction between the clump/depressor weight and the tether for a better management of the cable, avoiding the entanglement of wires and decreasing the drag induced to the cable by the waves and sea currents (Figure 2.3). But by common convention, the TMS is typically described as the entire subsea mechanism from the end of the umbilical (umbilical termination to the clump/depressor weight, cage or top hat) to the beginning of the tether. The vehicle handling system (subsea cage or top hat) houses the tether-handling mechanism as well as the vehicle itself and is launched with the vehicle either within the cage or attached to the top hat mechanism. Figure 2.4 shows the Panther XT Plus manufactured by SAAB Seaeye company inside its TMS in the deployment phase.

The ROV market is substantially segmented into four broad categories based upon vehicle size and capabilities:

1. Observation Class ROVs (OCROV): These vehicles go from the smallest micro-ROVs to a vehicle weight of 100 kg. They are generally small, DC-powered, inex-

Figure 2.4: *Panther XT Plus ready in its TMS. The Panther-XT Plus is a* 1000 *m rated ROV fitted with ten 500 VDC thrusters (eight horizontal and two vertical). It can be used as a free swimmer or in conjunction with a TMS. Image from* `http://www.saabseaeye.com`

pensive electrical vehicles used as either backup to divers or as a diver substitution for general shallow water inspection tasks. Vehicles in this classification are generally limited to depth ratings of less than 300 m and are typically hand launched from the surface with hand tending of the tether.

2. Mid-sized ROVs (MSROV): These vehicles weigh from 100 to 1000 kg. They are generally a deeper-rated version of the OCROVs with sufficient AC power delivery components and pressure housings capable of achieving deeper depths over longer tether/umbilical lengths. These also are generally all-electric vehicles (especially thrusters and camera movement controls) with some hydraulic power for the operation of manipulators and small tooling package options. Vehicles in this classification are sometimes termed "light work class" vehicles to fully differentiate them from OCROVs. Due to the weight of these vehicles, a Launch And Recovery System (LARS) as well as a TMS is often needed.

3. Work class ROVs (WCROV): Vehicles in this category are generally heavy electromechanical vehicles running on high-voltage (3000 V) AC circuits from the surface to the vehicle. The power delivered to the vehicle is converted immediately to mechanical (hydraulic) power at the vehicle for locomotion as well as all manipulation and tooling functions.

4. Special-use vehicles: Vehicles not falling under the main categories of ROVs due to their non-swimming nature such as crawling underwater vehicles, towed vehicles, or structurally compliant vehicles (i.e., non-free-swimming).

Table 2.1 depicts representative vehicle configurations and power/telemetry requirements.

Table 2.1: *General representative ROV characteristics.*

ROV Class	Input Power (VAC)	Vehicle Power	Telemetry Type	Depth rating (m)	Launch method	TMS	Thruster - Tooling	Tooling fluid flow (lpm)	Typical cost ($)
OCROV	110/220	Low-voltage DC	Copper only	300	Hand deploy	No	Electric only	Not applicable (Electric only)	100000
MSROV	440/480	Medium voltage DC or AC	Copper or fiber	> 1000	Crane or A-frame	Optional	Electric - Hydraulic	15	1.5 million
WCROV	440/480	High-voltage AC	Fiber only	> 3000	A-frame	Yes	Hydraulic only	70	5 million

Configurations vary within each category from vehicle to vehicle, but these represent the general characteristics of vehicles within the specified size category.

Finally, typical military missions for ROVs are outlined. Military applications for ROVs provided the genesis for UUV technology [156]. Initially, such systems were developed primarily for undersea observation and the recovery of lost devices and weapons. Since then, the technology has moved steadily forward, bringing with it a directly related increase in operational capability. Today, ROVs play a critical role in military applications involving three basic functions: MCM, object retrieval/recovery (torpedoes and mines), and inspection/security tasks. For the MCM mission, the ROV is sent to a location of targets identified through other sensors or means (mine-hunting sonar, laser line scanners, intelligence, etc.). Once the mine is located, some form of end effector is required in order to neutralize the mine for final disposition. For the MCM mission, the predominant vehicle is a special-use explosives delivery platform whereby the vehicle delivers a charge and then egresses the area for detonation. This charge delivery-then-evacuation vehicle is typically an MSROV with advanced forward looking sonar and a dexterous modular electric manipulator capability. Figure 2.5 shows two examples of these ROVs well-known for military applications.

For the object retrieval ROV, a heavy-duty WCROV is needed along with hydraulic manipulators and deep water capabilities. The inspection/security vehicle is clearly an OCROV with minimal sensor and tooling requirements.

2.1.3 Autonomous Underwater Vehicles

Autonomous underwater vehicles are conceived for autonomous navigation without the help of an operator. They do not use a tether for communication or power supply, and have instead an embedded control and a pack of batteries in order to power up all the sensors and actuators needed in their mission. This type of vehicle usually has an optimized hydrodynamic shape in order to improve its performance and decrease power consumption, i.e. they are almost all torpedo-shaped vehicles. The origin of AUVs should probably be linked to the Whitehead Automobile "Fish" Torpedo [208]. Torpedoes are named after the Torpedo fish, which is an electric ray capable of delivering a stunning shock to its prey. Whitehead's first torpedo achieved a speed of over 3 m/s and ran for 700 m. If one ignores the fact that it carried an explosive charge,

(a) (b)

Figure 2.5: *Two examples of ROVs largely used in the Navy community for mine identification and disposal up to* 600 *m. (a) The Pluto Gigas ROV, manufactured by idRobotica (*`http://www.idrobotica.com/pluto-gigas.php`*), while deployed from an Italian Navy Mine Hunting Vessel. (b) The Saab Double Eagle MKIII ROV (*`https://saab.com/naval/underwater-systems/remotely-operated-vehicles/double_eagle_mkii_iii/`*), with its rotatable multi-frequency sonar for detection and classification of mines.*

it might be considered the first AUV. Indeed, the first "true" AUV can be considered the Self Propelled Underwater Research Vehicle (SPURV) developed at the Applied Physics Laboratory of the University of Washington in the late 1950's. The SPURV-I, operational since the early 60's, supported research efforts through the mid 70's mainly making extensive Conductivity and Temperature (CT) measurements along isobaric lines in support of internal wave modeling [75].

Since then many universities and institutions have taken up the task of developing improved vehicles adapted to new requirements. Due to the limited power, AUVs are mainly dedicated to observation and data recollection, letting manipulation tasks to ROVs. However, in the last decade there have been AUV for intervation, called I-AUVs, like the Girona 500 [177]. AUVs are flexible and suitable for military, scientific or offshore uses.

A quick overview of the different capabilities and applications for the three AUVs' subclasses are described below.

2.1.3.1 Underwater glider

A particular case of AUV is the underwater glider, which uses small changes in its buoyancy by active ballast variation and displacement in conjunction with wings to convert vertical motion to horizontal. In fact, once the system is negative/positive buoyant and it has the appropriate pitch, the vehicle control surface will produce a net movement in the horizontal plane with very low power consumption [215]. Gliders follow an up-and-down, saw-tooth like profile (also known as yo-yo motion) through the water. Each time the vehicle resurfaces, it gets into GPS/satellite contact, transmit the data to a ground station, and receives further indication on the next route to pursue. Due to its movement, gliders are used for data collection in environmental surveys and other scientific studies. While not as fast as conventional AUVs, gliders using buoyancy-based propulsion represent a significant increase in range and duration compared to vehicles propelled by electric motor-driven propellers, extending ocean

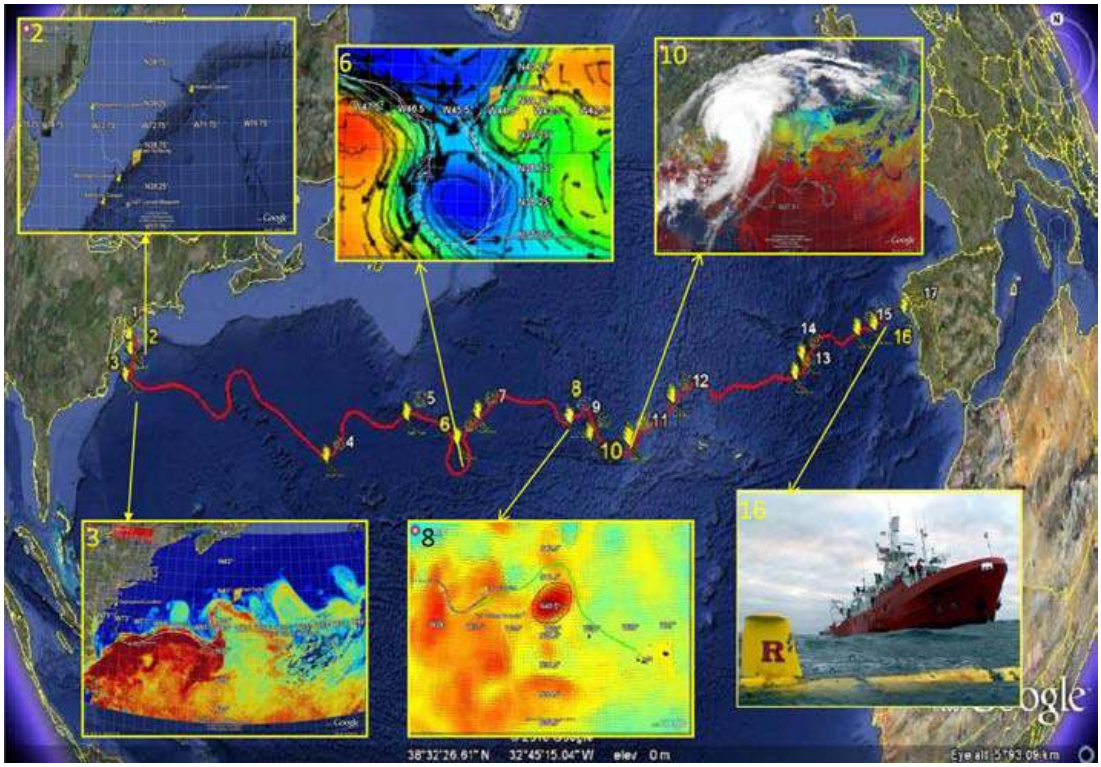

Figure 2.6: *From [90]. Track of Scarlet Knight (SK) with 16 significant events marker. Insets: (2) SK leaves the shallow water and fishing activity of the Mid-Atlantic Bight continental shelf; (3) SK navigates the meandering warm jet of the Gulf Stream flowing from Cape Hatteras to the Grand Banks; (6) SK, after encountering a strong head-current, flies around the southern side of a large cyclonic cold-eddy; (8) SK approaches the Phantom Eddy in the HyCOM forecast, an artifact generated by the data assimilation scheme; (10) Hurricane Bill leaves the U.S. East Coast and turns east toward SK; (16) RU27 is approached by the Spanish R/V Investigador for recovery (photo by diver Dan Crowell).*

sampling missions from hours to weeks or months, and to thousands of kilometers of range. They have already largely shown the ability of conducting ocean sampling mission of several months length [103], demonstrating high versatility in terms of mission reconfiguration and adaptation, also in coordinated missions with manned-unmanned platforms [126].

A famous example of these is the Scarlet Knight [204], the first submarine robot to cross the Atlantic Ocean (Figure 2.6). This record was reached in 2009, traveling from New Jersey (USA) in April and finishing in Baiona (Spain) in December, 221 days in total. The Slocum Glider *flew* over 7400 km, exploiting 200 m of water column, and used about 28 MJ, *i.e.* approximately 76 % of the available energy demonstrating the low consumption of gliders [110]. Although the transatlantic crossing was certainly a tremendous technical achievement, it was also a significant historical success because it was made possible thanks to educational and international outreach that this collaborative effort spawned. As a result, Rutgers University (RU) start to lead a foreign exchange student program, began a virtual Atlantic Crossing class that drew a diverse range of students, and increased heavily the undergraduate participation in lab activities [90].

(a) (b)

Figure 2.7: *The underwater snake robot Mamba implemented the at Norwegian University of Science and Technology. (a) Mamba moves inside a dummy underwater structure. (b) Mamba in the pool with the markers attached on the tail for position measurements.*

2.1.3.2 Biomimetic AUV

Inspired by the outstanding capabilities of soft animal and plant structures, researchers have developed biomimetic AUVs that copy the propulsion system directly from the animal world using electroactive polymer (EAP) and pneumatic artificial muscle (PAM) actuators. There are plenty of different models, but all are based on the movements of marine species such as jelly fish, tuna, octopus or rays. Nature-inspired design, exploited and implemented into a mechanical structure, may lead to improved efficiency and reduced consumption of underwater vehicles. A detailed state of the art and future research is presented in [118].

Figure 2.7 shows the Mamba snake robot, an example of these vehicles [117, 132]. This is a biologically inspired swimming snake robot created at NTNU (Norwegian University of Science and Technology) in the last five years which carry the potential of meeting the growing need for robotic mobility in underwater environments. This biomimetic AUV has a long, slender, and flexible body, enabling it to reach and operate in locations not accessible by larger and more conventional underwater vehicles. At the same time, a swimming snake robot carries manipulation capabilities as an inherent part of its body since it is essentially a mobile manipulator arm.

2.1.3.3 Propelled AUV

Unlike for ROVs, in the early '90s there was no commercially available AUV, *i.e.* a vehicle without a tether able to fulfill a mission in a completely autonomous way, mainly because of the difficulties linked to the absence of any kind of communication between the vehicle and a (manned) base station. In fact, without tether and without possibility of communicating with the vehicle, all the analysis of the navigation and experimental data must occur offline, in a post processing phase - if the vehicle has survived the experimental mission from the launch to the recovery phases. Tank tests are important, but not representative of the behavior at sea; and the risks associated to experimentation at sea foreclosed most of the research labs to assess their prototypes at sea.

In the '80s several USA research programs begun to provide significant funding to develop proof of concept prototypes. In particular, Draper Labs developed two large-scale, torpedo-shaped vehicles as test-bed for Navy projects [27]. It was clear and agreed that AUVs would find an important role into operational systems, but the technology was not mature enough to answer the high expectations raised by the researchers

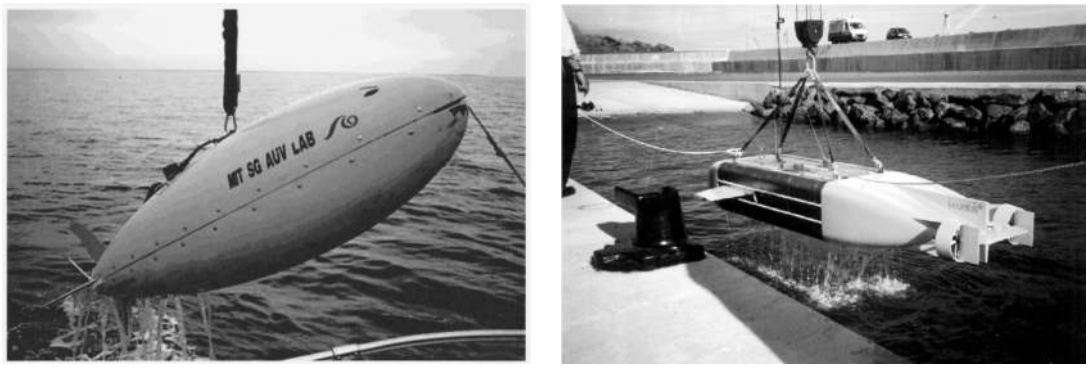

(a) (b)

Figure 2.8: *Two examples of research AUVs developed in the '90s. (a) An Odyssey IIB AUV, by MIT lab, being recovered after operations. (b) The Marius AUV designed and built by a multidisciplinary team of scientists and engineers from Denmark, France, and Portugal, with support from the MAST (Marine Science and Technology) Programme of the European Commission.*

themselves to gain support for the research program; very expensive experimentations had limited success leading to scepticism from the defense users on the whole AUV concept throughout the early '90s.

In parallel to the ambitious military-oriented programs, there were research groups focusing on the development of smaller vehicles for inspection and mapping purposes (Figure 2.8). Among these, the MIT group in the USA developed the Odyssey AUV [20] while in Europe the European Union sponsored the project that led to the MARIUS AUV [164]. A vision for the future of operational oceanography was put forward in [61], a famous paper in which the concept of Autonomous Ocean Sampling Network (AOSN) was formulated: it was envisioned that future oceanographic measurements would take place through a combination of fixed and mobile autonomous sensors, including AUVs, all connected in a network, some installed permanently, some deployed on demand, according to the evolution of the oceanic features of interest. As a matter of fact, AOSN has become an operational reality with the series of experiments in Monterey Bay which started about 15 years after the original paper [19].

By 1994 there was a growing awareness in the research community that the field was effectively maturing [225]; the second half of the '90s saw several initiatives that did address the critical technologies outlined in the cited report. In particular, Kongsberg Maritime in cooperation with the Norwegian Defence Research Establishment (FFI), the national oil company Statoil, and with additional support by university labs, developed the famous HUGIN class AUV designed for seabed and sub-bottom mapping surveys in deep water (Figure 2.9, [95]). Kongsberg found great success mainly thanks to the development of a fundamental in-house skill: the High Precision Acoustic Positioning (HiPAP) system for underwater localization and communication. It gave the possibility to monitor the mission from a surface ship providing georeferentiation to the vehicle. The Hugin 3000, rated to 3000 m depth, completed its acceptance and qualification tests in year 2000. The reliability of the system, despite its costs and the need of a surface platform to follow it during operation, made it an immediate success and gave special momentum to the AUV development. Now the HUGIN AUV is the indus-

(a) (b)

Figure 2.9: *Kongsberg Maritime milestones for AUV spread. (a) The HUGIN 1000 AUV being launched by a Norwegian Navy ship during deployment in MCMFORNORTH, Baltic Sea, 2004. (b) Clockwise from top left: HiPAP Acoustic Positioning Operator Station (APOS), hull unit with HiPAP transducer, the HiPAP family trandsducers (model 100 - 350 - 500).*

try standard for AUV-based offshore oil and gas surveying, having covered a collective distance of more than 120000 km on the seabed for offshore survey companies (from Kongsberg Maritime website, `www.km.kongsberg.com`). One particular aspect, from the commercial side, was the demonstration of the HUGIN superiority compared to equivalent deep-tow systems for survey [96]. For example in [46] Chance et al. indicated $4\tilde{}6$ hours as typical turn time when operating towed systems in deep water — while a well-designed AUV can do a $180\,^\circ$ turn in less than 30 s, regardless of depth, currents or other constraints. Moreover, data quality from the HUGIN AUV was better than what it was expected by customers. The success of the initiative led to the development of a defense version of the vehicle, and to yet another version for exploration of deeper sites (up to 6000 m) [94].

In the same period there were other two remarkable initiatives. The MIT group launched a long-term experimentation program together with the former NATO Undersea Research Centre (NURC) in Italy, now Centre for Maritime Research Experimentation (CMRE). The GOATS (Generic Ocean Array Technology Sonar) program allowed a series of test with the new-generation Odyssey vehicles employed as platforms for acoustic and oceanographic sensors. One of the clever aspect of the initiative was its openness to participation of research group from all over the NATO countries, with NURC making available its sea-going facilities and experience [29].

Finally, the development of the REMUS AUV was started in the second half of the ‘90s at the Woods Hole Oceanographic Institute (WHOI) [4]. The REMUS (Figure 2.10) is a very small, lightweight vehicle, specifically designed for coastal oceanography, easy to handle and deploy, and with costs of more than an order of magnitude less than the HUGIN. The WHOI team developed in the same years also the acoustic “Micromodem” [86] installed on the REMUS for both localization and communication. Of course the application domain of the REMUS was intended to be complementary to that of the HUGIN; but it was an interesting demonstration on how, focusing on the mission, it was possible to dramatically reduce the budget cost of the research, development and technology transfer, while reaching the mission goal. The potential of the REMUS

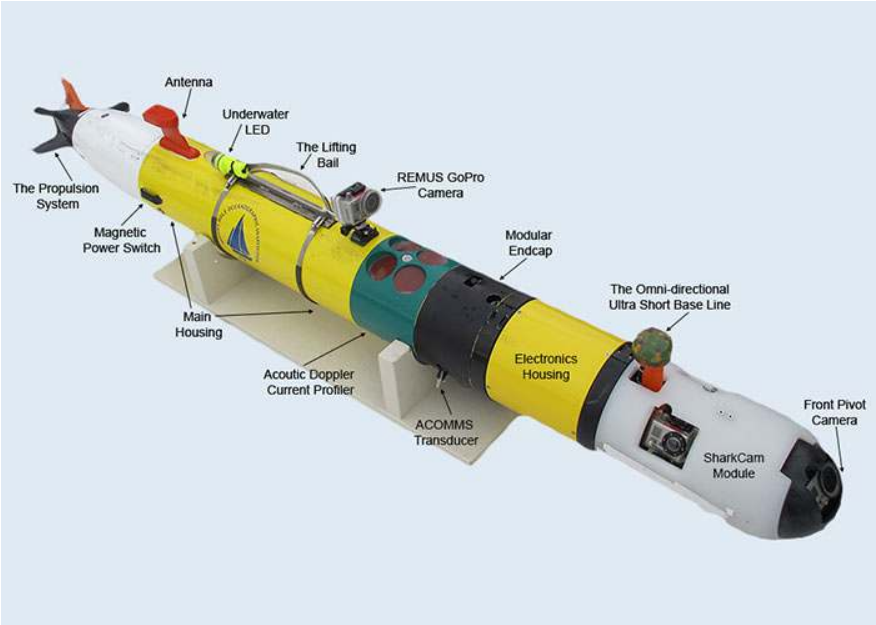

Figure 2.10: *A schematic view of a possible configuration of a REMUS 100 vehicle by WHOI. The strength of REMUS is its versatility. REMUS is commonly referred to as a pick-up truck, allowing the vehicle to carry a plethora of sensors. Indeed, because of REMUS' small size, it can be operated with only two people and can be launched and recovered from a small vessel with very minimal handling equipment.*

caused a renewed enthusiasm in Navy circles, and WHOI was asked to develop a Navy version to be employed in Mine Counter Measurements operation [197, 209]. REMUS vehicles are used in operational missions by the US Navy since 2003. In addition, REMUS has been brought to the market by WHOI spin-off Hydroid, which in turn has been acquired by Kongsberg Maritime.

In general, the HUGIN and REMUS projects, as well as the GOATS program, were instrumental in gaining visibility and appreciation from the users community, and at the end of the '90s the degree of confidence in the potential of AUVs was high both in the scientific and the defence community.

Presently, there are plenty of autonomous vehicles commercially available and relied upon by the user communities [154, 207, 216]. There is not yet widespread user exploitation of autonomous cooperative missions with AUV teams. This reflects the fact that, despite recent successful research experimentation [6, 39], the field is not mature enough, and research efforts have still to be exerted along this line. The underwater communication problem now moves from point-to-point communication to networked communication, since we do not expect to have simply a team of two vehicles. The acoustic communication channel is a time-varying, space-varying channel, with strong delays, limited bandwidth, fading and interference caused by multi-path acoustic propagation effects [196]. As autonomy increases, the need of longer operational hours increases as well; another research front that will play a key role in the future is that of energy efficient vehicles and battery reliability, possibly with renewable energy. Finally, AUVs involved in long duration deep water missions and operating without the aid of ship-based acoustic positioning systems require high precision on-board naviga-

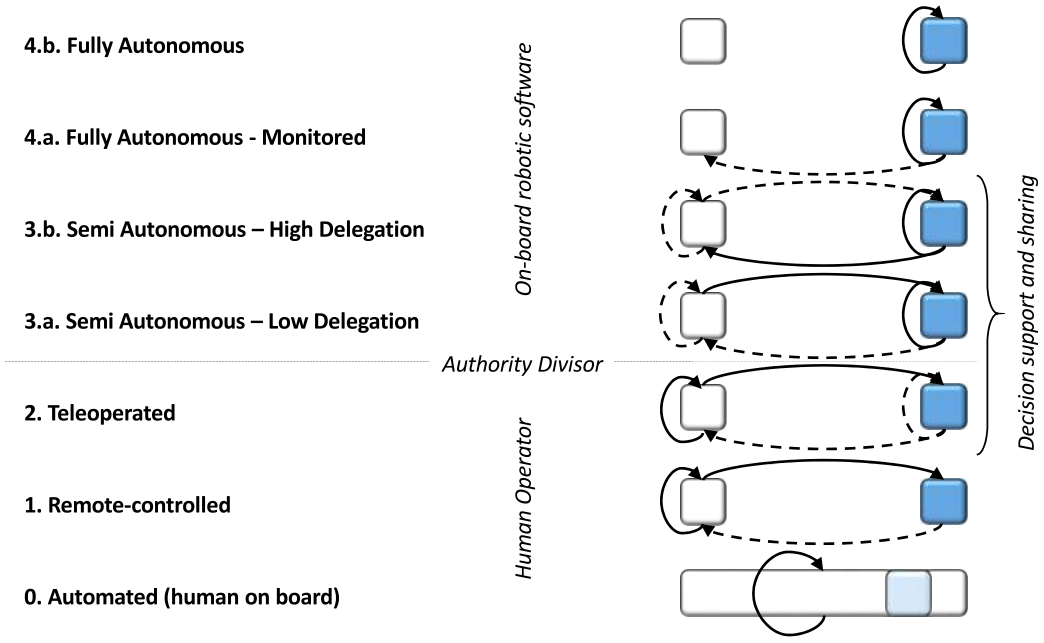

Figure 2.11: *Illustration of autonomy levels. White boxes represent human operators while blue boxes represent robots. Filled arrows indicate data and/or information based on initiative and authorisation that imply action in real world. Dotted arrows indicate data and/or information of less impact for the evolution of events. A loop around a box represents internal reasoning and cognitive capability/function. Arrows between boxes represent data and/or information flowing between humans and robot.*

tional system for the purpose of effective navigation and georeferencing itself in real time.

2.1.4 Autonomy Taxonomy

Extensive discussions have been conducted within the SEALab to define a shared taxonomy regarding autonomous robots focused on their autonomous capabilities, *i.e.* what exactly means "autonomous". Autonomy can be defined as a capability (or a set of capabilities) that enables a particular action of a system to be automatic or, within programmed boundaries, *"self-governing."* Autonomy is the UMV's own ability of sensing, perceiving, analysing, communicating, planning, decision-making, and acting, to achieve its goals as assigned human operators.

Autonomy may be characterized into levels with respect to factors including mission complexity, environmental difficulty, and level of operator interaction to accomplish the missions. This section describes the proposed taxonomy that does not aim at being formally rigorous, but rather it has the purpose of defining a common language for clarity of communication, lacking a reference agreed in the literature. The main referenced papers are [106, 160, 184], where the interested reader can find more formal definitions. What follows is the description of the five autonomy levels identified in ascendant order of autonomous capabilities for a robot. An illustration of the five autonomy levels is presented in Figure 2.11.

0. Automated robot performs tasks as a deterministic succession of states, following

pre-scripted plans and/or without adapting to changes in the environment. A typical industrial example is a Computer Numerical Control (CNC) machine. A typical UMV example is a vehicle with human operators on board who drive and control it.

1. **Remote-controlled robot** performs tasks in which a human operator controls the robot continuously, without benefit of video or other sensory feedback, directly controlling the actuators and maintaining the line of sight with the vehicle. In this mode the robot does not take initiatives and relies on the continuous (or almost continuous) input of the operator. A typical example is the remote control of an air or surface vehicle, based on the direct view by the operator of the vehicle movement and the operational situation.

2. **Teleoperated robot** performs tasks in which a human operator, using robot sensory feedback, either directly controls the actuators or assigns incremental targets/waypoints/reference signals on a continuous basis. The operator plays from off the vehicle and via a tethered or radio linked control device. A teleoperated robot will complete its last command after the operator stops sending commands, even if that command is complex or time-consuming. This is the main difference with respect to level 1: the UMV has on-board cognitive capability and has some degree of reasoning and ability to respond. It may sense the environment, report its state and suggest one or several actions to the operator, *e.g.* prompting the operator for information or decisions. However, the authority to make decisions is with the operator. The UMV will act only if commanded and/or permitted to. A typical example is a ROV: there are low level automatic controls on board the robot, which are performed on operator's request (*e.g.* auto-depth, auto-heading, auto-altitude, etc.); in addition, the operator guides the robot on the basis of the data collected by the robot sensors (*e.g.* cameras, detection sonar, altimeter, etc.)

3. **Semi-autonomous robot** performs tasks in which the robot and a human operator plan and conduct the task sinergically, requiring different levels of interaction between the robot and the man. For this mode the robot has a high decision-making capacity, it may sense environment, report its state and define actions and report its intention. The operator has the option to object to (veto) intentions declared by the UMV during a certain time, after which UMV will act. The initiative emanates from the UMV and decision-making is shared between the operator and the UMV; the operator can also interact with the robot to modify mission parameters, cancel a series of planned operations and/or replace them. The granularity of the operations for which authorization shall be required may be low (robot requests authorization for every change of state, *e.g.* turn or change of course) or high (robot requests authorization for new mission objective). For this reason this level is represented with two different diagrams in the Figure 2.11. A typical example is an AUV which, upon receipt of a mission planned by the operator, reports the status and mission parameters to the remote operator, and can receive commands from him to modify the mission, suspend it, or abort at any time (*e.g.* Hugin with HiPAP).

4. **Fully autonomous robot** performs tasks to accomplish its assigned mission, within a defined scope, without human intervention, adapting itself to environmental and

operational conditions. It includes *"Monitored"* and *"Autonomous"* autonomy levels, which differ only for the presence of a mission monitoring operator. The main difference to level 3 is that the on-board system invokes functions without waiting for (or expecting) a reaction from the operator. The UMV will sense environment, report its state, defines actions, decides, acts and reports about its action. The operator may monitor the events or not. A typical example is an AUV that independently performs an environmental sampling operation autonomously evaluating and picking the best sampling points and/or routes on the basis of the measured data and the sensed operational scenario. The initial plan is prepared by the operator prior to mission start, but the plan may be altered during the mission without operator interaction. The detailed behaviour of the system cannot be predicted.

Finally, it is important to note that the majority of UMV are designed to combine several of these autonomy levels at the same time for different functions, subsystem or components. For example, an deep-water AUV exploring a new area can assume the semi-autonomous role in the process of sea bottom exploration, but it can be, at the same time, fully autonomous in the process of navigation. In addition, the autonomy level is also likely changing over time and with operational circumstances. Therefore, the choice of appropriate control method should be based on understanding and definition of UMV functions, operational context and the consequences of changing conditions to the communication capacity.

2.2 The Folaga AUV

This section summarize the architecture and the main features of the AUV used for long-endurance experimentations: the *"Fòlaga"* hybrid vehicle [11, 35, 36].

Historically, the Fòlaga project was born as a combined research effort in which the IMEDEA (Center for Mediterranean Studies, Mallorca, Spain) provided the oceanographic specifications and requirements, ISME provided the system design, Graal-Tech (a spin-off company of the University of Genova, Italy) took care of the realization (mechanics, power, electronics, software implementation) and former NURC (now CMRE) provided advice for hydrodynamics, sealing, wet/dry part connections and acoustic communications.

Hybrid designs started to appear in the first half of 2000 notwithstanding the described classification for UMVs. Indeed, the high-level critical observation from which the Fòlaga [1] project was born was that the main limitations to the diffusion of AUVs in operational scenarios were essentially vehicle cost and user-friendliness [9]. From this starting point, the cited authors have proposed an AUV designed for specific investigation of ocean mesoscale dynamics in shallow coastal waters [10,31], with the capability of sampling the water column at specified geographical locations down to a depth of $50\,\mathrm{m}$, navigating autonomously from a sampling point to the next. With a clear goal in mind, a very simple and yet effective prototype was realized, with great reduction in costs.

Based on the above requirements, the first Fòlaga prototype [9] consisted of two fiber-glass cylinders (stern–bow sections) with $0.125\,\mathrm{m}$ diameter for a total length of $2.20\,\mathrm{m}$ and a connection wet frame in which a propulsion jet pump oriented in the

[1] Italian name of the coot aquatic bird

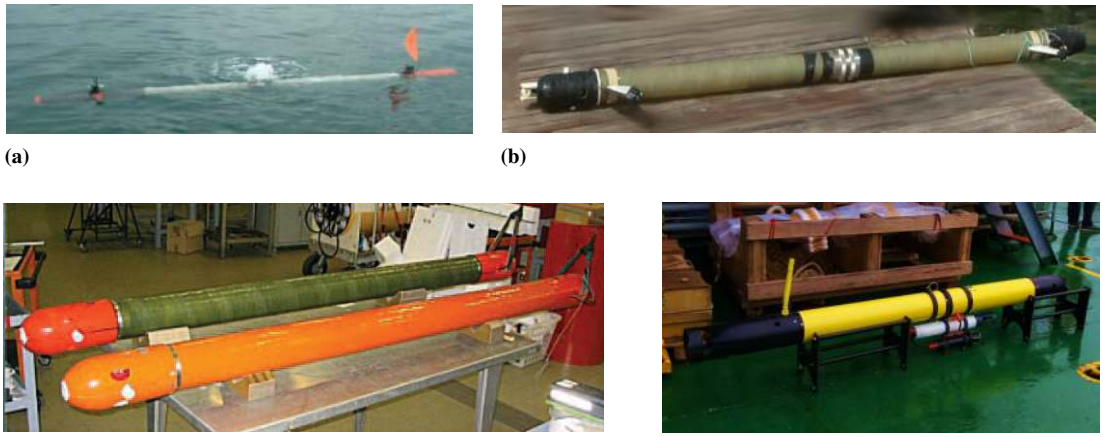

Figure 2.12: *The historical evolution of Fòlaga UUV. (a) Fòlaga I (2003-2004) beginning of diving phase; the diving jet-pump at mid-vehicle gets into action. (b) Fòlaga II (2005) with two pumps along the heave direction and placed at the bow and stern of the vehicle. (c) Fòlaga III (2006-2007) consisting in a single cylinder with two wet ends. (d) Enhanced Fòlaga (2008-2009) with a modular payload consisting of a CTD probe plus an acoustic modem, on board NRV Alliance before deployment.*

heave direction was positioned in order to dive during sampling missions (the vehicle was reemerging just by buoyancy). The stern and bow sections had also wet parts, with a propulsion jet pump oriented in the surge direction at the stern, and two directional jet pumps parallel to the sway direction at the bow. The dry part inside the cylinders consisted of the vehicle electronics and the battery pack. The vehicle was designed passively stable in roll and positively buoyant. The Fòlaga I was specifically designed to perform sampling missions in the water column after having reached a waypoint in surface navigation. Then, expensive navigation systems were avoided, and it was equipped only with a GPS receiver, a compass, a depth sensor (pressure gauge), a pitch sensor, and a general mobile radio service (GMRS) antenna to communicate with a remote station for mission monitoring, data transfer, and eventually remote control. With the earlier design choices, the Fòlaga I (Figure 2.12a) was characterized by not having extruding parts as control surfaces, rudder, fins, and blade propellers. In this way, damage risks due to collision in transportation or operation as well as due to the number of wet–dry part connections were sensibly reduced. The total weight of the vehicle was about $30\,\mathrm{kg}$, and the vehicle was easily transportable in two separate sections of about $1\,\mathrm{m}$ length each.

Although Fòlaga I did meet the design requirements, it can hardly be said that the design choices were optimized. Based on the same concept and requirements of the original design, the Fòlaga II prototype (Figure 2.12b) was a modification in which the pitch control was introduced by replacing the unique jet pump at mid vehicle with two separate jet pumps, still oriented in the heave direction, one in the wet stern section and one in the wet bow section. This way, the differences in thrust between the two pumps could be modulated to maintain the vehicle at $0°$ pitch during descent.

A remarkable source of inefficiency in energy management of the Fòlaga II was the use of jet pumps for propulsion instead of blade propellers. The major reasons for this

Table 2.2: *Comparison of the main technical characteristics of Fòlaga III and e-Fòlaga (without additional payload). The water density is assumed as* $1027\,kg/m^3$.

Parameter	Fòlaga III	e-Fòlaga
External diameter (m)	0.140	0.155
Length (m)	2.000	2.187
Mass in air (kg)	30	36
Mass variation range in water (kg)	± 0.500	± 0.350
Moving mass displacement range (m)	0.050	0.080
Battery type	Lead Acid	Li-Ion
Battery parameters (V x Ah)	12 x 72	27 x 44.4
Autonomy at full speed (h)	8	14
Diving scope (m)	$0 - 80$	$0 - 80$
Speed (m/s)	2	3

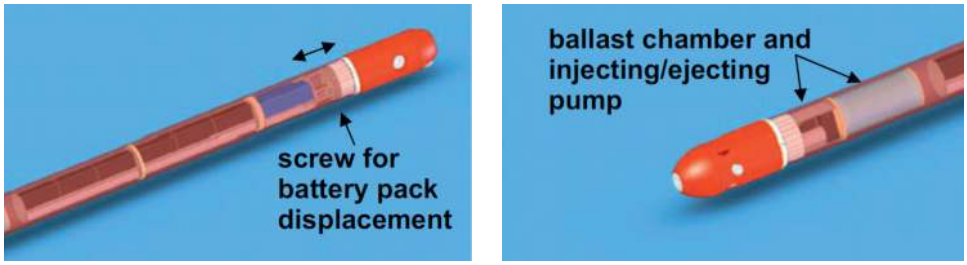

(a) **(b)**

Figure 2.13: *Close-up of main design characteristics for (a) battery displacement (attitude change) and (b) ballast chamber (buoyancy change).*

design choice had been the safety of humans in the proximity of the vehicle, reduced operational risks (leakage, collisions), and reduced costs in manufacturing. However, by the time of Fòlaga III development, the prototype had attracted enough attention to receive mission requirements from applications different from those of the primitive design [31]. For this reason, Fòlaga III came with two different propulsion possibilities, the standard jet pump (allowing a maximum speed of two knots – 1 m/s) and a blade propeller, driven by a brushless electrical engine, allowing a maximum speed of four knots, i.e., 2 m/s. Also, Fòlaga III was not composed of two different sections but by a single one for a total length of 2.0 m. The main characteristics of the Fòlaga III vehicle are shown in Table 2.2, alongside the characteristics of the enhanced version presented in 2.2.1 and currently offered by GraalTech.

Important engineering actions were derived from the consideration of the low efficiency of jet pumps to generate thrust in the heave direction. Wishing to preserve the no-extruding surfaces approach, the Fòlaga III design involved a major reshaping of the internal components, with the installation of a system similar to that of oceanographic gliders [110, 111]. In particular, vehicle diving was obtained by a controlled combination of buoyancy and attitude change through the presence of a ballast chamber and a wormscrew mechanism to internally displace the position of the battery pack (Figure 2.13).

Both buoyancy and attitude must be trimmed at the beginning of the mission in order

to have the vehicle neutrally buoyant with zero pitch. The combined use of buoyancy and attitude change allows the vehicle to dive in several different ways: from vertical dive with zero pitch for oceanographic data profiling, to combined attitude change and surge propulsion (with neutrally buoyant vehicle), to combined attitude and buoyancy change (with or without propulsion).

As a side product of the new diving mechanism, Fòlaga III has an actuation system that allows for underwater navigation (a possibility that was not available in the two previous versions). However, it still lacks sensors for underwater navigation because they would raise the cost of the vehicle far above the initial specifications (the sole cost of a commercial Doppler Velocity Log (DVL) was greater than the whole cost of the vehicle's components). To keep the costs controlled, a solution has been sought in terms of acoustic localization. In particular, the WHOI acoustic Micromodem has been selected because of its potential in providing range measurements and transmitting acoustic messages [86]. Multiple range measurements from surface buoys or from other vehicles may provide a cheap but sufficiently accurate way of underwater localization [16]. Underwater communication capability opened up the possibility of networking and cooperation among several vehicles in the fulfillment of a mission.

From the above discussion, it is clear that the Fòlaga mixes actuation mechanisms that are similar to those of oceanographic gliders and of self-propelled AUVs but that the resulting motion and functionalities are different from both. In particular, the absence of control surfaces is exploited to manoeuvre even at very low speed, not needing hydrodynamic lift. Nonetheless, an additional remark has to be made regarding the use of jet-pumps for steering. From the point of view of energy efficiency, jet-pumps are less efficient with respect to rudder steering but, from the point of view of the mechanical design (absence of transmission mechanisms), realization cost, robustness with respect to handling and deployment damages (no appendixes protruding from the main cylinder), the jet-pump design offers several advantages. The trade-off between efficiency and these other factors has resulted in the jet-pump choice for the Fòlaga. It must be clear that this choice can not represent the best trade-off in every situation, *i.e.* there are applications in which speed and efficiency are at premium with respect to other factors (*e.g.* patroling, port security).

2.2.1 The enhanced version of the Folaga

All the described features can be exploited in a number of different environmental monitoring and surveillance systems. The small dimensions, lightweight and very low cost of the Fòlaga make it also feasible for prototypal experimentation in multi-vehicle or multipurpose systems (*e.g.* [64, 87, 153]).

Indeed, one of the obstacles to these further developments was that the Fòlaga was originally specifically designed to carry a Conductivity–Depth–Temperature (CTD) probe as payload, and different payloads required design changes tailored on the payloads themselves. From an engineering standpoint, this was a major drawback of the vehicle, greatly limiting its potential. Recognizing the above, by the end of 2007 a joint research project was established by NURC, NUS (National University of Singapore), ISME and GraalTech in order to develop a new Fòlaga version able to carry one or more payload modules. The project gave also the opportunity of re-designing some of the components of the Fòlaga III, including the addition of lateral thrusters

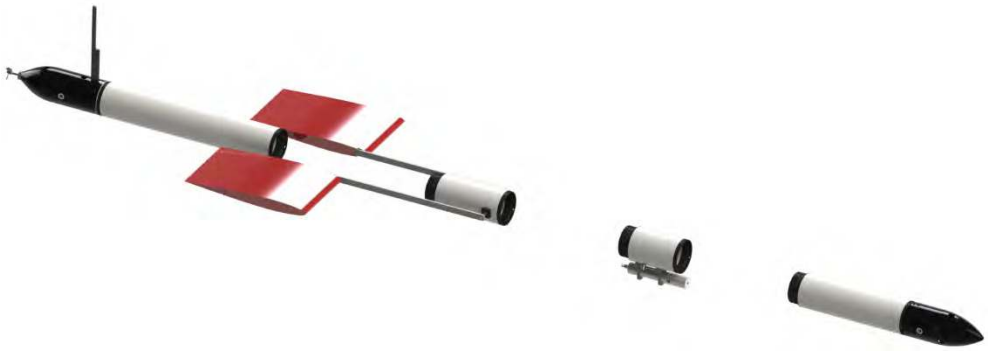

Figure 2.14: *Illustration of the eFòlaga concept, with separation at mid-vehicle to allow insertion of a universal payload.*

both at the bow and at the stern, to further increase the manoeuvrability of the vehicle. The modular Folaga, available since mid-2009, was named *eFolaga*, as for "enhanced Folaga" [35].

The Folaga III (Figure 2.12c) was essentially a fibre-glass waterproof long pipe, closed at both ends by waterproof bulkheads. All the fittings were going through the end bulkheads, that were capped by a wet cone that carried the thrusters. This very simple design was chosen because it is cheap and simplifies hull manufacture.

The basic idea at the start of the eFolaga project was to keep the Folaga III vehicle characteristics and actuation while allowing insertion of a *universal* payload module at mid-vehicle, recovering the two-section design of the original prototypes (Figure 2.14). Moreover, it was decided that the project should not develop payloads, but should define mechanical, electrical and electronics interfaces so that any third party could develop its own payload module, as appropriate, and mount it on the eFolaga. It is understood that vehicle safety (emergency sensors and watchdogs) must remain in charge of the native eFolaga system.

The first step in the project was the definition of mechanical modularity to separate the vehicle into forward and aft sections to interpose an extra piece of hull (the module) containing added functionality between the two (Figure 2.15). As the eFolaga hull is made of GRP (Glass Reinforced Polyester) filament wound, it was not possible to directly fashion a watertight interface between mating hull sections. Hence, it was decided to employ machined inserts, male on one section and female on the other, bonded into the GRP hull, which could then be sealed against each other with O-rings. The design of these coupling inserts ensured backward compatibility with the end bulkheads already in use. Electrical connections between sections are thus made through flying leads (Figure 2.16). The forward section contains all the yaw thrusters, buoyancy control and a third of the electrical storage capacity. Control and availability of all of this has to be communicated through the module stack to the aft section, which houses the vehicle's main computer.

The final eFolaga main design characteristics are reported in Table 2.2. From the point of view of the overall physical and hydrodynamic properties, the payload module(s) must have dimensions and balance to allow the eFolaga to operate under stable control without undue restriction when the module is fitted. Considering the technical characteristics of the eFolaga, GraalTech provides guidelines to which any payload

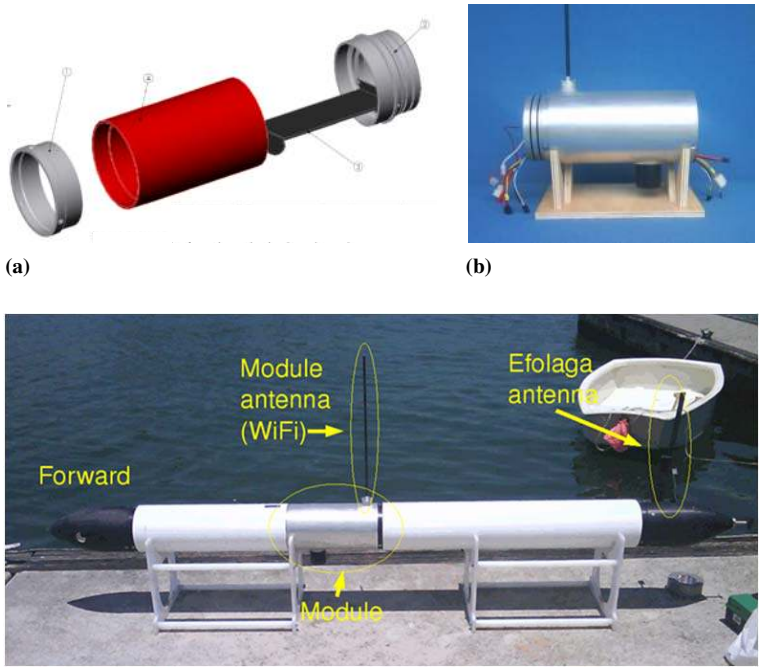

(a) (b)

(c)

Figure 2.15: *(a) The mechanical design of the module with the equispaced holes for mechanical coupling with the rest of the vehicle. (b) The first payload, developed by NUS, carrying a Wi-Fi antenna and an acoustic modem. (c) The first eFolaga with the NUS module mounted, ready for launch.*

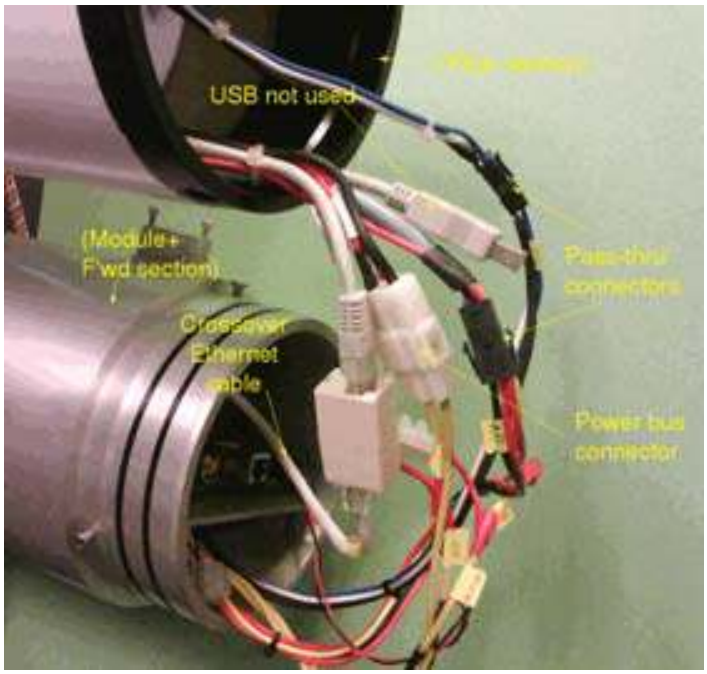

Figure 2.16: *Connections between eFolaga aft section and module.*

module must conform.

CHAPTER 3

The WAVE Project

As already introduced, long endurance in marine applications with AUVs represents one of the emerging trends in the marine robotics research. Reducing the energetic consumption of the vehicles by improving the efficiency of the power supply and the propulsion systems [21, 92, 214] is instrumental in extending the duration of a mission from hours to days, or even months in the case of gliders [72, 189, 215, 217]. A complementary approach consists in recharging the internal batteries of the vehicle during a mission in dedicated off-shore docking stations [97, 102, 115, 190]. This solution presents the major drawbacks of requiring a cable-link either to a ground station or to a support vessel and, most important, the suspension of the main mission of the vehicle in order to reach the installation and charge the batteries. A more flexible, almost unexplored idea would be to equip the vehicle with a portable device capable of harvesting energy from the surrounding environment. To this aim, the wave motion is particularly appealing because it is theoretically not restricted by time and place. Nevertheless, the difficulties in storing the wave generated power and the low efficiency of the energy conversion process has left the progresses in this direction confined to few, very recent prototypes [30, 202].

The latter line of research includes the project WAVE, an Italian National Research Projects of Military interest (PNRM) concluded in October 2017 and topic of this chapter. The project was conducted by a team composed of University of Pisa (node of ISME) and GraalTech company, under the supervision, steering and control of the CSSN. The final goal of the project WAVE was to study, develop and test a novel system for both energy harvesting from the wave motion and low energy propulsion, to be integrated on a generic, modular, torpedo-shaped AUV.

In Section 3.1, the project concept is presented. In Section 3.2, the prototype hardware and software are described in details, while the preliminary bench test and at sea

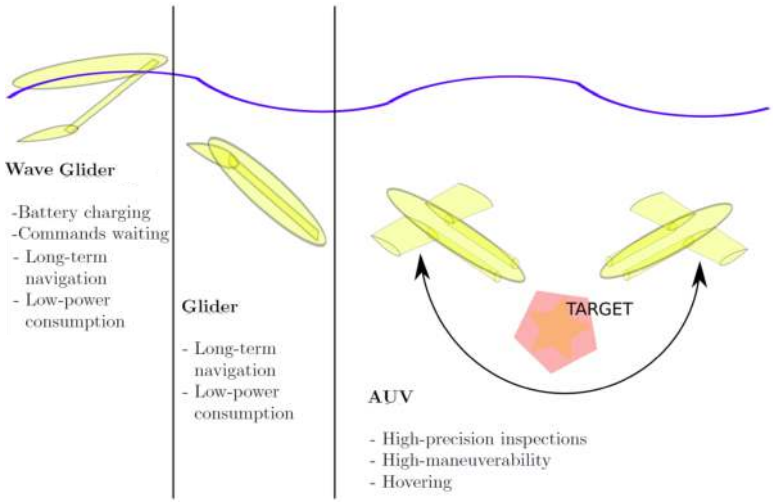

Figure 3.1: *The three function modalities of the WAVE prototype.*

experiments results are presented in Section 3.3. Finally, in Section 3.4, lessons learnt, conclusions and further related research topics are outlined.

3.1 The high-level concept

The goal of the WAVE project is to further develop the technology for autonomous long-term marine exploration and surveillance by exploiting energy from environmental renewable sources, such as solar and wave energy, as potentially unlimited power supply. In particular, the design and the prototypal realization of a hybrid oceanographic glider/AUV with battery recharging capabilities from the wave motion was considered within the project. The project technical requirements defined three different operation modalities the vehicle should provide (Figure 3.1):

- Wave Glider: the vehicle is floating on the sea surface to feed its internal batteries with energy recovered from the wave motion, waiting for new tasks from the remote control station. In certain conditions, it could exploit the wave motion in a similar manner to the Liquid Robotics Wave Glider [140, 217] but with the main difference that the latter uses a cable to link the floating part to the underwater wings while the WAVE uses a rigid rod to exploit the vertical oscillating motion due to waves;
- Glider: the vehicle acts as a classical underwater glider, performing long-term navigation at low power consumption by changing its buoyancy and pitch only;
- AUV: the vehicle activates its jet pumps and thrusters, enabling high maneuverability features.

The envisioned recovery system, namely the "WAVE module", is composed of two robotic, wing-terminated arms, free of moving about a unique rotational joint transversal to the hull (Figure 3.3a), to be installed on-board a generic carrier vehicle. During the wave recharger phase the vehicle rests at the sea surface, subject to wave induced motion, while the arms, that have negative buoyancy, are left free to move with respect

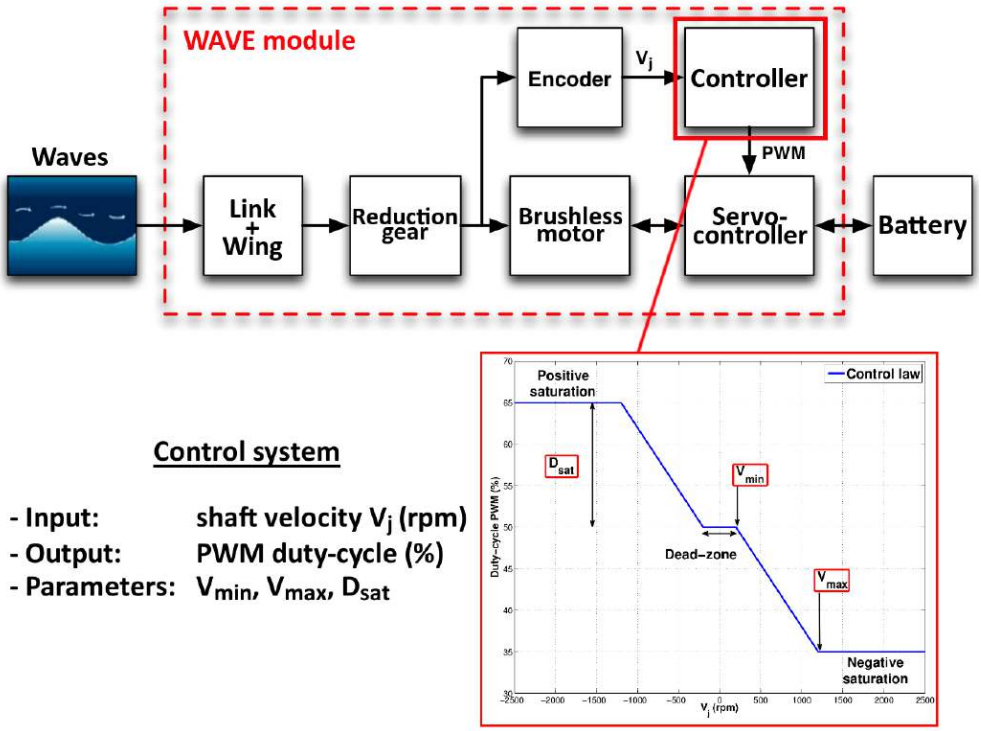

Figure 3.2: *The WAVE module conceptual diagram with specific emphasis of the implemented control system law.*

to the vehicle body. The relative motion activates the internal brushless motor, mounted on the rotational axis, which is controlled with an opposite torque in order to generate power, as shown schematically in Figure 3.2. When necessary, the two arms can be locked along the hull so that the two wings can act as active surfaces, jointly working with the internal variable buoyancy device, allowing the AUV to advance in a gliding fashion taking advantage from the lift forces exerted by the water on the wings. A first prototype of the WAVE module was built (Figure 3.3b) and installed on the hybrid AUV/glider eFolaga, presented in the previous chapter, in order to guide the development of the system towards a realistic experimental solution without losing the generality of the methodology itself.

Finally, apart from the complementary propulsion modes, the WAVE module was designed to exploit the modularity ensured by the eFolaga being perfectly integrable with other payloads (*e.g.* Side-Scan Sonar, passive hydrophones, CTD probe, acoustic modem). This high modularity - together with the possibility of combining different types of propulsion - make the WAVE vehicle suitable for various types of missions within different scenarios.

A preliminary assessment of the integrated system was performed at sea in April 2016, showing the practical feasibility of the proposed system [77]. A systematic experimental characterisation of the module capabilities was thus carried out in a controlled environment at the Italian National Research Council - National Institute for Studies and Experiences of Naval Architecture (CNR-INSEAN) test tank facility in Rome, Italy, and it will be presented in the next chapter.

(a) (b)

Figure 3.3: *The WAVE module: (a) rendering and (b) prototypal realisation.*

3.2 Prototype hardware and software description

This section describes in greater detail the functional, mechanical and electrical / electronic specifications of the developed WAVE module, expanding the works presented in [55, 77] and done during the WAVE PNRM Project. The bench test results and the first experiments at sea corroborate the fundamental concept of the project.

3.2.1 WAVE module design

The WAVE module CAD drawings are shown in Figure 3.4. In essence, the module consists of a watertight hull section, inside which the electromechanical components are housed, and two external arms ending with two hydrodynamic wings. In detail, the hull section is formed by a ”payload cylinder” (1) that hooks to the stern and bow section of the vehicle through a female connection (2) and a male connection (3) respectively. The electric actuation system, consisting of gear unit (35), motor (36) and relative sensor (37), is installed parallel to the major axis of the ”payload cylinder” (1) and is fixed to the motor support (40). The actuation system is coupled via a bevel gear wheel to the common shaft, which connects the left and right joints (see Figure 3.4b). On the shaft there is also an amortized articulated system formed by a movable rod (13) and specific ”parts” (18), (41), (28), (29); this mechanism allows to limit the movement of the joints.

The connection between the hull section and the external arms of the module is reported in detail in the ”payload tube passage” in Figure 3.4d. The transition from the dry section to the wet section is realized through the part ”04 A” (7), on which are mounted an internal (1) and an external (2) supports. The ”arm” (15) is connected to the joint on the hull through the "part 07-A" (4), while the opposite end of the arm ends with the "part 12" (6), on which the elastic joint is housed connecting the arm with the wing, shown in detail in Figure 3.4a. The joint consists of a bracket (7) connected to a movable rod (13), the latter hooked to the arm on the opposite side by means of another fixed bracket (12). Finally, the wing (34) is connected to the joint via the ”part 08” (6).

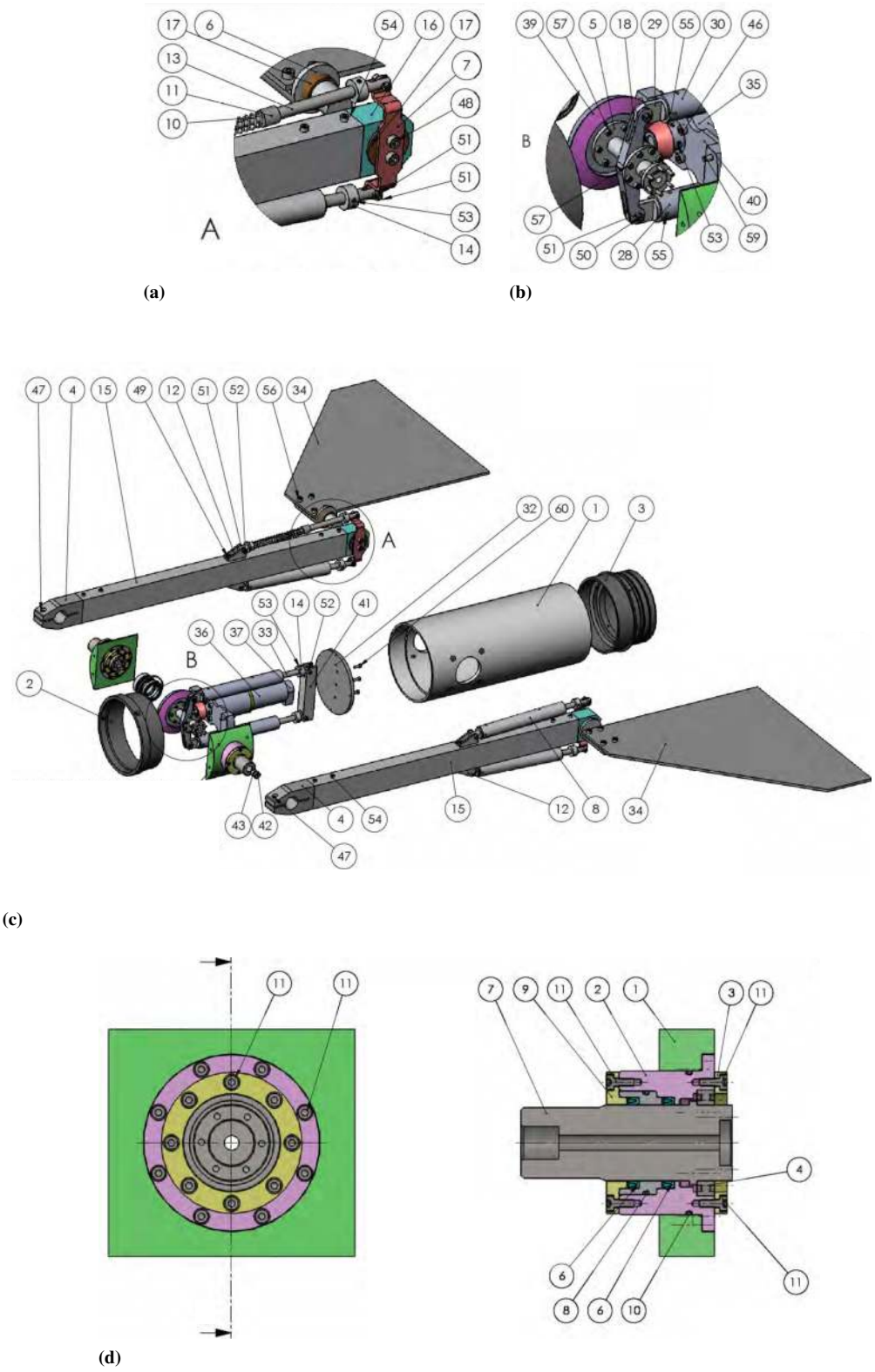

(a) (b) (c) (d)

Figure 3.4: *CAD drawings of the WAVE module (courtesy of GraalTech). (a) Close up of the arm-wing connection. (b) Close up of the joint-motor connection. (c) The whole WAVE module main CAD drawing. (d) Close up of the payload tube passage for the wet-dry transition.*

3.2.2 WAVE module prototype realization

In Figure 3.5 is shown the prototype realization of the WAVE module made in the project. Apart from the arms-wings wet parts, the module has a dry section that hosts the wave energy recover system (*i.e.* a brushless motor with its relative inverter).

As mentioned earlier, the wings have the dual purpose of recovering energy from the wave motion and/or provide a wave gliding propulsion capability when the vehicle is stationary on the surface, while they can provide lift in the navigation phase in glider mode. In fact, the wings increase the roll passive stability of the vehicle during underwater navigation. As a side effect, higher quality of the sonar image during Side Scan Sonar surveys can be obtained. To do this, the wings can be locked in the horizontal position thanks to an electromagnetic block. Once blocked, no energy is spent to keep the wings in place while the vehicle navigates.

As can be seen in Figure 3.6, the WAVE module was easily integrated on the eFolaga vehicle without the need to make any mechanical changes to the carrier itself. This is due to the fact that the WAVE module was designed taking into account the modular interface specifications of the eFolaga. From now the eFòlaga vehicle equipped with the WAVE module will be refered as *WAVE vehicle* for the sake of simplicity.

3.2.3 The WAVE Mission Control System (WMCS)

As mentioned in Section 3.1, the WAVE project had the secondary goal of integrating the WAVE module with other operational payloads (*e.g.* Side-Scan Sonar, passive hydrophones, CTD probe, acoustic modem) in order to make the WAVE vehicle suitable for long-endurance tasks within different scenarios. The WAVE Mission Control System (WMCS) integrates the modules specifically developed for the project with those already existing into the AUV eFòlaga, and it guarantees a high level of abstraction for the user set-up of an autonomous mission of the WAVE vehicle. The term *high level* means that the user does not have direct control of the hardware installed on the vehicle (both sensors and actuators), but interacts with them through an easily interpretable request-response mechanism made available by the WMCS.

Three basic functionalities are considered into the planning of an autonomous mission through the WMCS:

- Management of mission payloads: the user can switch on and off the additional sensors (CTD probe and Side Scan Sonar), verifying their operating status and acquired data;

- Control and Supervision of the mission: the user can communicate with the GNC system of the Folaga, giving new navigational tasks and monitoring the navigation status;

- Management of the operating mode: the user can control the operating mode of the vehicle (selectable between gliding, underwater navigation, surface navigation and surface recharging) depending on the available information and payloads.

In order to be effective, efficient and reliable, the WMCS has been designed and implemented in compliance with the following requirements:

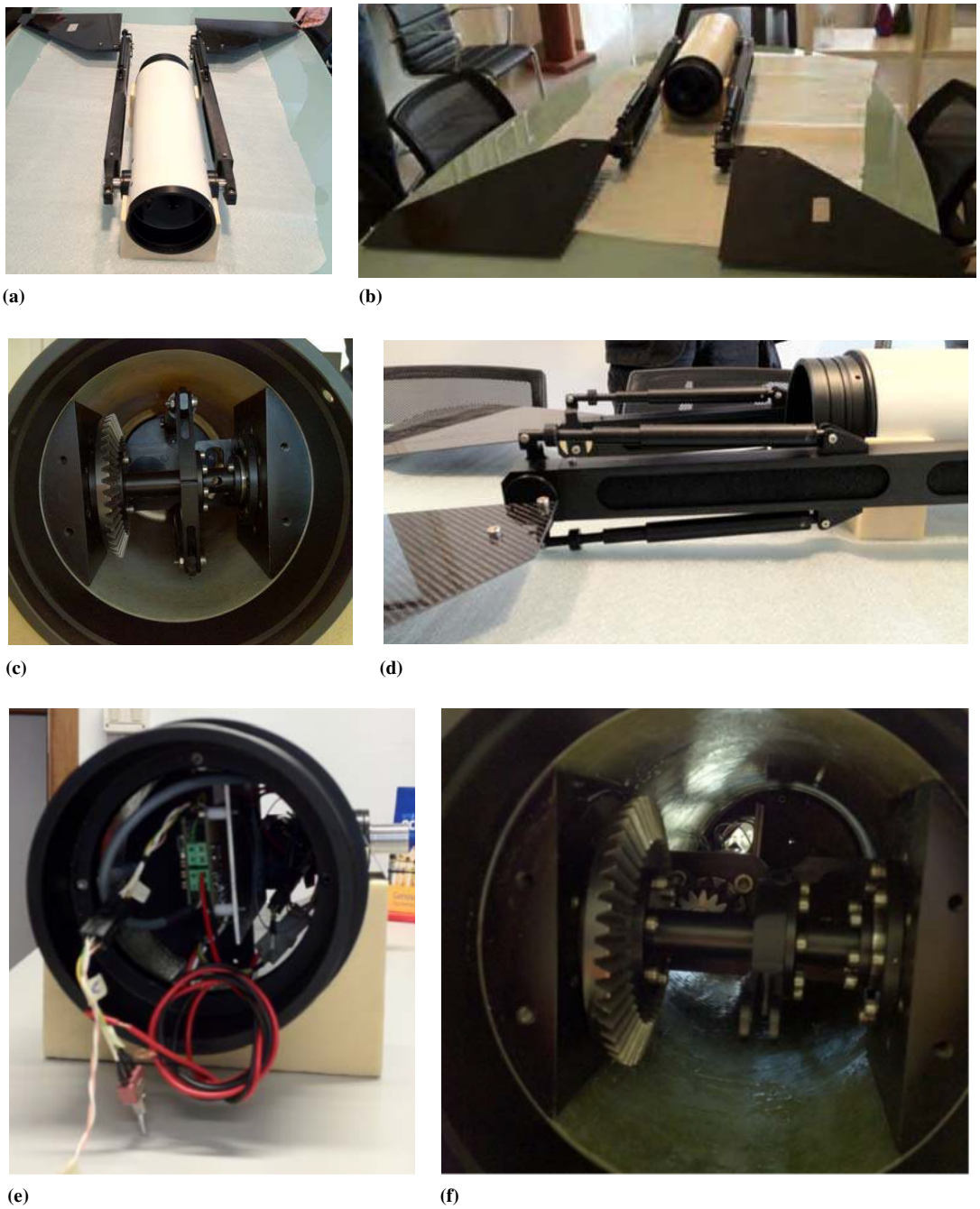

Figure 3.5: *Realization of the WAVE module prototype. (a) and (b) Overview of the prototype. (c) Close up of the mechanical coupling inside the module without the motor. (d) Detail of the telescopic movable joint that allows to vary the relative angle between the wing and the arm; note that the design of the wing connection allows an easily replacement of the wing itself with different dimensions and geometry shapes. (e) The cables outlet and the digital drive card with motor and all components installed. (f) The gearbox and the motor in their final mounting positions.*

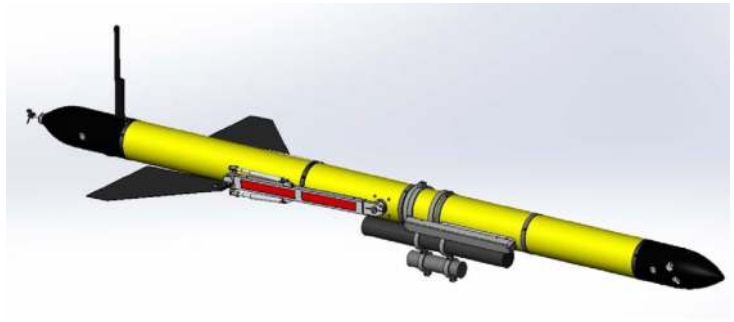

(a)

(b)

(c)

Figure 3.6: *Integration of the WAVE module prototype into the eFolaga vehicle. (a) Rendering of the WAVE vehicle with all the payloads integrated. (b) The WAVE vehicle fully assembled before its first dive in the test tank. (c) First tank test for the WAVE vehicle.*

Modularity and scalability thanks to the division of the system into different elementary modules. Each module has a specific task, favoring easier re-engineering of the system to cope with new needs and hardware changes;

Reconfigurability: the system keeps the same general interface architecture independently by the vehicle configuration (addition, removal or change of payload), which depends on the mission to carry out;

User-friendliness: the system must provide an intuitive and easy-to-use user interface for supervision and control of the mission;

Robustness: the system must be able to react autonomously with the most common unforeseen situations that may occur during the execution of a mission, returning proper feedbacks to the user.

3.2.3.1 ROS Implementation of the WMCS

The WMCS consists mainly of two subsystems:

- The Folaga Mission Control System (FMCS) onboard the vehicle, responsible for the management of mission payloads and interaction with the low-level control system of the Folaga vehicle;
- The Command and Control Station (C2S) on the base station (which can be placed ashore or on a support vessel), which provides a graphical user interface with all the tools to carry out mission supervision and control.

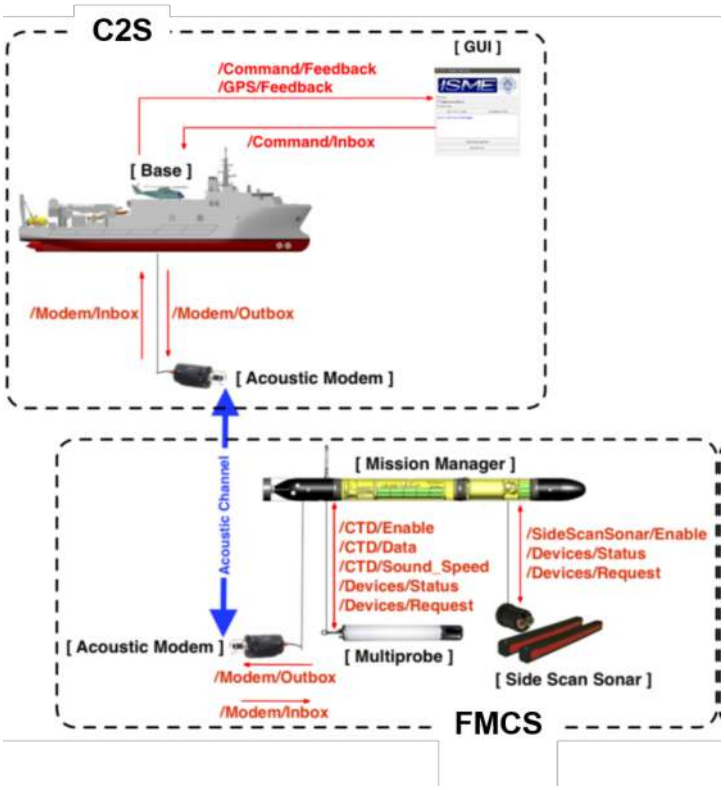

Figure 3.7: *Conceptual scheme of the WAVE Mission Control System (WMCS).*

Although the two systems are physically separate, they interact through the acoustic channel using the EvoLogics 18/34 acoustic modems mounted both on the base station and on the vehicle. This way, the user can send commands to the vehicle and receive proper notifications and information. To meet the requirements described before, the WMCS has been implemented in C++ language taking advantage of the features offered by the robotic middleware ROS.

ROS is an operating *metasystem* for the development of robotic applications, consisting of several software packages and libraries that make available services similar to those provided by a classic operating system. The architecture of the whole system is highly distributed, modular, based on the publish-and-subscribe paradigm: in this way, it is possible to separately manage a set of software processes (called ROS nodes) that can communicate with each other both asynchronously, through peer-to-peer exchange of messages via special structures called ROS topics, and synchronously, through the use of ROS services. A central ROS node (called master) always exists to manage nodes startup and shutdown.

The conceptual scheme of the WMCS is illustrated in Figure 3.7. The two main subsystems (FMCS and C2S, dashed boxes in the figure) consist of several elementary modules. Each module corresponds to a ROS node, indicated in square brackets, with a specific goal. The different applications communicate with each other exchanging information through the red highlighted topics: the arrows indicate the direction of the data flow between nodes. Within a topic, the data is encoded with a particular message structure specific to the considered topic.

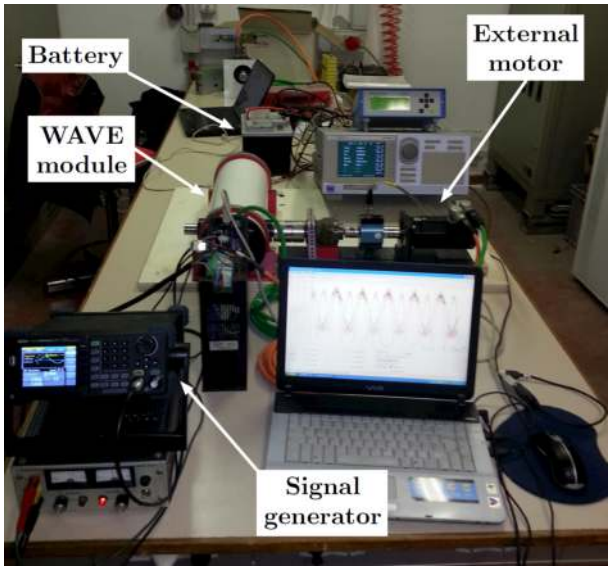

Figure 3.8: *Experimental setup of the bench tests.*

3.3 Experimental results

The WAVE vehicle was firstly characterized in laboratory through several Hardware-In-the-Loop (HIL) simulations. Then, sea-trials of the system were conducted in the Gulf of La Spezia, North Tyrrhenian Sea, with the support of the NRVs (NATO Research Vessels) Leonardo and Alliance, both manned by the Italian Navy. Although there was plenty of space for further optimization of the system performance, the results of the tests showed the practical feasibility of the proposed approach. The final successful experimental activities of the WAVE project, described in Section 3.3.3, concerned both the autonomous functions of the vehicle and its ability to perform complex tasks exploiting all the payload modules.

3.3.1 Bench tests

Starting from the indications given by previous simulative study, several bench tests were performed on the first version of the WAVE module prototype c/o the laboratories of the Department of Energy, Systems, Territory, and Construction Engineering (DESTEC), University of Pisa, and GraalTech. The purpose of these experiments was to establish, implement and calibrate the control law for the brushless motor in order to maximize the efficiency of the recharging process.

To this aim, an open-loop characterization of the system was carried out by setting up the testbed shown in Figure 3.8. The rotational joint on the hull of the module was linked to the shaft of an external motor and actuated with a constant velocity. Meanwhile, a PWM (Pulse-Width Modulated) signal corresponding to a current set-point was imposed to the internal brushless servo-controller in order to produce an opposite torque with respect to the motion induced by the external motor. Such a counteraction generates an electric current which flows towards the battery connected at the end of the chain. The reference velocity value of the external motor and the current set-point were then varied throughout all the respective operative ranges. The average efficiency

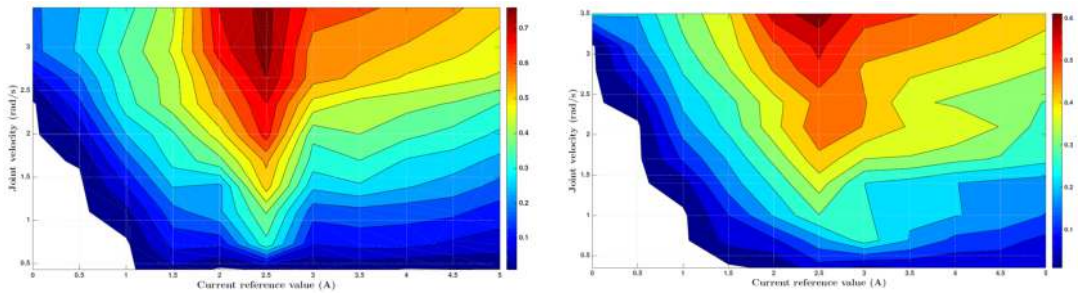

(a) (b)

Figure 3.9: *Efficiency maps obtained from the open-loop characterization of the recovery system. (a) Initial voltage level of the battery:* $9.7 - 10$ *V. (b) Initial voltage level of the battery:* $11 - 12$ *V.*

for each configuration was evaluated as the ratio between the average electric power at the battery and mechanical power applied at the joint. The calculated values were then interpolated to obtain a map over the entire operative region; Figure 3.9 shows the efficiency mapping with two initial voltage levels of the battery. As it can be noted, for any given velocity the maximum efficiency can be always achieved with a current reference of about 2.5 A, corresponding to a PWM percentage of $65\,\%$. The simplest control law is thus a bang-bang-like control, smoothed with a dead-zone and a linear piece as represented in the control system of Figure 3.2. The designed controller was then implemented on an Arduino MEGA and tuned during another experiment session. The setup of these trials was the same as in Figure 3.8, but the external motor was operated with a sinusoidal signal with amplitude and frequency such as to simulate the wave motion for each of the sea conditions reported in Table 5.2. The control law parameters were chosen to achieve the better trade-off between the battery charging efficiency and the mechanical stress suffered by the joints.

3.3.2 Preliminary sea experiments

The critical part of the project is the on-field effectiveness of the battery charging mechanism. The WAVE module was hence assembled in 2016 with an eFòlaga and integrated with the control system of the vehicle at the GraalTech facilities. A first experimental campaign with the WAVE prototype was then conducted in the Gulf of La Spezia, North Tyrrhenian Sea, on April 11^{th}-12^{th} 2016, with the support of the NRV Leonardo (Figure 3.10). The sea state during the two days was about Calm 2 and Smooth 1, respectively. Due to the sea current, it was necessary to frequently operate the vehicle by remote radio control to move it far from the vessel. Only the periods of non-actuation can thus be considered relevant for the evaluation of the recovered energy.

Since the goal of this first trial was to verify the behavior of the energy restoring mechanism and not to evaluate its performance, a high-impedance load was connected to the internal brushless motor instead of the battery to prevent any accidental damage to the power supply system. As a consequence, the generated current was not meaningful to evaluate and quantify the realistic amount of recoverable energy with such a system. However, the battery recharging capabilities of the prototype can be assessed

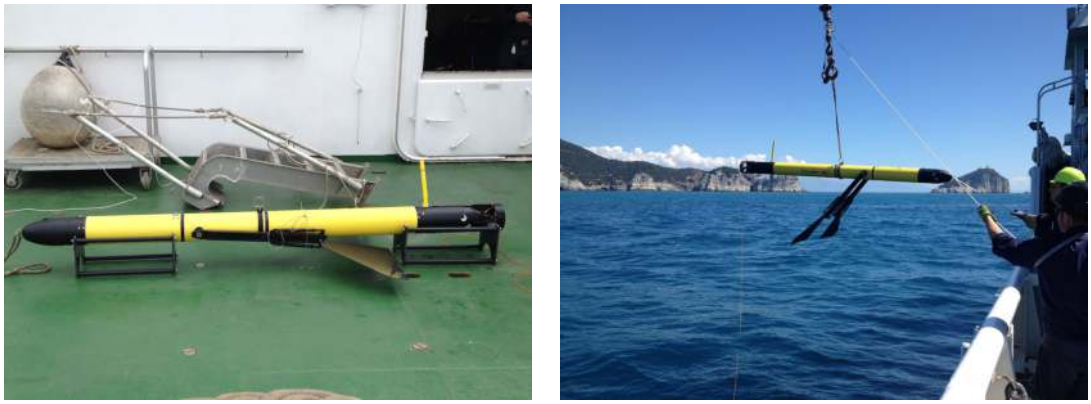

(a) (b)

(c)

Figure 3.10: *Pictures from the sea experiments. (a) The WAVE prototype on the deck of the R/V Leonardo, (b) the deployment phase, and (c) the vehicle in front of the Palmaria Island, La Spezia.*

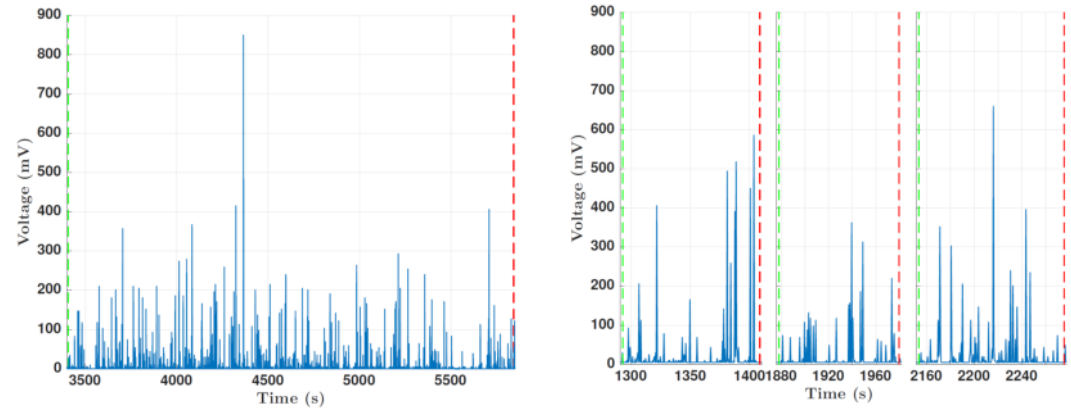

(a) (b)

Figure 3.11: *Samples of generated voltage during the non-actuated periods only. The dashed green and red lines represent the beginning and the end of a period of non-actuation, respectively. (a) refers to April 11th 2016 while (b) refers to the following test day.*

from the analysis of the produced voltage. In Figure 3.11 samples of the recovered voltage are shown for both the days. As it can be seen, the WAVE module is capable of consistently generating peaks of voltage from the wave motion, even with the moderate sea conditions in which the experiment took place.

3.3.3 Final at sea tests

The project validation and acceptance tests were performed in September 2017 in the water area of the military base of the CSSN, Gulf of La Spezia (Italy). In Figure 3.12 are shown the vehicle with all the available payloads and the operative area of the tests.

During the tests it was expected the activation of the wave energy recovery mode should occur when a selectable threshold on the vehicle battery level was reached; at that point, the vehicle had to re-emerge, turn off all non-vital components (*e.g.* mission payloads), release the WAVE wings and start the energy recovery process. To demonstrate this autonomy capability, this situation was simulated during the final experimentations, *i.e.* reaching the lower battery level limit was a fictitious event set by software. When the vehicle recognizes that event, it came to the surface and set its status to *wave energy recharging*. As can be seen in Figure 3.12b, the final tests took place within an harbour area and with meteorological conditions such that the wave motion was too low to successfully obtain a full recharge of the on-board energy system from waves. For this reason, the vehicle resumed the planned mission after another fictitious event, set via software, and corresponding to the battery recharge completed.

It is worth to note the WAVE prototype has an autonomous capacity corresponding to the level 3 of autonomy taxonomy (Section 2.1.4), corresponding to a *semi-autonomous robot* that performs tasks in which the robot and a human operator plan and conduct the task sinergically, requiring different levels of interaction between the robot and the man. During the various phases of the final tests, the mission was set by an human operator as a succession of macro-tasks; then, the on-board intelligence (composed of the on-

(a)

(b)

Figure 3.12: *(a) All the WAVE project developed payloads. From top to bottom, eFòlaga vehicle, CTD plus acoustic modem payload, WAVE module (left) and Side Scan Sonar payload (right). (b) The final tests operative area (yellow background) and the position of the C2S (green circle).*

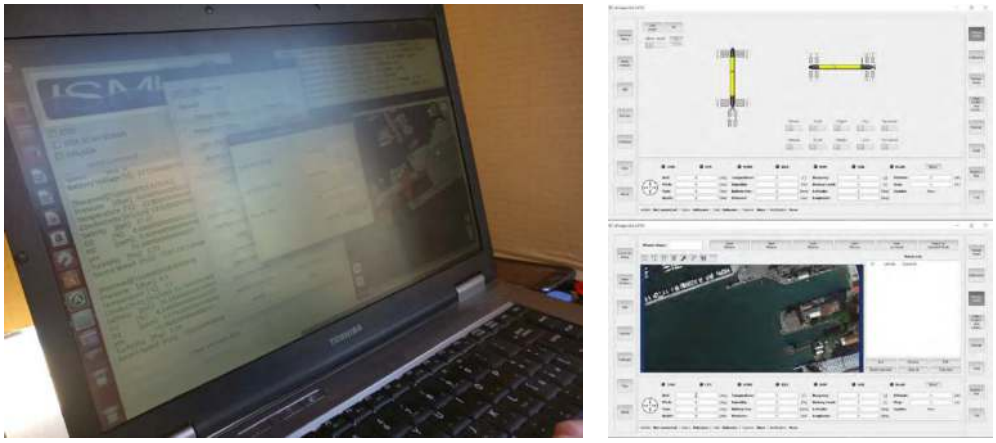

(a) (b)

Figure 3.13: *The management stations used in the experimentation. (a) The main ground station PC with a screenshot of the WMCS user interface. (b) The eFòlaga user interface used on board the support boat.*

board planner and the guidance, navigation and control system) organizes the sequence of micro-tasks for execution of the mission, without the need to receive authorization for their execution: the human operator only monitors the progress of the mission and can interpose to modify or abort it.

3.3.3.1 Experimental set-up

For all the four days of tests, the experimental configuration involved a support boat and two vehicle management stations (Figure 3.13):

- main ground station (green circle in Figure 3.12b), consisting of a PC acting as the Command and Control Station and connected to an USBL acoustic modem;
- secondary command station on board the support boat with the native eFòlaga interface installed on a tablet.

The purpose of the main ground station was the command and control of the autonomous mission of the WAVE vehicle, monitoring the tasks in real time thanks to the acoustic link with the vehicle. On the other hand, the secondary command station act as a backup low-level C2S ready to take the lead in case of malfunctioning.

The tests were divided according to the following scheme:

- The first two days aimed at demonstrating the correct integration of the project payloads. Both modules, in addition to the specific mission payload, integrated an acoustic modem for receiving commands and transmitting data concerning the mission to and from the main ground station. In particular, the vehicle was configured to send periodically (every 5 seconds) and/or on request information regarding the vehicle navigation status, the execution status of the current task and the operating status of the mission payload. The tests' sequence foreseen an increasing complexity, from simple elementary tasks to typical complete missions.

Figure 3.14: *WAVE vehicle in the environmental monitoring configuration.*

- The last two days aimed at testing the transition between the various operative modes of the WAVE vehicle (surface recharging, underwater motion and gliding) and so forth the vehicle was assembled with the WAVE module in addition to one of the other mission payloads.

3.3.3.2 Missions description

Day 1 was dedicated to testing the environmental monitoring module (Figure 3.14). The mission consisted of sampling the water column in order to collect environmental data with the CTD probe in several subsequent waypoints (Figure 3.15). The vehicle navigated between the waypoints on the surface exploiting the GPS and then dive up to a desired depth (variable between 2 and 3 meters) using the ballast chamber system (Section 2.2). The depth was chosen to be safe with respect to the average depth of 6 meters in the operating area.

Day 2 was dedicated to testing the bottom exploration module, equipped with the Side Scan Sonar. The path followed by the WAVE vehicle was the typical lawn-mower path at a constant depth, *i.e.* a series of parallel swaths traversed alternatively and equi-spaced. Once the uniformity of the seabed depth was verified on accurate bathymetric maps, it was agreed to set the reference depth to 3 m, in order to keep the vehicle at an optimal distance with respect to the sea floor for the acquisition of acoustic images with the installed side scan sonar [28].

To further verify the correct working of the sensor, a reference target - shown in Figure 3.16 - was anchored in the operating area at about 5 m from the sea surface. In Figure 3.17 are shown two complex bottom exploration missions done. For both missions, the odd numbered waypoints represent the starting points of a transect, and in particular the waypoint 7 indicates the final destination of the vehicle once the bottom exploration mission is completed. All previous waypoints are located on the surface, and the vehicle dive vertically in that positions to start the underwater navigation. The vehicle was not equipped with a sensor like a DVL, so the underwater navigation parameters were simply the sealane (direction with respect to magnetic north), the navigation time and the propeller power. For this reason, even numbered waypoints represent

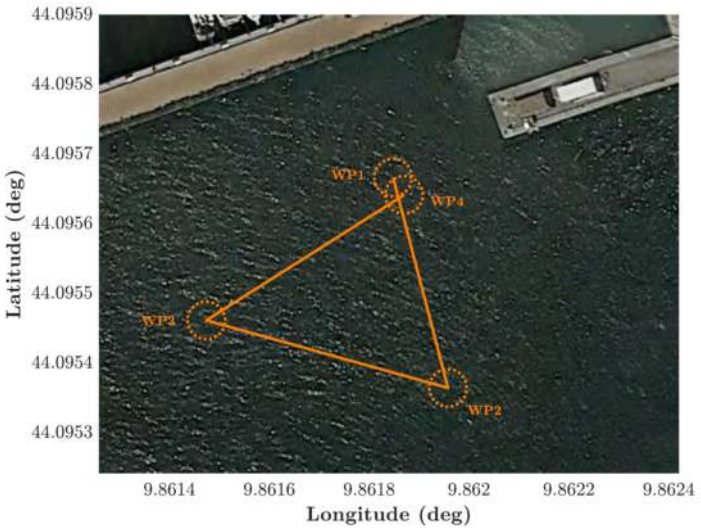

Figure 3.15: *Reference trajectory planned for the complex environmental monitoring mission. The dotted circumferences around the waypoints indicate the tolerance on reaching them,* i.e. *when the vehicle's GPS position is 3 m around the waypoint it considers to be ready to dive.*

approximately the expected end points of the corresponding transept at which the vehicle had to re-emerge. The transfer between one transect to the following was made on the surface.

Day 3 and 4 were dedicated to the WAVE energy recovery module tests, evaluating in particular the underwater gliding mode with the arms fixed so as to be aligned with the main body of the vehicle. The transition between the two main possible modes of propulsion (AUV and gliding) was also evaluated. Furthermore, it was an opportunity to experimentally verify the vehicle's ability to change its status to *wave recharging* once the low battery condition was identified, and to keep it until a sufficient charge level was reached[1]. For all the missions the vehicle was equipped with the WAVE module and the environmental monitoring module (CTD probe plus acoustic modem).

Specifically, the planned mission consisted of a departure from a waypoint near the quay (red diamond in Figure 3.18). Subsequently the vehicle was programmed to navigate in underwater gliding mode towards waypoint 1 (latitude: 44.095203 N, longitude: 9.860652 E) at a variable depth between 1 and 3 meters. Once the waypoint 1 was reached, the *low-battery event* was simulated and the WAVE vehicle rested 60 s at the surface for wave energy harvesting. At the end of the simulated recharging interval, the vehicle navigated towards the waypoint 2 (latitude: 44.095421 N, longitude: 9.862343 E) in AUV mode, *i.e.* exploiting the propellers. At waypoint 2, a water column profiling task was made up to a depth of 3 meters.

The objective of the experimentation was a qualitative validation of the prototype despite the operational constraints of the operational area. This was evident especially in the navigation phase in gliding mode. In fact, in gliding mode the vehicle should take advantage of large and continuous changes in depth (so called yo-yo movement). In the tests carried out, these changes were limited between 1 and 3 meters for safety reasons related to the maximum depth in the operative area. The predictable conse-

[1]These conditions were simulated via software

(a) (b)

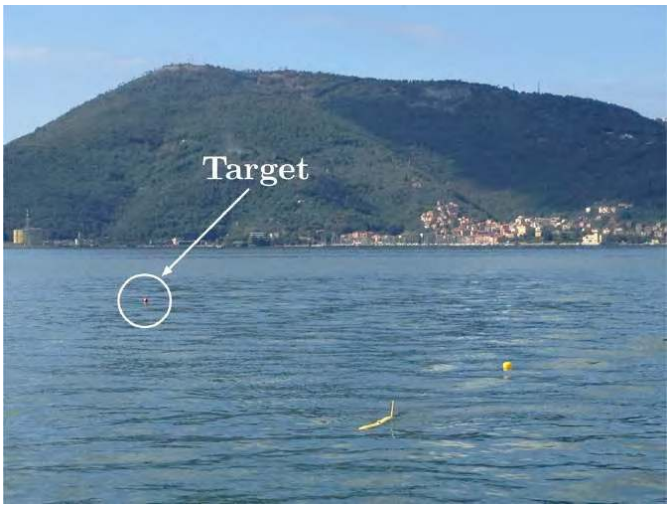

(c)

Figure 3.16: *Sea bottom exploration mission configuration. (a) The approximate location of the target within the operating area. (b) The target mock-up used during the test of the bottom exploration module. (c) Its position signalled by a surface buoy during the execution of the experimental test.*

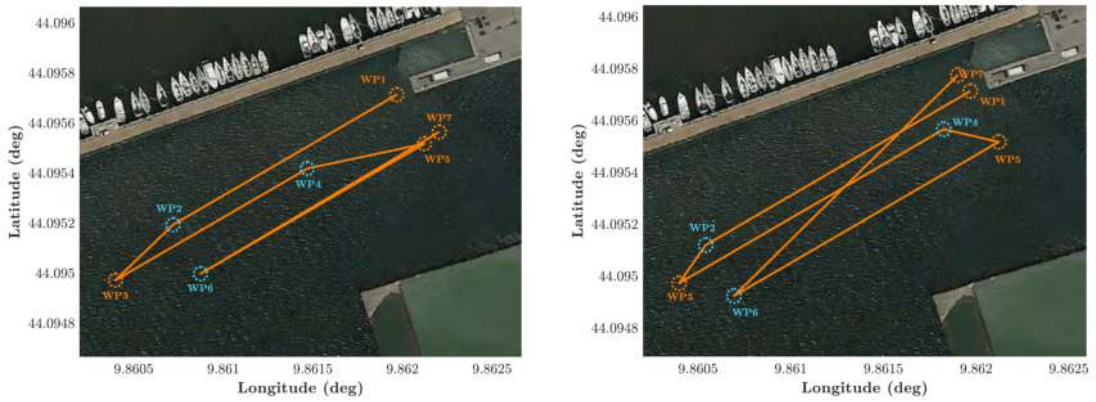

(a) (b)

Figure 3.17: *Examples of reference trajectories planned for complex sea floor exploration missions. The dotted circumferences around the waypoints indicate the tolerance on their reaching, set to* 3 *m.*

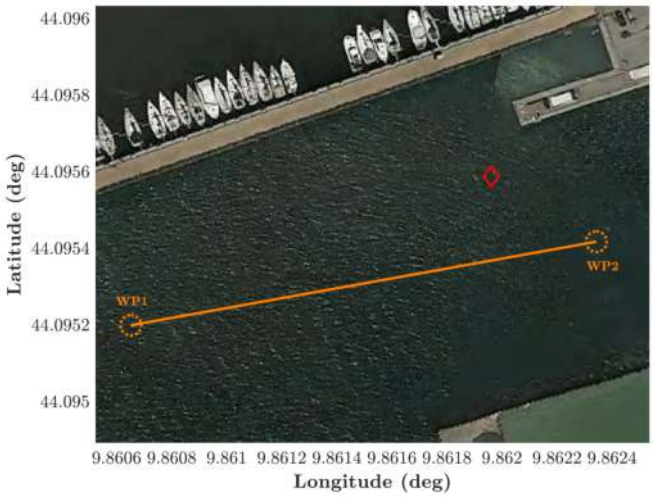

Figure 3.18: *Reference trajectory planned for the underwater gliding mission.*

quence was a slow average vehicle's motion; nevertheless it was possible to verify whether the vehicle's behavior was in line with expectations from the functional point of view. Moreover, the planned mission allowed to verify the physical compatibility of the WAVE module with other payloads in different operating modes. For this purpose, the experimentation was particularly relevant for the water column profiling task because the wing surface was orthogonal to the direction of motion, causing a high drag effect to vehicle dive.

3.3.3.3 Mission data post-processing analysis

The data collected during the experimental tests were analysed in a postprocessing phase, aimed at verifying the correct execution of the commanded missions and evaluating the performance of the prototype, identifying any malfunctioning and their causes.

The tests conducted on the first two days with the mission-oriented modules gave all positive results: the vehicle was able to complete the missions, both elementary tasks and complex ones. Figure 3.19a shows the path followed by the vehicle on the surface during the environmental monitoring mission defined in Figure 3.15.

Figure 3.19b shows the depth of the vehicle during the same mission. The blue line is the depth measured by the on-board pressure gauge while in red the one acquired by the depth sensor of the multi-parametric probe. Both were communicated in real time to the C2S. The difference in the depth measurement was due to the fact that the probe was mounted in the lower part of the hull (Figure 3.14) and because of the different sensitivity of the two depth sensors. The profiling tasks occurred at waypoints 1, 2 and 3, for which the reference depth was set at 3, 2 and 3 meters, respectively. Figure 3.20 show the temperature, salinity, depth and sound data in the 3 waypoints.

Experimental tests with the side scan sonar yielded positive results too. It is worth to remark that the underwater navigation mode is based on constant propulsion that can be set as a percentage of the maximum achievable. During underwater navigation the yaw is actively controlled with the horizontal jet pumps in accordance with the desired heading, measured by the vehicle digital compass. The GPS positions of the vehicle during

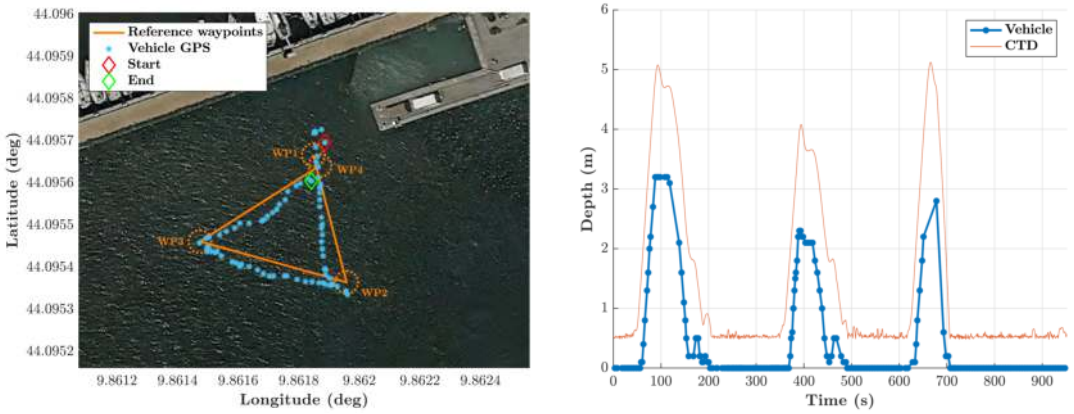

(a) (b)

Figure 3.19: *Results from the environmental monitoring mission. (a) In blue, the path actually followed by the vehicle during the water column profiling mission defined previously (indicated in orange). In particular, the blue asterisks indicate the GPS position of the vehicle transmitted to the C2S during the mission. (b) Measured depth of the WAVE vehicle during the water column profiling mission.*

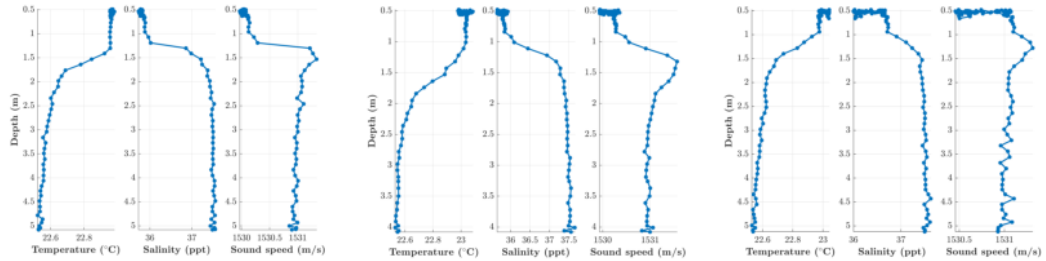

(a) (b) (c)

Figure 3.20: *Salinity and Sound speed data measured during the profiling tasks in the three waypoints.*

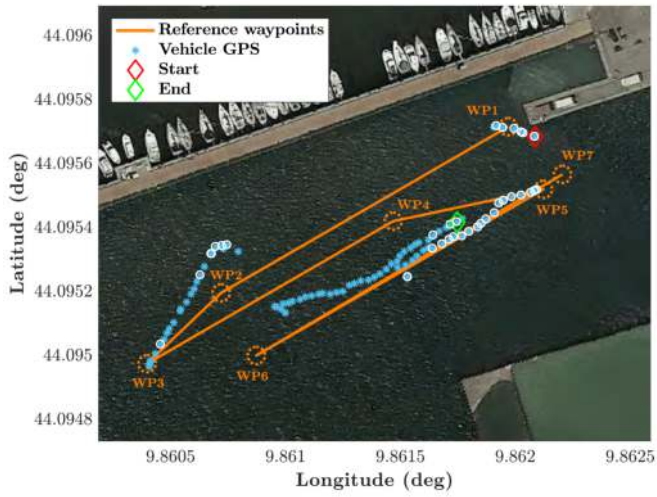

(a)

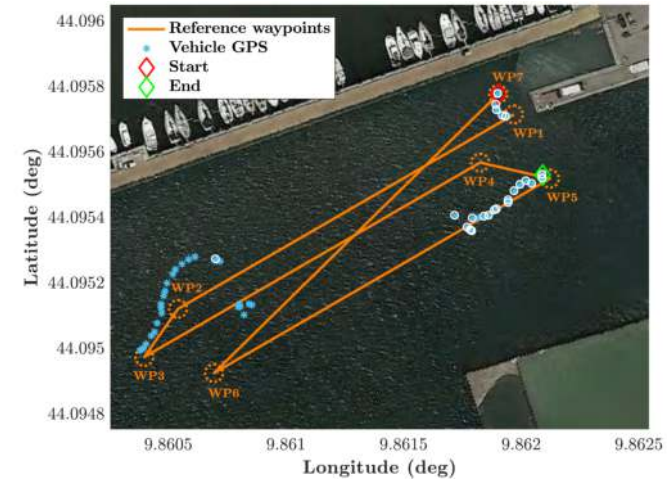

(b)

Figure 3.21: *WAVE vehicle GPS positions (blue asterisks) during sea floor exploration missions. The white circles indicate the GPS positions that were received real-time via acoustic communications. In orange the reference paths.*

both the complex sea floor exploration missions are shown in Figure 3.21 along with the reference path. The segments WP1-WP2, WP3-WP4 and WP5-WP6 were traveled at a depth of 3 m. For this reason, the GPS positions of the vehicle (blue asterisks) were available only at the resurfacing points. These positions were communicated in real time to the main ground station via acoustic modem. Notice that only a few vehicle's position acoustic communications actually reach the C2S among all the positions available (white circles in the figure). This is due to the well-known packet loss phenomena in precarious acoustic channel, such as the very shallow water where the mission took place. In addition, the harbour area is rich of magnetic disturbances that may have influenced the precision of the on-board compass and, consequently, of the vehicle underwater navigation. In fact, it is possible to notice how the vehicle resurface points do not coincide exactly with those expected (look, in particular, at the WP3-WP4 seg-

ment). Figure 3.22 shows the yaw and the depth of the vehicle that was received in real time from the C2S. The dives occurred at even numbered waypoints up to a depth of 3 m. The vehicle then navigated underwater towards the odd subsequent waypoint with a planned heading of 240°, 60° and 240°, respectively. Figure 3.23 shows two acoustic images collected by the side scan sonar during the transepts WP3-WP4 and WP5-WP6 of the second mission. The systematic presence of an object (circled in red) was identified, and it was coherent with respect to the size, intensity and relative position with the artificial target in Figure 3.16.

Regarding the last two days, the first objective was to functionally verify that the eFòlaga vehicle equipped with a payload module and the WAVE module was still able to perform the gliding mission. The vehicle has actually started to travel the desired trajectory towards the WP1 in glider mode, but, consistently with the expectations based on the considerations in Section 3.3.3.2, the motion was very slow. It was therefore decided to interrupt the mission to reinitialise it from a position closer to WP1 itself. The results of the gliding mission are summarized in Figure 3.24 where the depth measured by the vehicle's on-board pressure sensor is reported together with the same quantity measured by the CTD probe. The typical yo-yo trend is evident from the plot between the two subsequent resurfacing (*i.e.* vehicle at zero depth). However, the velocity was very low and the two resurfacing took more than 10 minutes.

The second mission was planned according to what is reported in Figure 3.25a that is similar to the previous one but with a starting point (red diamond) close to WP1 so that the first gliding task (already positively assessed in the first mission) could finish in short time. Once the short gliding task finished, the vehicle identifies the simulated low battery level input and start a 60 s period of wave recharging. Upon completion of the simulated wave charging phase, the vehicle resumes the original mission heading towards WP2 in surface navigation with propeller. Once the desired point has been reached, the vehicle carried out the profiling task up to the desired depth of 3 meters and then resurfaced successfully completing the total mission. In Figure 3.25b the measured depth is reported. The plot also shows the transitions between successive tasks whose timing has been obtained through the associated time stamps reported in the log files on board the vehicle. From the data collected it is possible to check the consistency between depth and performed task, confirming the correct timing of the tasks and the relative transitions between them.

To summarize, the last two days of tests have allowed to verify the correct functioning of the vehicle in carrying out the different types of tasks: gliding in the first mission, the other tasks (including a simulation of wave energy harvesting) in the second. Finally, the plot in Figure 3.25b is also useful to verify the dynamic behavior of the vehicle in the descent phase with the WAVE module in the fixed configuration, *i.e.* wings along the vehicle body. As can be seen from the graph, the vehicle was robust to the variation of the system's physics by performing a diving comparable to what was performed without WAVE module (Figure 3.19b).

3.3.4 Experiments in relevant scenario: the ASW-ODC17 sea trial

Immediately after the end of the specific activities of the WAVE project, but as a consequence of the SEALab collaboration, the WAVE vehicle participated in the ASW-ODC17 (Anti-Submarine Warfare - Operational Deployment of Concepts) sea trial ex-

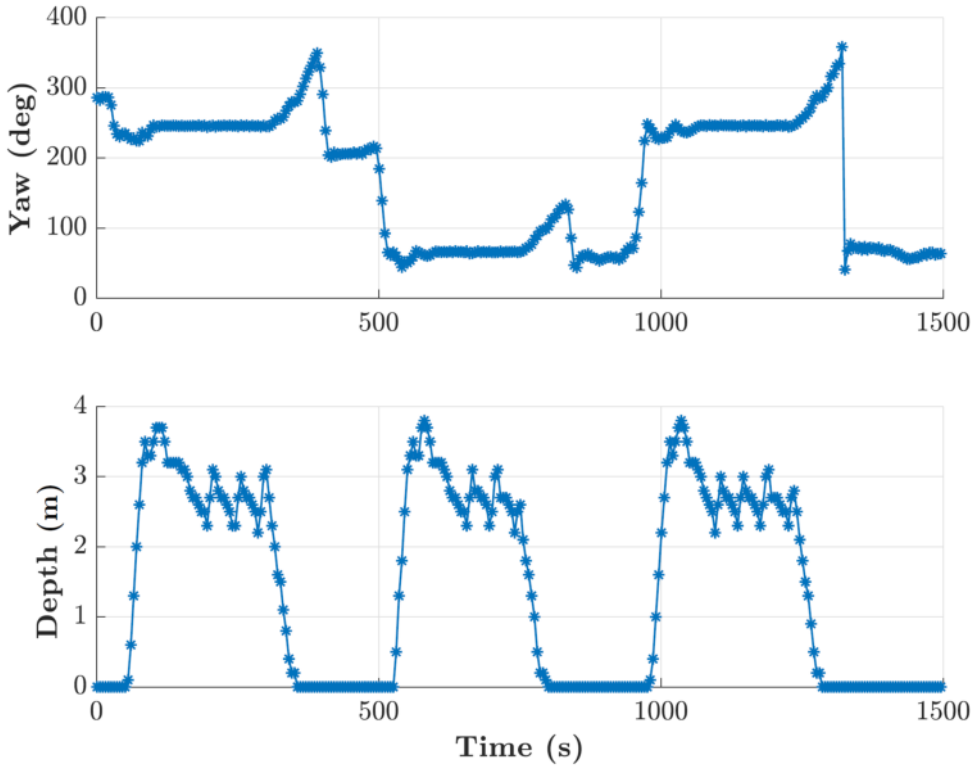

(a)

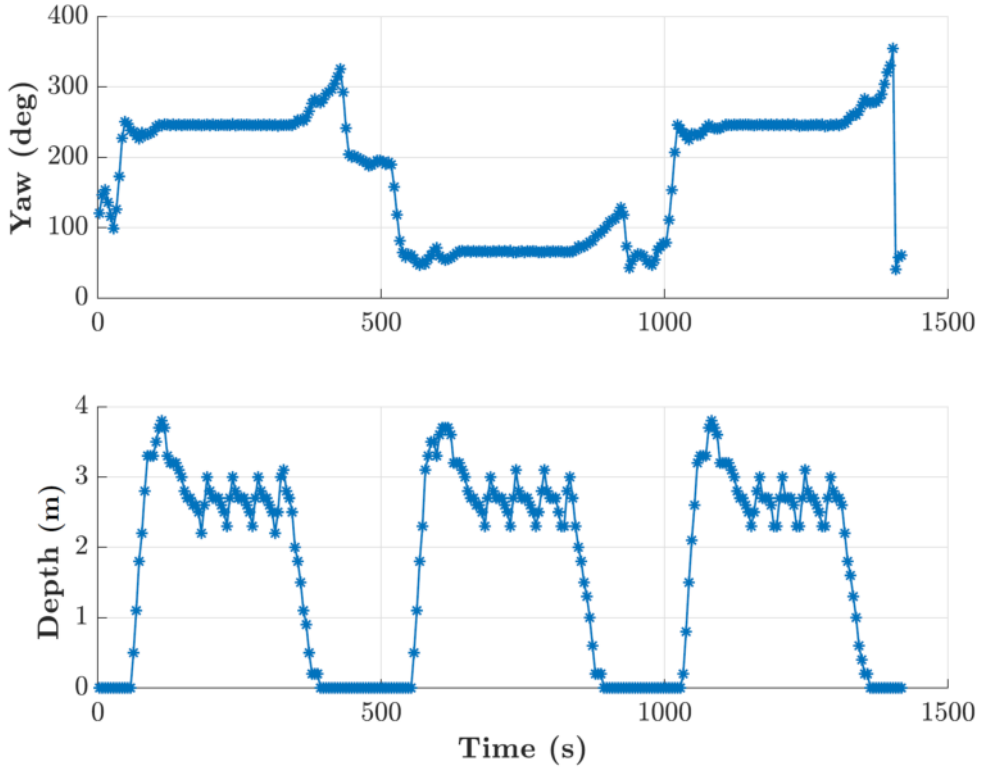

(b)

Figure 3.22: *Yaw angle and Depth of the WAVE vehicle during the two sea bottom exploration missions defined in Figure 3.16.*

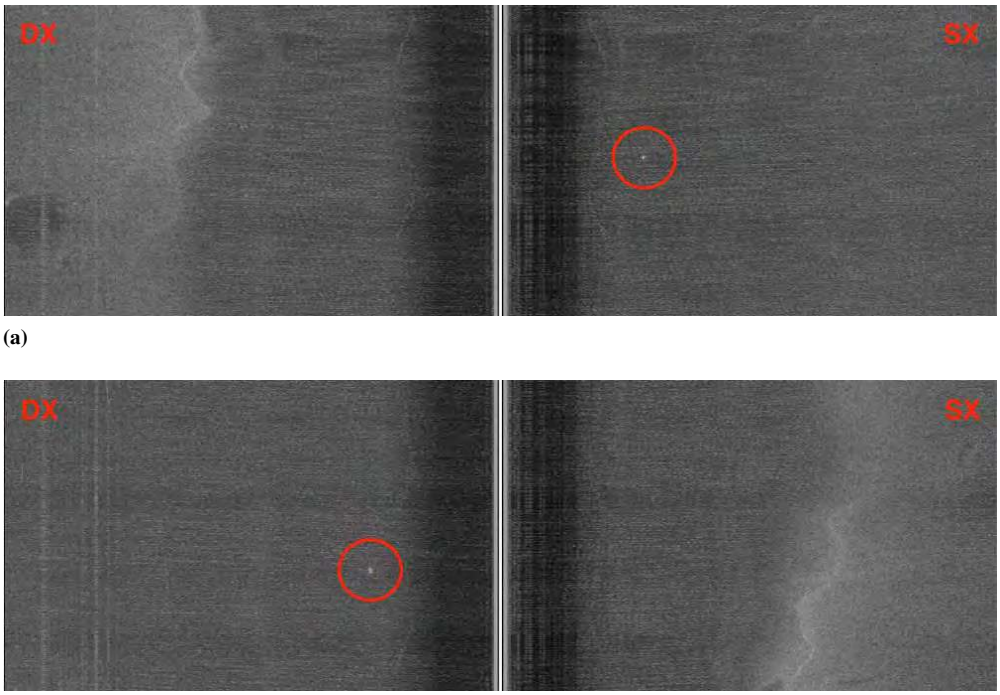

(a)

(b)

Figure 3.23: *Side scan sonar images collected on board during the second sea bottom exploration mission. The red circle indicates the mock-up target visible in WP3-WP4 (above) and subsequent parallel WP5-WP6 (below) swaths.*

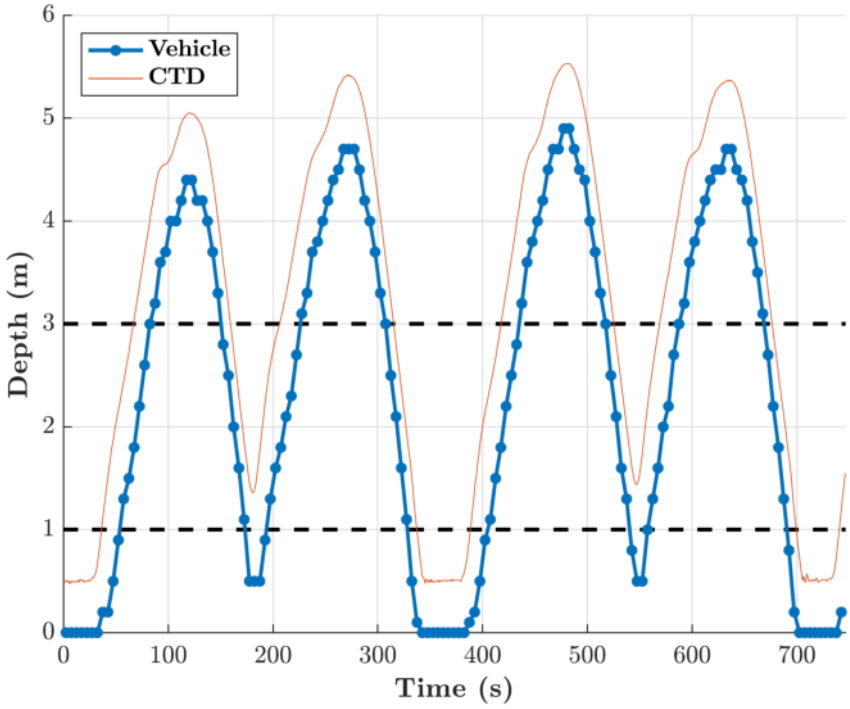

Figure 3.24: *Depth profile of the gliding mission. It is clearly visible the yo-yo path between two resurfacing points.*

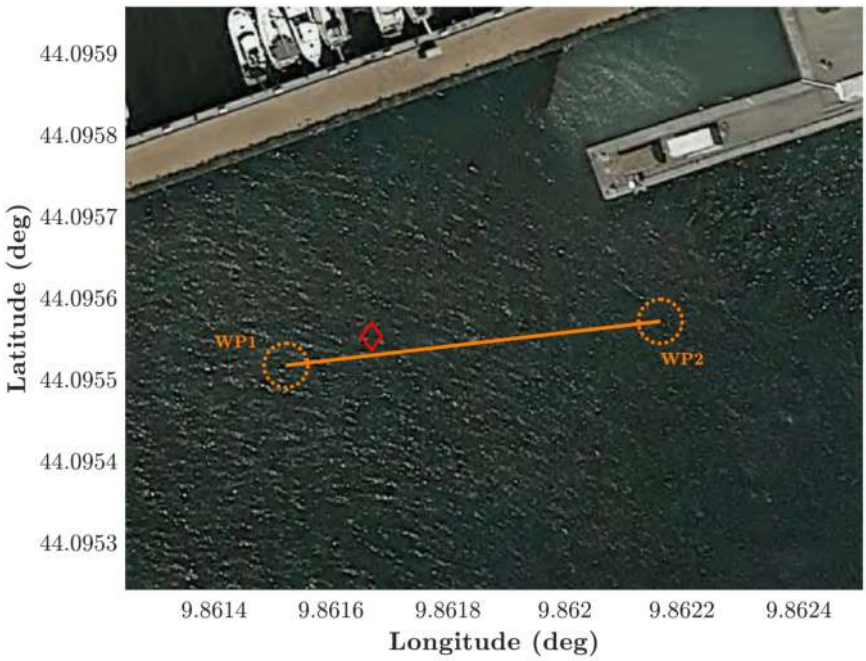

(a)

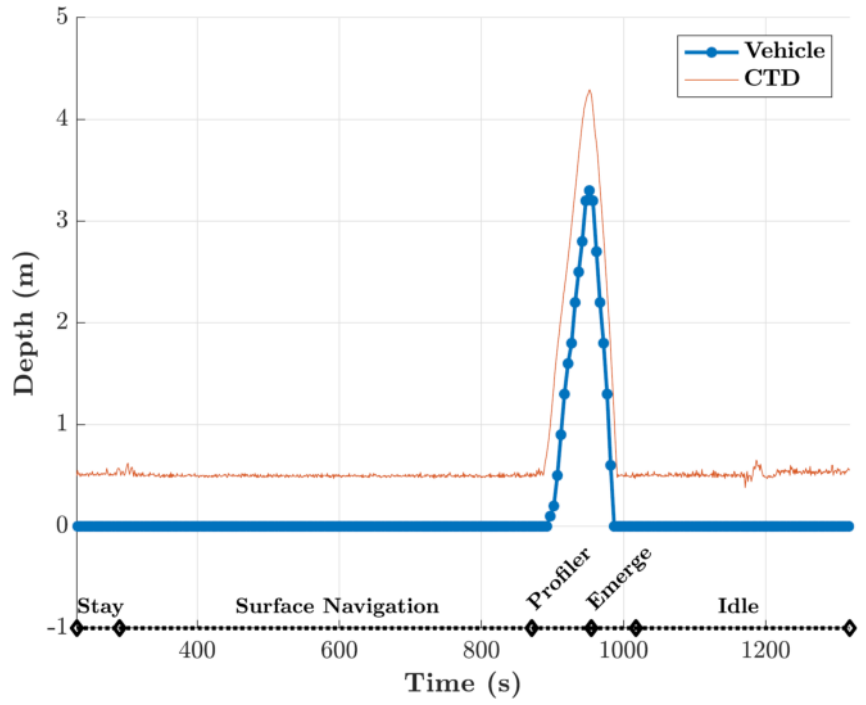

(b)

Figure 3.25: *Test day 4: complex mission results with the WAVE vehicle. (a) Definition of the second instance of the complete mission performed on day 4. Note that the starting point (red diamond) is closer to the position of WP1 than in the first instance of the mission Figure 3.18. (b) Depth of the vehicle measured by on-board sensor and by the multiparametric probe during the second gliding mission (after the reaching of WP1). The types of tasks associated with the various time intervals are shown below in the plot in correspondence of illustrative depth* $= -1\,m$.

ercise, held in October 2017 and partly conducted off the coast of La Spezia (Italy). The sea trials activities were organized in the context of the CMRE project MUS (Maritime Unmanned Systems) for ASW, in cooperation with NATO naval units. The final objective of the MUS project is the development and test at sea of a heterogeneous autonomous ASW network based on unmanned underwater vehicles implementing a multistatic active sonar system [55]. From the Italian partners' point of view, the goal was to demonstrate the interoperability of the WAVE vehicle within the CMRE robotic network for ASW [127] during a NATO operational exercise involving assets of different NATO Navies. The interoperability tests described in this section were conducted for four days (in the period 12 – 17 October 2017).

Interoperability capability was demonstrated by integrating the WAVE vehicle into the cited CMRE heterogeneous network by exchanging both commands and data. The challenge lay in the different robotics middleware of the WAVE vehicle, ROS - see Section 3.2, with respect to the one used by the CMRE network. The latter uses Mission Oriented Operating Suite – Interval Programming (MOOS-IvP), and the interested reader may find more information in [81, 127, 171]. Therefore, a ROS-MOOS bridge software was installed on a moored buoy acting as a gateway between underwater assets. The gateway was equipped with acoustic modems working on different frequencies, due to the peculiarities of the different AUVs involved in the experimentation in addition to the WAVE vehicle.

To have representative operational information, the WAVE vehicle was equipped during the trial with a CTD probe, the data of which were shared with the CMRE Environmental Knowledge and Operational Effectiveness (EKOE) team [91]. In addition, CTD data were made available for periodic updates of the environmental map in the area and for insertion into the MSTPA (MultiStatic Tactical Planning Aid) decision support tool [200], in which the onboard processed sound speed can be a valuable information. In particular, interaction with EKOE program allowed visualizing the positions of all the underwater assets (CMRE OEX AUVs and WAVE vehicle) on the EKOE C2 station. Furthermore, the WAVE vehicle position was available on board the NATO partners' Flag-Ship and at NATO Allied MARCOM (Maritime Command) command and control stations.

3.3.4.1 At-sea results and discussion

The planned interoperability tests started with a mission-planning phase, in which different parameters (e.g. waypoints, operating depth, and timeout) were sent from the CMRE C2S, where the WMCS was installed as an additional module, to the vehicle through the gateway buoy. After the vehicle started its mission, it automatically (at a selectable frequency) sent to the CMRE C2S its position and CTD data during profiling operation. Another test was the asynchronous request from the CMRE C2S to the vehicle of its position and CTD data. All the tests rely on acoustic communications between the gateway buoy and the vehicle. The complete mission done for all the considered experiments is shown in Figure 3.26. It is important to recall that it was possible to remotely add, start, stop or abort different tasks on the AUV during the mission. In particular, the vehicle was moving in gliding mode for about 250 meters in the first path between the starting point (red diamond) and the first dive point (orange asterisk). Then, it started doing four profiling tasks to characterize the water column

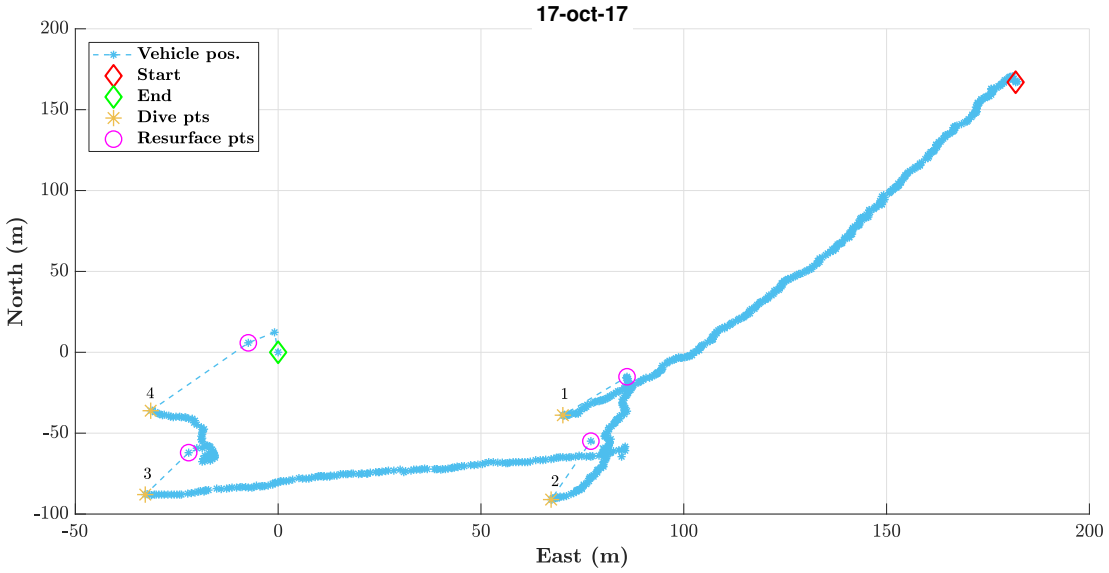

Figure 3.26: *The performed interoperability test mission in NED coordinates. Recall that the vehicle simply dives vertically using the ballast and the internal moving mass for profiling the water column. Only the vertical jet-pumps are used for finely trimming the pitch angle to 0°,* i.e. *it is free to drift during these kind of missions. As it can be seen, it was present a strong North-East sea current so that the vehicle resurfaced about* $30 - 40$ *meters away from the diving points. Finally, the first path from the red-diamond to the dive point no. 1 was done in surface navigation in this specific plot.*

down to 12 meters depth on a rectangular area of 5000 square meters.

In Figure 3.27, the gliding navigation and the following profiling tasks are shown. At the end of the last resurface, the vehicle was planned to autonomously reach a recovery point. Indeed, the mission timeout was achieved due to the tight operational schedule of the day. Hence, the vehicle did not complete the last profiling task and autonomously navigate to the mission final point.

This successful interoperability experimentation between different autonomous systems, with their own acoustic modems and middleware, was an important step to improve maritime situational awareness with respect to underwater assets during a joint NATO exercise. The WAVE software modularity makes it possible to incorporate a

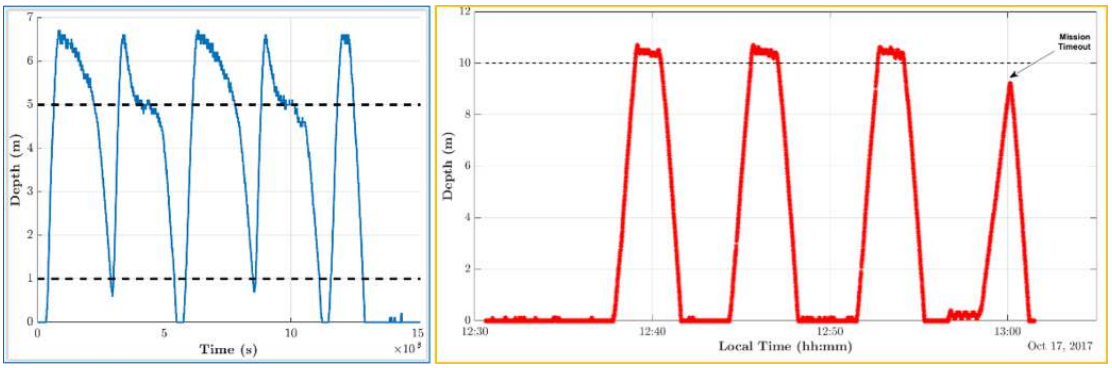

Figure 3.27: *Time versus Depth plots. On the left, the initial gliding phase. On the right, the four profiling tasks, autonomously interrupted by the vehicle.*

new AUV in the existing CMRE network, which in turn demonstrated its flexibility to integrate newly available assets thanks to its decentralized architecture.

Remarkable recent bridging applications are presented in [8, 65]. According to the authors' knowledge, however, no National interoperable approach had ever been fully tested and demonstrated before in an operational exercise involving NATO manned and unmanned assets. Moreover, this very rapid integration (*i.e.* less than one month since the project final tests) of the WAVE system in a multi-vehicle operation may be the best demonstration of the system effectiveness in an operational scenario.

3.4 Final conclusions on the WAVE project

The WAVE prototype was originally conceived as a hybrid vehicle capable of combining three different types of navigation, as shown in Figure 3.1. The project development can be divided into two main phases:

- Phase 1, in which the WAVE module and its integration into the vehicle were designed, and extensive bench tests were carried out to assess the feasibility of the wave-based propulsion and recharging concepts. The physical prototype was built in this phase too;

- Phase 2, in which the characterization of the prototype behavior in operationally relevant scenarios and the evaluation of the obtainable performances were performed.

The eFolaga vehicle was chosen as the carrier for the WAVE module mainly because of its inherent modularity. Thus, several mission modules (CTD probe for environmental monitoring and Side-Scan Sonar for sea bottom inspection) have also been realized in addition to the specific WAVE module. All of them have the possibility to include an acoustic modem for underwater communications. In fact, the specific WMCS and user interface developed during the project allow to exploit the acoustic channel to schedule missions, monitor their execution, and take the control in case of malfunctioning.

The project met all its technical requirements but with different performance levels; in particular, the performance related to the operational missions in the various configurations are all in line with the initial expectations, while the performance related to wave energy harvesting (which was the more innovative and risky aspect of the project) are only sufficient for the recharge of low power energy cells power. Indeed, the results obtained offer the possibility to define in a much more targeted way the field of use of the module, as well as several guidelines to improve its efficiency.

It is worth to note that the energy recovery system of the WAVE module is currently *unique* in the world; the WAVE prototype is in fact the first experimental example of an autonomous underwater vehicle capable of energy recovery from wave motion. Then, it should not be surprising that the experimental results eventually diverge from those expected lacking any previous experience. It is important to underline how the acquisition of experimental data allows to calibrate with greater precision and reliability the dynamical and simulation models, the relative energy recovery forecast, and the sizing of the module itself and its interfaces with onboard energy systems.

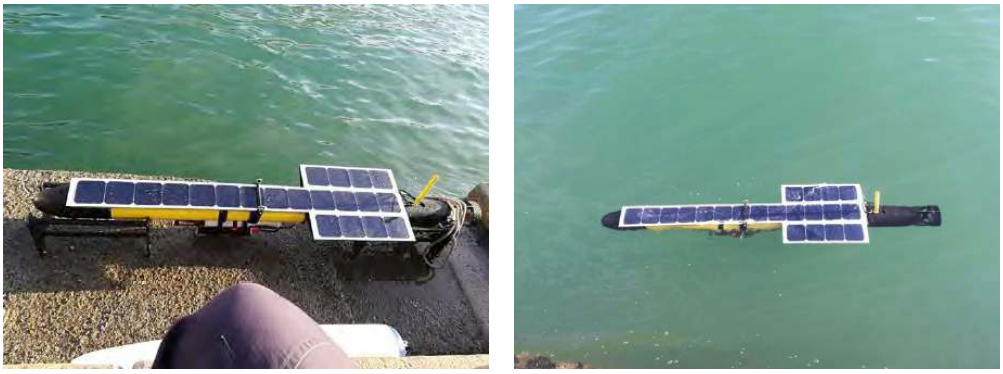

(a) (b)

Figure 3.28: *WAVE vehicle with the solar panels on the quay (left) and in surface navigation (right).*

3.4.1 Future directions

From the point of view of energy recovery from wave motion, the prototype showed capacities suitable for charging one or more battery cells with low charging power. Among the batteries already on the market, the Nickel-Metal Hydrate (NiMH) are certainly among the rechargeable ones from the WAVE module. It should be noted that battery cell technology is evolving rapidly, and it is to be expected that further technological developments may increase the range of batteries that can be compatible with the WAVE module.

Currently, in a vehicle such the eFòlaga, there is a Lithium-ion battery pack to supply the propulsion, actuators, on-board computers, payloads, and emergency systems. Some of these low-power devices can be powered by NiMH batteries (*e.g.* CTD and pressure sensors); it may be also possible to supply energy for the micro-controllers. However, the existing system is not able to power propulsion systems or payloads with high peak power requirements (*e.g.* Side-Scan Sonar). A re-design of the power supply system, dividing high- and low- consumption subsystems, would make the low-consumption part of the vehicle rechargeable by the WAVE module without affecting the high power battery pack. In this way, it would be possible to obtain a net energy saving that would be reflected in an increase of the overall vehicle endurance.

Moreover, the WAVE module could be used in synergy with other energy recovery systems; in particular, with solar energy systems which also have the advantage of being complementary to the operating modes of the WAVE module. In fact, the WAVE module is quite ineffective in sea state lower than 2, but in these situations solar irradiation is often present and therefore the energy recovered from the solar panels could supplement or complement the energy from the WAVE module. This improvement was already faced by GraalTech in a first prototype (Figure 3.28). Once more, note that this combination of energy recovery modules from different renewable sources can not work without a redesign of the entire vehicle energy supply system.

Finally, it has been shown that particular arm-wing configurations can results in a net advance in the surge direction of the vehicle. This possibility has been verified in simulation using the critically tuned model after the towing tank experimental campaign, and it is a scientifically and technologically relevant result of the project. From

an engineering point of view, it is necessary to design and install an arm-wing actuation system along with related real-time software on board the WAVE module. This implicates that the exploitation of the waves for navigation purposes would still require energy consumption to manage the arm-wing actuations and to measure the joint positions. This *energy trade-off* was outside the project specifications but it will be a necessary prerequisite for any other developments on this research topic.

CHAPTER 4

WAVE prototype experimental validation and characterisation

This chapter describes the systematic experimental characterisation of the WAVE module capabilities carried out in a controlled environment at the CNR-INSEAN test tank facility in Rome, Italy. During the three days experimentation (7-9 February 2017), a considerable quantity of data related to different recreated sea conditions and WAVE module configurations was collected. The energetic characterisation of the proposed system through a comparison of the performance of the different WAVE module layouts in terms of average generated power is detailed. The main result emerged from the presented analysis is the identification of the most effective configuration of the WAVE module for the battery charging. A deeper processing of data allows to critically tune the available dynamical model of the system introduced in the previous chapter and integrated in the next one. This way, it will be possible to evaluate, through simulations, the expected performance of the WAVE vehicle under typical wave profiles of the Mediterranean sea.

Note that this chapter is a revised version of the work presented in [42] and done during the WAVE PNRM Project.

In Section 4.1, the experimental setup is described with particular emphasis on the various configurations of the WAVE module. In Section 4.2, the experimental data analysis is reported along with extensive energy recovery performance comparison and discussion on generated electric power. Finally, in Section 4.3, conclusions and further related research topics are outlined.

Figure 4.1: *Overview of CNR-INSEAN test facilities. The Towing Tank no.2 (in red) was used for testing the WAVE module (`http://www.insean.cnr.it/`).*

4.1 Experimental setup

In order to characterise and assess the performance of the WAVE module, the tests of energy recovery and wave-induced propulsion systems were held from 7 to 9 February 2017 at the facilities of the CNR-INSEAN. CNR-INSEAN is a Research Institute active in the field of naval architecture and marine engineering within the frame of the National Research Council of Italy. Established in 1927, and known since then as "The Italian Ship Model Basin", it is located in the south-west suburb of Rome (Figure 4.1).

CNR-INSEAN has two towing tanks. Tank no. 1 is today one of the largest worldwide. It is $470\,\text{m}$ long, $13.5\,\text{m}$ wide and has a depth of $6.5\,\text{m}$. It is equipped with a towing carriage that can achieve a maximum speed of $15\,\text{m/s}$. Tank no. 2, used for the WAVE module experimentation, is of smaller size, with a slower carriage (Figure 4.2a). It is equipped with a $9\,\text{m}$ wide single-flap wave generator, that provides regular as well as irregular waves for the investigation of sea-keeping characteristics and ride comfort (Figure 4.2b). The wave generator is electro-hydraulically powered with 3 pumps of $38.5\,\text{kW}$ total power, controlled by a 100 harmonic components electronic programming device. Each harmonic may be modulated both in amplitude and frequency. Table 4.1 summarises the main characteristics of the Tank no. 2 and related wave generator and carriage structure.

For the purposes of the described experimentation, the vehicle equipped with the WAVE module was deployed from the tank-side and secured to the carriage through two ropes. The vehicle was tied such that it was completely free to move under the

Table 4.1: *Tank no. 2 main characteristics.*

Towing tank dimensions (m)			Wave generator characteristics			Carriage
length	breadth	depth	wave length (m)	wave height (m)	slope (deg)	max. speed (m/s)
220	9	3.5	1 to 10	0.1 to 0.45	1 to 9	10

(a) (b)

Figure 4.2: *Tank no. 2 facilities. (a) The carriage system. (b) View of the tank while the wave generator is in motion.*

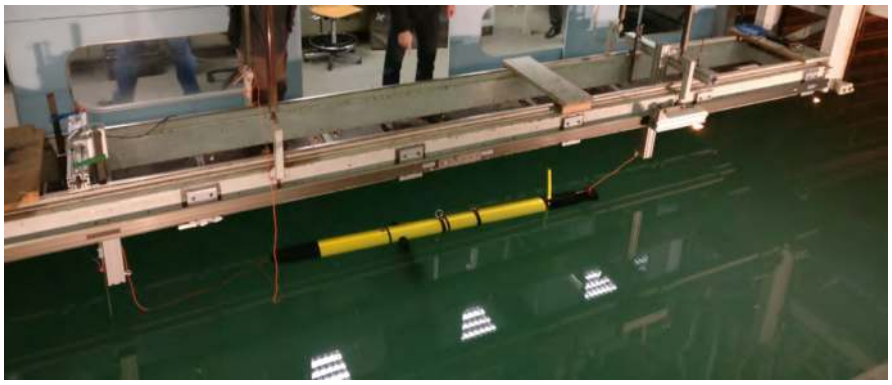

Figure 4.3: *eFòlaga vehicle with WAVE prototype during tank tests.*

action of the generated waves (Figure 4.3). Starting from the rest condition of the water in the tank, the wave generator was activated for about 5 minutes, with the vehicle having the bow directed in the opposite sense with respect to the wave propagation. During this period, the output voltage and current of the recharging circuit, as well as the vehicle pitch and the relative angle between the hull and the arms were measured and logged. After the end of each test, the wave generator was stopped for the time needed by the water in the tank to return in the rest condition (about 30 minutes in average). The period between one test and the next one was also exploited to change the configuration of the WAVE module. To recap, each test is organised into the following main phases:

WAVE module setup (30 minutes max) was made according to Section 4.1.1 while the water in the tank return in its rest condition.

Vehicle deployment (5 minutes max).

Wave generator activated (5 minutes) in line with the parameters described in Section 4.1.2.

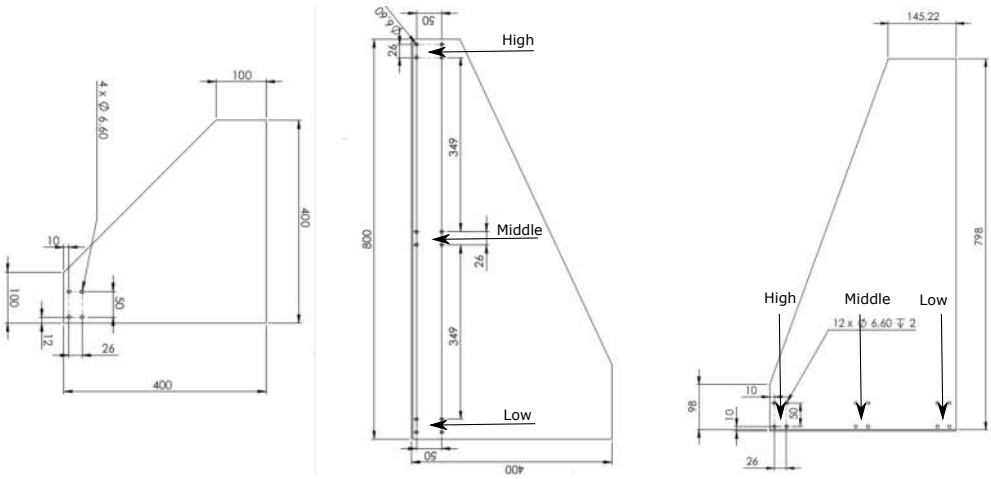

(a) (b) (c)

Figure 4.4: *Drawings of the wing sections used in the tank tests. (a) Type 1 and 1-bis. (b) Type 2. (c) Type 3.*

4.1.1 WAVE module configurations

The functioning of the wave energy recovery system was investigated for different configurations of the WAVE module, in order to derive a comparative analysis among the several different possible configurations in terms of developed average power.

Throughout the experimentation, the vehicle was maintained slightly buoyant with the center of mass and the center of buoyancy vertically aligned. The calibration procedure was carried out, if needed, after the configuration changes of the WAVE module. The calibration tuning parameters are the quantity of water inside the bow buoyancy chamber and the position of the rear battery pack (see Section 2.2 for further details). Moreover, the output of the internal recharging circuit was not directly connected to the battery of the vehicle, but on the measurement circuit used to evaluate the capability of electrical power generation. The circuit was composed of a constant load of $10\,\Omega$ in addition to both a current sensor and a voltage sensor. Separate dry tests were performed to evaluate the generated electrical power as the resistive load changes.

The WAVE module configuration was changed according to the following parameters.

Wing shape The impact of both wing dimensions and materials on system performance has been experimentally verified. The tests were done with four different profiles (Figure 4.4), whose characteristics are briefly reported in the following Table:

Type	Material	Max. length (mm)	Max. width (mm)
1	Carbon fiber	400	400
1-bis	Aluminium	400	400
2	Aluminium	800	400
3	Aluminium	400	800

(a) (b)

Figure 4.5: *Wing sections in the two mounting directions. (a) Right Side Up mounting direction. (b) Upside Down mounting direction.*

Wing mounting position The wing shapes type 2 and 3 are provided with fixing holes at three positions (Figure 4.4), corresponding to different possible mounting points of the arm. In the following, the labels *High*, *Middle* and *Low* will be used for those positions as indicated in the figure.

Wing mounting direction Each wing type was mounted according to the two possible mounting directions depicted in Figure 4.5. In the following, the configuration corresponding to the narrow part of the wing profile closer to the joint will be referred as *Right Side Up* (RSU, Figure 4.5a), whereas the opposite one will be labelled as *Upside Down* (UD, Figure 4.5b).

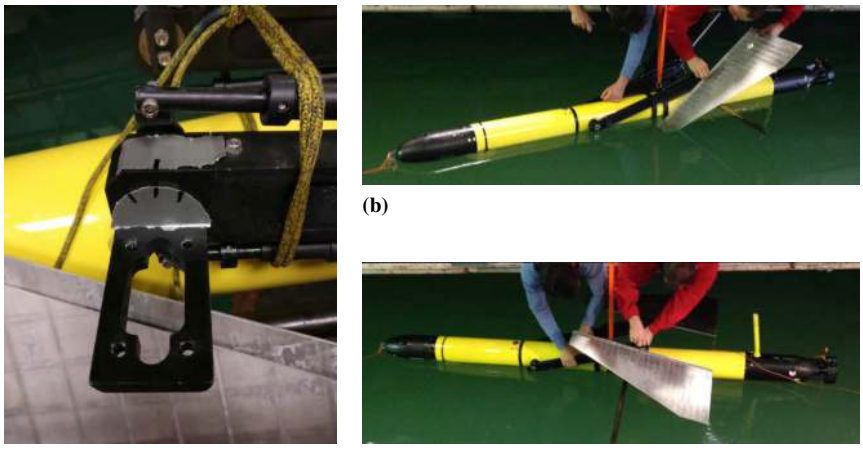

(a) (b) (c)

Figure 4.6: *Possible angular positions of the wings: (a) Joint end of stroke. (b) Knee configuration. (c) Foot configuration.*

Wing mounting angle Each of the two joints connecting the arms of the WAVE module to the wings can be rotated manually acting on two sliders connected to the arm (Figure 4.6a). Depending on the locking position of the sliders, the joint may be fixed with a desired angle or free to rotate between two angular positions located at about $\pm 30°$from the position in which the wings are perfectly aligned with the arms (*i.e.* 0°). During the energy recovery system tests the wings inclination was set at the two final angles, bringing the WAVE module in the configurations called

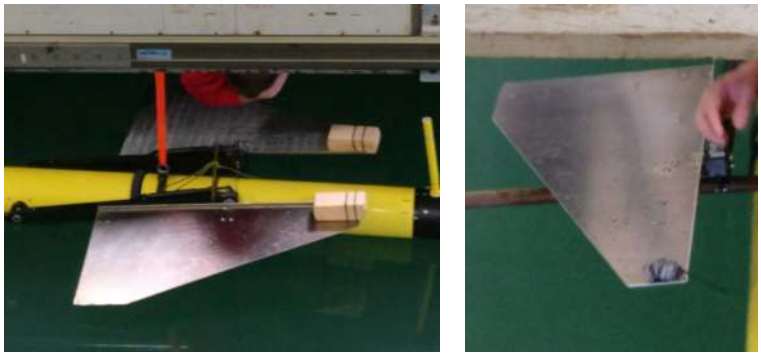

(a) (b)

Figure 4.7: *(a) Floats and (b) weights were added or removed to modify the buoyancy of the wings.*

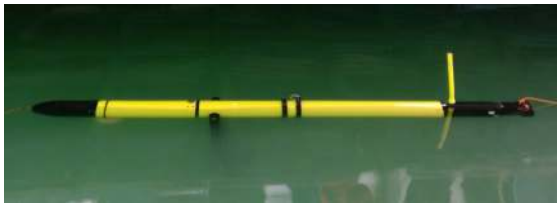

(a)

(b)

(c)

Figure 4.8: *The vehicle with three different relative positions of the WAVE module: (a) no additional module, (b) additional module at the bow and (c) at the stern of the energy recovery system.*

Knee ($-30°$ end of stroke) and *Foot* ($+30°$ end of stroke), shown in Figure 4.6b and Figure 4.6c, respectively. Finally, the configuration in which the joint is free to move between two positions was also tested and it will be indicated as $[a, b]$, where a and b are the selected limits of the movement.

Wing buoyancy The buoyancy of the wings was modified by attaching additional weights or floats as shown in Figure 4.7. In the following, an increase in the buoyancy of the wing profiles will be indicated with the sign "+"; vice versa a weight addition will be indicated with the sign "−".

WAVE module position The modularity of the WAVE prototype allowed to move the energy recovery system towards the stern or the bow by assembling on the vehicle an additional neutral-buoyant module as shown in Figure 4.8.

The setup of the WAVE module during the trials conducted with the energy recovery system is reported in Table 4.2 along with the experimental results. It is possible to notice that the configurations used in tests 2 and 23 are the same of tests number 1 and 15, respectively. This happened because the latter were affected by some experimentation anomalies that invalidate the mentioned tests, requiring a repetition of the runs.

Table 4.2: *Experimental test configurations and results. Average values of voltage, current and power obtained in the campaign are reported. The tests marked with the asterisks were performed by generating a wave profile with continuous spectrum and variable heights.*

Test	WAVE configuration parameters						Experimental outputs		
	Wing profile	Wing mounting position	Wing mounting direction	Wing mounting angle (°)	Additional weight per wing (g)	Additional module position	Voltage (mV)	Current (mA)	Power (mW)
1	1	-	RSU	0	0	None	152.18	13.69	6.30
2	1	-	RSU	0	0	None	137.34	12.29	5.04
3	1-bis	-	RSU	0	0	None	187.07	16.77	8.05
4	2	Middle	RSU	0	0	None	269.70	24.16	14.49
5	2	Low	RSU	0	0	None	253.19	22.83	15.01
6	2	Middle	UD	0	0	None	307.06	27.55	18.77
7	2	High	UD	0	0	None	198.83	17.81	10.17
8	3	High	RSU	0	0	None	256.63	23.14	14.63
9	3	Low	RSU	0	0	None	279.46	25.14	16.23
10	2	High	RSU	0	0	None	273.78	24.61	16.54
11	1-bis	-	UD	0	0	None	199.35	17.88	9.41
12	2	Middle	UD	0	$+380$	None	282.28	25.13	18.04
13	2	Middle	UD	0	-400	None	271.52	24.27	14.97
14	2	Middle	UD	0	0	None	304.34	27.27	18.70
15	2	Middle	UD	$+30$	0	None	345.85	31.03	26.93
16	2	Middle	UD	-30	0	None	302.93	27.20	18.04
17	2	Middle	RSU	-30	0	None	305.06	27.33	17.51
18	2	Middle	RSU	$+30$	0	None	386.35	34.42	28.56
19	3	Low	RSU	$+30$	0	None	321.78	28.82	20.43
20	3	Low	RSU	-30	0	None	294.33	26.55	17.33
21	3	High	RSU	-30	0	None	265.98	24.00	13.26
22	3	High	RSU	$+30$	0	None	338.96	29.99	23.06
23	2	Middle	UD	$+30$	0	None	391.66	34.99	30.70
24	2	High	RSU	$+30$	0	None	340.83	30.37	23.74
25*	2	Middle	UD	$+30$	0	None	8.16	0	0
26*	2	Middle	UD	$+30$	0	None	13.89	1.21	0.16
27	2	Middle	UD	$+30$	0	Bow	75.66	6.73	2.05
28	2	Middle	UD	$+30$	0	Stern	436.46	39.24	34.77
29	2	Middle	RSU	$+30$	0	Stern	409.72	36.76	30.75
30	2	Middle	UD	-30	0	Stern	243.90	22.05	10.50
31	2	Middle	UD	$[-30, +30]$	0	Stern	348.79	31.50	20.85
32	2	High	RSU	$[-30, +30]$	0	Stern	283.82	25.69	15.75
33	2	High	RSU	$[0, +30]$	0	Stern	266.32	24.10	13.78

In addition, the configurations of tests 6 and 14 are also the same in order to verify the repeatability of the results obtained on different days. It should also be noted that in the 3 days of experimentation the generated wave characteristics (*i.e.* height and frequency) were continuously monitored, and they proved to be coherent between them with differences below 5 %. This experimental verification, together with the fact that the duration of each test (about 5 minutes) made it possible to completely exhaust the initial transient of the generated wave motion, makes us confident that one experiment per configuration was enough to characterise the WAVE performance.

4.1.2 Wave parameters configuration

The parameters describing the generated wave profiles were kept constant at 0.45 m of height and 0.33 Hz of frequency for most of the tests, except for the numbers 25 and 26 which were performed using a wave profile with continuous spectrum and variable heights. The choice of the frequency and the amplitude of the generated waves needs a specific comment. The CNR-INSEAN wave generator is typically used for the testing of scale models of marine vessels. Hence, the parameters of the wave profile are in turn scaled with respect to those of the real sea state where the system under test would work. In the experimentation of the project WAVE the vehicle is a *full scale* model. The wave characteristics chosen for the most of the tests corresponds to the highest *full scale* sea state that could be replicated by the plant. According to the CNR-INSEAN engineers, the best trade-off configuration for the highest sea state corresponds to the lowest frequency at which the wave generator is able to produce the maximum wave height of 0.45 m, namely 0.33 Hz. The configuration, on the basis of the World Meteorological Organization sea state code (based on the *wind sea* definition of the Douglas Sea Scale), corresponds to a sea state 2, denominated *smooth (wavelets)*. A calmer configuration condition, according to the previous simulative analysis and confirmed by HIL tests, would not have provided an effective energy recovery (see chapter 3).

4.2 Data analysis and discussion

Table 4.2 summarises the average values of voltage, current and power generated by the WAVE recharging system for the different trials configurations described in Section 4.1.

Comparing the tests from 2 to 11, it is possible to notice that when the wing mounting angle is 0°, the best results in terms of developed power are obtained with the wing profile type 2, illustrated in Figure 4.4b. Looking at the test pairs 14-23, 4-18, 10-24, an evident improvement in system performance is achieved by tilting the wings in the so-called *Foot* configuration shown in Figure 4.6c. A further increase in the recovered average power is given by the displacement of the WAVE module towards the bow thanks to the insertion of an additional module as in Figure 4.8c, as demonstrated by the direct comparison between the test pairs 23-28 and 18-29. As expected, the tests 25 and 26 did not result in a significant outcome due to the under-sized parameters of the generated waves compared to those considered for the real scenario.

Figure 4.9 shows the power generated by the WAVE module in the two tests exhibiting the best performance, 28 and 29 respectively. The wave action causes an oscillatory motion of the arm of the WAVE module within a range of about $20°$ with respect to the

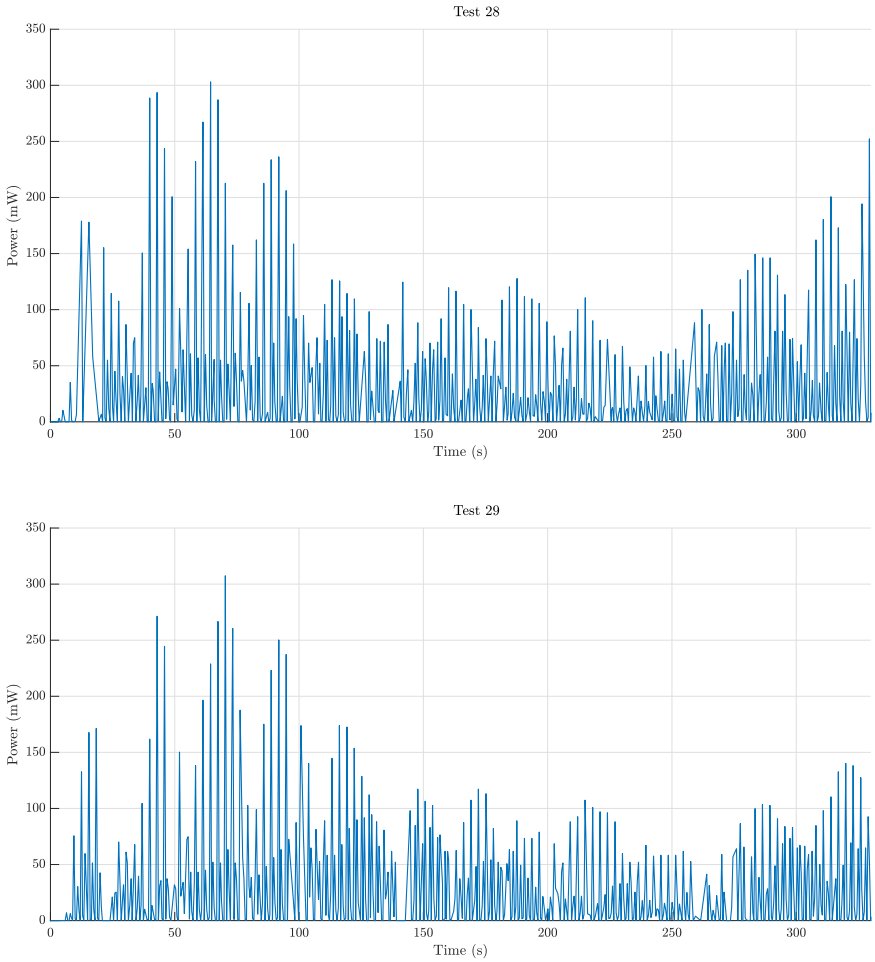

Figure 4.9: *Power generated by the WAVE harvesting system in the two tests exhibiting the best performance, no. 28 and no. 29.*

rest position as highlighted in Figure 4.10 that reports the relative angle between the arm and the vehicle body. This continuous motion triggers the energy recovery mechanism, which repeatedly generates voltage and current peaks as shown in Figure 4.11.

4.2.1 Experimental Data fitting

In this subsection the relationship between measured angular velocity at the hull-arm joint and generated electric power is highlighted.

The working point of the motor can be considered fixed due to the constant electric load in the experimental configurations. As expected, given the constancy of the motor working point, the data are consistent with the relation $P_{el} = k\omega^2$, where P_{el} is the generated electric power, ω is the angular speed of the WAVE module arm with respect to the vehicle body, and k is a constant of proportionality that can be determined from the data through the best linear interpolation obtainable according to the least squares criterion. The identified value is: $k = 647.7\,\text{mW s}^2\,\text{rad}^{-2}$. The experimental data, for all vehicle configurations without additional module and with monochromatic generated wave (test from no. 1 to 24), are shown in Figure 4.12 along with the linear regression

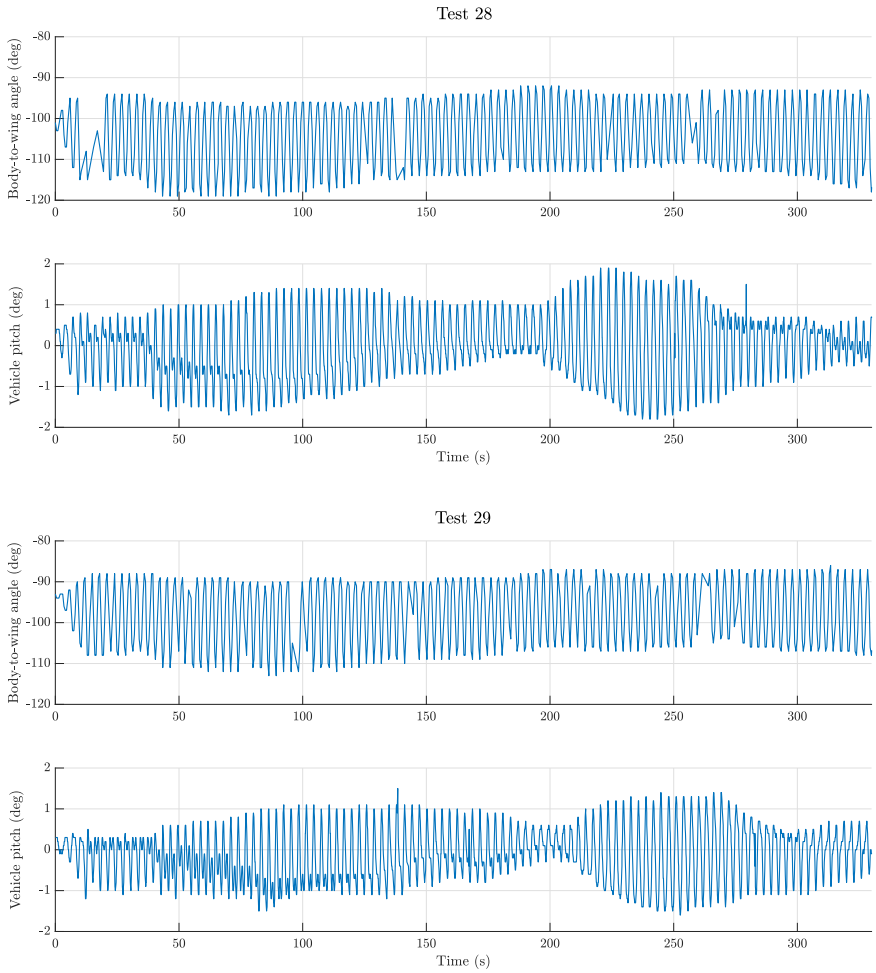

Figure 4.10: *The relative angle between WAVE arms and vehicle body and the vehicle pitch for test no. 28 and no. 29. It can be seen that the wave action causes an almost sinusoidal trend of this angle within about* $\pm 10°$ *with respect to the rest position.*

curve characterized by the angular coefficient k.

4.2.2 Bench-tests

In this section the analysis of the generated electric power with respect to the electric load and the WAVE arms angular velocity is presented.

In the experimental activity described in Section 4.1, the resistive load was constant and equal to $10\,\Omega$. In order to characterise the variation of the WAVE generated electric power with respect to the resistive load, bench tests have been carried out at the GraalTech facilities.

The voltage and current generated were measured while a single arm (without wings or additional weights) fell from the horizontal position (*i.e.* aligned to the vehicle body) until reaching the equilibrium position. For various resistance values between 1 and $51.7\,\Omega$, the procedure was repeated 10 times. All the dry tests showed a clear repeatability, as illustrated in Figure 4.13 where the data collected with resistive load equal to $10\,\Omega$ are reported. The maximum power value for each corresponding resistance

Figure 4.11: *Generated voltage and current by the WAVE harvesting system for test no. 28 (a) and no. 29 (b).*

was therefore chosen as the index according to which characterise the effect of the load variation on the performance of the energy recovery system. Figure 4.14 shows the trend of this index. The maximum electric power was obtained in a range of resistance values between 4.7 and 14.7 Ω, which includes the value of the load used in the tank experimentation.

4.2.3 Discussion on the battery technology

In this section, the possibility of using the energy recovered from the WAVE module for the recharge of all or some of the vehicle's on-board batteries is discussed. The charging of a generic battery can be typically divided into three distinct phases:

1. Pre-charge phase;
2. Constant current charge phase;
3. Constant voltage charge phase.

During the pre-charge phase it is necessary to supply a constant current equal to $1/10$ of the current used in the second phase. In the second phase, the battery needs a constant current of about $I = 1C$, where C is the battery capacity expressed in Ah. The battery voltage increases linearly until it reaches a limit value. In the last charge phase, the battery has to be supplied with a constant regulation voltage while the current decreases exponentially until it falls below a threshold value which indicates the complete charge of the battery (Figure 4.15). The energy produced by the battery

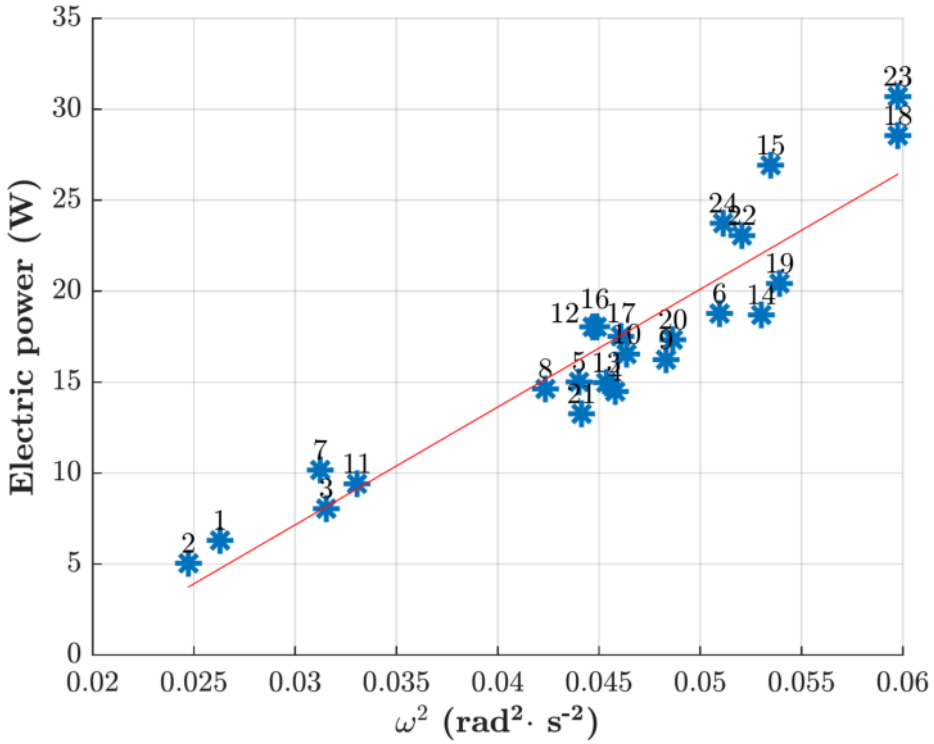

Figure 4.12: *The blue asterisks represent the values of average electric power generated as a function of the angular velocity of the WAVE arm measured in the first 24 tests. The red line represents the best linear approximation of the experimental data obtained with the least squares method.*

during discharging is:

$$E_{\text{Bat}} = \eta_{\text{Bat}} \int P_{\text{Bat}}\, dt \tag{4.1}$$

where E_{Bat} is the battery performance ratio, which can be assumed on average equal to 0.95.

Considering the battery pack of the WAVE vehicle, consisting of a Panasonic NCR-18650 A lithium ion battery with total capacity of 12.4 Ah, the pre-charge current required in the first phase is equal to 1.24 A. The minimum voltage required to be able to recharge the package is (as indicated by the manufacturer) equal to 4.5 V. The minimum power required is therefore at least 5.58 W which is one/two orders of magnitude the power that can be generated by the WAVE module. It is therefore evident that it is not possible to directly charge the entire battery pack with the current prototype.

The characteristics of individual cells of different classes of lithium ion batteries have been analyzed, *i.e.* which currents, voltages and powers are necessary for charging. In Table 4.3 are shown the nominal charging parameters for different type of batteries. The data here presented are extracted from the manufacturers' datasheets, in particular "Panasonic" for Lithium-ion and Cobalt-lithium ion cells (such as NCR-18650 A) and NiMH batteries, and from the "AA Portable Power Corp." datasheets for Lithium Iron Phosphate ion cells.

From the simulative and experimental data collected, it can be concluded that the WAVE module has the possibility of recharging Nickel-Metal Hydrate cells, provided

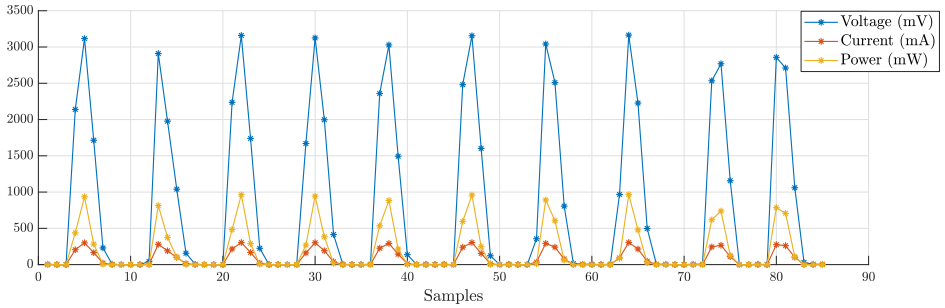

Figure 4.13: *Voltages (blue), currents (red) and corresponding electrical power (orange) measured during the 10 lab tests performed with resistance equal to 10 Ω.*

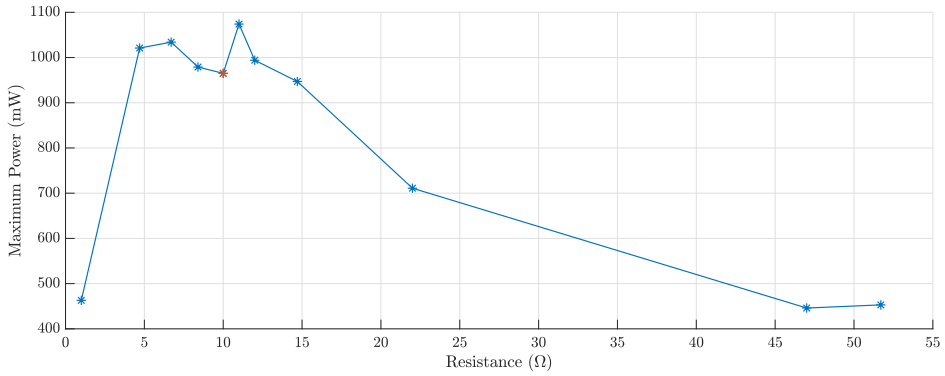

Figure 4.14: *Maximum power measured in the bench test with various resistive loads connected to the motor. In red, the value used in the experimental activity.*

that the frequency of the waves is relatively high (*i.e.* greater than 0.1 Hz). The charging of individual cells can have operative meaning for charging some types of payloads (*e.g.* CTD probe, acoustic modem). Some engineering modifications to the WAVE module can be outlined to increase the electric power recovered. In particular, two factors have a direct impact: the size of the wing and the electric motor acting as a dynamo. These two factors are considered individually in the following paragraphs.

The simulations carried out in the design phase showed how the mechanical energy transferred to the electrical system increases with the increase of the wing area. This relationship is confirmed by the experimental data, which indicate a greater energy recovery with the wings type 2 and 3 with respect to the smaller type 1. The creation of larger wings (within the operability limits of the vehicle) does not imply any further modification to the module or the vehicle.

About the electric motor, the one installed in the WAVE module has a high reduction ratio at the coupling engine - arm. The current solution was preferred because of the minor design complexity. Indeed, a high reduction ratio leads to a lower efficiency (taken into account already in the design phase, assuming an efficiency of 70% for the reduction gear). Therefore, an engine with lower reduction ratio can improve the efficiency implying a more complex gearing design of the module.

It is worth pointing out that the two actions described above can lead to an increase in the electrical power estimated between 40% and 60%. This means that the charging process remains confined to the single cell and not to the entire battery pack, but the

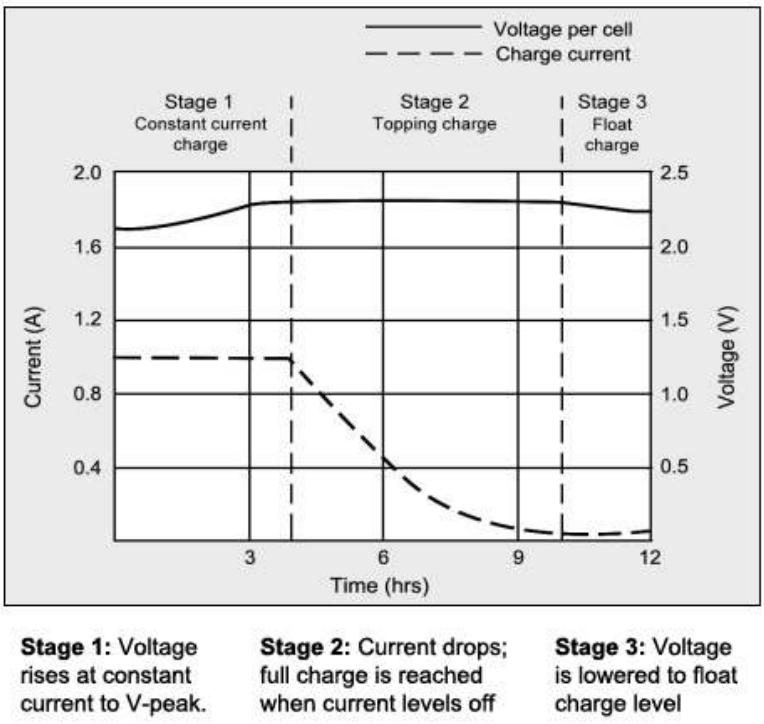

Figure 4.15: *Typical charge stages of a lead acid battery.*

battery types to which the charge can be applied is extended.

Even more complex solutions have been hypothesized, such as the effect of adaptive displacement of the wing position and/or adaptive control of its inclination. Finally, the combined experimental and simulative results give confidence that the WAVE system is suitable for charging single cells of NiMH batteries, possibly even more than one in parallel. This can be very useful for payloads and low power auxiliary systems, but not for the main power supply system of vehicle actuators. The sea conditions in which this is possible range from state 1 to state 4 (no sea conditions 5 and above have been simulated), provided the wave frequency is sufficiently high. The ”long wave” conditions are not favourable for energy recovery, regardless of the amplitude of the wave itself.

4.3 Conclusions and further research

A comparative analysis of the experimental performance of energy recovery obtainable from several different configurations of the WAVE module was described. The comparison is based on the data collected through an extensive experimental campaign carried out in a controlled environment, the CNR-INSEAN tank equipped with a wave generator. During three days of activity the configuration of the module, mounted on a eFòlaga as testing vehicle, was modified while maintaining the same generated wave characteristics corresponding to sea state 2. For the 33 performed tests, generated electric power was indirectly computed from measurements of current and voltage. This procedure allowed to qualitatively understand the effect on the generated electric power due to wing shape and mounting configuration (position, direction, and angle), and to

Table 4.3: *Main characteristics of several types of batteries used in AUVs.*

Battery type	Electric charge (mAh)	Pre-charge current (mA)	Charge current (mA)	Pre-charge voltage (V)	Charge voltage (V)	Pre-charge power (mW)	Charge power (mW)
Nickel - Cobalt	2000	200	1330	4.2	4.2	840	5586
Lithium iron phosphate (LFP)	400	40	400	3.2	3.2	128	1280
Nickel–metal hydride (standard)	500	50	50	1.2	1.2	60	60
Nickel–metal hydride (fast charge)	500	50	250	1.2	1.2	60	300
Nickel–metal hydride (slow charge)	500	25	25	1.2	1.2	30	30

module buoyancy and position.

From a preliminary analysis of the data shown, it is clear that for the considered configurations the WAVE system is not sufficient to fully guarantee the necessary energy supply for long-endurance missions. Indeed, the collected experimental results constitute a solid reference database for a critical tuning of the dynamic model of the system characterised during the first phase of the project. This way, it will be possible to carry out further simulations that can reliably predict the performance of the system even in conditions not tested yet due to the physical limits of the tank facility. Performance related to different wing shapes and mounting configurations may be inferred by means of the model without the necessity of additional experiments with considerable advantages in terms of time and costs.

The combination of the experimental and calibrated simulative results will allow to draw further analysis on the achievable performance in terms of both expected wave energy harvesting capability and also wave-gliding navigation skills with respect to the vehicle consumption. This outlined analysis is the topic of the next chapter.

CHAPTER 5

Feedback from field-test to modelling and simulation

Modelling and simulation are powerful and effective approaches to study how complex real-world systems behave over time. In addition, simulation is frequently the only mean to analyse autonomous underwater systems optimization prior to implementation because of the the timely and costly at sea experimentations.

For this reason, a modelling and simulation phase of the WAVE project was needed to understand how the system behaves under uncertain and different scenarios not easily replicable at sea because of the peculiarities of the wave energy harvesting concept. System dynamics approach is used to model and simulate the WAVE vehicle from a high system-level viewpoint, *i.e.* in terms of feedback and delays. It was useful for identifying the important variables and causal linkages in the system, and for structuring many aspects of prototype development.

This chapter is organised as follow. Section 5.1 illustrates in depth the ordinary differential equations that govern the system dynamic model and the related simulator of the WAVE module. This section is mainly inspired by the work in [38], that lay the groundwork in 2012 and that is broadly extended in this chapter, where the classic direct kinematics and differential kinematics problems are addressed, introducing also a Lagrangian approach to model the forces acting on each part of the multi-body system. The WAVE vehicle simulator is presented in Section 5.2 with preliminary simulative tests prior to the experimental trials. In fact, the extensive experimental campaign performed in these years, both in lab, controlled environments and in field (see Section 3.3), allows a fine tuning of the simulator parameters. This fitting between simulative and field data, along with the identification of the system parameters, is presented in Section 5.3. The validation of the simulative results opens up to new ideas applicable to the WAVE module that can be accurately predicted by the simulator. Sec-

Table 5.1: *DH parameters for the modeling of the WAVE vehicle.*

d	ϑ	a	α
0	$\pi/2$	0	$\pi/2$
p_n	0	0	$-\pi/2$
p_d	$-\pi/2$	0	$-\pi/2$
0	q_1	a_1	0
0	q_2	a_2	0
0	q_3	a_3	0
0	0	0	$\pi/2$

tions 5.4 and 5.5 outline the simulative predictions of innovative solutions to improve the wave recharging and wave gliding capabilities, respectively.

5.1 Modelling and Simulation of the WAVE vehicle

This section describes a control-oriented modelling approach for a hybrid autonomous underwater vehicle equipped with the WAVE module, summarizing the works presented in [38, 40] and done during the WAVE PNRM Project. The resulting WAVE vehicle is able to change its geometry depending on the specific task and battery level. Thus, a novel modelling approach for the dynamics of the vehicle incorporating its geometric variability was elaborated. The model can be directly used for the development of control laws for the navigation and guidance of the WAVE vehicle.

It is worth mentioning that the dynamical model of torpedo-shaped underwater systems has been established in the literature by Fossen [84, 85], and complex models have been proposed for a hybrid class of AUV/glider with variable mass and Center of Gravity (CoG) such as the Fòlaga vehicle [37]. However, during the wave recharging mode, since there are no variations of the overall mass and of the CoG position, the resulting model can be derived from the standard form of Fossen, with the exception of body-fluid interactions. In order to derive a dynamical model for the longitudinal plane motion (surge, heave and pitch), a Lagrangian approach was chosen. However, neither roll nor yaw nor sway are described by the model.

5.1.1 Direct kinematics

The traditional approach for modelling complex robotics systems is based on the use of several reference frames combined together to describe the position, orientation and velocity twist of the different parts of a multi-body system. According to the classic Denavit-Hartenberg (DH) convention [67], it is necessary to represents successive roto-traslation of reference frames using two pure rotations described by angles ϑ and α and two pure translations described by displacements d and a.

The corresponding DH parameters for the WAVE vehicle are summarized in Table 5.1. The i-th part of the multi-body system is described by the i-th row of Table 5.1, and then the transformation of the reference frame with respect to the $(i\text{-}1)$-th reference

frame is of the kind:

$$T_i^{i-1}(d_i, \vartheta_i, a_i, \alpha_i) = \begin{bmatrix} \cos(\vartheta_i) & -\cos(\alpha_i)\sin(\vartheta_i) & \sin(\alpha_i)\sin(\vartheta_i) & a_i\cos(\vartheta_i) \\ \sin(\vartheta_i) & \cos(\alpha_i)\cos(\vartheta_i) & -\sin(\alpha_i)\cos(\vartheta_i) & a_i\sin(\vartheta_i) \\ 0 & \sin(\alpha_i) & \cos(\alpha_i) & d_i \\ 0 & 0 & 0 & 1 \end{bmatrix}. \tag{5.1}$$

The base reference frame $O_b = [x_b, y_b, z_b]$ is assumed to be the North-East-Down (NED) frame as usual in marine robotics. The different reference frames used and the geometric parameters involved are shown in Figure 5.1.

It is important to note that exists an additional transformation to recover the end-effector reference frame, which has origin coincident with the wing aerodynamic center, see Figure 5.1b, which is the point where all hydrodynamic forces, generated by the relative motion between the wing and fluid, can be assumed to be applied [1]. This reference frame was chosen to model easily the drag and lift forces in the (x_e, z_e) plane and the torque around the y_e axis; other choices are also possible. The end-effector position p_e^b and orientation R_e^b in the base frame $\{b\}$ are described by combining all DH relative transformations T_i^{i-1} into

$$T_e^b(q) = T_1^b T_2^1(p_n) T_3^2(p_d) T_4^3(q_1) T_5^4(q_2) T_6^5(q_3) T_e^6 = \begin{bmatrix} R_e^b(q) & p_e^b(q) \\ 0^{\mathrm{T}} & 1 \end{bmatrix}, \tag{5.2}$$

where $q = [p_n, p_d, q_1, q_2, q_3]^{\mathrm{T}} \in \mathbb{R}^5$ is the vector of the generalized positions and the final roto-translation T_e^6 is obtained by the extra DH row with $d_6 = 0, \vartheta_6 = 0, a_6 = 0, \alpha_6 = \pi/2$. Note that the first two joints, p_n, p_d, are modelled as *virtual* prismatic joints, in fact they have null masses and inertias. They provide the distance travelled by the vehicle along the north-axis of the base reference frame x_b and the heave motion along the z_b axis, respectively. The third joint q_1 is rotoidal and models the pitch angle of the vehicle; the joint q_2 is the rotoidal joint between the hull (link 1) and the arm (link 2); q_3 is the rotoidal joint between the arm and the wing (link 3).

5.1.2 Differential kinematics

To relate the velocities $\dot{q}$ of the joints to the velocity of a particular point p_*^b, the approach of the geometric Jacobian can be used:

$$J^b(q, p_*^b) = \begin{bmatrix} \begin{pmatrix} J_{P1} \\ J_{O1} \end{pmatrix} & \cdots & \begin{pmatrix} J_{Pn} \\ J_{On} \end{pmatrix} \end{bmatrix}, \tag{5.3}$$

where

$$\begin{bmatrix} J_{Pi} \\ J_{Oi} \end{bmatrix}(q, p_*^b) = \begin{cases} \begin{pmatrix} z_{i-1} \\ 0 \end{pmatrix} & \text{if joint } i \text{ is (P)} \\ \begin{pmatrix} z_{i-1} \wedge (p_*^b - p_{i-1}^b) \\ z_{i-1} \end{pmatrix} & \text{if joint } i \text{ is (R)} \end{cases} \tag{5.4}$$

shows the different contributions in case of prismatic (P) joints or rotational (R) ones. Based on the definition of the Jacobian matrix (5.3), we have

$$v_*^b(q, \dot{q}) = \begin{pmatrix} \dot{p}_*^b \\ \omega_*^b \end{pmatrix} = J^b(q, p_*^b)\dot{q}, \tag{5.5}$$

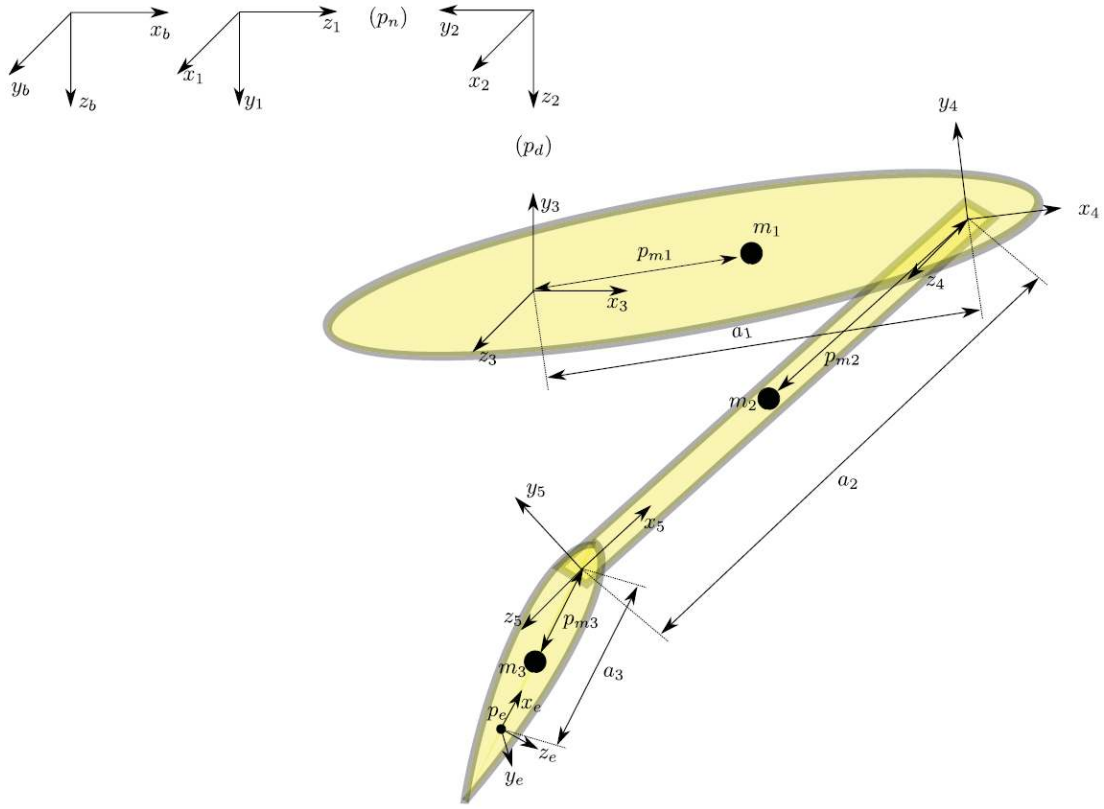

(a)

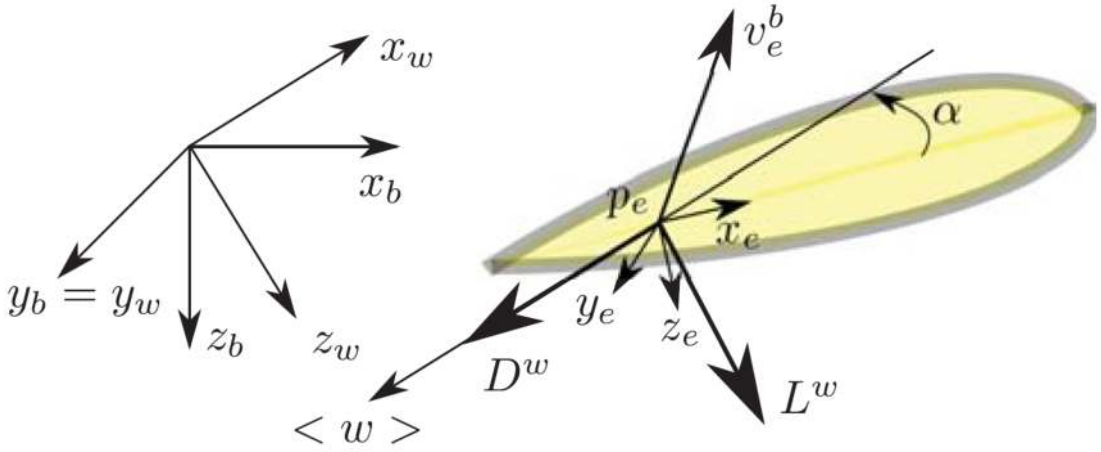

(b)

Figure 5.1: *Reference frames of (a) the vehicle equipped with the WAVE module and (b) the WAVE module end-effector.*

being $\dot{p}_*^b$ and ω_*^b, respectively, the linear velocity of the point p_*^b and the angular velocity of the relative rigid body.

Since the effects of the hydrodynamic parameters act on a single part of the multi-body system, the local velocities in a general frame $\{u\}$ are considered:

$$v_*^u(q,\dot{q}) = \begin{bmatrix} R_b^u & 0 \\ 0 & R_b^u \end{bmatrix} J^b(q,p_*^b)\dot{q} = J_b^u(q)J^b(q,p_*^b)\dot{q}. \tag{5.6}$$

Finally, we remark the duality property valid for a generalized force f_*^b applied at the point p_*^b, that corresponds to the joint generalized force

$$\tau(q,p_*^b) = J^b(q,p_*^b)^{\mathrm{T}} f_*^b. \tag{5.7}$$

5.1.3 Vehicle Dynamics via Lagrangian Modelling

The dynamics equations are here derived via a standard Lagrangian approach, based on the differential equation

$$\frac{d}{dt}\left(\frac{\partial \mathcal{L}}{\partial \dot{q}}\right) - \left(\frac{\partial \mathcal{L}}{\partial q}\right) + \left(\frac{\partial F_d}{\partial \dot{q}}\right) = \tau^{\mathrm{T}}, \tag{5.8}$$

where $\mathcal{L} = \mathcal{T} - \mathcal{U}$ is the Lagrangian function, $\mathcal{T}$ is the kinetic energy, $\mathcal{U}$ is the potential energy, q is the configuration vector, τ is the vector of the generalized forces and F_d is a Rayleigh-like dissipation function, used to model the viscous effects acting on the serial-chain joints. To model the dynamics of a vehicle moving in a fluid, also added masses, hydrodynamic damping and restoring forces have to be considered as shown in the next subsections.

Remark 1: The hydrodynamic forces, the wave potential and the generalized forces generated by the wings are included in the term τ. This is an interesting novelty because the hydrodynamic effects of each body part, in terms of added masses and centripetal contributions [84], are considered as applied in each local reference frame and then projected into the whole body. The hydrodynamic forces on each body part are then modelled following the classic analytical approach of [50]. The same approach is used for the generalized forces generated by the underwater wing.

5.1.3.1 Kinetic energy

Let p_{mi}^b be the centre of mass of the link i, having mass m_i and inertia I_{mi}^j with respect to the reference frame $\{j\}$. The kinetic energy of the link i is

$$\begin{aligned} \mathcal{T}_i(q,\dot{q}) =& \frac{1}{2} m_i \dot{q}_i^{\mathrm{T}} J_{Pi}^*(q,p_{mi}^b)^{\mathrm{T}} J_{Pi}^*(q,p_{mi}^b)\dot{q} + \\ &+ \frac{1}{2}\dot{q}_i^{\mathrm{T}} J_{Oi}^*(q,p_{mi}^b)^{\mathrm{T}} R_i^b(q) I_{mi}^i R_i^b(q)^{\mathrm{T}} J_{Pi}^*(q,p_{mi}^b)\dot{q}. \end{aligned} \tag{5.9}$$

The notation J_i^* indicates that the Jacobian takes into account the contributions up to the link i of the serial chain. Recall that the first two joints are modelled as virtual, *i.e.* they have zero masses and moments of inertia.

Finally, the total kinetic energy is obtained by summing all the contributions of the single links:

$$\mathcal{T}(q,\dot{q}) = \sum_{i=1}^{5} \mathcal{T}_i(q,\dot{q}). \tag{5.10}$$

5.1.3.2 Potential energy

The potential energy describes the effects of restoring forces, such as buoyancy and gravity, and additional terms due to the wave-body interaction. In particular, the potential energy of the link i is

$$\mathcal{U}_i(q) = (\rho V_i - m_i) {g_0^b}^{\mathrm{T}} z_{mi}^b, \tag{5.11}$$

where ${g_0^b}^{\mathrm{T}} = [0, 0, g]^{\mathrm{T}}$, g is the gravity acceleration, V_i is the volume of the link i, ρ is the fluid density.

The wave potential energy is modelled as a two-springs system, one acting on the (vertical) heave axis and one along the pitch axis, because it is quite natural to assume that the vehicle is not rigidly constrained on the sea surface. Therefore the potential energy of the waves can be modelled as follows.

$$\mathcal{U}_w(f_w) = \frac{1}{2} k_d (p_d^b - f_d^b)^2 + \frac{1}{2} k_1 (q_1 - f_1)^2, \tag{5.12}$$

where k_d, k_1 are positive constants to be identified and $f_w = [f_d^b, f_1]^{\mathrm{T}}$ are functions describing the chosen wave characteristics.

A realistic way of modelling the wave profile is given by considering a sinusoidal wave of amplitude A_w and frequency $\omega_w/(2\pi)$:

$$f_d^b(t) = A_w \sin(\omega_w t), \qquad f_1(t) = \arctan(A_w \omega_w \cos(\omega_w t)). \tag{5.13}$$

Obviously, the total potential energy is given by the sum

$$\mathcal{U}(q, f_w) = \mathcal{U}_w(f_w) + \sum_{i=1}^{5} \mathcal{U}_i(q). \tag{5.14}$$

5.1.3.3 Drag modelling

The viscous friction acting on the joints due to body-water interaction is modelled as a linear function of the joints velocities:

$$D_q \dot{q} = \left(\frac{\partial F_d}{\partial \dot{q}} \right)^{\mathrm{T}}. \tag{5.15}$$

The hydrodynamic effects acting on the i-th body part can be represented in a linear form as:

$$\tau_h = -\left(J_q^i(p_{mi}^b, q) D_{hi} J_b^i J^*(p_{mi}^b, q) \dot{q} \right) = -D_{hi}(q) \dot{q}. \tag{5.16}$$

Remark 2: The description of the hydrodynamic drag $D_{hi}(q)$ of the i^{th} link is directly provided in its respective local reference frame. This technique simplifies the modelling effort, since the single hydrodynamic contribution can be efficiently computed using a standard finite-element-analysis approach.

Remark 3: Since it is expected that the WAVE Fòlaga navigates at the sea surface with low speeds (less than 2 m/s), it is possible to assume that the body-fluid relative motion is dominated by a laminar flow. This way, the small Reynolds numbers that characterize the laminar condition allow to simplifies the drag characterization of each link. In addition, the shape of each vehicle part was simplified as ellipsoidal. As a result of these simplifications, the analytical results of [50] were used to describe the corresponding viscous drag forces.

5.1.4 Added masses

Since a moving body and the surrounding fluid can not occupy the same physical space simultaneously, some of the fluid around the body surface is moved (or deflected). The mass and inertia of the fluid, which acquires a certain acceleration, must be considered in the dynamics of the system.

For the sake of simplicity, the hull of the robot was modelled as prolate ellipsoid while the arms and the wings as prisms [84]. Calculating the added masses of an ellipsoid and prisms is straightforward, *i.e.* diagonal matrices are obtained. Moreover it is advantaging to consider bodies with axis symmetries.

Letting ρ_i be the density of the i-th link obtained as the ratio between body mass m_i and its volume (equal to that of an ellipsoid) $V_i = \frac{4}{3}\pi a b^2$, the eccentricity is defined as:

$$e = 1 - \left(\frac{b}{a}\right)^2 . \tag{5.17}$$

Notice that in the following formulation the subscripts $\{u, v, w\}$ represent the components due to linear velocities along x, y, z axis, respectively, while subscripts $\{p, q, r\}$ represent the moments due to angular velocities.

The diagonal matrix of the added masses of an ellipsoid is defined as:

$$M_a = -\begin{pmatrix} x & & & & & \\ & Z_w & & & & \\ & & K_p & & & \\ & & & M_q & & \\ & & & & N_r & \end{pmatrix} \tag{5.18}$$

It is now possible to explicitate the terms of the matrix in (5.18) in which, for the symmetry of the ellipsoid along the longitudinal axis and with respect to the medial axis, we have $Y_v = Z_w$ and $M_q = N_r$:

$$\begin{aligned} X_u &= -m\frac{\alpha_0}{(2-\alpha_0)}, \\ Y_v &= -m\frac{\beta_0}{(2-\beta_0)}, \\ K_p &= 0 \\ M_q &= \frac{m(a^2-b^2)^2(\alpha_0-\beta_0)}{5\left[2a^2-2b^2+(\alpha_0-\beta_0)(a^2+b^2)\right]}. \end{aligned} \tag{5.19}$$

The terms α_0 and β_0 are defined as [84]:

$$\alpha_0 = 2(1-e^2)\left(e - \frac{1}{2}\ln\left(-\frac{e+1}{e-1}\right)\right)\left(\frac{1}{e^3}\right) \tag{5.20a}$$

$$\beta_0 = \frac{1}{e^2} + \ln\left(-\frac{e+1}{e-1}\right)\frac{(e^2-1)}{2e^3} \tag{5.20b}$$

Moreover, the robot kinetic energy (5.10) was summed to the added masses kinetic energy so that $E_{\text{kinetic-total}} = \mathcal{T}(q,\dot{q}) + \mathcal{T}_{M_a}(q)$, where $\mathcal{T}_{M_a}(q)$ is the total kinetic energy

due to added masses calculated as:

$$\mathcal{T}_{M_a}(q) = \frac{1}{2}\sum_{k=1}^{5} q^{\mathrm{T}} J_{pm_i}^{\mathrm{T}} M_{a_i} J_{pm_i} q \tag{5.21}$$

5.1.5 Hydrodynamic Damping

Exploiting the theoretical framework of [84], it was possible to directly calculate the hydrodynamic damping matrix under the assumption of prolate symmetrical ellipsoid bodies, *i.e.* $b = c$.

Thus, the hydrodynamic damping matrix will be diagonal:

$$D_h = -\begin{pmatrix} F_x & & & & & \\ & F_y & & & & \\ & & F_z & & & \\ & & & M_x & & \\ & & & & M_y & \\ & & & & & M_z \end{pmatrix} \tag{5.22}$$

Notice that for the symmetry of the ellipsoid the forces and moment acting along the vertical and medial axis are the same, *i.e.* $M_x = M_z$ and $F_x = F_z$. The viscosity coefficient of the water is defined as $\mu = 0.0105\rho$, where ρ is the sea water density. With the eccentricity definition in (5.17), it is possible to further define:

$$L = \log\frac{1+e}{1-e}. \tag{5.23}$$

It is now possible to develop the terms of (5.22):

$$\begin{aligned} F_x &= \frac{16\pi a\mu e^3}{(1+e^2)L - 2e}, \\ F_y &= \frac{32\pi a\mu e^3}{(3e^2-1)L - 2e}, \\ M_x &= \frac{32\pi a^3\mu e^3(1+e^2)L - 2e}{3(1-e^2)}, \\ M_y &= \frac{M_x}{1-e^2}. \end{aligned} \tag{5.24}$$

5.1.6 Dynamic model

Considering the contributions shown in the previous subsections, the following dynamic multi-body model can be derived.

$$B(q)\ddot{q} + C(\dot{q})\dot{q} + D(\dot{q})\dot{q} + G(q, f_w) = \tau_w + J^b(q, p_e^b)^{\mathrm{T}} f_e^b + \tau_c \tag{5.25}$$

where

- $B(q)$ is the system inertia matrix (including added mass);

- $C(\dot{q})$ is the Coriolis-centripetal matrix (including added mass);
- the damping matrix has a constant term and a linear one, namely $D(\dot{q}) = D_q + D_h(q)$. The first one represents the drag on each joint, while the second one is generated by the body-fluid iteration and is q-dependent.
- $G(q, f_w)$ is the gravitational term, representing gravitational and buoyancy forces and moments;
- τ_w is the wave potential analysed in Section 5.1.8;
- $J^b(q, p_e^b)^{\mathrm{T}} f_e^b$ describes the drag and lift forces on the wing;
- τ_c is the vector of control inputs.

In the dynamics equation (5.25), the end-effector wrench generated by the wing $f_e^b(R_e^b, R_w^b, v_e^b, v_w)$ is actually due to the end-effector orientation R_e^b and velocity v_e^b, besides the wave front orientation R_w^b and velocity v_w^b.

5.1.7 Wave motion model

The modelling of the wave motion model is mainly adopted by [182]. For simplicity, it was assumed the robot navigates on a progressive planar wave, moving in the x-direction, modelled as:

$$\eta(x, y, t) = A \sin(kx - \omega t), \tag{5.26}$$

In the state of rest, the ocean surface coincides with $\eta = 0$. When waves are present, the surface is located at $\eta(x, y, t)$, where t is time. A is the wave amplitude in meters, k is the wavenumber $k = \frac{2\pi}{\lambda} = \frac{\omega^2}{g}$ in m^{-1}, $g = 9.8\,[\mathrm{m\,s^2}]$ is the gravity constant, λ is the wave length in meters, $\omega = 2\pi f$ is the wave angular frequency measured in rad/s, and f is the frequency in Hz [224]. The frequency ω is always positive; the wavenumber k can be positive or negative. If k is positive, then the wave moves to the right, toward positive x. If k is negative, the wave moves to the left. The *wave height* - the vertical distance between the crest and the trough - is equal to $2A$. The bottom is assumed flat, and it is located at $\eta = -H$, where H is a constant equal to the depth of the area.

It is possible to calculate the velocity potential of the wave as a function of the position x and elevation d:

$$\Phi = \frac{gA}{\omega} e^{kd} \sin(kx - \omega t). \tag{5.27}$$

Subsequently, it is possible to calculate the local velocity components (u, v), horizontal and vertical respectively, of the fluid:

$$\begin{aligned} u &= \frac{\partial \Phi}{\partial x} = \omega A e^{kd} \cos(kx - \omega t), \\ v &= \frac{\partial \Phi}{\partial d} = \omega A e^{kd} \sin(kx - \omega t). \end{aligned} \tag{5.28}$$

The velocity potential shows an exponential decrease in velocity with increasing depth, and in addition the velocity profile has a circular trend. Notice that the term d represents an elevation above the surface of the fluid, so considering the base frame $\{O_b\}$ it will

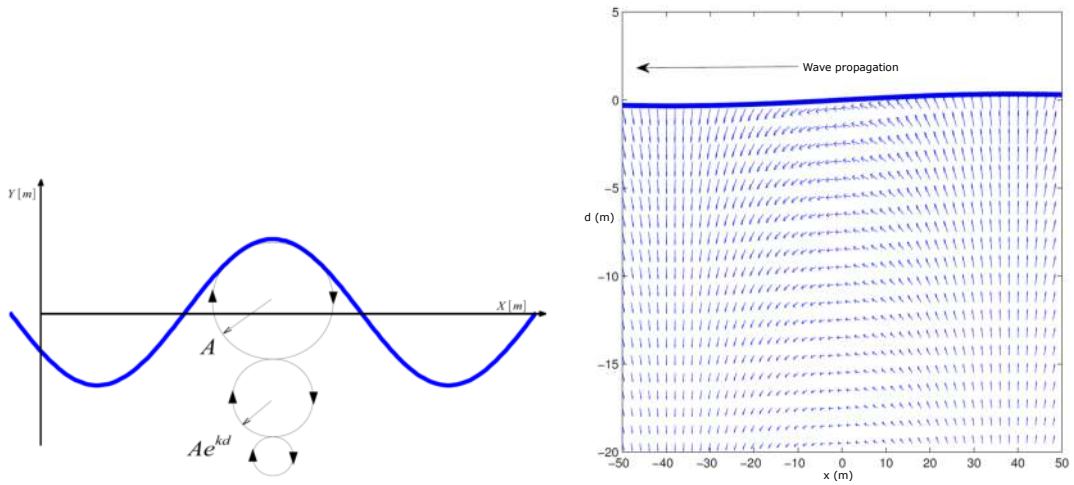

(a) (b)

Figure 5.2: *Wave motion modelling. (a) Velocity potential and (b) velocity of fluid particles in a progressive planar wave.*

vary as $-z_b$. Figure 5.2 shows the trend of the wave velocity potential and the actual distribution of the fluid velocity for a progressive planar wave.

There are two important restrictions about this modelling which must be explained:

- The presented modelling is accurate until $A|k| \ll 1$. It means that the wave height must be small compared to the wavelength. In other words, the wave must have a small slope. This condition bound the discussion on waves called *linear waves* by oceanographers.
- The presented equations assume that the wave is neither being forced nor dissipated, *i.e.* it is a free wave. The equations apply best to the long ocean swells between the point at which they are generated by storms and the point at which they dissipate by breaking on a beach.

5.1.8 Robot-Wave model

During the wave-gliding phase, it is assumed that the vehicle does not use any type of active propulsion and therefore the hull remains floating on the surface under the action of the sole pressure forces due to the planar incident wave of (5.26). The τ_w in (5.25) is the *wave potential*, *i.e.* the term that models the floating behavior of the robot's hull. In fact, in order to simulate that the robot's hull is not only floating on the surface but also aligned with the wave profile, the wave-hull system has been modeled as a spring-damper system, thus generating forces and torques that make the hull's CoG following the wave profile (along z-axis) passively. Moreover, it is expected that the vehicle pitch follows the wave slope. Then, the τ_w torques acting on the p_d and q_1 joints, describing the hull's floating behavior, are modelled as a classic PD control problem:

$$\tau_w = \begin{pmatrix} K_{p_z} & \\ & K_{p_q} \end{pmatrix} \begin{pmatrix} e_z \\ e_{q_1} \end{pmatrix} + \begin{pmatrix} K_{p_d z} & \\ & K_{p_d q} \end{pmatrix} \begin{pmatrix} \dot{e_z} \\ \dot{e_{q_1}} \end{pmatrix} \tag{5.29}$$

where the errors to minimize are:

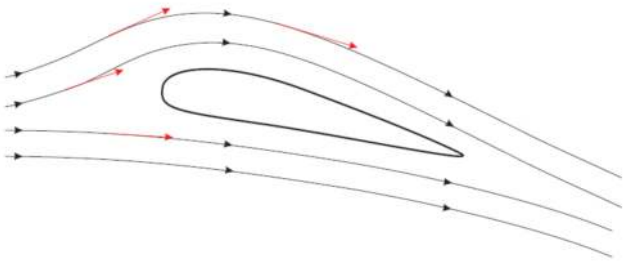

Figure 5.3: *Wing - fluid interaction.*

- The error e_z is the difference between the wave profile and the CoG of the hull:

$$e_z = A\sin(kx - \omega t) - (p_d - p_{m_1}\sin(q_1)). \tag{5.30}$$

- The error e_{q_1} is the difference between the slope of the wave and the pitch angle q_1:

$$e_{q_1} = \arctan\left(\frac{\partial A\sin(kx - \omega t)x}{\partial x}\right) - q_1. \tag{5.31}$$

5.1.9 Forces acting on the wings

A wing immersed in a fluid is subject to a lift force generated by the pressure difference between its lower and upper surfaces. This difference generates a resultant force whose parallel component - opposite to the velocity - is the drag D while the orthogonal component is the lift L:

$$F = L + D = \oint_{\partial\Omega} p\mathbf{n}d\partial\Omega, \tag{5.32}$$

where p is the pressure, $\mathbf{n}$ the versor orthogonal to the surface and $\partial\Omega$ is the integration surface. The shape of the wing modifies the field of motion around the surface, causing a change in the local tangential velocities on the wing profile: the velocities are greater along the extrados than along the intrados (Figure 5.3).

Under the hypothesis of an incompressible steady fluid flow, without viscosity, Bernoulli's Theorem demonstrate that the fluid particles with higher pressure corresponds to lower velocities and vice versa [1]. The Bernoulli equation is a useful tool for estimating the pressure of the fluid on the wing and therefore the forces on the wing at low speeds and small wing-arm angles.

$$p = p_0 + \frac{\rho}{2}V^2. \tag{5.33}$$

The theory of circulation is a more precise instrument that presupposes the knowledge of Helmholtz's theorems of conservation of vorticity and Kutta-Zukovskij's theorem [1]. Circulation is the linear integral of the fluid velocity on a closed path C enclosing a body:

$$\Gamma = \oint_C V\, dl. \tag{5.34}$$

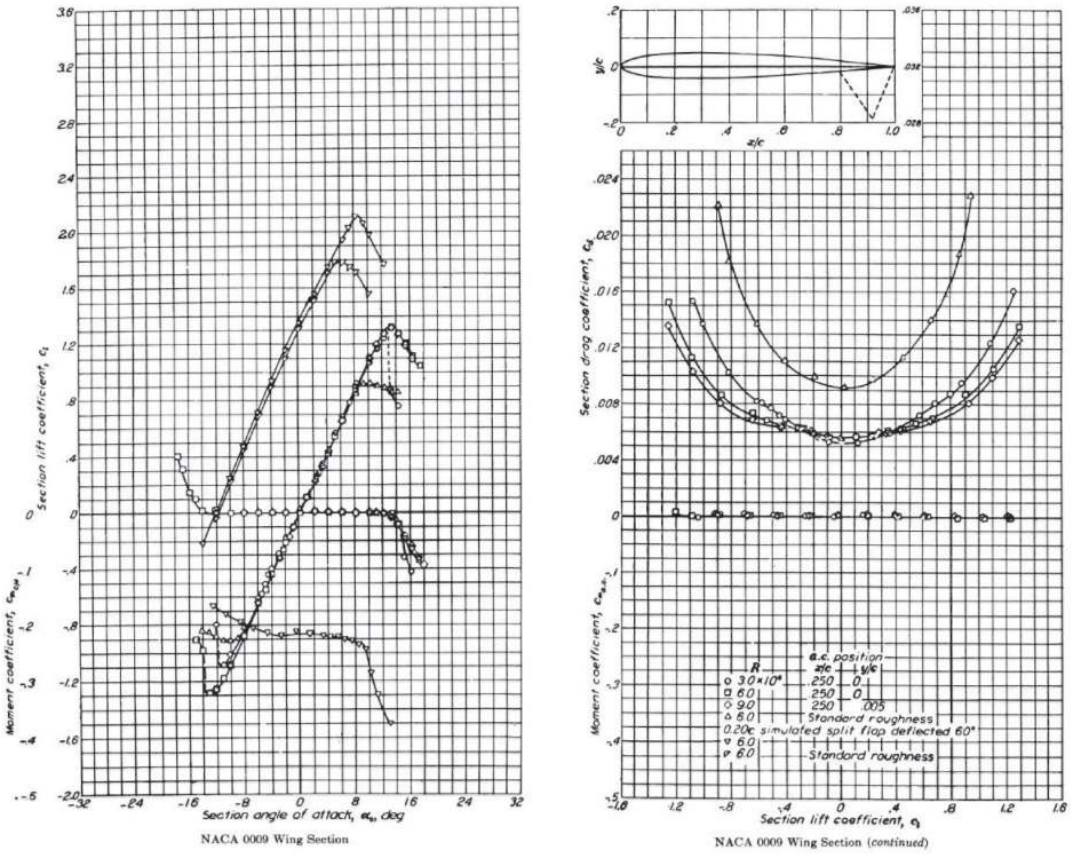

Figure 5.4: *Lift and Drag coefficients for a NACA 0009 wing profile.*

Applying the circulation theory to the case of a wing profile under the effect of a fluid current, the lift is calculated as:

$$L = -\rho V \Gamma. \tag{5.35}$$

To study the lift force on the wings of the WAVE vehicle, it has been hypothesized an incompressible steady flow and - given the slow velocity of the phenomenon - it has been considered negligible the vortex effect. Under these hypotheses, it has been considered that the generation of lift and drag forces depend on the surface of the wing, on the density and speed of the fluid, and on the coefficients of lift c_l and drag c_d specific for the considered wing profile [1]:

$$L = \frac{1}{2}\rho S V^2 c_l \tag{5.36}$$

$$D = \frac{1}{2}\rho S V^2 c_d \tag{5.37}$$

The lift coefficient for the chosen profile National Advisory Committee for Aeronautics (NACA) 0009 has a linear trend for small angles, while increasing angles corresponds to strongly non-linear behaviour (Figure 5.4). Therefore, in the model it was decided that the lift coefficient should maintain its non-linear trend, and it was estimated using a Fuzzy estimator [213] applied to the curve of the lift coefficient for low Reynolds number; a Gaussian approximation was made obtaining the estimate in Figure 5.5

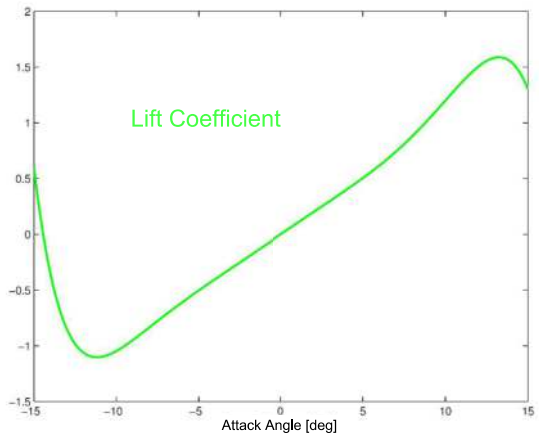

Figure 5.5: *Fuzzy estimate of the lift coefficient.*

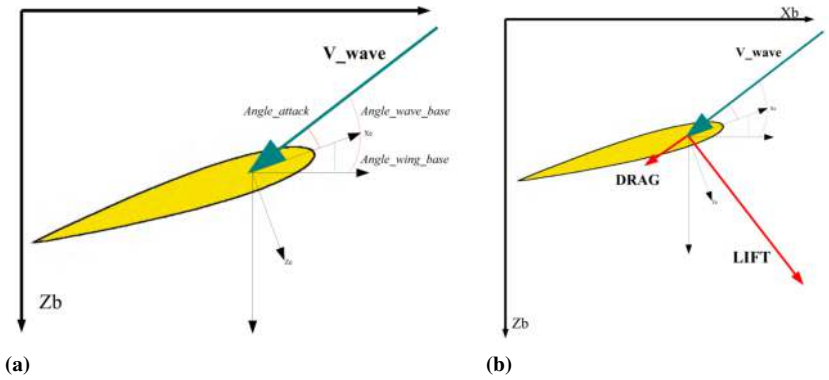

Figure 5.6: *Wing modelling and forces. (a) Attack angle and (b) lift-drag forces modelling.*

The drag coefficient is composed by two terms: one, always present, is the shape coefficient that for the wing NACA 0009 is $c_{d_0} = 0.009$; the second is a drag coefficient induced by the lift and proportional to the square of the lift coefficient $c_{d_i} = 1.427410^{-4} c_l^2$.

The attack angle is calculated as the difference between the angle formed by the velocity of the water particles and the angle of orientation of the wing with respect to the base frame (Figure 5.6a).

The drag is generated in the opposite direction of the fluid velocity, while the lift is generated perpendicular to it (Figure 5.6b). Therefore, a hybrid model has been implemented, *i.e.* the wing generates lift only for attack angles between -15 and 15 degrees, while outside this range only drag force is generated proportionally to the form coefficient c_{d_0} and always parallel to the velocity of the fluid. In fact, outside the interval $[-15, 15]$, the wing surface exposed to the water flow increases, thus offering greater drag. In these conditions, the wing can be approximated to a thin and flat surface whose drag coefficient c_d depends on the Aspect Ratio (AR), *i.e.* the ratio between the

wingspan and the length of the profile chord. In particular [172]:

$$\text{AR} \approx 1 \rightarrow c_d = 1.1$$
$$\text{AR} \gg 1 \rightarrow c_d \approx 2$$

The calculated hydrodynamic forces are expressed in the reference system of the fluid velocity and applied in the aerodynamic center of the wing, recalling that the direction of the fluid velocity vector, due to the velocity potential, varies as expressed in (5.28).

The resulting force applied to the wing must be considered in the basic reference system:

$$f^b_{\text{wing}} = R_y(\alpha_{\text{attack}}[F_{\text{drag}}, 0, F_{\text{lift}}]^{\text{T}}) \tag{5.38}$$

Finally, the joint torques generated by the hydrodynamic force acting on the wing are calculated using the kinetostatic duality (5.7):

$$\tau_{\text{wing}} = J^{\text{T}} f_{\text{wing}}. \tag{5.39}$$

5.2 The WAVE vehicle simulator

In this section, the WAVE vehicle simulator will be outlined. The software implements in MATLAB© the modelling framework previously presented and it is a continuous development project since 2012. A conceptual scheme of the whole simulator is given in Figure 5.7.

All the main body parts of the WAVE vehicle (hull, arms and wings) are implemented as MATLAB classes, that manage the prolate ellipsoid and right prism geometrical and dynamical parameters in a coherent way. In particular, the wings parameter are easily customizable to see their effect on the achievable performance (Section 4.1.1). A complex class *PROTOTYPEWAVE* describe the implementation of the dynamic model of the WAVE prototype, taking as input the properties of the hull, links and wings and returning the model for the WAVE vehicle as a bi-dimensional serial manipulator in the surge-heave-pitch plane [38, 67]. The class maintains the evolutions of the joint positions, CoG and Center of Buoyancy (CoB) of the bodies, for post-processing evaluation.

It is important to recall that a FEA (Finite Elements Analysis) is adopted, with a linear mesh to model the effects on the hull and the wings (the arms are assumed to have neglectable effect). The subdivision of the whole bodies into smaller parts favours a more accurate representation of complex geometry and the capture of local effects. The hull and the wings can be subdivided in a selectable number of discrete parts to evaluate their interaction with the wave motion. In the WAVE vehicle simulation, this technique helps in visualize forces and moments distribution along the bodies.

About the wave modelling (Section 5.1.7), the simulator allows to change amplitude A, frequency f and sea depth H, and estimates also the particle velocity of the waves.

Before running the simulation, the initial condition of $q = [p_n, p_d, q_1, q_2, q_3]^{\text{T}}$ vector and its first derivative must be defined. At each simulation time step (typically 0.01 s) $q, \dot{q}, \ddot{q}$ are computed and stored.

Finally, the ODE (Ordinary Differential Equations) Solver [187] must be chosen between the following:

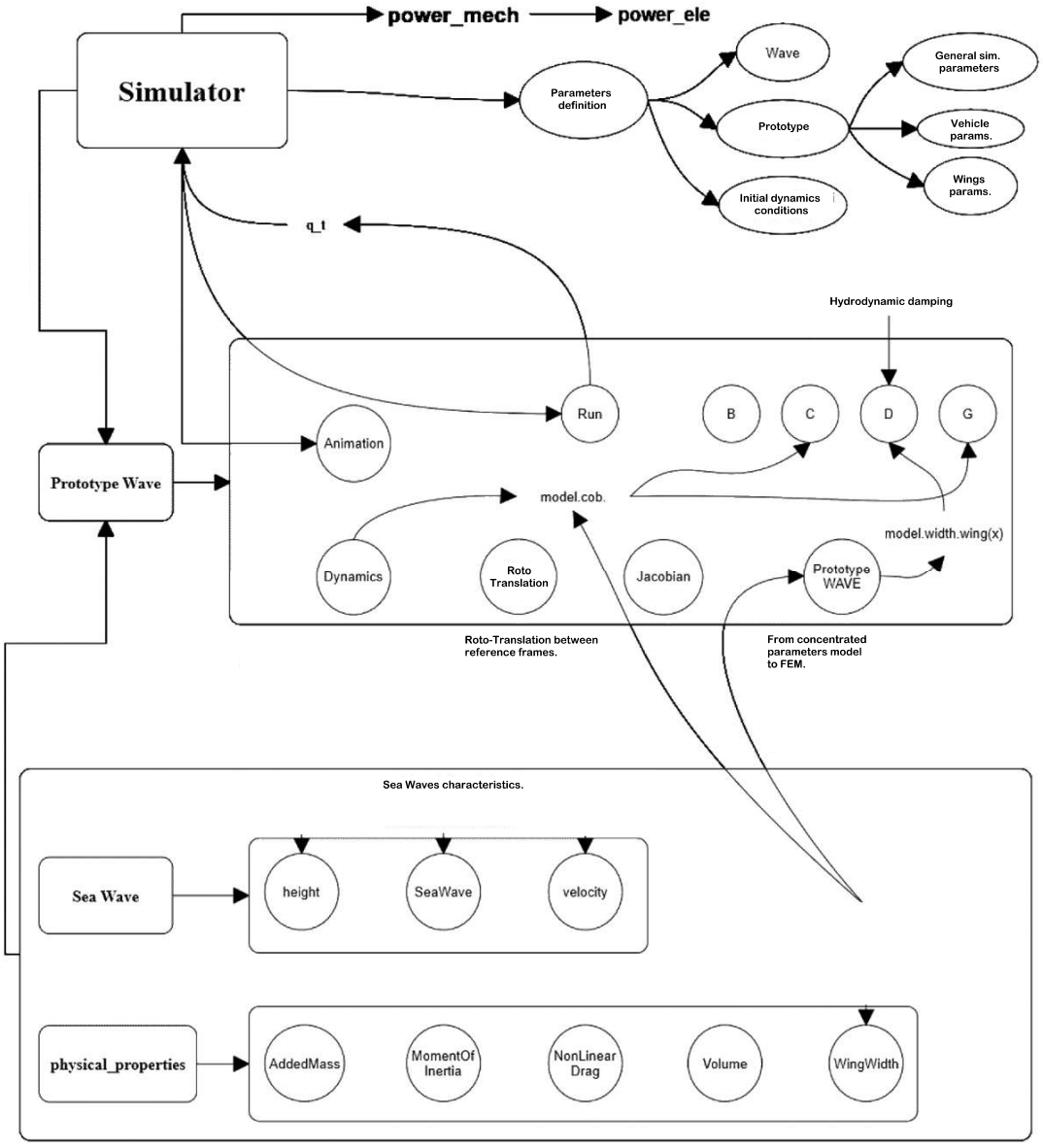

Figure 5.7: *The overall conceptual diagram of the WAVE simulator. The four main classes are represented in the rectangles on the left of the figure. The* Simulator *class generates the model (*Prototype WAVE *class) on the basis of the defined parameters of scenario and vehicle configuration. The Prototype WAVE class is also feed by two other classes:* Sea Wave *and* physical-properties*, with their own peculiar members. The* run *member function of the Prototype WAVE class calls all the other functions to estimate the state vector of the vehicle according to its dynamics.*

Table 5.2: *Simulated values of mechanical and recoverable energy for typical wave parameters of the Mediterranean sea.*

Sea state	Amplitude (m)	Frequency (Hz)	Mechanical Energy (Wh)	Recoverable Energy (Wh)
Calm 1 (Beaufort 1)	0.3354	0.1	3.00	2.77
Calm 2 (Beaufort 1)	0.3354	0.062	1.10	0.90
Smooth 1 (Beaufort 2)	0.8216	0.1	19.34	18.02
Smooth 2 (Beaufort 2)	0.8216	0.062	5.13	4.66

- a fifth-order Runge-Kutta method called ode5, a fixed time step solver useful for simulations without control, *i.e.* full passive WAVE vehicle behaviour for wave recharging;
- classical nonstiff ODE solver ode45, one of the most versatile ODE solver in the MATLAB suite. It is powerful to manage *events* during the simulation, *i.e.* implement the brake mechanism for wave harvesting propulsion.

For the data analysis, the simulator provides wave velocity, vehicle velocity and vehicle positions animated plots and video. In addition, all the forces acting on the wings are analysable. Finally, the mechanical and electrical power are calculated.

5.2.1 Wave energy harvesting preliminary simulative results

Preliminary simulations were run before the actual prototyping of the WAVE module.

A plane wave model, with only constant amplitude and frequency as parameters, was employed to describe the sea-waves motion and to study the interaction forces with the hull and the wings (Section 5.1.7). The simulations were performed by considering the typical values of the Mediterranean Sea for the wave parameters [45], corresponding to sea-states 1 and 2 of the Beaufort scale. These sea states have been chosen as they cover over 50 % of the annual observations of sea conditions in the Western Mediterranean, that was the initial application scenario for the WAVE project, even if better performance are expected with higher sea states. Furthermore, the sizing of the mechanical robustness of the system was not analysed in the design phase while it is necessary to ensure WAVE operations with sea state greater than 2.

The free parameters on which sensitivity studies have been carried out, within the mechanical limits imposed by the envisioned configuration of the module, are:

- length of the hull-wing link (*i.e.* arm);
- surface of the wings.

In the different sea conditions, the mechanical and the corresponding (theoretically) recoverable energy were simulated with respect to different values of the above parameters (see Table 5.2).

The simulations were aimed, above all, at the characterization of the system with respect to the expected environmental conditions in which the WAVE vehicle will probably operate. Table 5.3 shows the expected wave types that can be met assuming a

Table 5.3: *Seasonal percentage of time in which the different sea conditions occur along the Leghorn-Barcelona route. The Smooth 1 sea situation exhibits a fairly stable statistical behaviour as the seasons change, around 30% of the time.*

Season	Calm 1 (%)	Calm 2 (%)	Smooth 1 (%)	Smooth 2 (%)	Others (%)
Winter	13.72	1.79	28.72	10.01	45.76
Spring	24.19	3.85	31.46	13.78	26.72
Summer	39.45	4.33	29.95	9.61	16.66
Autumn	20.20	2.83	30.32	11.00	35.65

Table 5.4: *Average available power per season and average full recharge time per season. The average available power is calculated on the basis of the power that can actually be used by the vehicle battery as the sum of the contributions of the two arms of the WAVE module.*

Season	Average power available (W)	Average charging time (hours)
Winter	12.20	41
Spring	13.54	37
Summer	12.68	39.5
Autumn	12.90	38.5

route from Leghorn (Italy) to Barcelona (Spain) equal to a distance of about 700 km, *i.e.* 378 nm [45]. It should be noted that the data on wave frequencies are very sensitive to wind conditions and then they are less accurate especially for medium-low waves' amplitude (between 0.25 m and 0.50 m) and short wave period as in the case of Calm 1 sea state.

The simulations for energy recovery were carried out precluding the operation of the system in sea state higher than Smooth 2. Operationally, it was considered the situation in which the WAVE vehicle is moving in wave-gliding mode and it is desired to recover 500 Wh. The average power available for recharging the vehicle battery and the average charging time with respect to the seasons are shown in Table 5.4.

On average, a complete recharge occurs in 39 h. Clearly, with the same method, recharge time estimates can be made for other geographical areas or based on monthly statistics.

5.3 The tuning of the simulator based on the experimental results

Recalling the extensive experimental campaign described in the previous chapter, and in particular the aggregated data analysis (Section 4.2.1), simulations were carried out on the model developed for the WAVE vehicle choosing all the mechanical, geometrical and wave parameters corresponding to the experimental tests presented in Figure 4.12.

Knowing the measured electrical power, the parameters of the simulator have been critically tuned with respect to drag and hydrodynamic damping coefficients of the hull, arms and wings, in order to obtain the best approximation of all experimental data with the same parameters configuration.

Specifically, the tests with the wing profile no.2 were considered because it was the best wing profile in terms of recovered power according to the experimental data. The simulative results with the identified set of optimal parameters are shown in Figure 5.8

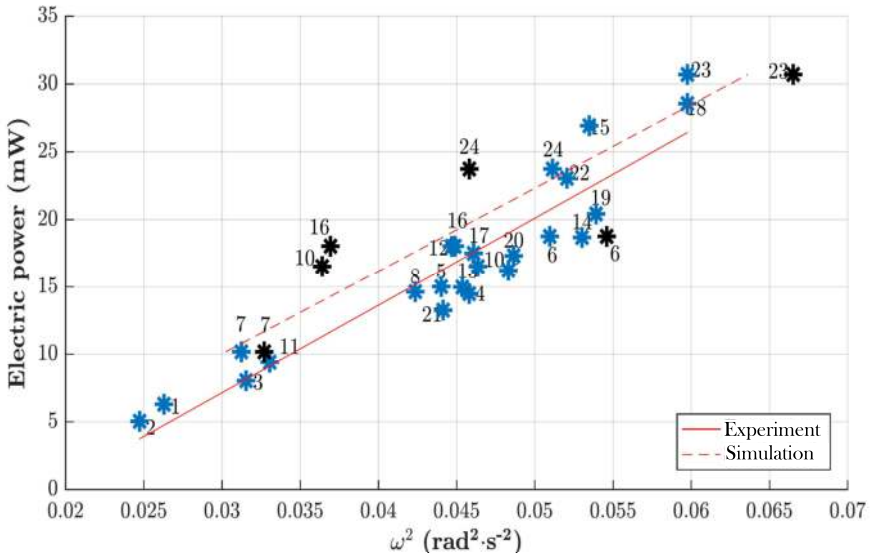

Figure 5.8: *Generated electric power as a function of the square of the angular speed of the WAVE module arm. The blue asterisks are the experimental data while the black ones are the simulation results with the same mechanical conditions and using the same wave profile. The red lines represent the data trend: solid for the experimental results, dashed for the simulative regression.*

vis-a-vis experimental results. It is worth to note that the agreement between the experimental and the simulated data has to be considered very good, both in terms of one-to-one correspondence and in terms of linear trend. The identification of the parameters was made with a linear function that considers a combination of the ordinary least squares method and a slope estimator. In other words, it was decided to assume a higher residual absolute error with respect to a completely wrong slope estimation. In fact, the final goal of the simulator is to predict the performance of the WAVE vehicle in non-tested cases, thus it is important to preserve the experimental data trend within a reasonable percentage error of about $10\,\%$. On the contrary, looking for a lower residual error, not considering the general trend, may lead to unrealistic fitting beyond the experimental data set, *i.e.* not quasi-parallel linear regressions.

It is necessary to observe that the linear trends identified (both in experimental and simulative case) show the presence of a dead band of the system, *i.e.* the fact that below a certain average quadratic angular velocity the generated power is zero. From the regression carried out on the experimental data, this threshold is equal to $\omega_t = 0.019\,\text{rad}^2\,\text{s}^{-2}$. This fact further supports the WAVE project analysis that found sea state 2 as a lower limit to obtain wave energy harvesting with the WAVE prototype.

5.4 Simulative predictions of the recharging capability

This section describes the evaluation carried out with the calibrated simulator of the energy recovery performance obtainable by new conceived wings profiles and considering an actuation system to properly brake the WAVE arms in order to increase the recoverable power. It is worth to note that the parameters of the simulated sea wave are

kept constant at 0.45 m of amplitude and 0.33 Hz of frequency for all the tests as done during tank tests (Section 4.1.2).

For the sake of clarity the (5.25) is reported here:

$$B(q)\ddot{q} + C(\dot{q})\dot{q} + D(\dot{q})\dot{q} + G(q, f_w) = \tau_w + J^b(q, p_e^b)^{\mathrm{T}} f_e^b + \tau_c.$$

In fact, in this equation the hydrodynamic damping term damping $D(\dot{q})\dot{q}$ is particularly important as it includes the contributions related to the effects of the forces on the wing. These forces will be fundamental to analyse and develop new geometrical profiles. The resolution of the previous equation allows to obtain the values of the variable $q, \dot{q}$. In particular, the knowledge of the velocity at the joint q_2 makes it possible to calculate the average mechanical power generated by the rotation of the link with respect to the robot's hull:

$$P_m = 2\mu \dot{q_2}^2 \tag{5.40}$$

where μ is the friction of the link. This parameter was identified after the experimental campaign, and it is equal to 19.468 Kg m/s. The double product was used to include the rotary effect of both the WAVE arms. Of course, the electrical power recovered by the WAVE module is directly proportional to P_m.

5.4.1 Wing profiles comparison

The analysis of the best performing wing profiles for energy harvesting started from the study of the three geometries used in the experimental tests in order to define a performance benchmark for new wings profiles. In the following we will refer to the nomenclature, widely reported in Section 4.1.1, regarding wing configurations. Notice that the material chosen for the simulations is the aluminium that has a density (at room temperature) of 2700 kg/m^3.

The original choice of using a trapezoidal profile with increasing surface along depth was linked to the study of wave motion whose speed (and therefore force) decreases along this direction. An increase of the wing bottom area would ensure uniform wrenches throughout the profile.

The simulation results obtained by varying the wing shape, mounting direction, angle and position, have shown the general superiority of the profile number 2 as seen in experimental tests. The best performance has been obtained in the *knee* configuration and with $q_5 = +30°$, resulting in an average mechanical power equal to 2.37 W, *i.e.* about 39.5 mW of electrical power recovered. Benchmark simulations have allowed to observe that increasing the wing surface does not guarantee an improvement in recharging performance. In fact, the profile number 3 has an area equal to 0.2304 m^2 against the 0.2141 m^2 of the profile 2; nevertheless it has a lower energy performance of about 20 % in all configurations.

5.4.1.1 Parabolic profile

The first straightforward change to wing geometry was the implementation of a parabolic profile as shown in Figure 5.9 in three alternative forms that retained the width and length of original trapezoidal profiles. Since the wave velocity module is higher close to the surface, the goal was to face a larger wing area to the wave motion. For this reason, it was decided to increase the area at the top of the profile. From the

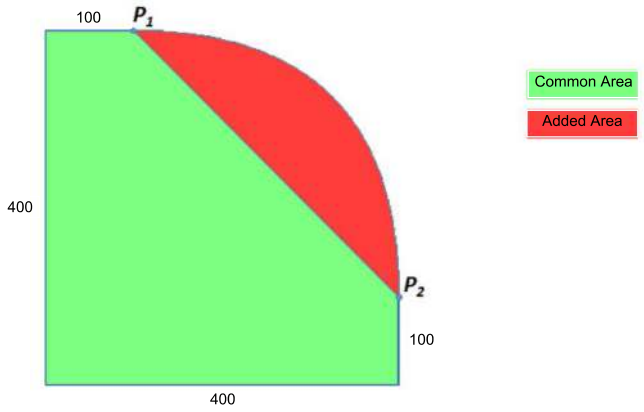

Figure 5.9: *The parabolic profile developed. Notice that the dimensions, in millimetres, are the same as trapezoidal profile number 1. In the same manner, the alternative forms follow the dimensions indicated in Table 4.1.1. In green is reported the area common between the two wing profiles, while in red the added area. The parabola axis of symmetry is parallel to the longest wing side.*

simulative results the parabolic profile demonstrate superiority with respect to the trapezoidal one in all the wings configurations. In addition, the simulations with parabolic geometry confirmed that the best result, equal to $2.44\,\mathrm{W}$ of average mechanical power (*i.e.* $40.7\,\mathrm{mW}$ of electrical power), was obtained with the wing configuration: $($middle mounting position, $+30°$- *knee* mounting angle , right side up mounting direction$)$. Finally, the simulation results with the parabolic profile confirmed that the surface of the wing is not the only factor increasing the mechanical power. Once again, profile number 3 was energetically worse than profile 2 of about $20\,\%$ despite having a larger area ($0.2603\,\mathrm{m}^2$ vs. $0.2494\,\mathrm{m}^2$).

5.4.1.2 Wing forces analysis

The design of alternative geometries was based on an in-depth analysis of the wrenches acting on the wings, given the confirmation of the fact that increasing the wing area is not sufficient to ensure an analogue increase in the recovered energy. In order to make the analysis general (*i.e.* not related to specific geometries or configurations of the wing), the study was carried out on a rectangular geometry with $q_5 = 0$. The plots in Figure 5.10 show the wrenches and the relative velocities with respect to the water acting on each element of the wing FEM model. First, it is clear that the trend of the wrenches follows that of relative velocities. Furthermore, it was noted that the central elements have smaller wrench contributions on average. Based on these considerations, two more geometries have been designed: *hourglass* and *rhombus*, described in detail afterwards and shown in Figure 5.11. In summary, the first profile was designed to amplify the effect of increasing the extreme areas of the wings; the second profile tests the opposite case in which the central area is maximized to compensate for the smaller wrenches.

5.4.1.3 Rhombus profile

As mentioned, this geometry has been studied with the intention of considerably increase the central area of the wing in order to face the minor wrenches. The aim is

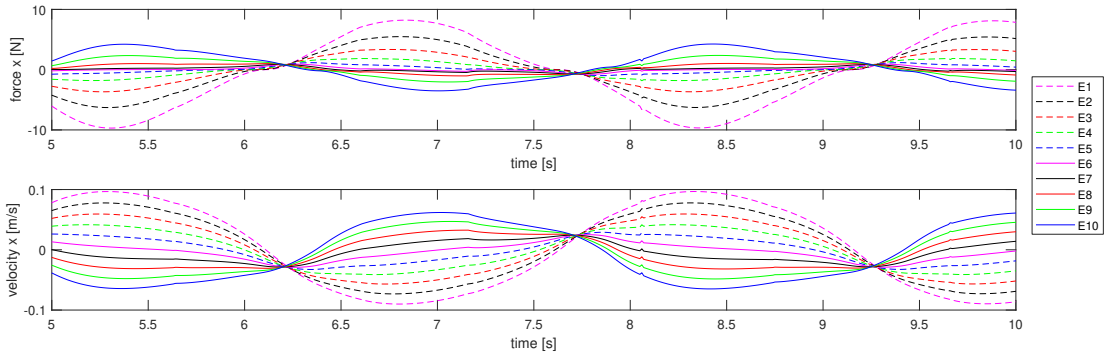

(a)

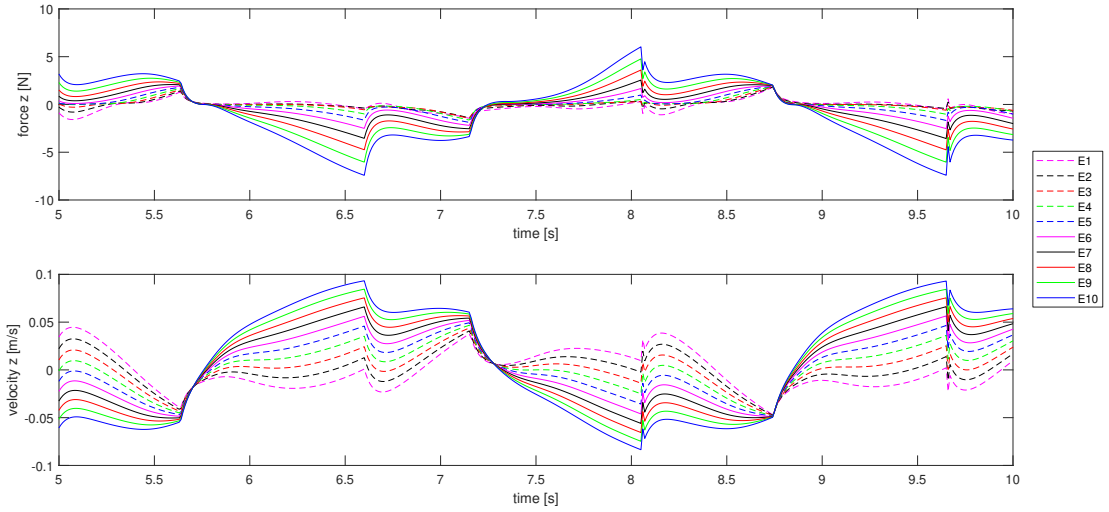

(b)

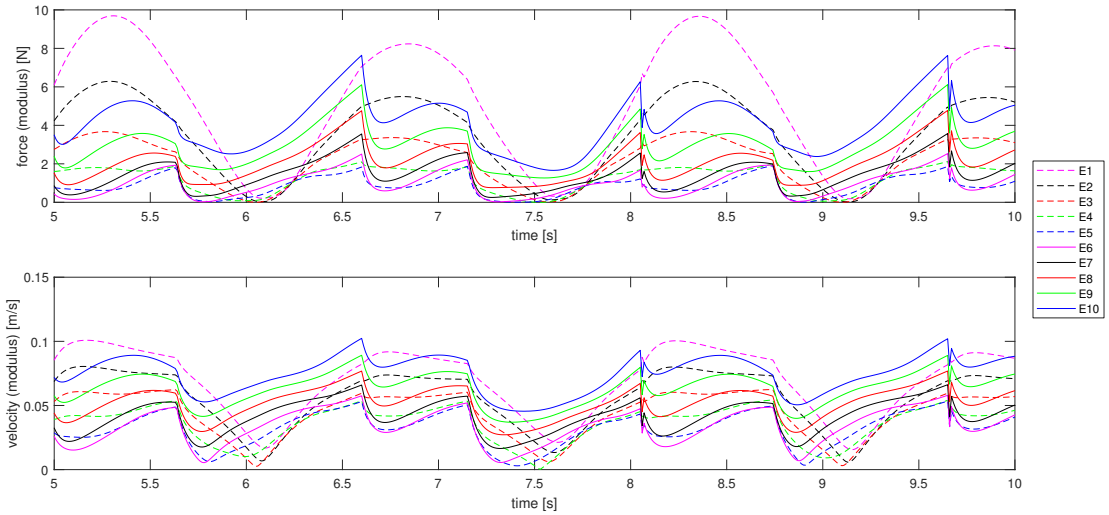

(c)

Figure 5.10: *Forces and relative velocities (in Earth-Fixed reference frame) acting on a rectangular wing profile along (a) x-axis and (b) z-axis. The magnitudes of the two vectors are reported in (c). The wing is mounted in the middle position and with $q_5 = 0$. Equispaced elements are numbered from the upper part of the wing to the lower side.*

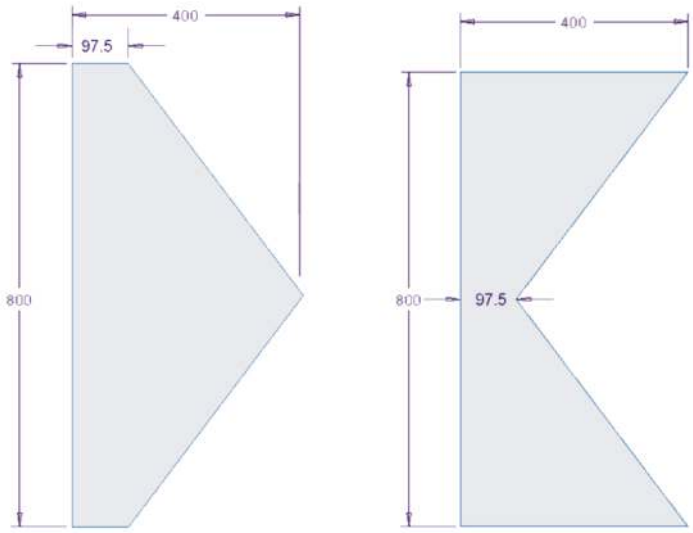

Figure 5.11: *The new conceived wing profiles: rhombus (left) and hourglass (right). The dimensions are in millimetres. Width and length are the same of the original trapezoidal profiles for correct comparison.*

Table 5.5: *Simulated values of mechanical power for the rhombus wing profile in various wing mounting configurations.*

Attack angle (°)	Mounting position	Mechanical Power (W)
-30	Low	0.9464
	High	1.8073
	Middle	1.7153
0	Low	1.5946
	High	1.9499
	Middle	2.0879
$+30$	Low	1.9653
	High	1.9878
	Middle	2.2657

to obtain uniform forces along the wing profile at various depth. The simulation results are shown in Table 5.5: the average mechanical power is less than in the previous cases. Indeed, it should be noted that exists, even for this geometry, a monotonically increasing trend in mechanical power when the angle of attack increments from $-30\,°$ to $+30\,°$.

5.4.1.4 Hourglass profile

The third proposed geometry, the *hourglass* profile, aims to maximize the area where the forces are expected to be most intense. This solution gave the best results among the various geometries (Table 5.6). Even with the hourglass profile, the highest mechanical power values are obtained with $q_5 = +30$ degrees. For completeness, it must be said that the parabola 2 geometry resulted in higher mechanical power, but with a significantly bigger area ($0.25\,\mathrm{m}^2$ vs. $0.2\,\mathrm{m}^2$). Finally, it can be stated that all the simulated

Table 5.6: *Simulated values of mechanical power for the hourglass wing profile in various wing mounting configurations.*

Attack angle (°)	Mounting position	Mechanical Power (W)
-30	Low	0.9224
	High	1.9696
	Middle	1.7598
0	Low	1.8062
	High	2.1929
	Middle	2.2343
$+30$	Low	2.1941
	High	2.2261
	Middle	2.4186

Table 5.7: *Comparison between best performance of mechanical power for each wing profile. The mounting position is* middle *and the attack angle is fixed to* $+30°$.

Wing Profile	Mechanical Power (W)	Area (m^2)
Rectangular	2.4644	0.32
Trapezoidal 2	2.3242	0.2304
Parabola 2	2.4369	0.2498
Rhombus	2.2657	0.199
Hourglass	2.4186	0.199

tests show that mechanical power and wing area are not linearly correlated. This aspect will be further investigated in the next sections.

5.4.2 Systematic study on factors influencing energy recovery

After a first phase in which the width and length of the profiles were left unaltered (*i.e.* the area was variable), simulation tests were carried out with different shapes and constant area. From an analysis of the results of the previous geometries, it seems difficult to extrapolate a function that correlates mechanical power and area of the wing. For example, as can be seen in Table 5.7 summarizing the best cases, the hourglass and rhombus profiles lead to substantially different results with the same area, although the hourglass proves to develop a mechanical power comparable and/or superior to the other geometries despite a smaller surface. For this reason, an in-depth analysis of the other factors - beyond the area - influencing energy recovery was performed.

In fact, new wing profiles correspond to new geometric parameters but also the mass and inertia of the bodies change. Therefore, simulations have been conducted with the four considered profiles, proportionally varying their dimensions to characterize the mechanical power obtainable keeping the area constant. The results of the simulations are summarized in Table 5.8 and shown in Figure 5.12.

A linear fitting is not applicable to relate mechanical power and wing area. On the contrary, as the area increases, there is an initial relevant increase in mechanical power on average, followed by a strongly decreasing phase for all the geometries. The latter trend can be explained by the mass increase due to larger surface. In fact, despite the wrenches on the wing elements are generally augmenting in magnitude, this increase

Table 5.8: *Mechanical power achievable for each wing profile with respect to the wing area. The mounting position is* middle *in all cases.*

Wing Area (m^2)	Mechanical Power (W)						
	Rectangular	Trapezoidal 2 - foot	Trapezoidal 2 - knee	Parabola 2 - foot	Parabola 2 - knee	Rhombus	Hourglass
0.199	2.1979	2.2684	2.3001	2.2397	2.2699	2.2657	2.4186
0.25	2.4000	2.4632	2.4590	2.4385	2.4450	2.4488	2.4941
0.32	2.4644	2.4843	2.4144	2.4782	2.4391	2.4644	2.3577
0.4	2.3130	2.2977	2.2106	2.3061	2.2513	2.3852	2.1122
0.5	1.9976	1.9976	1.9185	1.9496	1.9668	1.9627	1.7993

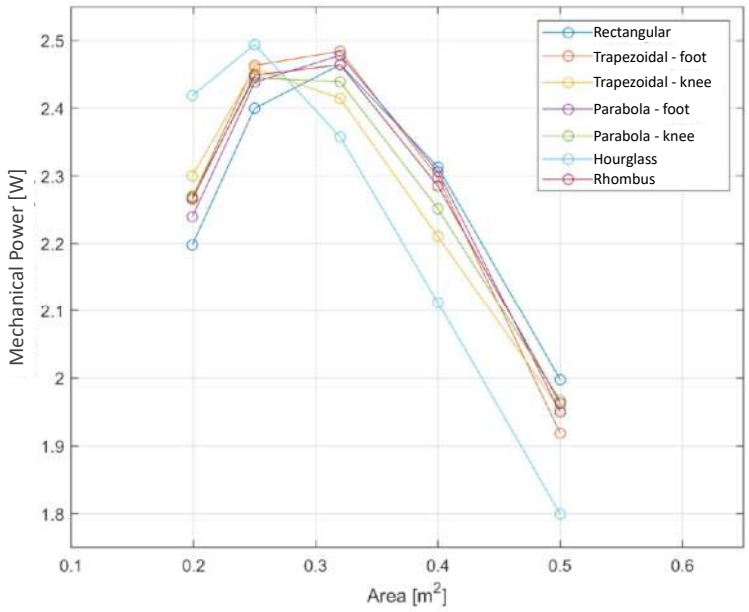

Figure 5.12: *Comparison of the mechanical power achievable with the different wing profiles. The simulated areas are:* $[0.199.0.25, 0.32, 0.4, 0.5]\, m^2$.

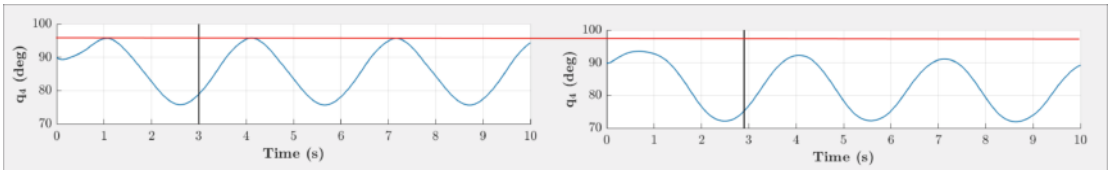

Figure 5.13: *Comparison of the variable q_2 (hull-arm joint) for the same wing geometry* hourglass *with different area:* $0.1990\,m^2$ *(left) vs.* $0.5\,m^2$ *(right). The angular difference is about* $5\,°$.

is not enough to compensate for the higher mass and inertia of the wing, resulting in a smaller rotation of the hull-arm link q_2 (Figure 5.13).

5.5 Simulative predictions of the wave gliding capability

Until now, the *long-endurance* solution outlined is a hybrid vehicle, with both gliding and classic propulsion capacities, equipped with a particular module can be configured in a specific state to recover energy from the wave motion while the vehicle stays on the surface. Indeed, the endurance of the vehicle may also be increased by tackling the problem in another way, *i.e.* by making the WAVE vehicle able to navigate exploiting the wave motion.

In order to ensure wave gliding fashion navigation, the wing must generate a resultant force that makes a contribution to the robot's passive propulsion, *i.e.* the lift would be much greater than the drag effect. In the first design phases of the WAVE project, it was chosen to constrain the joints q_2 and q_3 with springs, *i.e.* with a proportional control. The best preliminary simulative results were obtained by binding the q_2 (hull-arm) and q_3 (arm-wing) joints such that they are approximately parallel.

The simulations have been performed assuming that the WAVE vehicle is hit on the bow by wavefronts perpendicular to its longitudinal direction. Note that this condition was observed during experimental tests both in the tank and at sea when the vehicle was leave free to drift on the surface (*i.e.* no control system activated) in the presence of waves.

In the experimental campaign reported in Chapter 4, it was observed that the vehicle always draw back between 2 and 10 meters (depending on the specific configuration) with respect to its initial position after about 5 minutes of wave generated motion. In particular, in this section, the simulative results obtained with the critically calibrated simulator are reported to highlight the recoil of the vehicle under certain test conditions. Those results are summerized in Table 5.9, and they are highly coherent with experimental observations.

In a second phase of the experimentation, shorter than that dedicated to the recharge capability assessment, the possibility of obtaining passive longitudinal propulsion was evaluated by braking the hull-arm joint q_2 . The WAVE module was installed according to the configurations shown in Table 5.10. Notice that tests 36 and 37 were carried out with the stern of the vehicle directed towards the wave. During the tests, an operator tried to verify the possibility of moving the vehicle against the wave motion using the electric brake of the WAVE module, which is able to block the arms oscillation. The brake controls were given using the vehicle's Wi-Fi interface on the basis of the motion observation. At first, the brake was activated only when the vehicle reached the wave

Table 5.9: *Simulation results related to the draw back of the WAVE vehicle during wave energy harvesting tests,* i.e. *with the arms free to move under the action of the wave motion. Although there was not a tracking system of the vehicle position during the tests, the simulation results are consistent with the experimental evidence. Notice that backward movement is relative to the wave direction,* i.e. *the vehicle was dragged back by the wave motion.*

Test no.	Average quadratic angular velocity $\dot{q}_2$ (rad^2 s^{-2})	Average backward velocity (m/min)
6	0.055	1.03
7	0.033	2.05
10	0.036	1.29
16	0.037	0.44
23	0.067	1.72
24	0.046	1.68

crest and released in the other phases: this method did not produce appreciable results for any of the tested configurations (test no. 34-36). Consequently, the brake action was tested alternatively in the wave ascent phase (test 37) or in the descent phase (test 38-40): a sporadic contrasting action at the backward movement caused by the wave was experimentally observed.

An interesting phenomenon that has emerged during the use of the latter actuation strategy is that the effectiveness of the brake seems to depend on the wave period compared to the vehicle's length. In fact, the advancement of the vehicle by applying the brake to each wave crest was appreciably less than in the case in which the brake was actuated every two periods. Furthermore, decreasing the vehicle length (test 39-40) produced a qualitatively lower recoil compared to the long vehicle case (test 38); this effect may be due to the fact that the vehicle, in order to follow the wave profile and generate a propulsion action, shall have a shorter length than the wave itself. It should also be noted that the actual braking action on the arm movement during the tests was non-blocking, *i.e.* the arm exhibited a residual rotation movement under the action of the wave motion. Finally, it has been observed that the *knee* wings configuration was potentially capable of producing a propulsion motion, and that configuration was not

Table 5.10: *Experimental test configurations for the wave gliding capability assessment. The configuration in which the wing joints are free to move between two positions is indicated as* $[a, b]$*, where* a *and* b *are the selected end strokes of the movement.*

Test	WAVE configuration parameters					
	Wing profile	Wing mounting position	Wing mounting direction	Wing mounting angle (°)	Additional weight per wing (g)	Additional module position
34	2	Middle	UD	$+30$	0	Stern
35	2	Middle	UD	-30	0	Stern
36	2	Middle	UD	-30	0	Stern
37	2	Middle	UD	-30	0	Stern
38	2	High	RSU	$[-30, 0]$	0	Stern
39	2	High	RSU	-30	0	None
40	2	High	RSU	$[-30, 0]$	$+500$	None

optimal for wave energy harvesting (Section 5.4).

5.5.1 Simulative results

The preliminary tank tests were intended to give experimental evidence of the feasibility of advancing by exploiting the wave motion appropriately, offering insights to study with the calibrated simulator.

In order to better evaluate the vehicle wave gliding capability, simulations have been carried out considering the following conditions:

- Variation of the vehicle's center of mass, from 0.05 m behind the nominal CoG (COG1) to 0.05 m ahead (COG3). The nominal CoG is called COG2. The conditions COG1 and COG3 correspond to positive or negative vehicle pitch, respectively.
- Variation of the wing locking mechanism, considering the following strategies:

  B0 no block for benchmarking (*i.e.* arms are free to move);

  B1 block when the wave speed acting on the wing has a positive component along the vehicle's longitudinal axis;

  B2 block at the simultaneous occurrence of the following three events:
  - wave speed acting on the wing with a positive component along the longitudinal axis of the vehicle;
  - angle of the arm with respect to the vehicle greater than $90°$;
  - zero angular velocity of the arm.

  B3 block when the wave speed acting on the wing has a positive component along both the vehicle's longitudinal and down axis;

  B4 same as B2 eliminating the last condition.

The basic idea of these blocking strategies is that the arm and the wing must be locked when the speed of the wave motion can contribute to the forward thrust of the vehicle, presenting the largest possible surface to the positive force of the wave motion; when the wave motion would contribute to the backward thrust of the vehicle, the arms and the wings would be free to move, thus accompanying the motion of the wave without opposing it. It should be noted that the speed considered by the brake condition is a weighted average speed between those acting on the various modelling elements of the wing.

This situation is represented in Figure 5.14, where two snapshots of the simulation are shown to highlight the WAVE module behaviour with different wave velocity directions. The same waves characteristics of the experimental tests have been used.

5.5.2 Comparison of the different braking strategy

For the sake of clarity, here are summarized the main simulation parameters used to specifically compare the different braking strategy:

- Wave motion with amplitude 0.45 m and frequency 0.33 Hz;
- Vehicle CoG: 1.1585 m (no added module);

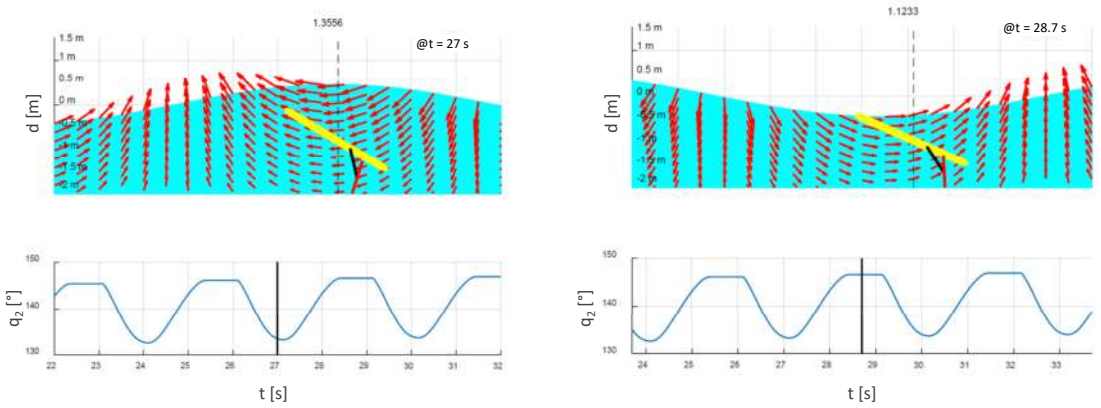

Figure 5.14: *Two snapshots of the simulation with WAVE in COG3-B2 configuration. For both figures, the vehicle's bow in pointing right. On the left, at the time $t = 27\,s$: the arms are free to move because the local speed on the wing due to the wave motion has a negative horizontal component. On the right, at the time $t = 28.7\,s$: the arms are blocked because the speed has instead a positive horizontal component. At the bottom of both figures, it is shown the relative angle q_2 between the arm and the body of the vehicle in which the braking periods can be noted.*

- Original wing profile no. 2, in the middle position, right side up mounted, aligned with the arm (*i.e.* $0\,°$ of attack angle).

The comparison of the simulative results of wave gliding propulsion are summarized in Figure 5.15. In all simulated cases the vehicle go back under the effect of the waves. In particular, braking strategies B1, B3, B4 are better than B0 in contrasting the wave motion, while B2 provides the worst results. For all the simulated configurations, the CoG has an oscillatory motion along the horizontal direction in phase with the wave motion, and also the vehicle's pitch oscillates around a rest position, especially in the B1 and B3 cases.

After this first comparison of the braking strategies, further simulations were carried out using the wing configuration yielded the most promising results during experimental tests (*i.e.* attack angle $-30\,°$, called knee configuration), varying sea state, CoG, and braking conditions.

In particular, the wave amplitude and frequency were chosen to match the experimentally generated ones, sea state 2 and sea state 3 (Table 5.11):

Table 5.11: *Simulated values of sea state for WAVE vehicle wave-gliding capability characterization.*

Sea state	Amplitude (m)	Frequency (Hz)
Wave generator tests	0.45	$0.1 - 0.33$
Average Sea state 2	0.82	$0.1 - 0.3$
Average Sea state 3	1.5	$0.1 - 0.33$

Different CoGs were simulated by moving the nominal CoG of the vehicle 5, 10 and 15 centimetres towards the bow.

Over 120 simulation tests have been performed. In order to effectively analyse the results, a function has been implemented to calculate an index linked to the average speed of the vehicle during its oscillatory movement. In summary, the arithmetic mean

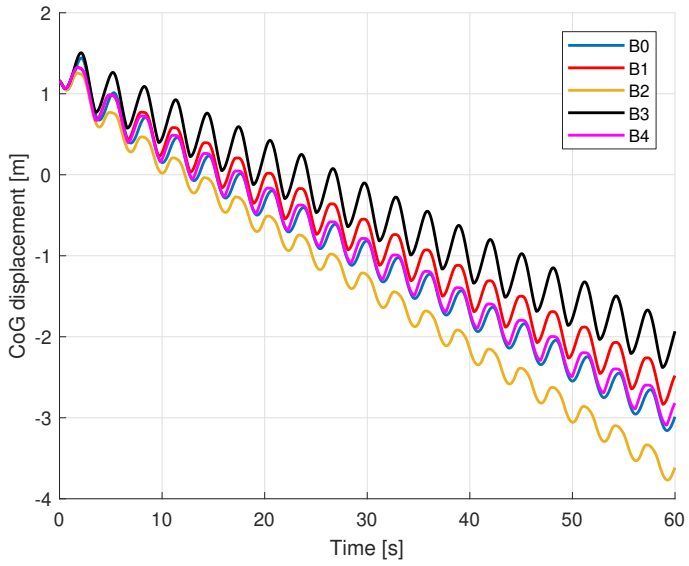

(a)

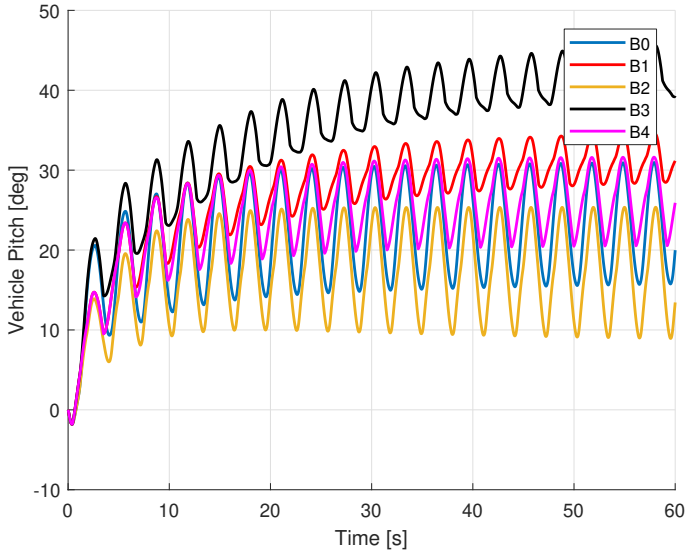

(b)

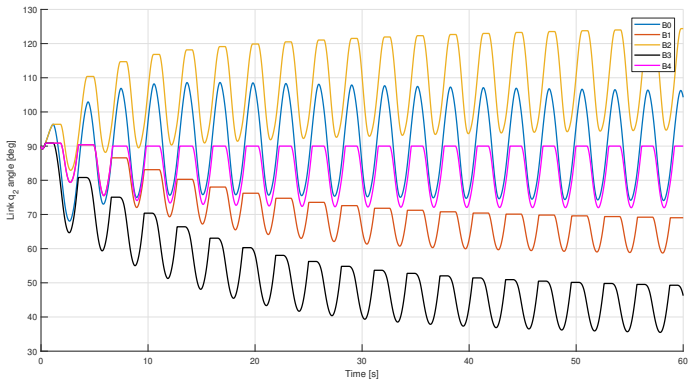

(c)

Figure 5.15: *Comparison of the different braking strategies. (a) CoG displacement, (b) pitch and (c) q_2 angle of the WAVE vehicle are shown.*

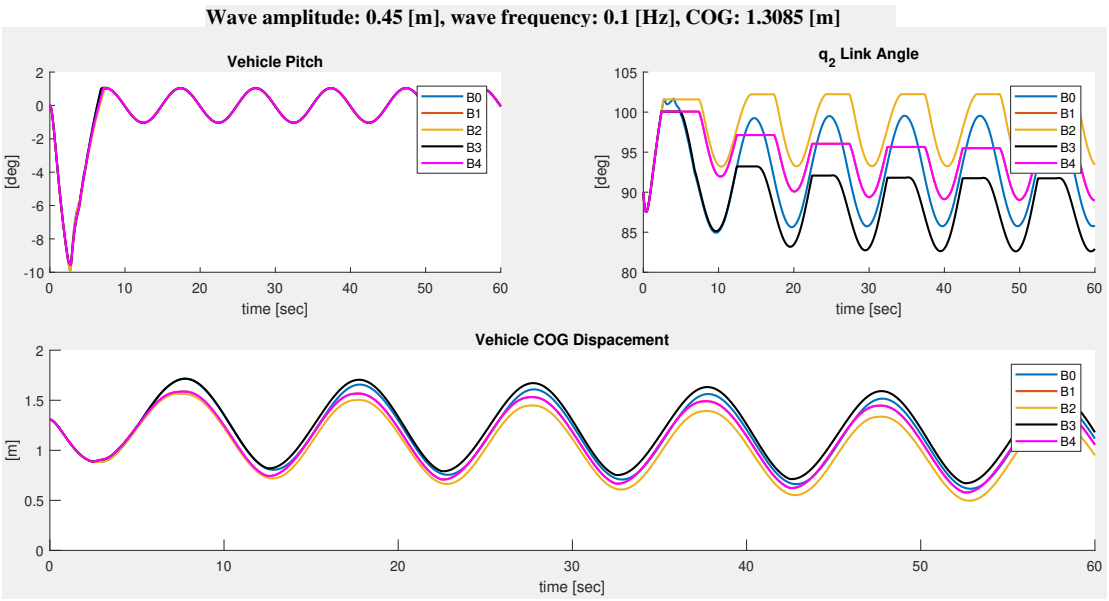

Figure 5.16: *Simulative results in the best conditions for wave gliding. The pitch of the vehicle change accordingly with the wave period of* 10 *s. It can be noticed that in the upper right plot B1 and B4 are superposed,* i.e. *they are equivalent because* $q_4(t) > \pi/2$ *always.*

between 2 significant indices, $\alpha_{v_{max}}$ and $\alpha_{v_{min}}$, was used. They are calculated by identifying the local maximum and minimum points, respectively, of the CoG trend along the North axis and characterizing this trend with the angular coefficient of the linear least squares fitting corresponding to these points.

This way, the test configuration that gave less backward movement was identified (*i.e.* a mean velocity of -0.00406 m/s along North axis):

CoG: 1.3085 m (nominal CoG $+15$ cm);

wave amplitude: 0.45 m;

wave frequency: 0.1 Hz;

braking strategy: B3.

Figure 5.16 shows the comparison plots of the braking strategies in this optimal configuration. Examining the results in terms of average velocity, the braking strategy B3 turns out to be the best in almost all the tests carried out while the B2 strategy is often worse than B0 and always worse than the other identified strategies.

5.5.3 Exponential wing profile

In order to enhance the wave gliding navigation performance, an exponential wing profile was designed. It can be analytically described as follow:

$$w(x) = \begin{cases} D, & \text{if } x \geq L - l, \\ d + (D - d)\dfrac{1 - \exp^{-\alpha \frac{x}{L-l}}}{1 - \exp^{-\alpha}}, & \text{if } x \leq L - l. \end{cases} \tag{5.41}$$

In (5.41) the following notation is used:

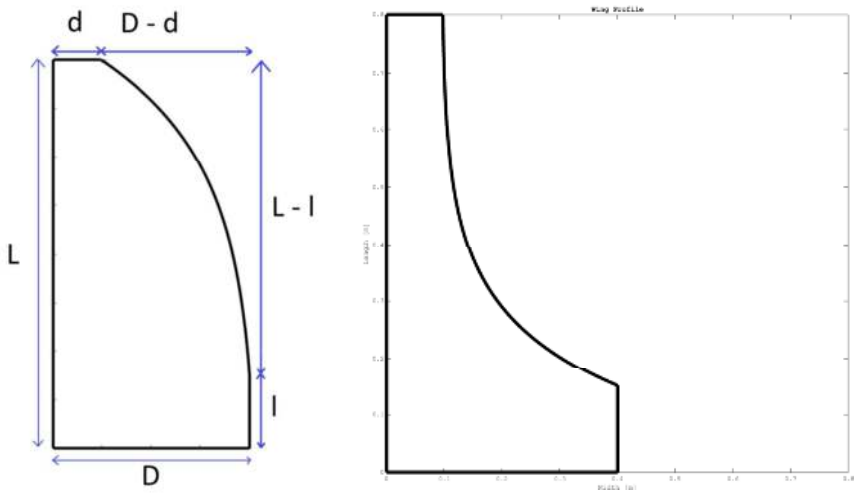

Figure 5.17: *Exponential wing profile with explication of the geometrical parameters L, D, l, d. α can assume both positive (left) or negative (right) values.*

Table 5.12: *Geometrical parameters of the wing profiles implemented in the simulations. For the parameters definition, refer to* (5.41)

Wing profile	L (m)	l (m)	D (m)	d (m)
Exponential 1	0.8	0	0.4	0
Exponential 2	0.8	0	0.4	0.0975

- x is the wing height ($x \in [0, L]$);
- w is the wing width as a function of x;
- D and L are the maximum wing dimensions;
- l and d are the dimensions of the rectangular part of the wing, *i.e.* before the wing starts to curve;
- α is the actual exponential decay constant that characterize the geometry $\alpha \in \mathbb{R}$.

Figure 5.17 clarifies the analytical description.

5.5.3.1 Exponential wing simulative results

Having identified the optimal configuration to reduce the back-warding of the vehicle, the exponential wing profile was also tested. First of all, two variants of this profile have been defined (Figure 5.18), whose characteristics are reported in Table 5.12. Several values of α were chosen for the exponential wings in order to analyse the behaviour of the WAVE vehicle with respect to the wing surface S. The reference value $S_{\text{ref}} = 0.2217\,\text{m}^2$ is the area of the rectangular profile that yielded the best wave gliding results. The simulation tests and the results of average speed magnitude are reported in Table 5.13. From the analysis of the new simulations it can be concluded that, with the same condition of sea, surface and wing mounting, the exponential wing profile 1 is slightly better than any other configuration in terms of less receding.

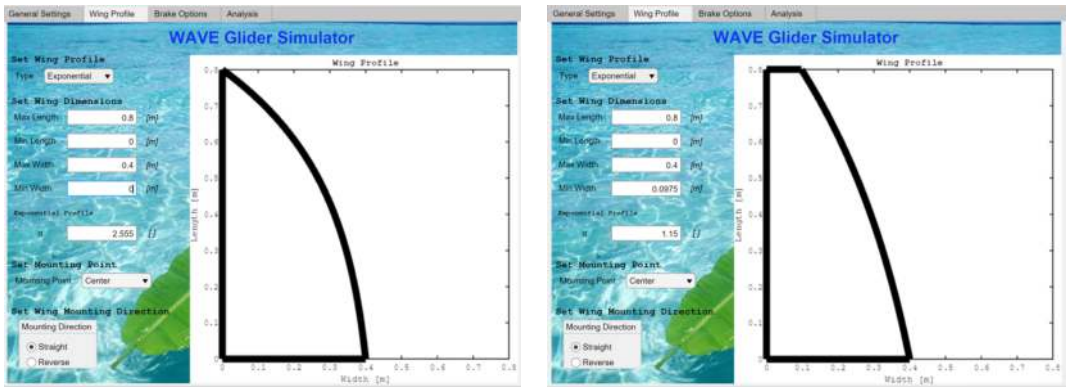

(a) (b)

Figure 5.18: *The exponential wing profiles tested: (left)* $\alpha = 2.555$ *and (right)* $\alpha = 1.15$*. The* α *values are such that the wing area is the same as the wing used in the best case with trapezoidal profile.*

Table 5.13: *Simulated values of average velocity along North axis obtainable with different variants of exponential wings. The wing surface is expressed both with respect to* S_{ref} *and in square meters.*

Test no.	Wing profile	Wing Surface (w.r.t. S_{ref})	Wing Surface (m^2)	α	Average velocity along North (m/s)
1	2 (best config.)	1	0.2217	–	-0.00399
2	Exponential 1	0.8	0.1774	0.658	-0.00359
3		0.9	0.1995	1.537	-0.00379
4		1	0.2217	2.555	-0.00397
5		1.10	0.2439	3.852	-0.00411
6		1.20	0.2660	5.827	-0.00424
7		1.30	0.2882	10.05	-0.00435
8	Exponential 2	0.8	0.1774	-1.093	-0.00374
9		0.9	0.1995	0.025	-0.00389
10		1	0.2217	1.15	-0.00403
11		1.10	0.2439	2.439	-0.00415
12		1.20	0.2660	4.19	-0.00425
13		1.30	0.2882	7.58	-0.00435

Finally, the simulation tests indicate a relationship between the average speed and the wing surface (Figure 5.19), although it is still not exactly characterized. Indeed, it

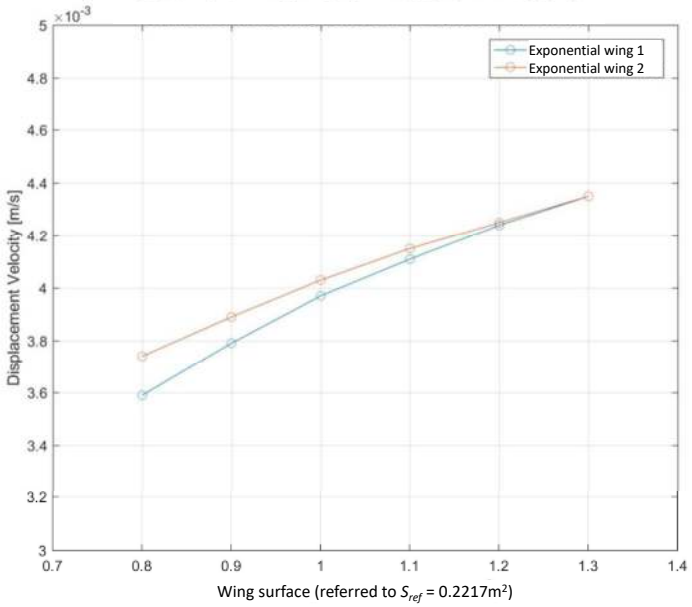

Figure 5.19: *Average displacement velocity with respect to the wing surface of the exponential profiles.*

can be observed that as the wing surface increases, the vehicle moves faster towards the stern, *i.e.* a larger wing may led to worse wave gliding performance.

5.6 Conclusions and Future directions

The dynamic simulator, accurately tuned according to experimental results, was deeply described in this chapter. The comparison of simulative and experimental data validate the overall simulator and give confidence in the simulative predictions carried out. It is remarkable that - although several restrictions and hypothesis in the proposed mathematical model exist - it is still applicable and valuable for the research on the recharging capabilities and wave-induced movement mechanism of the WAVE vehicle. Extensive simulations were performed in order to correctly size the electro-mechanical components of the WAVE module, mainly its mounting position, wings' configuration and actuation strategy, and to conceive new solutions to maximize its performance.

Recharging-aimed and wave gliding motion simulations with respect to various factors (either vehicle's and waves' parameters) were conducted. Numerical results characterize the dynamic response of the WAVE vehicle over different sea conditions. In particular, for the wave gliding propulsion, simulative predictions suggested possible forward surge movements that were impossible to be observed in field tests because of the towing tank physical limits. On the other side, the simulation analysis carried out to determine the best wing profile for wave energy harvesting led to the conclusion that the best among those designed up to now is the *hourglass* profile with an area of $0.25\,\mathrm{m}^2$. More generally, the middle mounting position and q_5 joint equal to $+30°$ (*foot* configuration) have always been the best ones for all the tested wings.

Furthermore, the wave recharging performance may be improved by adjusting the following factors in future works, both at sea and through simulative analysis:

- Excessive wing area increases can lead to a decrease in performance. Appropriate weight and area relationship between the WAVE vehicle main bodies would modify the behaviour of the vehicle and may lead to a more efficient utilization of wave energy.
- It seems pertinent to further investigate geometries that develop more along the length of the vehicle, maximizing the wing area where the forces acting on are greater (*i.e.* towards wing's ends). Clearly, these indications need to be re-evaluated in field tests.

Several aspects must be kept in strict consideration in the evaluation of the results, although notable, presented in this chapter in order to ensure a technological transfer of the prototype to more operational scenarios:

- It may be evaluated, both in simulation and experimentally, the behavior of the WAVE vehicle with higher sea states, with more complex waves of the monochromatic wave so far considered, as well as with disturbances due to wind and currents. The first experimental indications seem to preclude the operation of the vehicle under rough operating conditions, *i.e.* above sea state 4.
- It will be interesting to check the performance in case the vehicle alternates periods in gliding mode with periods in wave gliding mode, *i.e.* if it would be possible to further increase the passive long-endurance navigation capabilities of the WAVE vehicle by combining these operating modes.
- Through intensive simulations, different braking strategies were identified for the WAVE module arms that could allow the vehicle to counter the wave motion, although none of these result in an effective wave-gliding navigation. Furthermore, it must be taken into account that the simulated block and release actions of the WAVE module arms must be in phase with the appropriate wave direction, *i.e.* require a complex automation system. In fact, a suite of appropriate sensors and actuators with sufficiently high dynamics would be needed to avoid delays in blocking and releasing the arms. All this could result in a substantial increase in implementation costs as well as in a comparable energy consumption with respect to glider mode navigation.

Part II

Design, implementation and testing of an Underwater Test Range for autonomous navigation validation

AUVs are remarkable inventions that revolutionized the process of collecting data autonomously in harsh marine environments. In their early years, deploy expensive vehicles navigating autonomously in an hostile environment, and expecting them to return safely was a true act of faith in engineering. In the last decade, with the effective improvements in computational power, miniaturization of electronic systems, and power supply technology, AUVs became suitable to be used as test beds for new techniques for data processing and new navigation algorithms. The accessibility of this new technological domain has resulted in an exponential increase in AUV development and deployment with many thousands of operations around the world corresponding to a huge amount of data. Most of the advances in AUV capabilities are driven by new application scenarios side by side lower cost of data acquisition, automating the process of data fusion with precise georeferentiation.

Indeed, the quality of data collected during AUV missions is strongly dependent on the performance of the navigation system. The absence of GPS signal together with the well-known limitations of the acoustic channel make AUV navigation and localisation still difficult tasks [124, 166]. Different approaches have been proposed based on the integration of high-performance navigation sensors (*e.g.* DVLs or FOGs) with efficient sensor fusion algorithms that can keep bounded the navigation error [7, 41].

Experimental validation of the proposed methods is often reported, but a systematic assessment of the vehicle navigation accuracy is difficult to obtain in many cases because of the lack of a reliable ground-truth and, in general, of testing standardisation and facilities. To do that, the second part of this thesis deals with the design, implementation and testing of an easily deployable Underwater Test Range (UTR) for V&V of AUVs autonomous navigation skills.

CHAPTER 6

Review of underwater localization and tracking

The first fundamental aspect in considering the UTR design is the choice of the proper tracking algorithm. Underwater acoustic target tracking has aroused wide attention both in military and civil fields.

Hence, the need for accurate target localisation in a marine context led to a continuously deepened research for the target tracking problem, which is one of the mostly required tasks in Underwater Wireless Sensor Networkss (UWSNs) [73, 98, 137]. This chapter reviews the state-of-the-art in this field.

6.1 Theory of underwater target tracking

Tracking could be defined as the process of estimating the state vector (*i.e.* position, velocity, and acceleration) of single or multiple moving targets in a precise and accurate manner, as quickly as possible by using the available measurements collected from various sensors. The measurements include direct distance estimation, slope distance, Direction of Arrival (DoA) of the target signal, Received Signal Strength Indication (RSSI), Time of Arrival (ToA) or Time Difference of Arrival (TDoA), as well as the frequency difference between signals received by sensors caused by the Doppler frequency shift.

There are various review articles about target tracking in Wireless Sensor Networkss (WSNs), [66, 98, 192] to name a few. UWSNs are an extension of traditional target tracking in the underwater environment, with peculiar differences between underwater acoustic target tracking based on UWSNs and target tracking using WSNs:

Communications The underwater channel is highly variable over time and space due to the characteristics of the transmission media and the environment itself. The

Table 6.1: *Detection theory hierarchy.*

Detection Theory	
Level 1. Known signals in noise	1. Synchronous digital communication 2. Pattern recognition problems
Level 2. Signals with unknown parameters in noise	1. Conventional pulsed radar or sonar, target detection 2. Target classification (orientation of target unknown) 3. Digital communication systems without phase reference 4. Digital communication over slowly fading channels
Level 3. Random signals in noise	1. Digital communication over scatter link, orbiting dipole channel, or chaff link 2. Passive sonar 3. Seismic detection system 4. Radio astronomy (detection of noise sources)

main problems are related to large propagation delay, limited bandwidth and high bit error rate (BER) [163].

Estimation rate In the underwater domain, the sensors are deployed exploiting the 3D-space while drifting with the current. The tracking is highly dependent on the accuracy of the sensor positions knowledge as will be demonstrated in 7.2.1, which implies challenging real-time requirements for underwater acoustic tracking algorithms compared with those based on WSNs. This situation is worsened by the mentioned limited bandwidth resulting in low communication rates.

Tracking modality Acoustic modems consume tens of Watts during the transmitting process, and tens of milliWatts during receiving processes, unlike RF modems. The asymmetry in power consumption makes it generally preferable for UWSNs to work in passive mode for energy-efficiency.

Nonetheless, the tracking process both in visual tracking and non-visual tracking has some important common components such as target detection, position determination, target model construction and state filtering and prediction. These components will be briefly outlined in the following subsection.

6.1.1 Target Detection

In a very simplified way, an acoustic (non-visual) sensor *detects* the target when the received signal strength exceeds a calculated threshold. Indeed, many sophisticated algorithms for detecting targets with low false alarms probability exist. A hierarchy for detection problems is presented in Table 6.1 [206].

With acoustic imaging sonar, detection process means finding a moving target in the image sequences and describe its characteristics (such as position and size). Currently, the commonly used idea is to subtract the moving target from the difference image obtained by comparing the background image and the current image [199].

6.1.2 Target Position Localisation

For non-imaging acoustic sensors, the position of the target may be determined knowing the location of detecting sensors. The relative distance information is easily obtained from active sensors, while passive sensors measure only bearing information and the target position can be computed by three bearings from different non-collinear sensors, as done in the proposed UTR. By definition, triangulation is the process of determining the target position and orientation based on angle measurements, while trilateration methods involve distance measurements. Because of the availability of angle measurement systems, triangulation has emerged as a widely used, robust, accurate, and flexible technique [74]. The triangulation term applies to a wide concept, which does not specify if the angles are measured from the robot or the beacons, nor the number of angles used [169].

On the contrary, in acoustic imaging the position determination represent the localization of the target area in each frame through the relationship quantification of adjacent frames, *i.e.* target matching. Target matching works well until the center position and size of the target change smoothly in consecutive images during a small sampling interval [120].

Further description of the target position localisation algorithm used in the UTR is given in Section 7.3.

6.1.3 Target Modelling

In most cases, at least two models are needed to investigate target tracking problems. One is the target behavior represented by the dynamic and/or kinematic motion model; the other is the observation model of the sensing system. The dynamic motion model and observation model can be collectively referred to as the state space model, and can be a mixture of linear and non-linear systems. Of course, no real world system can be perfectly described by a mathematical model; then model uncertainty must be incorporated into the problem. Indeed, the accuracy of target motion model directly affects the tracking precision. If the model is far different from the actual situation, it may lead to the divergence of the subsequent filtering process [43, 137]. However, putting numerous variables into models can be counterproductive, because its higher complexity directly translates in a higher difficult in the final filtering and estimation process. For underwater targets such as submarines, the changing course and speed are the most common manoeuvre types. Thus, in the marine environment, there are three frequently used target motion models: the constant velocity (CV) model, the constant acceleration (CA) model and the turning model.

The state space model of the proposed UTR is detailed in 7.2.

6.1.4 Target State Filtering and Estimation

Target tracking is a typical uncertainty problem. The sources of uncertainty come from modeling of target motion, observation model, and false noise incurred by multi-target and the dense cluttered environment. These uncertainties are modelled by process and measurement noises. Therefore, the essence of target tracking is estimating and predicting the state of the target by filtering algorithms to reduce the problem uncertainty. The term ”filter” is often used to describe a device in the form of a piece of

physical hardware or software that is applied to a set of noisy data in order to extract information about a prescribed quantity of interest. A filter could perform three basic information processing tasks:

Filtering means the extraction of information about a quantity of interest at time t^* by using data measured up to and including time t^*.

Smoothing differs from filtering because the result is not needed at time t^*, and data measured later than time t^* can be exploited in carrying out the calculation, *i.e.* smoothing is a non-causal filtering. In fact, smoothing operation produces delayed result of interest. Moreover, smoothing is expected to be more accurate in some sense than filtering since it uses data obtained after time t^*.

Prediction is the forecasting side of information processing. The aim is to project the quantity of interest at some time $t^* + \tau$ in the future, by using data measured up to and including time t^*.

Filters can be classified as linear or nonlinear. A filter is said to be linear if the filtered, smoothed, or predicted output quantity is a linear function of the observations applied to the filter input. Otherwise, the filter is nonlinear.

According to the problem modelling, the choice of the correct filtering algorithm to meet the specific requirements of the underwater target tracking is the key to success. Therefore, the basic filtering algorithms commonly used in underwater target tracking are here summarised:

Bayesian estimation Its objective is the estimation of successive values of a parameter vector x given an observation vector z. Bayesian estimation assumes that both the parameters to be estimated and the observed data are stochastic entities, and it consists of two processes: prediction and update. The goal of prediction is to obtain the prior density function by the target motion model. The process of update introduces the measurement value obtained from the observation model into the output of the prediction step to correct the probability so that the posterior probability of the target state is acquired.

The prior density function $p(x)$ includes all that is known and unknown about the parameter vector x prior to the availability of any observational data. If the true parameter value of x were known, then the probability density of z is given by the conditional density or likelihood function $p(z|x)$ and the complete statistical properties of z would be known. Once measurement are made, Bayes' law can be used to obtain the posterior conditional density of x:

$$p(x|z) = \frac{(p(z|x)p(x))}{(p(z))} \tag{6.1}$$

Therefore, within the Bayesian framework, the posterior density $p(x|z)$ incorporates everything to know about x after an experiment z is carried out. The denominator of (6.1) can be found from:

$$p(z) = \int_{x \in \mathbb{R}} p(z|x)p(x)\, dx \tag{6.2}$$

For the full Bayesian estimation problem, the statistical model is fully described by joint density of the parameter and observational vectors:

$$p(x, z) = p(x|z)p(z) \tag{6.3}$$

Let $z_{1:k}$ the measurements obtained from time instant 1 to k, $p(x_{0:k}|z_{1:k})$ the posterior density function before time k, and the probability of the initial state of the target is assumed to be known. The state vector x_k obeys the first-order Markov process generally, *i.e.* the current state is dependent only on the previous state, the posterior density function can be recursively obtained using the measurements $z_{1:k}$. Assuming that $p(x_{k-1}|z_{1:k-1})$ has been calculated, the probability of a one-step prediction is described as:

$$p(x_k|z_{1:k-1}) = p(x_k|x_{k-1})p(x_{k-1}|z_{1:k-1})\, dx_k \tag{6.4}$$

where $p(x_k|x_{k-1})$ represents the state transition probability. In the update phase, the observation value obtained at time instant k are exploited to update the prior probability. The posterior density function can be then derived as:

$$p(x_k|z_{1:k}) = \frac{(p(z_k|x_k)p(x_k|z_{1:k-1}))}{(p(z_k|z_{1:k-1}))} \tag{6.5}$$

$$p(z_k|z_{1:k-1}) = \int p(z_k|x_k)p(x_k|z_{1:k-1})\, dx_k \tag{6.6}$$

where $p(z_k|z_{1:k-1})$ acts as a normalization constant, while $p(z_k|x_k)$ represents the likelihood probability. Interested reader is referred to [99] for a comprehensive study of the methods currently in use for statistical dynamic system estimation in a Bayesian framework: linear and nonlinear, Gaussian and non-Gaussian.

Indeed, in linear conditions, the Bayesian filter can acquire the approximately optimal solution, namely the KF. But in many cases interesting dynamic systems are not linear by nature, so the traditional Kalman filter cannot be applied in estimating the state of such a system. In these kind of systems, one or both the dynamics and the measurement processes can be nonlinear. Then, EKF, based on Taylor series approximation of the joint distribution, and UKF, based on the unscented transformation of the joint distribution, are presented. These filters will also be analysed for the specific UTR problem in the next chapter. Finally, Particle Filter (PF) is introduced.

EKF It extends the scope of Kalman filter to nonlinear optimal filtering problems by forming a Gaussian approximation to the joint distribution (6.3) using a Taylor series based transformation (see, for instance, [17]). The filtering model used in the EKF is

$$x_k = f(x_{k-1}; k-1) + q_{k-1} \tag{6.7}$$

$$z_k = h(xk; k) + r_k \tag{6.8}$$

where $q_{k-1} \sim \mathcal{N}(0; Q_{k-1})$ is the process noise, $r_k \sim \mathcal{N}(0; R_k)$ is the measurement noise, $f(\cdot)$ is the (possibly nonlinear) dynamic model function and $h(\cdot)$ is the

(again possibly nonlinear) measurement model function. The EKF approximates the distribution of state x_k given the observations $z_{1:k}$ with a Gaussian:

$$p(x_k|z_{1:k}) \approx \mathcal{N}(x_k|m_k; P_k) \tag{6.9}$$

where m_k and P_k are the estimated mean and covariance of the state, respectively, on time step k after seeing the measurement. Especially when the target maneuvering is limited, EKF can achieve satisfactory results. However, if the nonlinearity of the system is serious, tracking algorithms adopting EKF will result in large errors due to the Taylor series linearization [114].

UKF Instead of Taylor series based approximation, the unscented transform (UT) [113, 212] can be used for forming a Gaussian approximation of the joint distribution of random variables x, z. In UT, sampling points (called "sigma points") are deterministically chosen in order to capture the desired moments (at least mean and covariance) of the original distribution of x exactly. After that, sigma points are propagated through the non-linear function $h(\cdot)$ and estimate the moments of the transformed variable from them. The advantage of UT over the Taylor series based approximation is that UT is better at capturing the higher order moments caused by the non-linear transform, as discussed in [114].

PF It is a sub-optimal class of the Bayesian filter, which approximates the posterior probability density function based on a set of discrete and random sampling particles. Also the PF can be divided into two phases: prediction and update. The prediction phase estimates the state of particles at the next step according to the modelled target dynamics. The update phase recalculates the particles weights exploiting newly obtained measurements at the current time. In the end, the weighted sum of all particles is the final estimate result. Estimating the form of a density based solely on a set of random samples from that density arise, of course, the question of how those samples were obtained in the first place. For a complete discussion of the origins and fundamental developments of both general Monte Carlo integration methods and sequential importance sampling methods, the reader is referred to the book [179] and the article [133].

6.2 Taxonomy of underwater target tracking algorithms

A widely applicable classification criterion for underwater acoustic target tracking algorithms is proposed in [137]. The adopted taxonomy is illustrated in Figure 6.1, which divides the algorithms into instrument-assisted, mode-based, and tracking optimization methods.

6.2.1 Instrument-Assisted Methods

Due to the underwater domain attributes, the common sensors used for underwater tracking need to be presented. The reason that acoustic rather than electromagnetic waves are used in seawater is simple: electromagnetic waves are strongly attenuated in salt water and would, therefore, have too short a range to be useful for most applications [104]. An important technical application of acoustics is related to undersea

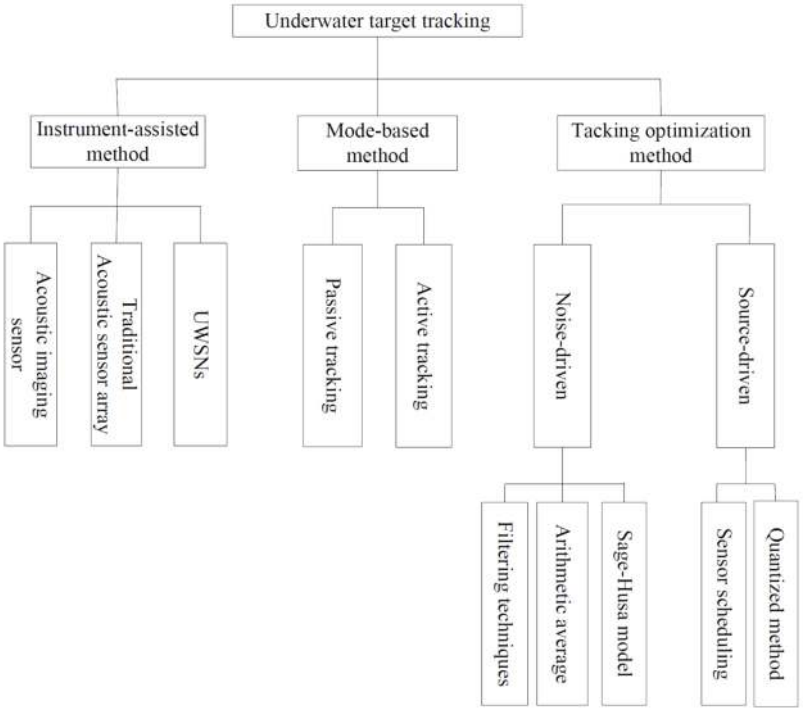

Figure 6.1: *Classification of the underwater target tracking algorithms, adopted from [137].*

activities, where acoustic waves are used in much the same way that radar and electromagnetic waves in general are used *above the surface* for the detection and location of objects, and for communications. As the only carrier that can propagate over a remote distance in the marine environment, acoustic waves have always been the most widely used medium in underwater target tracking. Then, the commonly used tracking instruments are acoustic sensor arrays, UWSNs, and acoustic imaging sensors. In this section, they are briefly introduced.

6.2.1.1 Acoustic sensor array

Large acoustic arrays of transducers are needed to achieve high directivity for accurate bearing determination and noise rejection. In active arrays, sufficient power is needed for range determination of distant targets. Arrays also provide flexibility in shaping both active and passive acoustic beams [34]. Figure 6.2 show examples of arrays used in sonar: cylindrical and truncated spherical active arrays and a conformal passive array. Schloemer has given a comprehensive review of hull-mounted sonar arrays in [185]. Active arrays for medium range detection usually operate in the $2 - 10$ kHz frequency band, while those for shorter range applications, such as mine or torpedo detection, use frequencies up to 100 kHz [143]. Passive naval arrays for surveillance tasks include linear arrays that are towed far astern.

The main concerns of acoustic arrays arise when sensors are close together in an underwater system, since then the sound field of each one affects all the others [218]. In hull-mounted passive arrays flow noise and structural noise excited by water flow and machinery are more important than ambient sea noise except at very low speed.

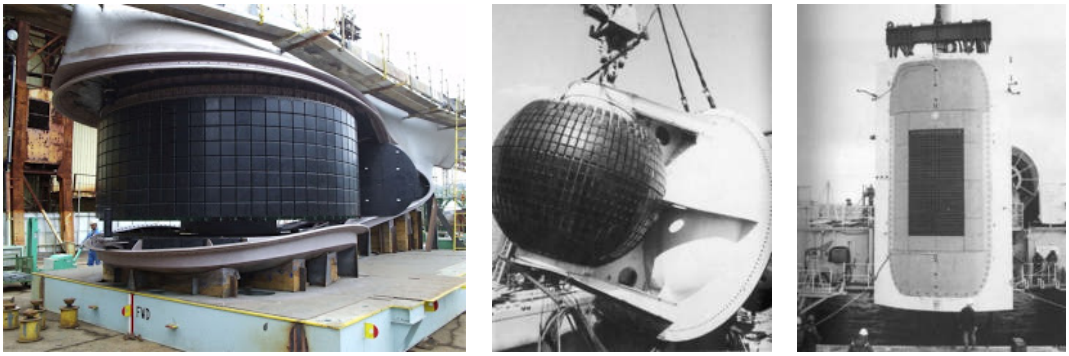

(a) (b) (c)

Figure 6.2: *Examples of sonar arrays. (a) The bow sonar of an US Navy Arleigh Burke class is an example of a cylindrical scanning array. (b) Submarine sonar spherical array undergoing tests. (c) A panel of a submarine conformal array during testing.*

Towing passive arrays reduces the ship noise, but they are limited by their own flow noise and flow-excited structural noise.

Finally, a single line array is omnidirectional in the vertical plane and therefore, when horizontal beams are formed, the well-known "Ambiguity Problem" makes it impossible to distinguish returns from port or starboard side. There are several methods available to resolve this ambiguity:

- Operationally, the tow vessel may change its heading in order to resolve the ambiguity as shown in Figure 6.3. Indeed, the procedure can be very time-consuming, particularly for a long array, and cannot be used for a single ping. Nevertheless, the true target bearing is often quickly resolved, but may need some assumptions about the target motion.

- Twin (or multiple) arrays can be towed parallel exploiting the time delays between the signals arriving at the arrays to resolve the ambiguity. However, maintaining the correct spacing between arrays is an actual problem, particularly for long arrays and during heading changes.

- Cardiod technology could be employed, based on arrays made up of triplets, *i.e.* each array element is made by three hydrophones in the vertical plane (Figure 6.4a). All digitalized channels are sent back to a central processor that employs time delays between all three pairs for beamforming so that the ambiguity can be resolved regardless of any rotation of the array. In particular, the beamforming is made in two phases: at the triplet level, using signal processing to form a cardioid responses, and at the linear array of triplets level, doing the processing in the azimuthal plane [108]. The cardioid beam pattern can be conceived as the sum of scalar omni and vector dipole hydrophones, with voltage amplitude and phase adjusted for equal far-field pressure amplitude and phase, yielding the normalized true cardioid beam pattern function, $P(\vartheta) = (1 + \cos\vartheta)/2$, illustrated in Figure 6.4b. Adequately large array diameter is essential to house the triplets and to produce measurable time delays.

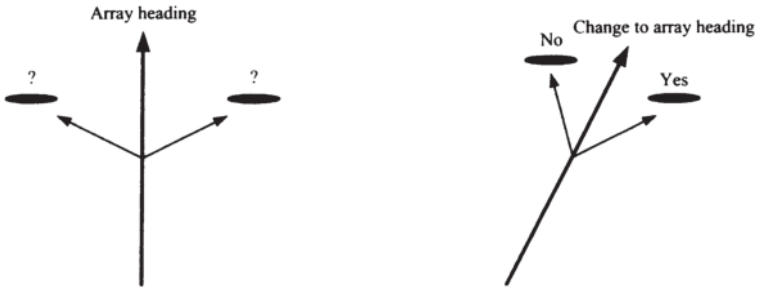

Figure 6.3: *Simplified concept of left-right ambiguity. The change of course of the tow ship allows to discern the target real bearing. Image from [211].*

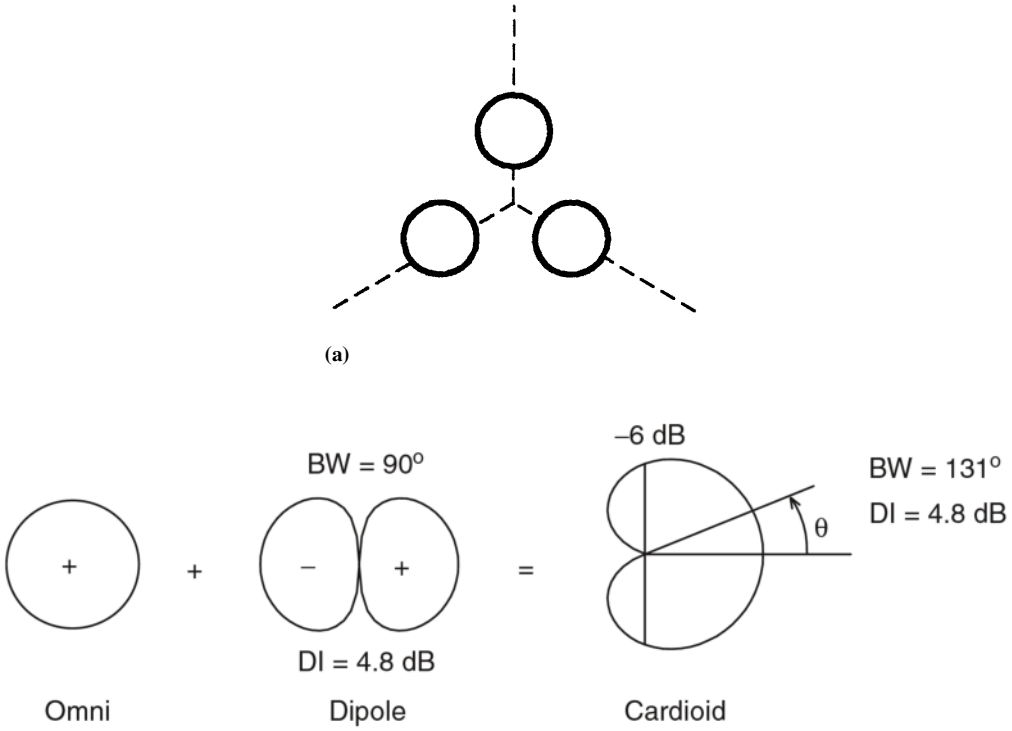

Figure 6.4: *Illustrative sketches of the cardioid technology essentials. (a) Each element of a cardiod array is an hydrophone triplet. Image from [211] shows the vertical plane section of the array. (b) Synthesis of a cardioid pattern, from [34]. This pattern has a null at* $180\,°$*, is* $6\,dB$ *down at* $90\,°$*, and has a* $3\,dB$ *down beam width of* $131\,°$*.*

The authors in [32] eliminated the port-starboard ambiguity in an optimal way by introducing the ambiguity into the model and then deriving the full Bayesian posterior distribution of the target state. In addition, the paper proposes the use of AUVs towing acoustic sensor array constituting a peculiar UWSNs to estimate the target kinematic state at each time scan. During the data fusion process, different from classic "track-to-track" approach, the fusion and filtering are completed at the same time because the estimated tracks obtained from independent sensors are still dependent due to the common process noise.

Another problem arises when an array is used to obtain bearing information, because the quality of tracking is highly dependent on the relative position between the interest target and the array. AUVs towing acoustic arrays have great potential when merged with mobile/moored manned/unmanned nodes [127]. Therefore, the authors in [79] aimed at investigating the autonomous decisions for moving tracking platform to improve tracking performance, proposing an adaptive control strategy for the vessel towing the array to keep the target at the broadside as much as possible by the acquired measurement information. The simulation results show that the algorithm significantly minimizes the estimation error of the target position and provides a method of maintaining the track.

Different from previous papers, the authors in [69] using matched-field processing (MFP) to overcome the problem of tracking error incurred by environment uncertainty; however, this algorithm is only appropriate for tracking the target emitting signals with a certain strength, which restricts its underwater domain application.

6.2.1.2 UWSNs

UWSNs address the aforementioned issues demonstrating their superiority over acoustic sensor array with respect to low-cost, self-organization, fault tolerance and rapid deployment [73]. UWSNs consist of sensor nodes equipped with a limited capacity of data processing and communication via acoustic modems [39].

Typically, many homogeneous or heterogeneous nodes are deployed randomly or strategically across the interested area [135]. The multi-sensors data collected can be used to compute the state vector of the target and then transmitted to a central node which has higher processing ability and generally acts as a gateway connecting the network and application layers. Subsequently, data fusion algorithms provide more accurate estimation of the target state vector [24]. Some peculiarities can be outlined for UWSNs:

- Due to the GPS absence, effective node localization algorithms are needed to avoid a significant negative impact on tracking performance;
- Efficient node cooperation and communication can reduce the amount of messages exchanged;
- Measurements obtained from underwater sensor nodes are severely corrupted by noise, particularly in enclosed scenarios. Therefore, outlier rejection is a challenging but necessary topic;
- The distribution of future-position estimation between network nodes may be taken into consideration to maximize node scheduling strategy efficiency;

- The network energy management is a key factor for any target tracking algorithms based on UWSNs. Then, good trade-off between tracking accuracy and energy consumption must be pursued.

It is worth to note that novel tracking systems has been proposed thanks to the development of AUVs, incorporating acoustic sensor array and acting as (or with) heterogeneous UWSN nodes.

In [223], a tracking algorithm based on distributed UWSNs tackles the energy efficiency problem. This algorithm includes a wake-up/sleep (WuS) and valid measurement selecting (VMS) scheme. The estimated position of the target provided by KF is used to wake up sensors which could detect the target. The scheme of VMS determines the valid sensors which can detect the target among activated sensors and passes their measurements to the processing node to update the state of the target. An extension of this work proposes a combination of the Interacting Multiple Models (IMMs) with energy-efficient schemes WuS and VMS to track a mobile target [222].

Since UWSNs can consist of numerous sensors, the topology of these sensors will also have a great effect on the tracking performance [227]. Inadequate sensor configuration will yield significant tracking errors no matter what tracking algorithm is utilized. Therefore, there are some papers that consider the configuration of sensor deployment to improve the tracking performance. The authors in [146] investigate the problem of optimal sensor deployment for underwater target tracking using range-only measurements, while in [24] sensor-target geometries which minimize the uncertainty ellipse are identified for range-only, time-of-arrival-based and bearing-only localization. The optimal geometries for an arbitrary number of sensors are derived and it is demonstrated that they are not, in general, unique. The importance of understanding the influence of the sensor-target geometry on the potential localization performance is highlighted via formal analytical results and a number of illustrative examples. An experimental demonstration of this problem has been reported in [153] where a constellation of surface nodes adapts its geometrical distribution to improve the localisation performance of an AUV performing an underwater mission.

The fact of having lots of mobile sensors, like AUVs, can be exploited to more efficiently achieve the desired mission goal. In [152], a novel data-driven algorithm for AUVs team for adaptive sampling of oceanic regions is proposed, where each agent shares its knowledge of the environment with its teammates and autonomously takes decision in order to reconstruct the desired oceanic field. In particular, sampling point selection is made in order to minimize the uncertainty in the estimated field while keeping communication contact with the rest of the team and avoiding to repeatedly sampling sub-regions already explored.

Finally, the outlined issues in UWSNs can be solved not only by effective algorithms but also by the tracking instrument itself. Recently, some researchers are focused on designing acoustic modems for underwater target tracking to solve the problems incurred in the underwater environment. The authors in [186] provide a comprehensive survey of underwater acoustic modems.

6.2.1.3 Acoustic Imaging Sensor

Underwater acoustic imaging technology provide a mature alternative approach for underwater target visual tracking. The most widely used acoustic imaging sensor is

the forward looking sonar, usually installed on AUVs' bow. The imaging sensor elaborates the received back-scattering echoes generated by its acoustic ping. One of the important tasks related to acoustic imaging sensor is to identify objects on the seabed or in the water column [167]. Different tracking algorithms have been developed so that obstacles can be avoided [109]. An interesting collaborative mine-countermeasure system was proposed in [68], in which a USV tracks and maintains the target in the field of view of an imaging sonar, while compensating for wind, waves and currents. At same time, it commands an UUV, while tracking it with the imaging sonar itself, to deploy a payload to neutralize the target.

In [138] a tracking filter that fuses USBL measurements and acoustic image measurements is developed. The filter provides robust tracking performance, even in the case that either USBL or image measurements are not available. USBL measurements are used for tracking underwater objects with the advantage of easy deployment and relatively long tracking range while providing target position [195]. The rough target position measurement provided by USBL is used by the imaging sensor to set the region of interest in where the target is located. Then the estimator updates the target position with precise image measurements when the imaging sensor finds the target in its region of interest.

As a matter of fact, acoustic imaging sonar tracking algorithms are limited to the target in close range. For marine targets which are far from tracking platforms, long range propagation of acoustic waves must be used in the ocean environment. Nevertheless, tracking based on visual data can also be an alternative method, especially in close-range tracking application, as mentioned in the previous cases.

6.2.2 Mode-Based Methods

An acoustic sensor typically has two working modes: it emits sound waves and it receive sound waves, at the same time or not. A receive-only acoustic sensor is called a hydrophone. There are a plethora of acoustic tracking systems which can be simplified as an active system or a passive system according to the working mode of sensors. In the latter, the tracker can only estimate the state of the target by the signal directly emitted from the target. In general, the obtained measurement is the relative bearing of the target to the tracker. Active systems can acquire also the range information about the target by measuring the echo ToA or TDoA.

Active acoustic systems can be further subdivided into monostatic systems (a single sensor transmits and receive as well) and multi-static systems, where one sensor of the system only accomplishes the task of transmitting or receiving sound waves. In particular, the bistatic system is the simplest type of multi-static system with a single source-receiver pair as in Figure 6.5 [52, 80].

In this subsection, algorithms based on different tracking mode will be introduced and compared. The technology and measurements adopted in every algorithm are also recapped.

6.2.2.1 Passive Tracking

The problem of tracking using passive measurements can be formulated as Bearing-only tracking (BOT) which is a technology of determining the state of a target solely

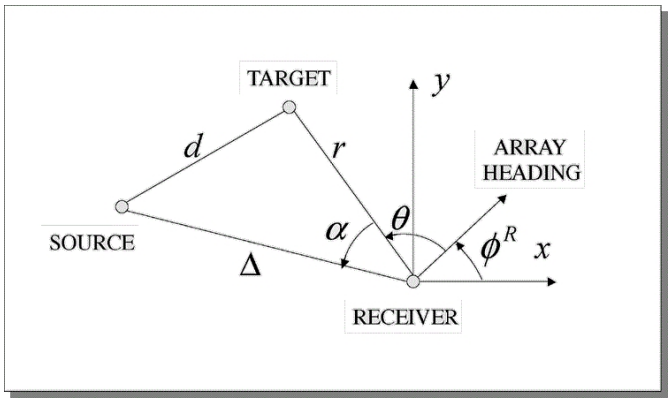

Figure 6.5: *Bistatic source–target–receiver geometry for a single source–receiver pair,* i.e. *the source and receiver are not colocated. Image from [52].*

through measurements obtained from the signals originated from the target. Bearing-only passive target localisation has a long research history starting from the pioneering work of Stansfield [193]. Due to the high non-linearity introduced by the underwater passive measurements, the design of an efficient bearing-only tracking process is still a challenging task [137].

More recently, due to the spread of long-endurance, silent, small, relatively low-cost autonomous platforms, passive sonar systems hosted on networks of mobile unmanned vehicles have been proposed [87, 201]. This way, the extra range information about the target can be obtained in passive tracking by using multiple detecting platforms [83]. In addition, [3] proposes a method to exploit the bottom and surface reflections of sound in ocean environments to obtain the target range.

6.2.2.2 Active Tracking

In conventional active sonar systems, a pulsed signal is transmitted to the target and the scattered echo is sensed by a receiver, which may not be located with the transmitter. Directional receivers, *i.e.* arrays, are required to estimate the target bearing, typically through beamforming algorithms [44]; the range of the target is derived from the echo time delay. A gain in detection performance can be obtained through the increase of spatial directivity afforded by towing a linear array of hydrophones.

The main division of active sonar systems is between monostatic and multistatic systems [59], which refers to the geometry of the sonar configuration. In the first, the source and receiver are on the same platform. The ship-towed array is a classical example which implies less geometrical uncertainties and conceptually simpler processing methods. A multistatic system is composed of more than one source and receivers in a certain scenario. This is the natural application of heterogeneous robotic assets in a sonar system, with several advantages such as the possibility of exploiting spatial diversity and higher flexibility [149]. Spatial diversity is particularly important in active sonar as the target scattering response is always highly angle dependent [93]. As an example, [79] describes a multi-static system, where a sonar transmitter (located on a buoy or a vessel) emits a ping and the echoes scattered from the target are received by multiple AUVs towing sensor array. On the other side, multistatic geometries lead to increased signal processing challenges, especially with moving assets. In [82] a control

strategy for AUVs behaviour when acting as receivers of a multistatic system is presented. Driven by the mission goals, the algorithm select the best decisions for the AUV by evaluating the evolution of the tactical situation over a future time window in order to make AUVs navigation robust to possible misleading target measurements. The approach, tested at-sea in a realistic multistatic surveillance experimentation, shows the advantages of using non-predefined paths.

6.2.3 Tracking Optimization Methods

A last classification can be made looking at the the tracking optimization methods, such as the introduced KF, EKF, UKF, and PF, used to estimate the state of the target and decrease the noise-induced uncertainty. The acoustic sensors used for underwater target tracking are typically characterised by limited energy and communication constraints, which motivated the research on effective sensor scheduling strategies and relative quantization algorithms. Then, tracking optimization methods that consider these peculiar limits are also briefly introduced.

6.2.3.1 Noise-Driven Optimization Methods

EKF and UKF are widespread variations of the KF for nonlinear problems, then the tracking algorithms can be split into KF- and PF- based. In addition, underwater target tracking deals with more serious noise interference than *above-the-surface* tracking. Therefore, data pre-processing techniques are often required.

Filtering techniques

KF-based Based on the introduced UTR design, this section is focused on passive localization problem. EKF estimator plays a major role in the field of bearing-only tracking [70, 76, 119]. It linearises the non-linear bearing measurement equation about the current mean and covariance and exploits the Jacobian matrices of the process and measurement functions to propagate the estimates. This may lead to well-known shortcomings and possibly to the instability of EKF, as analysed in the latter cited works. An alternative to the EKF is the UKF [113], that is capable of better preserving the first four moments of a Gaussian distribution through a non-linear transformation. UKF performance has been investigated for several applications, including target tracking [181, 221]. A recent extension of UKF tracking approach for the bearing-only problem is described in [121, 123], called Integrated UKF, where different sensor pairs of a towed acoustic array are considered. Each of them provides bearing measurements and the relative covariance matrix to calculate a raw estimation of the target state through conventional UKF. This vector of raw estimations is then optimised with a least square estimation to obtain the final processed result. The proposed technique seems to achieve suitable tracking performance using bearing-only measurements in underwater scenarios even with high environmental noise. On the other hand, the cost of increased computation complexity and time may be accepted. A recent example of combining Kalman filters joined with Probabilistic Multi-Hypothesis Tracker (PMHT) is outlined in [131]. The presented performance are very good even in clutter environment and with a lower complexity compared to PF; nevertheless,

the achieved performance are highly dependent on estimate initialisation of the target state vector. Finally, distributed Kalman filtering based on consensus in sensor networks seems very promising for the multi-target tracking problem, in which the number of targets and their states are time-varying [158].

PF-based Two-phases PF-based algorithm is proposed for tracking multi-target based on passive tracking in [89]. In that work, a variation filter named the Mixture PF samples from a mixture of important densities containing the prior and the observation likelihood instead of the traditional PF sampling. To solve the problem of tracking an unknown number of multiple targets, two Mixture PFs are employed, one for clustering target detection and the other for tracking task. There are several PF-based distributed tracking algorithms for WSNs [101,107,188]. Unfortunately, all existing distributed algorithms are not suitable for underwater surveillance using cooperative robotic networks mainly because of communication-related implications, *e.g.* limited bandwidth of the underwater domain.

Pre-processing techniques Even employing complex filtering techniques, performance limitations arise in the underwater domain as a result of:

- Propagation loss through the water channel, which mainly depend on the sound speed profile along the water column, but also on the signal frequency as well as the characteristics of sea bottom and sea surface, especially in shallow waters;
- Ambient noise at the receiver, especially for passive sensors and at long range for active sensors;
- Other effects of the environment [58], such as a wide variety of channel dispersions in time, frequency, and angle.

For instance, in [122], a novel tracking algorithm is proposed to address the problem of noise interference. The measuring error in bearings is removed by pre-processing progress using arithmetic average. The pre-processing technique efficiently reduces the noise effect by correlating present and previous projected measurements assuming unbiased noise. In [174], a statistical estimation model named as Sage-Husa is employed to estimate the measured noise online to reduce the tracking error significantly. In addition, the pre-processing technique make the actual estimation process converge rapidly, especially when the noise is unknown.

6.2.3.2 Source-Driven Optimization Methods

Tracking optimization means not only enhancing tracking accuracy but also taking into account the source restrictions. Due to the small communication bandwidth, the amount of underwater messages must be limited. Compressing the data through quantization methods is one of the most effective way to reduce the length of communications. However, this procedure may degrade the performance of tracking accuracy because of the information loss. In addition, deployed acoustic sensors have limited energy, which implies the need of effective network scheduling strategies.

Quantization techniques The underwater channel obliges to use quantized measurements in order to save energy and efficiently exploit the limited bandwidth. In [141] optimal quantization of the data collected by the sensors is presented. The method aims at jointly optimize the estimate accuracy and the quantization level under fixed and variable transmitting power. The described adaptive quantization scheme indicates that the sensors with bad channels or unsatisfactory measurement quality should decrease their quantization resolutions or become inactive. A new distributed quantization method is proposed in [62], where the sensors adjust their quantization threshold based on the transmission from other nodes. In underwater target tracking, there are small number of studies on quantized methods. The listed WSN quantization methods require heavy computation, while a simplified objective function for offline quantization threshold optimization is proposed in [230]. The threshold can be predetermined thanks to the independence of the function from sensor locations and target state. Finally, Gaussian mixture-cardinalized probability hypothesis density (GM-CPHD) [88] tracker was used in a multistatic sonar scenario. The sensing area is divided in quantized cell in which probabilistic associations of the possible contacts are made for tracking. On all the data sets analysed, the GM-CPHD proved to be very flexible in terms of number of sensors, and generated satisfactory tracks. Again the quantization threshold is fixed.

Sensor scheduling strategies The sensor scheduling strategy is useful to choose which sensor (or group of sensors) should operate at each time-step to maximize a certain utility function focused on trade-off between communication rate and tracking accuracy. This objective function can be composed of deterministic and stochastic parts. The former part can include the energy cost for a given (movement and/or sensing) action or bandwidth costs during the communication. The latter part can account the predicted tracking accuracy or the predicted probability distribution of interest (*e.g.* target location) and the predicted information gains [48].

To further reduce the energy, it is worth to note that four sensors can determine the position of one target in 3D underwater environment. Indeed, in [170] a sensor scheduling strategy picks the most informative sensors from the candidate ones, *i.e.* located within the sensing area of the target. However, the algorithm merely based on distance neglect the influence of node topology on the tracking performance. On the contrary, in [100], the posterior Cramer-Rao lower bound (PCRLB) was used for multisensor scheduling in the presence of clutter. The approach is to use optimization techniques to control the measurement process in order to achieve accurate target state estimation. Under some standard assumptions, the effect of the measurement origin uncertainty can be expressed as a state-dependent information reduction factor which can be calculated off-line. This allows to fast calculation of PCRLB and to exploit it in real-time sensor management.

Most of the scheduling strategies mentioned before are based on global information, which is impractical for underwater acoustic tracking. A sensor scheduling strategy based on local node selection is proposed in [228], where only a small part of nodes are active at each time. Considering limited computing power and real-time tracking requirement, the distributed Kalman filtering fusion with feedback is used.

6.3 Conclusions and Future Directions

In this chapter, a review of the main underwater acoustic target tracking algorithms was made. Underwater target tracking is still a crucial part in civil and military systems. Future research efforts must deal with some challenges in underwater target tracking, summarized in Table 6.2. It is evident that all the research topics in the underwater world are highly interconnected, suggesting a holistic approach to future operational developments.

Table 6.2: *Description and possible solutions for major existing challenges in the underwater tracking field.*

Challenge	Problem description	Existing and possible solutions
Low target detection probability	Tracking using acoustic echoes poses difficulty in detection mainly because of the acoustic waves attenuation. Moreover, the development of acoustic concealment technology has result in lower Signal to Noise Ratio (SNR). Acoustic imaging sensors has the problem of low contrast and visibility in marine environment.	With respect to detect-before-track (DBT), TBD is a promising technology to solve the problem [47, 125]. Moreover, the histogram probably multiple hypothesis trackers (H-PMHT), which enhance traditional TBD, demonstrates higher real-time performance [63].
Sound Speed Variation	Many tracking algorithms assume constant speed in the water column, which is unrealistic and may result in large tracking errors, especially in trilateration.	[175] adopt one of the relationships described in [144] to construct an accurate sound speed model. The simulation result demonstrates that the tracking accuracy of this algorithm is significantly improved compared with that using constant speed sound. A more universal sound speed model is presented in [128], which is a function of temperature, depth, salinity, and latitude.
Port-Starboard ambiguity	When using a sensor array to realize underwater target tracking, Port-Starboard ambiguity is unavoidable due to the symmetry of the array. Different processes to eliminate this ambiguity exist, but usually makes tracking algorithms more complicated, difficult to apply in operational scenario, and can results in performance degradation.	The single linear array is still the first choice in underwater applications for the simplicity of deployment and integration on board AUVs. Adopting multiple platforms (mobile/fixed and manned/unmanned) towing line arrays is effective in removing the ambiguity exploiting the spatial diversity. In addition, the authors in [79] optimize the disambiguation calculating the full Bayesian posterior Probability Density Function (PDF) of the target without bringing any extra cost.
Tracking accuracy–energy consumption trade-off	Lowering the energy consumption is a core requirement for USWNs. However, reducing the energy cost means tracking accuracy drop. There are few papers taking both into consideration when proposing tracking algorithms. The final goal could be to automatically balance the energy consumption and the tracking accuracy with respect to the mission goal.	[47,229] are among the few examples considering energy consumption and tracking accuracy jointly in order to estimate the relationship between both factors. This way, the tracking algorithms try to automatically adapt the number of sensors active to meet the requirement of specific applications. As mentioned in 6.2.3.2, there are few underwater acoustic target tracking algorithms that consider the quantization issue. However, the bandwidth limit in underwater channel makes it impossible to transmit big data.
Multiple target tracking	Few of the presented algorithms are suitable to track multiple targets, while according to the actual trend of modern naval warfare, ships, submarines, helicopters and unmanned assets will operate in a highly integrated way. Difficulties arise in the association of detected contacts to the targets, since multiple targets may be present at the same time in the operative area.	Promising approaches for tracking multiple targets are the Joint probabilistic data association (PDA) filter, the MHT tracker, and the IMM algorithms. A quantitative comparison is provided in [173]. Belief Propagation Tracker (BPT) can achieve a very attractive performance-complexity compromise [145], making it applicable for resource-limited assets, *e.g.* AUVs. While many spatially distributed AUVs collecting many data are desirable for multiple target tracking, the design of a fully distributed tracking architecture in the underwater domain remains an open research problem.
Motion strategies for mobile sensors	Underwater target tracking is usually realized in large scale areas, where sensors with mobility outperform static sensors. Considering the influence of topology, how to design effective coordinate motion strategies for sensor is an active research topic. In addition, the large-scale UWSNs bares additional challenges for communication and networking protocols in a low quality channel [163], where the relative motion of the transmitter or the receiver may create the Doppler effect.	The review work [83] underlines the development of advanced robotic networks for underwater surveillance applications. Once deployed in the operative area, robots can cooperatively form an intelligent network achieving high performance with significant features of scalability, adaptability, robustness, persistence and reliability. On the other hand, they also present new issues for underwater distributed sensing, data processing and analysis, autonomy and communications, interconnected with the other topics here outlined.

CHAPTER 7

Towards an autonomous underwater vehicles test range

As already introduced, AUVs must be able to achieve a highly autonomous state of behavior and be able to interact with their surroundings navigating accurately. This advancement will require an ability to understand and adapt to their environment, and an ability to collaborate with other autonomous systems, along with the development of new V&V techniques to prove the new technology does what it should.

To ensure the safety and reliability of autonomous systems and to fully realize the benefits of these systems, new approaches to V&V are required. V&V is the process of checking that a product, service, or system meets specifications and that it fulfills its intended purpose. Today's V&V processes will be severely stressed due to the growth in the amount and complexity of software installed on an autonomous platform. Without new V&V processes specifically designed for autonomous assets, the result will be either extreme cost growth or limitations on fielded capabilities due to weak trust in autonomous systems.

Despite the growing availability of AUV technology, there are still no comprehensive methods to evaluate vehicle navigation accuracy, neither testing arenas to certify AUVs skills. With this motivation, my research group started a study to implement an easily deployable UTR that would be mainly located in the marine area of the CSSN in La Spezia (Italy). This chapter and the following two are based on the works presented in [53, 54, 56]

Section 7.1 presents the UTR main concepts and design choices. Then, the UTR theoretical problem formulation is described in Section 7.2, providing the modelling of both the cooperative target and the observations adopted in the Kalman Filters implemented. In addition, the approach to investigate the effect of perturbated sensor positions on filters performance is described, along with the UTR network architec-

ture and optimal sensor placement algorithm. Finally, the implementation of non-linear Kalman filters (EKF and UKF) is outlined in Section 7.3.

7.1 The Underwater Test Range concept and design

The envisioned infrastructure is composed of a set of acoustic modems with USBL capabilities. Upon the reception of a message from a compatible acoustic transponder installed on the mobile cooperative target (an AUV or ASV), the USBL devices measure the relative DoA. Through the integration with low-cost data processing and Micro-Electro-Mechanical Systems (MEMS) sensors for motion compensation, these devices constitute a bearing-only measurement system. This scenario set-up was successfully demonstrated at sea in [41]. This way, the DoA can be expressed in a common reference system and shared on the surface through a Wi-Fi network with a ground station, where the measurements are fused to estimate the position of the target.

The choice of using a *passive sensor network* for localizing the target has a twofold motivation. On the one hand, the devices do not need to transmit packets towards the AUV under test. In fact, the UTR long-term purpose is not to support the AUV navigation task, but rather the systematic characterisation and, ultimately, the certification of the navigation algorithm in terms of performance. On the other hand, this kind of architecture presents the considerable advantage of allowing the scalability of the network while maintaining the infrastructure simple and affordable. An additional range information may be made available at the expense of either an increased complexity of the system for the design of a dedicated two-way communication protocol or a higher cost required by the use of synchronised atomic clocks on both the network beacons and the target [150, 176, 191].

It is worth to note that the target depth, measured on-board the target itself, can be sent within the transmitted acoustic packet. This way, the localisation can be reduced to a planar problem and the vehicle depth measured by the onboard pressure sensor can be used as an additional information exploitable by the implemented estimator systems. This signal is sufficiently accurate not to require an external system based on acoustics for validation. Moreover, it is worth to highlight that the indirect measurement of depth from pressure is not affected by the typical phenomena to be considered when dealing with acoustics, *e.g.* multipath.

7.2 The Bearing-only localization problem modelling and related methods

A 2D localization problem with bearing-only measurements taken by three sensors is considered. A typical analysis of this problem can be found in [71]. The general bearing-only localization problem is depicted in Figure 7.1, where $\mathbf{X}$ is the target of the problem (*i.e.* the vehicle under test). Its dynamics is described by the state vector $\mathbf{X}(k) = [x(k)\ y(k)\ \dot{x}(k)\ \dot{y}(k)]^T$, containing the coordinates and velocities along the two axes (with the superscript T denoting vector transpose operation). The target

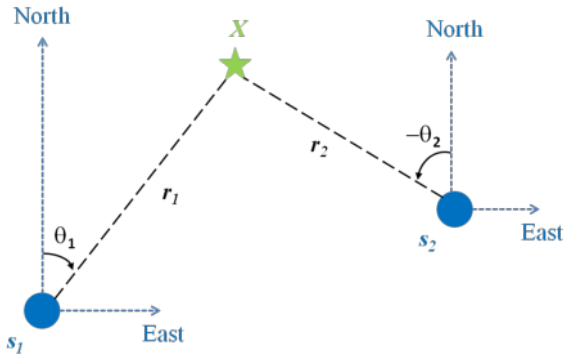

Figure 7.1: *Geometry of the considered bearing-only localization problem.*

behaviour can be expressed through the discrete-time Wiener velocity model [17]:

$$\mathbf{X}(k) = \begin{bmatrix} 1 & 0 & \Delta t & 0 \\ 0 & 1 & 0 & \Delta t \\ 0 & 0 & 1 & 0 \\ 0 & 0 & 0 & 1 \end{bmatrix} \mathbf{X}(k-1) + \mathbf{q}(k-1) \tag{7.1}$$

where Δt is the sampling period, and $\mathbf{q}(k-1)$ is the zero-mean Gaussian process noise with covariance:

$$E[\mathbf{q}(k-1)\,\mathbf{q}^T(k-1)] = \begin{bmatrix} \frac{1}{3}\Delta t^3 & 0 & \frac{1}{2}\Delta t^2 & 0 \\ 0 & \frac{1}{3}\Delta t^3 & 0 & \frac{1}{2}\Delta t^2 \\ \frac{1}{2}\Delta t^2 & 0 & \Delta t & 0 \\ 0 & \frac{1}{2}\Delta t^2 & 0 & \Delta t \end{bmatrix} \sigma_Q^2$$

where σ_Q^2 is the variance of the process noise, *i.e.* the acceleration variance is assumed equal along both x and y axis.

In Figure 7.1, $\mathbf{s_i} = [x_{s_i}, y_{s_i}]^T$ with $i = \{1, 2, 3\}$ are the fixed beacons, considered to be placed at known depth in their nominal North-East positions. Note that all the plots use a NED coordinate system, as commonly done in underwater problems.

In the figure, the geometrical parameters are also shown. The range between each sensor and the target is denoted as $r_i(k) = \|[x(k), y(k)]^{\mathrm{T}} - s_i\|$, where $\|\cdot\|$ indicates the Euclidian norm of the vector. The true azimuth bearing $\vartheta_i(\mathbf{X})$ from sensor i to the target $\mathbf{X}$ is measured clockwise from the North direction and such that $\vartheta_i(\mathbf{X})$ spans over $[-\pi, \pi)$.

The noisy bearing measurement taken by the i-th sensor can be modelled as:

$$z_i(k) = h(\mathbf{X}(k), \mathbf{s_i}) + w_i(k) = \arctan\left(\frac{y(k) - y_{s_i}}{x(k) - x_{s_i}}\right) + w_i(k) \tag{7.2}$$

It is assumed that the measurements noise $w_i(k)$ is an additive white Gaussian noise (AWGN) with variance $(\sigma_W^2)_i$. Since the measurements are independent, the relative covariance matrix $\mathbf{W}$ is diagonal with components equal to the measurements noise variances. The function $\arctan(y/x)$ is the inverse tangent and represents the non-linearity of the problem. According to [24], it has been implemented through the *atan2*

function, that is the four-quadrant inverse tangent. Equations (7.1) and (7.2) can be rearranged in the following compact form:

$$\begin{aligned} \mathbf{X}(k) &= \mathbf{F}\,\mathbf{X}(k-1) + \mathbf{q}(k-1) \\ \mathbf{z}(k) &= h(\mathbf{X}(k), \mathbf{s}) + \mathbf{w}(k) \end{aligned}, \tag{7.3}$$

where $\mathbf{s} = [\,\mathbf{s}_1^T\ \mathbf{s}_2^T\ \mathbf{s}_3^T\,]^T$ and $\mathbf{z}(k) = [\,z_1(k)\ z_2(k)\ z_3(k)\,]^T$.

7.2.1 Optimal Placement of sensors

In the majority of the tracking works cited in Chapter 6, the localisation performance was not related to the UWSN geometry. The problem of geometry optimisation is widely elaborated in the recent literature [24,105,142] typically employing the Cramer-Rao Lower Bound (CRLB), that is proportional to the inverse of the Fisher Information Matrix (FIM), to obtain the optimal sensor placement geometry. A remarkable experimental analysis has been described in [153] where surface nodes change their geometrical configuration to enhance the localisation performance of an AUV performing underwater tasks. These CRLB-based optimisation methods has an inherent gap in the hypothesis of perfect knowledge of sensors position for CRLB calculation. However, such an assumption may result unacceptable for many marine applications.

In our previous works [53, 54], at least two unavoidable issues were identified:

- the sensor deployment position cannot be exactly the nominal one, due to the deployment done by operators on a boat or using a crane, and because of sensors drifting in water;
- also the measured sensor deployment position (that is different from the theoretical one) is affected by uncertainty.

In these works, both EKF and UKF tracking performance were examined with extensive Monte Carlo simulations for the bearing-only localisation problem. The main results are summarized in the next chapter.

In order to determine the optimal placement of sensors to localize the target, a metric must be defined. The starting point is the Cramer-Rao inequality, that lower bounds the covariance achievable by an arbitrary unbiased estimator (under some regularity conditions usually held) to the inverse of the FIM. Under the standard and adopted assumption of Gaussian errors, independent from X, the FIM is given by:

$$\text{FIM}(\mathbf{X}) = J_X\vartheta(\mathbf{X})^{\mathrm{T}}\Xi^{-1}J_X\vartheta(\mathbf{X}) \tag{7.4}$$

where $J_X\vartheta(X)$ is the jacobian of the measurement vector with respect to $\mathbf{X}$ and Ξ is the error covariance matrix.

When the FIM is invertible, the CRLB matrix is symmetric positive definite and its eigenvalues-decomposition determines an ellipse within which the positioning error lies with a given probability. This so-called uncertainty ellipsoid (indeed, an ellipse for bidimensional case) gives a picture of the theoretical accuracy of the estimates, and the ellipse area is a meaningful scalar measure of total uncertainty for this 2-D problem [24]. Conceptually, the determinant of the FIM is well-representative of the area of that ellipse and assuming it as the objective function to maximize has a well-proved evidence in the literature. This optimization solution is known as the *D-criterion* [203].

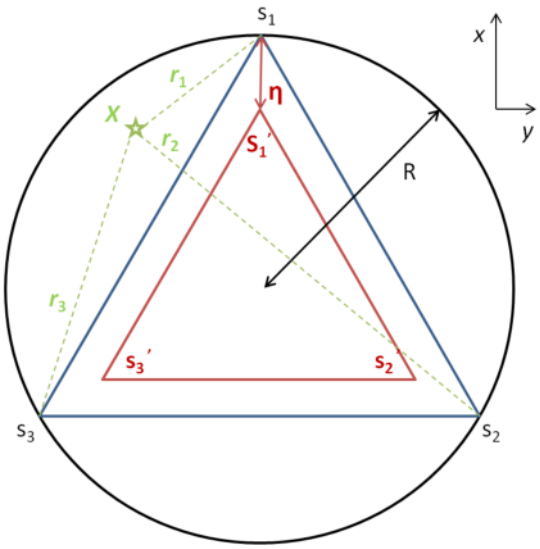

Figure 7.2: *Operational scenario, with the representation of the characteristic parameters R and η.*

To summarize, a sensors configuration is said optimal if it maximizes the FIM determinant, with defined but arbitrary sensor-target ranges. Detailed calculations can be found in [71]. More generalized expressions for the determinant are provided in [24], also for arbitrary number of sensors. As a matter of fact, we use a simplified statement of Theorem 5 in latter reference, used for the specific scenario considered for the UTR:

Theorem 1. *Consider the bearing-only localization problem with $\varphi_i, i \in 1,2,3$ denoting the angular positions of the sensors. Then, the following are equivalent expressions for the FIM determinant for bearing-only localization:*

$$\det(\textit{FIM}) = \frac{1}{\sigma_\varphi^4} \sum_s \frac{\sin^2(\varphi_j - \varphi_i)}{(r_i r_j)^2}, \tag{7.5}$$

$$\det(\textit{FIM}) = \frac{1}{4\sigma_\varphi^4} \left[\left(\sum_{i=1}^{3} \frac{1}{r_i^2} \right)^2 - \left(\sum_{i=1}^{3} \frac{\cos(2\varphi_i)}{r_i^2} \right)^2 - \left(\sum_{i=1}^{3} \frac{\sin(2\varphi_i)}{r_i^2} \right)^2 \right] \tag{7.6}$$

where $s = \{\{i,j\}\}$ is the set of the three pairs $\{i,j\}$ with $i,j \in \{1,2,3\}$ and $j > i$.

The positions of the three sensors are fixed in an equiangular (and thus equilateral) triangular configuration, recalling the purpose of this work is to set up a deployable underwater test range, without implementing sensor motion coordination algorithm at the moment. This appealing angular placement maximizes the FIM determinant in the case of equal sensor-target ranges (*i.e.* when the target is at the center of the operational area in our scenario): equivalent proofs are presented in [23, 24].

Starting from this crucial theoretical fact, we defined a common parameter for all the sensors, called η, as the oriented distance from the bound of the operational area to each vertex of the triangle (Figure 7.2). This way, it is possible to calculate the best scenario $S(R,\eta)$ such that the FIM determinant is above a chosen threshold ψ over the entire operational area, *i.e.* $99.73\,\%$ of estimated target positions lie within 5 meters around the real target positions. The best values of range R and distance η calculated

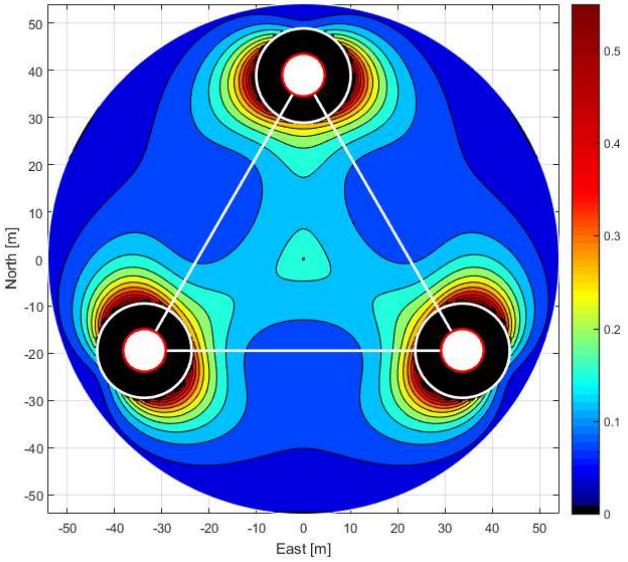

Figure 7.3: *Contour plot of the determinant of the FIM, in m^{-2}. Notice the performance degradation in the zone behind the sensors. White contoured areas represent the Sensor Uncertainty Areas (SUAs). For proper comparison and simulation repeatability, the threshold on the FIM determinant was $\psi = 0.039\, m^{-2}$.*

by means of simulations, were $(R, \eta) = (54\,\text{m}, 15.12\,\text{m})$. The defined scenario, shown in Figure 7.3 with the respective determinant contour plot, maximizes the effective operational area with the chosen threshold ψ.

In order to set realistic conditions, we defined a Sensor Uncertainty Area (SUA) forbidden for the vehicle, due to the uncertainty in sensors deployment and to safety reason (*e.g.* collision avoidance). The SUA is equal for each sensor and is defined as a circular area of radius $10\,\text{m}$ around them. In this first conservative approach, we have equally weighted the contribution of uncertainty in sensors placement (*i.e.* by people from a boat, or using a crane) and the contribution of maneuvering capacity of a typical AUV. Nevertheless, further studies would allow tuning the SUA with respect to these two parameters.

7.3 Application of the EKF and UKF to the bearing-only localization problem

Given the non-linearity of the system in (7.3), the defined bearing-only localisation problem was addressed with two extensions of the Kalman Filter to the non-linear case.

First, an EKF-based implementation was developed in [53]. The EKF approximates the non-linear transformation of a Gaussian-distributed variable to another Gaussian-distributed random variable using a Taylor series–based transformation. The most common is the first order EKF, which linearises the non-linear transformations and uses their Jacobian matrices in the prediction and/or in the update steps. The EKF is widely disseminated and relatively easy to implement when, as in our case, is available *a priori* the closed form of the Jacobian matrices. Despite these facts, it has some demonstrated

disadvantages [114]:

1. Its inherently linear approximation produces reliable results only when also the error propagation can be well approximated by a linear function. If this is not true, the performance of the filter can be extremely poor and it may diverge.
2. There are real cases where Jacobian matrices do not exist.

In order to try to overcome these issues and inspired by the work of [212], the presented UTR was implemented also with an UKF in [54]. The UKF uses the UT to approximate the non-linear transformation of the original distribution to a Gaussian one [113, 114]. The first step of the UT is a deterministic choice of a fixed number of sigma points, which *exactly* capture (at least) the mean and covariance of the original distribution of $\mathbf{X}(k)$. This is not always true for the Taylor series–based approximation underlying the EKF. Then, the sigma points are propagated through the non-linear transformation to estimate the moments of the resulting variable. Another advantage of UT over the Taylor series–based approximation is that it can well catch the higher order moments of the transformed variable as analysed in [114]. In addition, no Jacobian matrices are needed, making UT suitable also in case of functions with discontinuities.

The implemented UKF algorithm is greatly inspired by the work of Wan and Van Der Merwe [212]. The problem of estimating the position of the target can be expressed in the following form more convenient for UKF approach. Suppose that the target estimated position, at a certain sample time k, is $\hat{\mathbf{X}}(k-1|k-1)$ and its estimated covariance is $P(k-1|k-1)$. The prediction step of the UKF starts with the choice of a set of sigma points $\mathbf{X_i}(k-1)$, so that their sample mean and sample covariance coincide with the estimated ones. Recalling that five sigma points are necessary and sufficient for our bidimensional problem [114], the choice of their places at each iteration is done according to the following scheme (sample time k is omitted for the sake of clarity):

$$\begin{aligned} \mathbf{X_0} &= \hat{\mathbf{X}} \\ \mathbf{X_i} &= \hat{\mathbf{X}} + \left(\sqrt{(2+\lambda)P}\right)_i, i = 1,2 \\ \mathbf{X_{i+1}} &= \hat{\mathbf{X}} - \left(\sqrt{(2+\lambda)P}\right)_i, i = 1,2 \end{aligned} \tag{7.7}$$

where λ is a scaling parameter defined as: $\lambda = \alpha^2(2+\gamma) - 2$, with $\alpha \in (0,1], \gamma \geq 0$. The term $\left(\sqrt{(2+\lambda)P}\right)_i$ is the i-th column of the matrix square root of $(2+\lambda)P$ calculated via singular value decomposition.

In addition, specific weights are associated with each sigma point (where superscript (m) denotes a weight for mean value calculation, while (c) denotes a weight for covariance and cross-covariance calculation):

$$\begin{aligned} W_0^{(m)} &= \lambda/(2+\lambda) \\ W_i^{(m)} &= [2(2+\lambda)]^{-1} = W_{i+2}^{(m)}, i = 1,2 \\ W_0^{(c)} &= W_0^{(m)} + (1-\alpha^2+\beta), \beta \in \mathbb{R}_{>0} \\ W_i^{(c)} &= W_{i+2}^{(c)} = W_i^{(m)} = W_{i+2}^{(m)}, i = 1,2 \end{aligned} \tag{7.8}$$

The (m)-weights can be positive or negative but their sum must be equal to 1 in order to provide an unbiased estimate [114].

It is important to recall that the choice of the scaling parameters α, β, γ can make the UKF diverge if not properly set, and only some *rules-of-thumb* are provided in the existing literature [112,212]. Indeed, $\beta = 2$ was set in our UKF since it is demonstrated its optimality for Gaussian distributions in [114]. α and γ were set heuristically to 1 and 0, respectively, according to previous experience of the authors [5, 7].

Once obtained the sigma points $\mathbf{X_i}(k-1)$, along with their relative weights, they undergo the process function. At this point, the weighted mean $\hat{\mathbf{X}}(k|k-1)$ and the covariance matrix $P(k|k-1)$ are calculated to compute the new sigma points $\mathbf{X_i}(k|k-1)$ using (7.7). Then, each $\mathbf{X_i}(k|k-1)$ is instantiated through the nonlinear measurement function in (7.2) to yield the set of transformed sigma points $\mathbf{Y_i}(k|k-1)$. The transformed points mean $\hat{\mathbf{Y}}(k|k-1)$ will be the weighted average of the transformed points, while their covariance $S(k)$ is the weighted outer product of the transformed points and the cross-covariance $C(k)$ is calculated between $\mathbf{X_i}(k|k-1)$ and $\mathbf{Y_i}(k|k-1)$.

To complete the correction step of the estimate, computation of the filter gain $K(k)$, the updated state mean $\hat{\mathbf{X}}(k|k)$ and covariance $P(k|k)$ are calculated:

$$\begin{aligned} K(k) &= C(k)S(k)^{-1} \\ \hat{\mathbf{X}}(k|k) &= \hat{\mathbf{X}}(k|k-1) + K(k)[\mathbf{Y(k)} - \hat{\mathbf{Y}}(k|k-1)] \\ P(k|k) &= P(k|k-1) - K(k)S(k)K(k)^{\mathrm{T}} \end{aligned} \tag{7.9}$$

Notice that no Jacobian matrices were calculated, making UKF applicable also to functions with discontinuities.

7.3.1 Correct use of angle measurements with UKF

Each of the considered bearing-only sensor gives an angle measurement between $[-\pi, \pi)$, *i.e.* values not belonging to an Euclidean space. Special care must be put in adding, subtracting and averaging angular variables [25]. For this reason, it is very important to wrap angles sums or differences to the interval $[-\pi, \pi)$. Furthermore, given N angles α_i between $[-\pi, \pi)$, their average is defined as $\bar{\alpha} = \mathrm{atan2}(s_N, c_N)$, where the arguments are the mean cosine and the mean sine of the angles:

$$c_N = \frac{1}{N}\sum_{i=1}^{N}\cos(\alpha_i) \qquad\qquad s_N = \frac{1}{N}\sum_{i=1}^{N}\sin(\alpha_i) \tag{7.10}$$

CHAPTER 8

Simulative results

In this chapter, both EKF and UKF tracking performance are examined with extensive Monte Carlo simulations for the bearing-only localisation problem. First, a static target and three sensors placed in uncertain locations were simulated. The analysis of the results (see Section 8.1) shows that the two filters demonstrated equivalent performance in the operative area, confirming the need of other methods to counteract the uncertainty in sensor positions. Indeed, UKF provides better results in the area nearby the sensors, where the FIM presents its minima.

The assumption of a static target enables to generally characterise the reachable performance over the operative area, independently from the kinematics or the dynamics of the vehicle under test. From this benchmark result, an important advance is the conception of standard trajectories to properly evaluate AUVs navigation skills (*i.e.* manoeuvring target problem), as presented in Section 8.2. In order to correctly estimate its position, the AUV must travel along sufficiently informative trajectories. In the literature several ways of determining optimal trajectories are presented; the approach followed in this work is based on the choice of the trajectory that maximises the FIM determinant of the specific localisation problem as commonly done for both range-only and bearing-only tracking problems [71, 147, 161].

In Section 8.3 the simulative results are recapped and two important remarks are made.

8.1 Static target

The (constant) state vector $\mathbf{X}(k) = [x(k)\ y(k)]^{\mathrm{T}}$ defines the static vehicle location in Cartesian coordinates. The state transition matrix is therefore a 2-by-2 identity matrix.

The simulation was firstly run over all the operational grid assuming the nominal

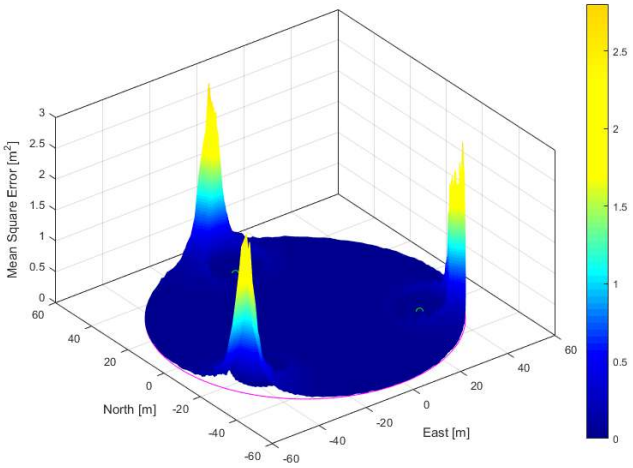

Figure 8.1: *Mesh of the MSE in the nominal case, in m², for the EKF. Notice the function is considerably sharpe (high values only in the area behind the sensors). Numerically, about* $95\,\%$ *of MSE in the nominal case was caused by the bias.*

sensors position. For each point of the grid, that represents all the possible static target positions, the tracking process was applied for localization estimation until the determinant of the covariance matrix $P(k)$ converges to zero (*i.e.* 10^{-5} threshold assumed for simulations). Without loss of generality, the initial estimated position for both filters is calculated according to simple geometric triangulation using the first set of 3 noisy measurements by the sensors. The estimated covariance matrix is initialized as:

$$P(0) = \begin{bmatrix} (r_{\text{op}}/3)^2 & 0 \\ 0 & (r_{\text{op}}/3)^2 \end{bmatrix} \tag{8.1}$$

where r_{op} is the considered operational range. In other words, we just assume the error in the initial estimated vehicle's position could not be greater than r_{op}.

The static simulation results with nominal sensors positions set a benchmark for the performance obtainable with the filters, in terms of Mean Squared Error (MSE) (Figure 8.1), recalling that:

$$\text{MSE}(\mathbf{X_e}(k)) = trace(\text{Var}(\mathbf{X_e}(k))) + \|\text{bias}(\mathbf{X_e}(k), \mathbf{X}(k))\|^2 \tag{8.2}$$

where $\mathbf{X_e}(k)$ is the estimated position and $\text{Var}(\mathbf{X_e}(k))$ is the covariance matrix of the estimator.

To reliably determine the error, those metrics were calculated with Monte Carlo simulation consisting of 100 runs for every point. After this benchmark simulation, the analysis of the perturbation effect on localization algorithm was carried out. As explained in Section 7.2.1, the SUAs were modelled as circular areas around the sensors positions. Then, we picked 1000 sets of perturbated sensors positions from a Gaussian distribution with zero mean and standard deviation σ_{unc} such that $3\,\sigma_{\text{unc}}$ equals to $5\,\text{m}$ (*i.e.* the simulated sensors positions lie in a circle of radius $5\,\text{m}$ around nominal sensors position).

For each sensors configuration, the filters were run over all the operational grid and the error statistics were calculated. In the update step of the filters the nominal sensors

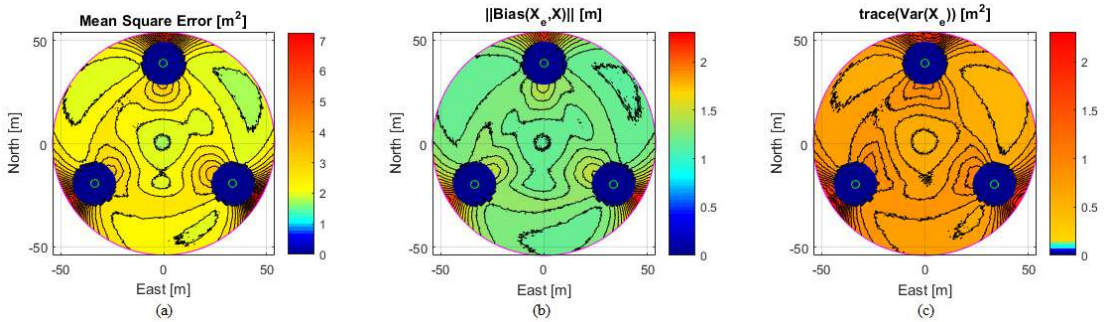

Figure 8.2: *This figure illustrates the simulative results underlying the effect of sensor positions uncertainty. The SUAs are represented by blue circles around nominal sensor positions. For proper comparison, the colormap is the same of the nominal case (*i.e. *gold corresponds to the nominal maximum values). In (a), the contour plot of the MSE over the operational area is shown. In the perturbed case, MSE is mostly above the maximum MSE in the nominal case everywhere. In (b), the contour plot of the norm of the estimation bias is given. Note that the minimum of the bias is about* $1\,m$ *for the perturbed case, while is almost null for the nominal case. In (c), the contour plot of the trace of the covariance matrix represents the spread of the estimated target position with respect to its actual position. The estimation is like to be unconfident if the uncertainty in sensor positions is not considered.*

position is considered to correct the target localization. The final simulative comparison was obtained averaging those error statistics (MSE, trace of covariance and bias) over the 1000 random sensors configuration and comparing them with respect to the nominal case.

In the depicted localization scenario, the vehicle position takes all the possible values (x, y) on the operational grid. The operational area $S(R, \eta)$ was simulated over a polar grid (ρ, φ) with 200 samples for the range $(0 \leq \rho \leq R)$ and 180 samples for the angle $(0 \leq \varphi \leq 2\pi)$. The standard deviation of the noise on the bearing measurements is $0.05\,\text{rad}$ (about 3 degrees) according to previous field experiments with suitable USBL modems [57].

In Figure 8.2, contour plots of the total MSE, the bias norm, and the trace of the covariance matrix in the perturbed case are given for the EKF. For proper comparison, the color scale used in the nominal case is preserved (*i.e.* gold corresponds to the maximum values of the nominal case). The bias norm in the perturbed case has a maximum value of about $2.3\,\text{m}$ versus $1.6\,\text{m}$ in the nominal case. In fact, despite its simplicity, the major shortcoming of EKF in bearing-only localization is the high estimation bias. This problem has been studied to some extent in the target localization literature with a multitude of approach as in [70, 129]. As it can be noticed, the trace of the covariance increase significantly with respect to the nominal case, up to an order of magnitude higher, with a maximum of $2.29\,\text{m}^2$ versus $0.12\,\text{m}^2$ of the nominal case.

Through a direct comparison, the perturbed MSE results greater over the whole area with respect to the nominal one because of the sum of the two mentioned effects. The core statistics are listed in Table 8.1 (all values are in square meters). The influence of the sensors positions uncertainty on the localization performance appears to be significant for the proposed bearing-only problem, recalling that a variance on sensors placement uncertainty of $2.78\,\text{m}^2$ produces a maximum perturbed MSE of $4.8\,\text{m}^2$ above the nominal case. This degradation mainly invalidates the estimation of the target position

Table 8.1: *Statistical comparison between nominal and perturbed case for EKF. All values are in square meters. Sensors placement uncertainty variance is* $2.78\,m^2$.

Parameter	Statistics	Nominal case (m^2)	Perturbed case (m^2)
Mean Square Error	Max value	2.8038	7.6082
	Min value	0.0027	1.9974
	Mean value	0.0401	2.5133
	Standard dev.	0.1316	0.3765
Square of bias norm	Max value	2.7506	5.4098
	Min value	0.0021	1.4497
	Mean value	0.0345	1.7646
	Standard dev.	0.1282	0.2577
Trace of covariance matrix	Max value	0.1228	2.2949
	Min value	0.0002	0.5419
	Mean value	0.0056	0.7487
	Standard dev.	0.0045	0.1212

if not taken into proper account.

Applying the UKF algorithm (Section 7.3) to the proposed static problem means that the sigma points $\mathbf{X_i}(k-1)$ remain the same (*i.e.* the process matrix is the identity matrix). Again, the calculation of the benchmark for the localization performance obtainable using UKF is done in the same way as for EKF. Then, the sensor positions uncertainty is modeled and the localization performance is compared with the nominal case.

For the nominal case, the statistics show better performance for the UKF especially in terms of accuracy: the norm of the UKF bias is about the half of the EKF case. Nevertheless, the focus of our analysis is to understand the effect of imperfect sensors position on the estimation performance and to verify if the two proposed approaches succeed in managing this unavoidable issue. Then, in Figure 8.3, contour plots with the same color scale show the distributions of the norm mean bias for both filters in the perturbed case. As it can be seen, the UKF does not significantly suffer from the perturbation effect and keeps the bias below $25\,\text{cm}$ in the operative area surrounded by the sensors, while the bias was the principal weakness for the EKF in the perturbed case. It is especially interesting to notice that the range of bias values for the UKF is less than a half of the EKF, resulting in more predictable performance over the entire operational area.

In Figure 8.4, the trace of the covariance matrix is presented for both filters. As expected, the UKF provides a better moments matching than EKF, resulting in an effectively better estimation almost over the whole area. Results show that the UKF is clearly characterized by a lower variance. Although the covariance matrix is not diagonal in general, its trace defines the total estimate uncertainty along the principal axes. This means that, also in the perturbed case, the UKF determines more precise target position estimates than the EKF.

Moreover, to propose an explicit and direct comparison, the average error statistics were compared on a point-by-point base to understand how much the UKF overperforms the EKF in the stated problem over the entire operational grid. The effective simulated operational area (*i.e.* without the SUAs) is about $8600\,\text{m}^2$. In roughly $6400\,\text{m}^2$

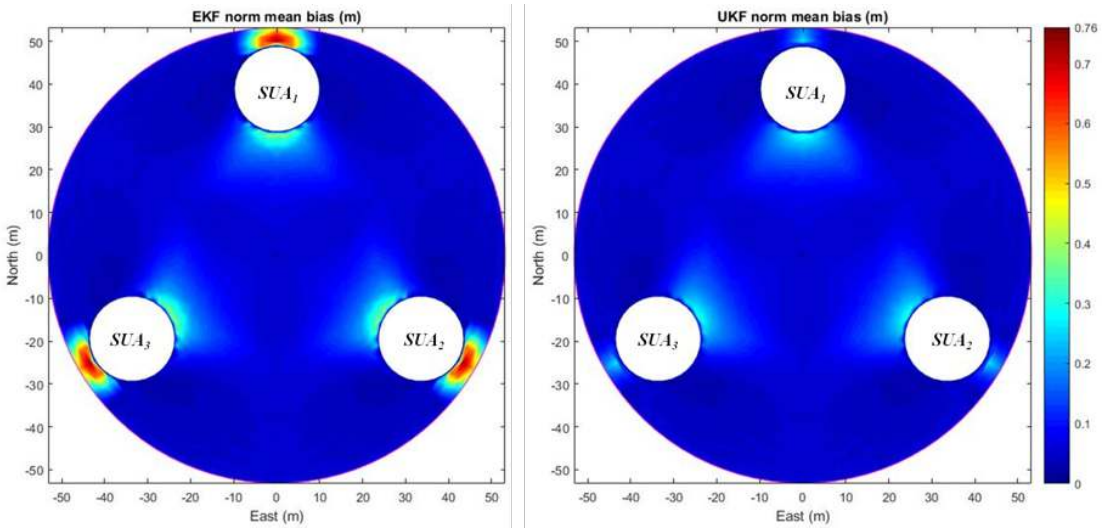

Figure 8.3: *Contour plot of the norm of the EKF (left) and UKF (right) estimate mean bias in the perturbed case, in meters. The EKF bias is below* $0.4\,m$ *almost over all the grid, except from areas around the sensors where it doubles. The worst UKF error is* $0.3\,m$*, reached only in negligible areas.*

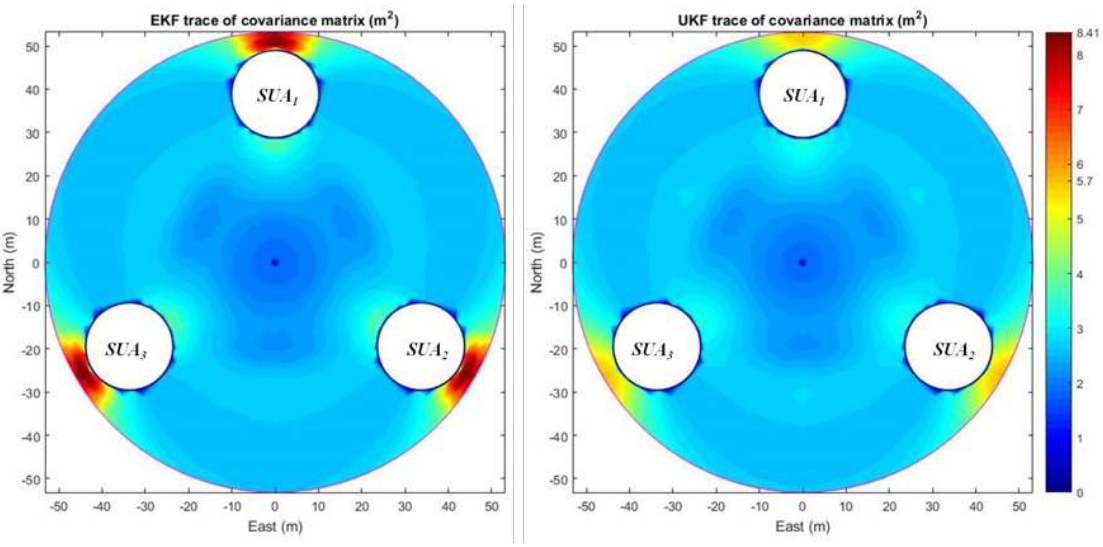

Figure 8.4: *Contour plot of the EKF (left) and UKF (right) trace of the covariance matrix, in square meters, in the perturbed case. Critical areas for the EKF remain bounded around the sensors. Values below* $3\,m^2$ *are attained in the major part of the operational area for the UKF.*

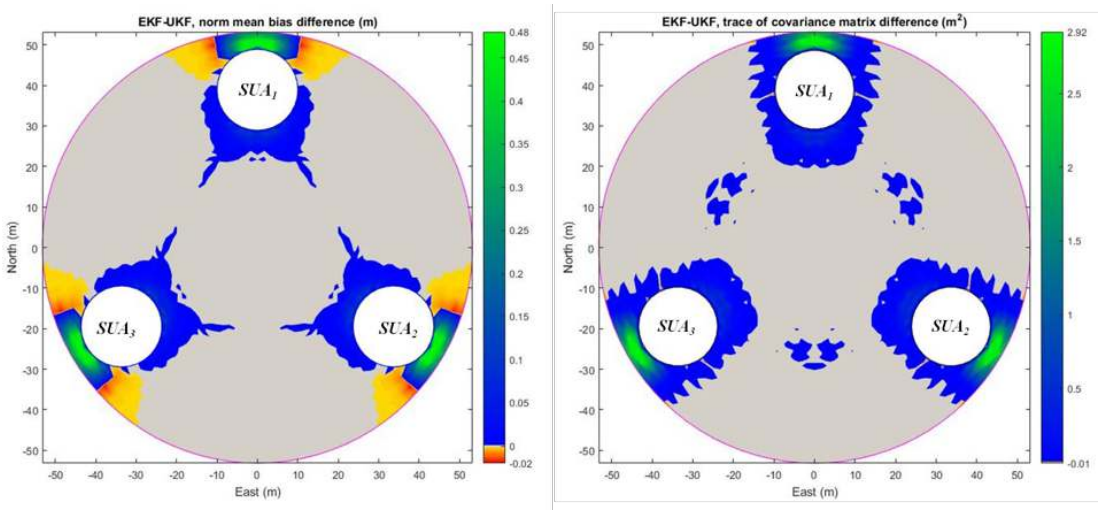

Figure 8.5: *Point-by-point comparisons of the norm of the mean bias (left) and the trace of the covariance matrix (right). In cold coloured areas, the EKF performs worse than the UKF. Vice versa, in hot coloured areas the EKF achieves slightly better values. In grey areas the filters are equivalent.*

the filters present almost equivalents results, *i.e.* the difference between them is below $1\,\text{mm}$ for the bias and $1\,\text{mm}^2$ for the trace of the covariance matrix. In the remaining area, the UKF mean bias norm is lower than the EKF one in the 95% of the cases. Looking at the covariance error matrix trace, the UKF is better than the EKF in the 99% of the area. Figure 8.5 shows in cold colours the area where UKF overcomes EKF. The grey areas represent the zones where the filters are considered equivalents.

To sum up, this analysis shows that over a significant part of the operational area the UKF has better performance than the EKF in the perturbed case. It is worth to note that it is especially true where the bearing-only problem presents the minima of FIM [24]. The UKF might be preferred to the EKF in bearing-only localization to contrast the imperfect knowledge of underwater sensors position, corroborating the hypothesis.

8.2 Moving target

The benchmark localisation performance obtainable using EKF and UKF is evaluated on the basis of the simulative framework established before, which is straightforward to extend to the case of a mobile target.

The depicted localisation scenario is shown in Figure 8.6a. The fixed reference frame adopted is a NED coordinate system with the origin located on the surface in one of the three sensors position. The nominal sensor positions (indicated with black circles) define a triangular area representing the *operative area* of the UTR, which is bounded with dashed green lines. Notice that these positions do not respect the best possible geometry stated in Section 7.2.1, *i.e.* an equilateral triangle shape. Indeed, this suboptimal simulated configuration matches the delimited marine area where the experimental tests presented in Chapter 9 were carried out. The target vehicle is moving on a straight path (solid black line) at $2\,\text{kn}$ ($1.03\,\text{m/s}$). Moreover, the process and measurement noise variances, respectively σ_Q^2 and $(\sigma_W^2)_i$, are chosen accordingly to authors' experience. In particular, σ_Q^2 is set to $0.01\,\text{m}^2/\text{s}^4$ due to the experimental ev-

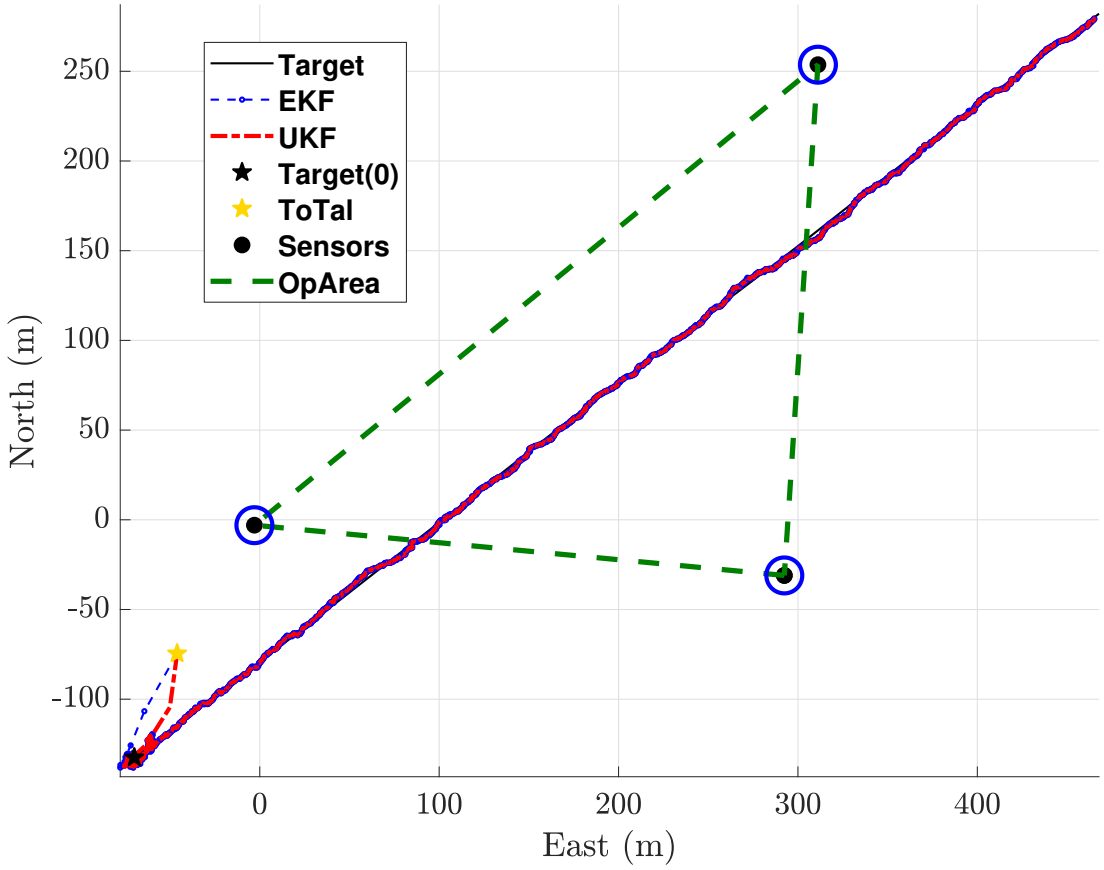

(a)

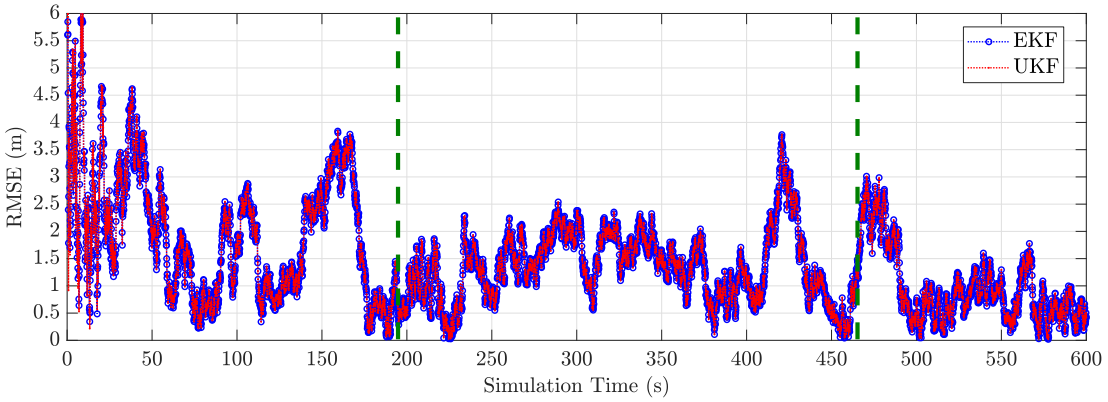

(b)

Figure 8.6: *Simulation of the UTR in the case of a mobile target. (a) Scenario considered for the simulation. The target trajectories estimated by EKF and UKF are represented with blue and red dashed lines, respectively. It can be noticed that they are almost perfectly superposed. (b) RMSE on the estimated target position in metres, averaged over 1000 Monte Carlo simulations. The colormap is the same as above. After about 20 s, the RMSE difference between the two filters is negligible.*

idence of the vehicle capability to keep a fixed speed during the sea trials. $(\sigma_W^2)_i$ is set to $0.0025\,\text{rad}^2$ for each sensor $\mathbf{s_i}$ as it emerged from the analysis in [57] and already done for the static target case. In addition, an initialisation phase is needed for the proposed algorithms. Specifically, the EKF requires a good initialisation to avoid divergence [129]. The initial estimated position for both filters is calculated according to state-of-the-art triangulation algorithm, known as ToTal (Three object Triangulation algorithm) [169], that works in the whole plane and for any bearing-only sensor ordering. The authors propose also a reliability measure of the triangulation result that can be used to initialize the Kalman filters covariance matrix.

The comparison between the two filters is carried out in terms of the Root Mean Squared Error (RMSE) averaged over 1000 random sensors configurations picked from a Gaussian distribution with zero mean and three standard deviation equals to $5\,\text{m}$ (*i.e.* same as the simulated SUAs for static target). These SUAs are represented by blue circles around each nominal sensor position (black). For each sensors configuration, we run the filters over the test path, considering the nominal positions in the update step. The orange star represents the filters' initialisation, while the black star is the actual starting point of the target. Finally, the EKF and UKF estimated trajectories are marked with blue and red dashed lines, respectively. The two filters perform equivalently in the operative area with a RMSE below $1.4\,\text{m}$, and it seems that there are not strong reasons to prefer one over the other (Figure 8.6b).

8.3 Conclusions and remarks

In this chapter, the first simulative approach in the development of an UTR is presented. Firstly, the effect of the mismatch between ideal and real network sensors location was illustrated with extensive simulations. In practical applications, the perfect sensor positions are not available, and the filters performance degradation was quantified. As shown in Section 8.1, the localization Mean Squared Error is dramatically increased when perturbated sensor positions are considered (the simulated perturbed results are about one order of magnitude worse than in the nominal case, with a peak MSE above $7.5\,\text{m}^2$ considering a simulated sensors placement uncertainty variance of $2.78\,\text{m}^2$). This shows the worthiness of the analysis proposed when approaching a real-world estimation scenario.

Then, the effectiveness of the UKF in bearing-only target localization in presence of unknown sensors position is shown through a precise comparison with the EKF performance. Comprehensive simulative analysis, considering a bearing measurements noise variance coherent with previous authors experience, confirm the improvement obtainable using UKF instead of EKF in estimating the position of a cooperative target. The UKF is marginally affected by the perturbation effect with respect to the EKF: its bias is always below $30\,\text{cm}$ and its covariance matrix trace is considerably less than the EKF one. Our evaluations indicate that an UKF-based filter offers better performance than EKF in both ideal and realistic assumptions on a localization UWSN.

Finally, the EKF and UKF performance are evaluated for the mobile cooperative target case in Section 8.2. The two filters perform almost equivalently in the operative area with a RMSE below $1.4\,\text{m}$.

Two final remarks must be considered about the simulative results obtained:

1. In the real experiments, one of the sensors was mounted on a drifting buoy (Subsection 9.1.2), a condition not simulated in the presented results;

2. The simulated measurement data were synchronised among them, *i.e.* three new measurement are available each sampling time $\Delta T = 0.1\,\mathrm{s}$. Moreover, no outliers were simulated, which is far from being realised in the real scenario (Section 9.2).

CHAPTER 9

At-sea experimentation of bearing-only tracking algorithms

This chapter describes the first in field experiments for the conceived measurement network. In particular, the experimentation was conducted during the NATO CMRE CommsNet17 sea trials, exploiting the use of the CMRE Littoral Ocean Observatory Network (LOON) [13]. The LOON is a permanent test bed developed by the CMRE with the objective to foster research on underwater communications and networking. During CommsNet17 [168], three USBL acoustic modems were deployed, one installed in the LOON and two added for the UTR testing. This enabled the tracking of an ASV, equipped with Differential GPS as position ground truth.

Results show the performance of the proposed UTR in a challenging marine environment due to low depth, surrounding structures and sources of magnetic disturbances characterising the experimentation area. Indeed, the RMSE of the estimation carried out by both EKF and UKF was below $10\,\mathrm{m}$ in all experimental tests. The analysis here described is to be considered an early step towards a reliable tracking system that may be used in the future,*e.g.* to compare different navigation approaches, to evaluate the performance of different vehicles or to quantitatively assess the impact of the temporary or permanent lack of a sensor on the overall navigation capabilities.

This chapter is organised as follows. Section 9.1 reports the overall experimental set-up and at-sea trials, emphasising the involved autonomous assets and the algorithm implementation. Experimental results of the proposed UTR are thus detailed in Section 9.2, where different error statistics are reported and discussed. Finally, conclusions and future works are drawn in Section 9.3.

9.1 UTR at CommsNet17: experimentation description

CMRE is a very active player in the underwater communications domain, jointly working with academia and industry toward a future of underwater full interoperability, system optimisation, and persistent maritime presence.

In this framework, the CommsNet17 experimentation followed the previous CommsNet and Rapid Environmental Picture (REP) series of experiments [14,33,41,64,191]. The main objective of these series of trials is to test and evaluate at sea the performance of software, algorithms and protocols developed by CMRE for the creation of *ad-hoc*, reliable, robust and secure underwater networks. Additionally, this kind of trials is usually open to external collaborators and academia to foster joint research and activities. CommsNet17 [168] was organised by CMRE and held from November 27$^{\text{th}}$ to December 6$^{\text{th}}$, 2017. The experimental campaign took place in the Gulf of La Spezia (Italy), inside the CSSN military base (where CMRE is hosted).

A network consisting of eleven nodes was deployed, including static and mobile assets. The LOON was used as the network backbone [13]. During CommsNet17, SEALab participated in the communications and networking activities. In particular, two additional acoustic modems with USBL capability were integrated within the LOON as bearing-only sensors. The two additional USBL modems, together with the one already installed on the LOON, provided the possibility to experimentally evaluate the proposed UTR through a post-processing analysis. This way, it would be possible to derive a reference performance for further comparison after subsequent UTR developments and with respect to the CMRE tracking solutions.

This section provides the details of the different assets involved in the UTR experimentation with information on the LOON facility and on the additional devices integrated to complete the scenario.

9.1.1 LOON description

The LOON consists of four bottom-mounted tripods (M1, M2, M3 and M4), with distances between nodes ranging from about $250\,\text{m}$ to $700\,\text{m}$. Each tripod is equipped with different acoustic modems (Woods Hole Micro-Modem and EvoLogics S2C medium frequency - $18/34\,\text{kHz}$ - modem). The tripods are cabled to a shore command and control station that provides data connection and power supply. The LOON includes also various environmental sensors, *i.e.* a thermistor chain, sound speed sensors, an Acoustic Doppler Current Profiler (ADCP) for wave measurement, and a meteorological station. These sensors are used to correlate the performance of the investigated protocols with the characteristics of the acoustic channel. The four LOON nodes are installed on the sea bottom at depth of about $10\,\text{m}$. The acoustic modems are installed at about $1.5\,\text{m}$ from the sea bottom facing upwards (Figure 9.2a). Only the EvoLogics acoustic modems were involved in the framework of the experimental activity related to the described work. In particular, M3 is the only LOON node with USBL capability and it was used as one of the three involved bearing-only sensors (from now on, it is referred as *USBL-M3*). A calibration procedure was run in the past to identify its orientation with respect to a NED frame. The identified relative orientation is used to derive the bearing data from the DoA measurements. Data are shared with the LOON Command and Control Station through the cable link available for this node. A satellite view of

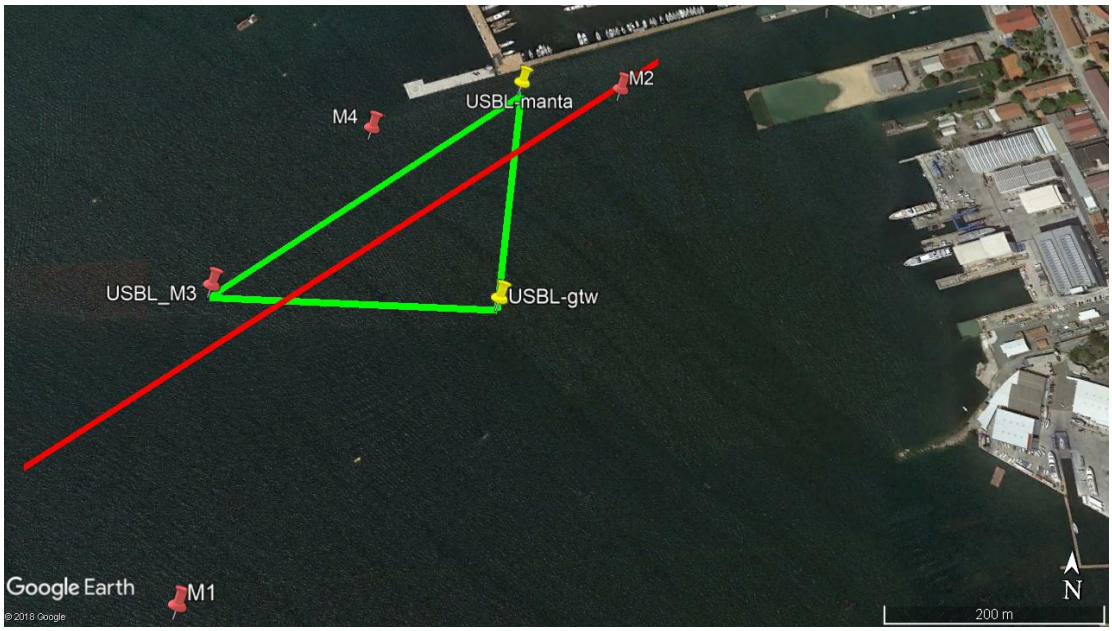

Figure 9.1: *The scenario of the presented sea trials, where the green triangle represents the operative area defined by the sensors and the desired target test path is marked in red (Google Earth image, accessed on 26th September 2018)*

the experimental area is displayed in Figure 9.1.

9.1.2 Additional assets

Besides the LOON, the additional assets composing the UTR used in the experimental activity described in this work are:

Portable drifting USBL buoy (*USBL-gtw*) An EvoLogics S2CR 18/34 USBL modem was mounted on an easily deployable drifting buoy (Figure 9.2d), developed by CMRE, equipped with a commercial GPS (1 Hz data rate). The USBL modem was deployed at a depth of about 7.5 m facing upwards. Through cable connection the USBL measurements were acquired by a Single Board Computer (SBC), integrated on the buoy, within a watertight canister. The SBC was connected to a Wi-Fi antenna on the dry part of the buoy. By means of a Wi-Fi link, data were transmitted to the LOON Command and Control Station for real-time monitoring. The orientation of the USBL was estimated in real-time through an AHRS fixed to it. This signal was used to compute the bearing data from the USBL DoA measurements. All the measurements with the associated time-stamp were logged both on the SBC and onshore for post processing analysis.

Manta with USBL (*USBL-manta*) Another EvoLogics S2CR 18/34 USBL modem, fixed on a tripod facing upwards (Figure 9.2b), was connected to a Manta gateway system (Figure 9.2c) and deployed from the pier. Although in a fixed pose, the USBL-manta was deployed only for the time of the described test. Thus, a calibration procedure to derive the orientation of the sensor was not performed. As for the USBL-gtw, the orientation of the USBL was estimated in real-time through an AHRS fixed to it. This signal was used to compute the bearing data

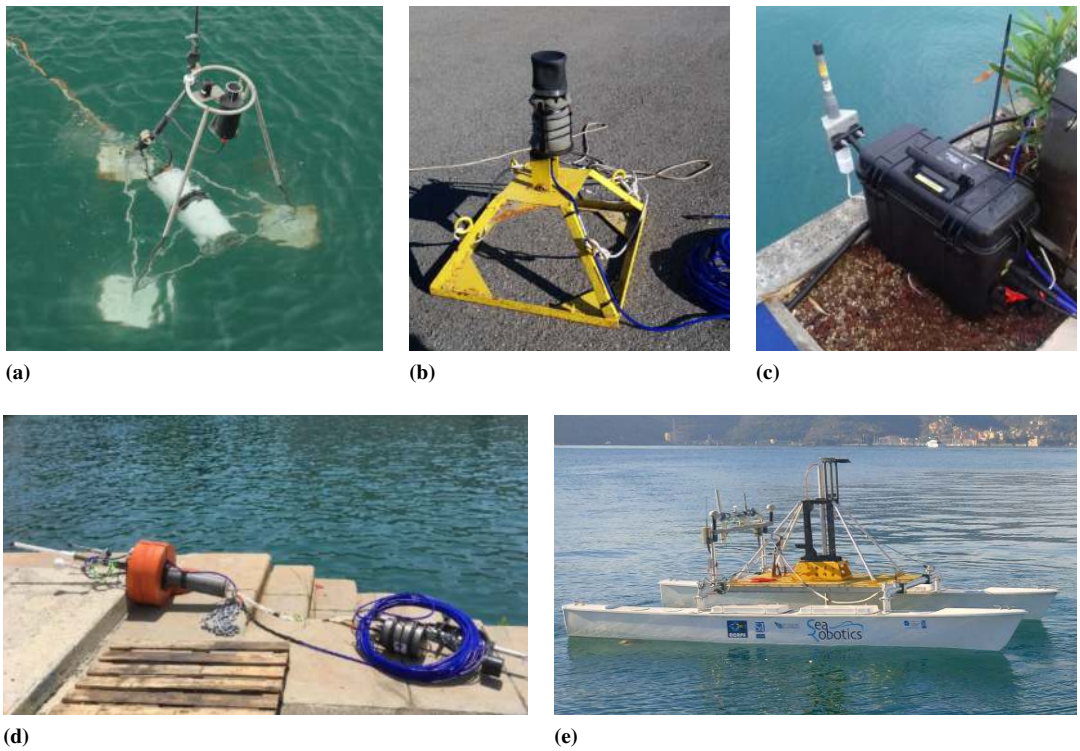

Figure 9.2: *The assets involved in the experimentation. (a) One of the LOON modem tripods. (b), (c) and (d) Additional measurement assets involved in the experimentation. In particular, (b) and (c) show the USBL-manta components, whereas (d) illustrates the USBL-gtw. (e) Gulliver ASV used as target vehicle.*

from the USBL DoA measurements. The Manta includes radio connectivity (Wi-Fi 2.4 GHz) and an embedded board to run locally the required software. By means of Wi-Fi connection, acquired measurements are shared with the LOON Command and Control Station.

The vehicle used as target to be tracked by means of the deployed UTR is described in the following:

Gulliver ASV The vehicle is a 5.7 m length autonomous catamaran, developed by the CMRE from a Sea Robotics ASV (Figure 9.2e). Its weight is about 350 kg, it has two fixed 2 kW electric thrusters (differential steering, 24 VDC, digital interface) and it has an endurance up to 18 h at 4 kn. In addition to the SeaRobotics' standard navigation sensors, Gulliver ASV is equipped with:

- a Novatel© SMART-V1 DGPS system (10 Hz data rate), designed for harsh environments and capable of a horizontal position accuracy of 20 cm (RMSE reported in the data sheet);
- attitude sensors, a dual GPS heading measurement system, and a yaw rate sensor;
- a MicroStrain's 3DM-GX1 IMU;
- Teledyne RD Instruments' Phased Array Explorer DVL;
- Blueview Forward Looking Sonar (FLS) P450-130 with a Field of View (FOV) of 130 deg and working at 450 kHz;
- CMRE *in-house* developed Short BaseLine (SBL) system.

For this specific experimentation, Gulliver ASV was equipped with an EvoLogics acoustic modem compatible with the USBL ones composing the UTR system. The modem is installed on a rigid structure at a depth of about 1.5 m facing downwards, and it was controlled to send messages at different rates (between 1 and 1.3 packet per seconds).

Gulliver ASV was moving according to different paths (*e.g.* lawn mower, spiral around sensors). The path of interest for the assessment of the proposed system is shown in red in Figure 9.1. It was travelled at different constant speeds (between 1 kn and 2 kn). The length of the path ranged between 500 m and 700 m corresponding to test durations from 600 s to 1200 s.

The geographic location of LOON (red pins) with the additional SEALab USBL modems (yellow pins) is shown in Figure 9.1. Precise measurements of the LOON modem absolute positions are available and have been exploited for offset calibration.

The USBL-manta node was deployed close to the pier for practical convenience, while USBL-gtw was installed on a drifting buoy to optimise the geometry of the sensors with respect to localisation accuracy [24].

However, it is worth to notice that the UTR geometry for the described experimentation was slightly different from the envisioned one, *i.e.* the optimal equilateral triangle configuration, because of the operational constraints coming from La Spezia port authority.

Table 9.1: *Bias and standard deviation $(\sigma_W)_i$ calculated via the calibration for each USBL.*

UTR node	Bias (rad)	$(\sigma_W)_i$ (rad)
USBL-gtw	0.072	0.047
USBL-M3	0.004	0.014
USBL-manta	0.002	0.006

9.2 Experimental Results Analysis and Discussions

In this section, two separate analyses are presented as the sea trial had a double goal. First, a characterisation of the deployed sensors based on dedicated experiments with particular emphasis on real scenario issues. Then, performance evaluation of the described tracking algorithms is carried out. The modelling of the BOT problem is the one formally defined in previous chapters for the manoeuvring target case. Nonetheless, it is important to recall that some simulative conditions reported in Chapter 8 are not valid at sea.

First of all, an offset calibration procedure was needed for each USBL modem to identify bias affecting bearing measurements and to characterise sensors noise, exploiting the knowledge of LOON static nodes absolute positions. Hours of bearing measurements from the LOON nodes have been collected by the three USBL modems for the purpose. Per each USBL, the bias has been calculated by comparing the average of the bearing measurements with the respective ideal values (*i.e.* the bearing expected exploiting the knowledge of LOON static nodes absolute position). In addition, the variance of the error has been computed. The two quantities have been exploited for the experimental evaluation of the tracking algorithms and the values for each USBL are reported in Table 9.1. In particular, the bias was used to compensate all the measurements whereas the variances determine the diagonal components of filters $\mathbf{W}$ matrix (Equation (7.2)).

It is worth to note that the identified values are different for each sensor. In fact, error sources affecting the measurements include declination between magnetic north (used by the USBL internal AHRS) and true north (*e.g.* about $2.6\,^\circ$ in La Spezia area in December 2017), the inherent noise of the USBL modem and the uncertainty on their actual positions due to GPS error (nominal uncertainty of 5 m characterises the receiver installed on the two additional USBL).

In Figure 9.3 the raw bearings observations taken by the three USBL modems are reported for one specific trial. It can be noticed the presence of spurious measurements. In the whole experimental campaign a percentage of measurements outliers between $2\,\%$ and $7\,\%$ was reported. In the presented experimental trial, the outliers percentages were $6.89\,\%$, $5.47\,\%$, and $2.12\,\%$ respectively for USBL-gtw, USBL-M3 and USBL-manta. These outliers are likely due to multipath phenomena and other acoustic propagation effects. In fact, the harbour environment of the experimentation area is far from ideal with respect to an underwater acoustics point of view. The presence of commercial shipping and the very shallow water (depth minor than 15 m) significantly affect the quality of the acoustic channel.

In that scenario, it becomes difficult to discern between the direct arrival and multipath interference, and the rejection of outliers becomes a key issue [205]. The method

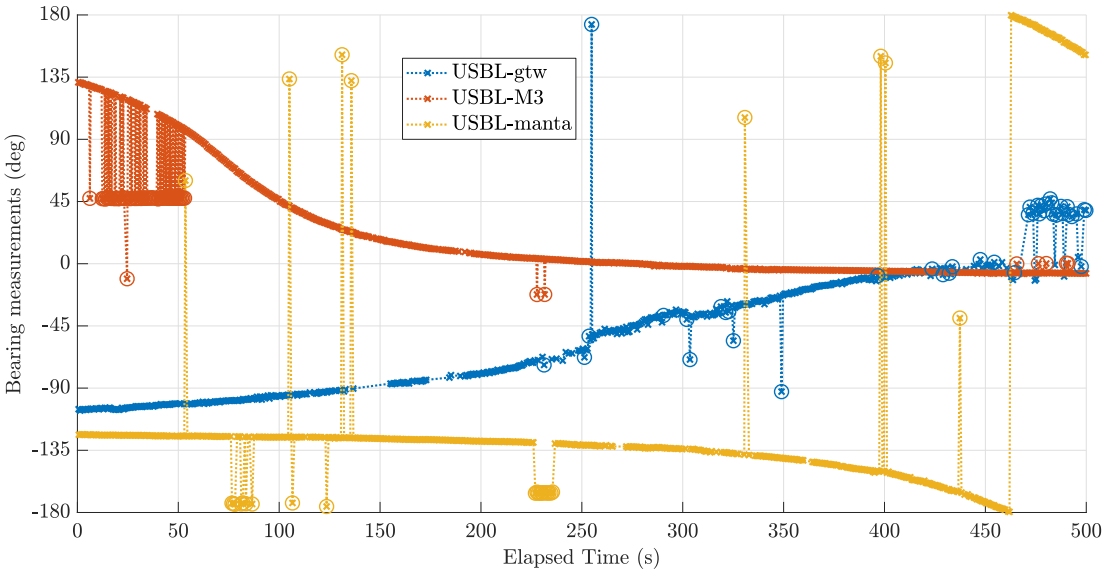

Figure 9.3: *Bearing measurements obtained from the three USBL modems. Remark that the UTR nodes were enclosed between two piers during CommsNet17 experimentation in shallow water. Given that scenario, a reasonably high number of outliers were identified for all modems (circles in the plot).*

implemented here for the identification of the outliers was based on the knowledge of the kinematics of the vehicle, *i.e.* test path and speed. Those measurements that present a difference between successive samples inconsistent with the expected length traveled by the ASV were filtered out.

An important issue regarding the measurements availability must be considered for both the filters in the experimental implementation of the UTR. In fact, the acoustic data received at each sample time are not predictable due to the intentional absence of a synchronisation protocol. Hence, the actual size of the measurement vector $\mathbf{z}(k)$ for the filter update phase changes from time to time: since the USBL receives packets at different instants, a sampling time $\Delta T = 0.1\,\mathrm{s}$ has been fixed for the filters - as in the simulative case - and the sensors are checked for a new measurement at each ΔT. If none is available, the corresponding component of $\mathbf{z}(k)$ is excluded, and the size of the sensor noise covariance matrix $\mathbf{W}$ is adjusted according to it.

Therefore, it is worth to underline that at each iteration the prediction step is executed whereas the correction one is calculated only if a new measurement arrived during last period ΔT. The maximum error on the measurement time thus corresponds to $0.1\,\mathrm{s}$. In the current implementation this is not compensated. Synchronism compensation will be addressed in the coming implementations of the system by encoding the transmission timestamp in the ping. Moreover, considering the irregularity of acoustic measurements, the ToTal initialisation is done as soon as possible, *i.e.* when at least one measurement is taken from each sensor.

The UTR performance is characterised through the RMSE, the estimated covariance matrix trace, and the absolute velocity estimation error. The ground truth for the filters estimates is given by the DGPS data collected on board of Gulliver ASV. Ten runs of the path presented in Section 9.1 were performed, while the plots reported here are referred to one representative scenario. Inspired by the work of [71, 147, 161], the

trajectory of the Gulliver ASV was chosen as the optimal to maximise the determinant of the FIM of the specific bearing-only localisation problem as calculated in [53]. This approach is valid under the assumption of efficient estimation algorithm, *i.e.* with an error covariance matrix close to the CRLB [116]. Moreover, using the FIM simplifies the analysis as it is demonstrated that the maximization of its determinant over different sensor positions is equivalent to minimizing the RMSE [71].

Figure 9.4a shows the estimated trajectories provided by both EKF and UKF, along with the DGPS trajectory and the positions of the sensors. The origin of the NED frame is the USBL-M3 position. In particular, the black line represents the Gulliver ASV DGPS fixes, that in this work it is assumed as the ground truth. The dotted lines represent the estimated trajectories by the EKF and UKF, respectively in blue and red. The red square is the M3 node of LOON network, whereas in yellow USBL-manta (square) and USBL-gtw (triangle) measured positions are reported. The green dashed triangle connecting them represents the operative area. Finally, the starting point of the real trajectory and the ToTal initialisation are marked with black and orange stars, respectively.

Together with the estimated trajectories, the RMSE is reported over the entire path in Figure 9.4b with the same colour convention used for the algorithms. The green dashed bounds identify the operative area as defined in Subsection 8.2. The mean RMSE in that area is 6.95 m, and it differs by 1 mm among the filters, which was already defined as *equivalence condition* in [54]. Looking at all the tests, the RMSE changes between 6.5 m and 8.0 m with no remarkable differences between the filters.

The Kalman filters provide a confidence index of the estimation, that is the covariance matrix $\mathbf{P}$ of the estimation error. From Figure 9.5, the determinant of covariance matrix $\mathbf{P}$ is bounded between $0.4\,\text{m}^2$ and $1.8\,\text{m}^2$. The instants of determinant decrease are associated to correction steps of the filters.

Figure 9.6 shows the Euclidean norm of the estimated velocity of the target compared with the DGPS measured speed. In the initial 20 s the error reaches its maximum at 5 m/s. Then, despite the simple kinematic model used, both the algorithms present an error of the velocity estimate that never exceeds $\pm\ 0.34$ m/s.

For completeness, it was noted that augmenting σ_Q by orders of magnitude has a negligible effect on UKF performance, while it makes the EKF diverge. This remark needs further analysis, but it seems a hint of superior skills of the UKF against scenarios for which the dynamical model is almost completely unknown. This may be the interesting case of non-cooperative target.

9.3 Conclusion and future works for the UTR implementation

This chapter describes a first experimental assessment of a tracking system for underwater vehicles based on bearing-only sensors, where the estimation of target trajectory is performed via a non-linear Kalman filtering approach. With roots in previous simulative results [53,54], it has to be considered a fundamental intermediate step in the development of an easily deployable facility for the V&V of AUV navigation systems.

In the framework of CommsNet17 experimentation, the activities included a first deployment of the envisioned system. This allowed an extended acquisition of bearing-only data from a mobile target by means of three USBL modems, confirming that

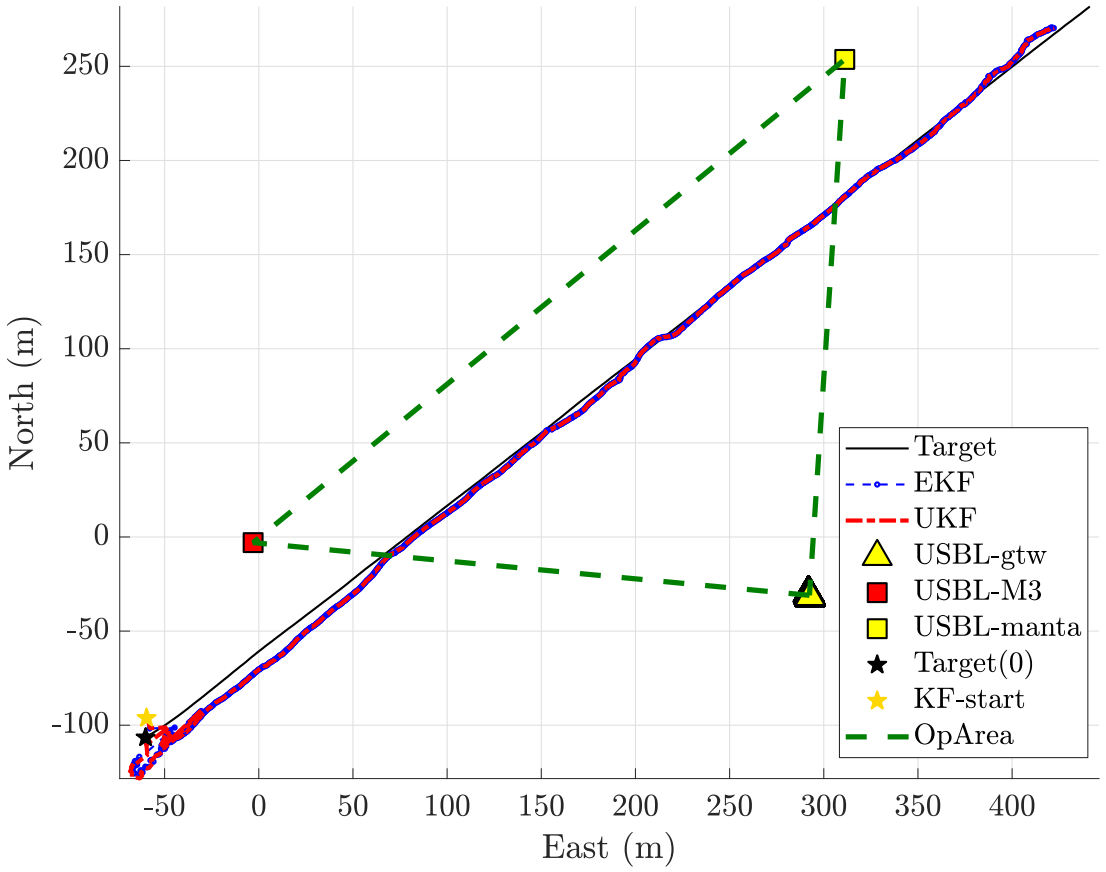

(a)

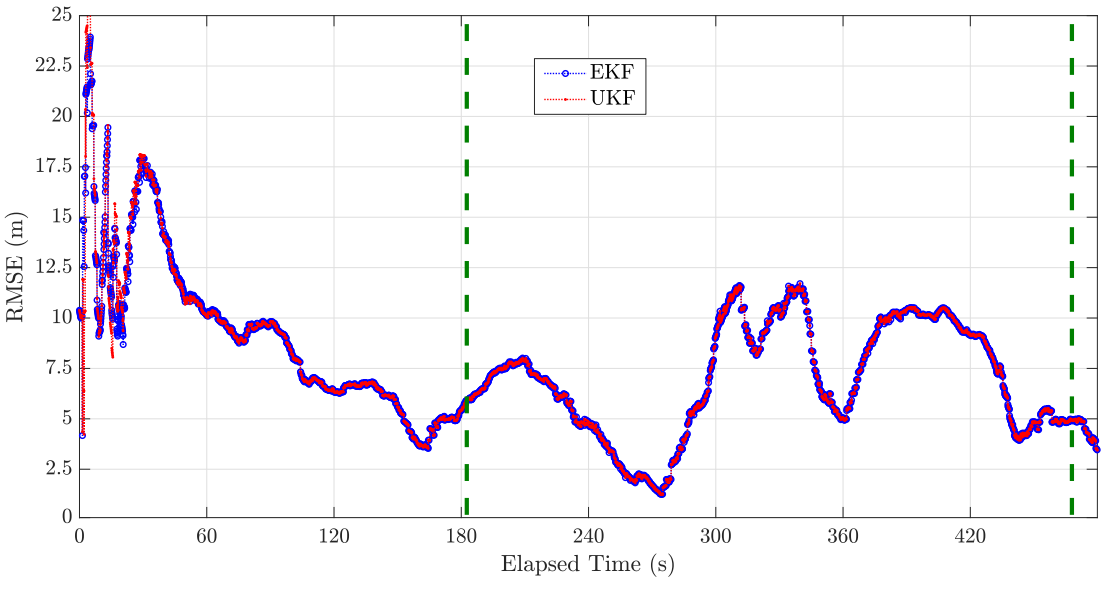

(b)

Figure 9.4: *Above, the estimated ASV trajectories with both filters. The EKF (blue) and the UKF (red) tracks are almost superposed and well estimate the trajectory measured by the DGPS on Gulliver ASV (black). The stars represent the starting point of the target (black) compared to the filters initialisation (orange). Below, the Root Mean Squared Error of the estimates. In both figures, the operative area is bounded by green dashed lines.*

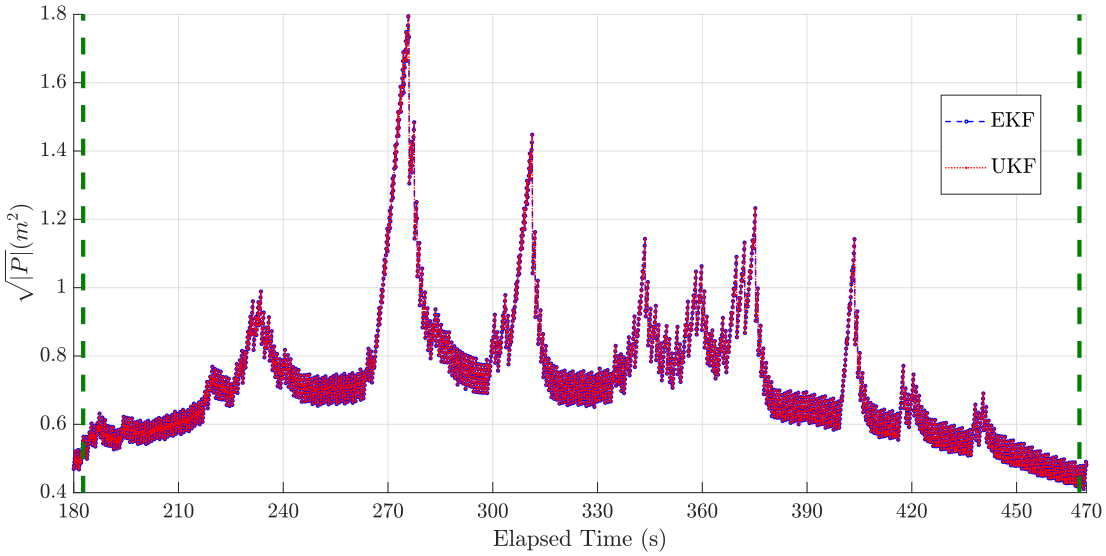

Figure 9.5: *Square root of the covariance matrix determinant in the operative area in m^2. This metric gives a measure of estimation confidence for both filters.*

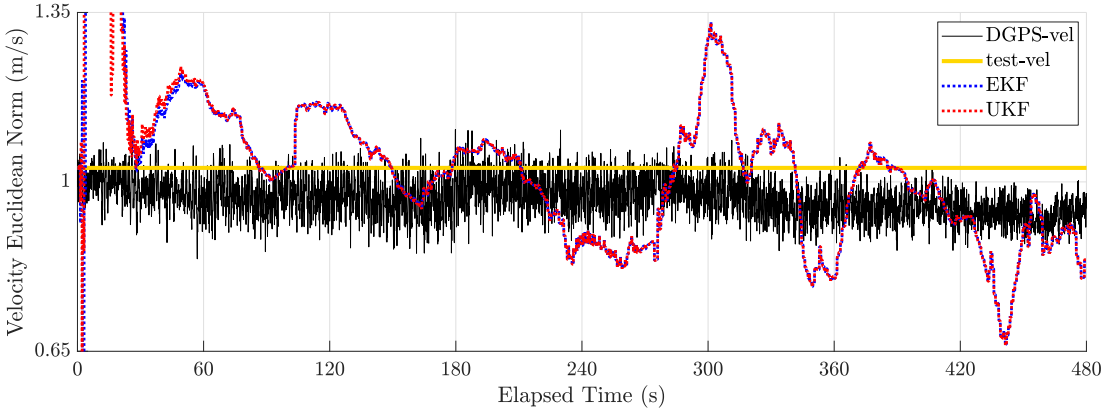

Figure 9.6: *The Euclidean norm of the estimated target velocity. In orange, the speed desired for the specific test (1.03 m/s). In the first 20 s, not shown here for clarity, the maximum error was 5 m/s.*

the conceived system provides frequent measurements at the same time. A trajectory ground truth is available as the target is a surface vehicle (Gulliver ASV) mounting a very accurate DGPS (error < 20 cm from data sheet).

Data processing included an initial phase of system calibration and sensors characterization. Results of this step are an essential base for the further carried out analysis and for the future of this research activity. Quantitative evaluation of tracking performance was fulfilled for the several trials. Details related to one of them, as representative results, are reported and discussed.

Future work will continue along the research path towards the described vision perspective. In particular, following steps will aim to extend the results presented in this paper using moving sensor platforms that can operate in deeper water. This forthcoming improvement will allow optimal geometry control for tracking performance maximisation. Side by side, the results need to be extended to a generic N sensors network in order to verify whether network scalability can mitigate the perturbation effect.

Furthermore, the performance obtainable with respect to the specific physical parameters of USBL modems used as bearing-only sensors (*e.g.* beamwidth, frequency and bandwidth) will be evaluated.

The smoother counterparts of the presented filters will also be investigated. The tracking resulting from the *smoothing* approach is based on all the measurements, *i.e.* the outcome is a smoothed estimate of the *history* of the filter state.

Finally, it is under preliminary study a distributed approach exploiting range measurements between USBL sensors and the AUV under test [60, 151]. This capability may be integrated with the existing bearing-only tracking and it would imply the design of proper MAC policy to ensure the sharing of the acoustic channel between the different sensors [191].

These future extensions fall in the broader vision of designing an UTR with enhanced capabilities.

Bibliography

[1] I. H. Abbott and A. E. Von Doenhoff. *Theory of wing sections, including a summary of airfoil data*. Courier Corporation, 1959.

[2] P. Agrawal and J. M. Dolan. Colregs-compliant target following for an unmanned surface vehicle in dynamic environments. In *2015 IEEE/RSJ International Conference on Intelligent Robots and Systems (IROS)*, pages 1065–1070, Sept 2015.

[3] M. S. Allahparast, S. Allahparast, and C. Laschi. An improved tracking algorithm for underwater vessels using the passive sonar. In *Control Conference (ICC), 2016 Indian*, pages 426–431. IEEE, 2016.

[4] B. Allen, R. Stokey, T. Austin, N. Forrester, R. Goldsborough, M. Purcell, and C. von Alt. Remus: a small, low cost auv; system description, field trials and performance results. In *Oceans '97. MTS/IEEE Conference Proceedings*, volume 2, pages 994–1000 vol.2, Oct 1997.

[5] B Allotta, A Caiti, L Chisci, R Costanzi, F Di Corato, C Fantacci, D Fenucci, E Meli, and A Ridolfi. An unscented kalman filter based navigation algorithm for autonomous underwater vehicles. *Mechatronics*, 39:185–195, 2016.

[6] B. Allotta, A. Caiti, R. Costanzi, F. Di Corato, D. Fenucci, N. Monni, L. Pugi, and A. Ridolfi. Cooperative navigation of auvs via acoustic communication networking: field experience with the typhoon vehicles. *Autonomous Robots*, 40(7):1229–1244, 2016.

[7] B. Allotta, A. Caiti, R. Costanzi, F. Fanelli, D. Fenucci, E. Meli, and A. Ridolfi. A new AUV navigation system exploiting unscented Kalman filter. *Ocean Engineering*, 113:121 – 132, 2016.

[8] B. Allotta, F. Fanelli, N. Monni, C. Petrioli, L. Picari, A. Ridolfi, and D. Spaccini. Enabling cooperation and networking in heterogeneous underwater networks composed of multi-vendor vehicles and modems. In *OCEANS 2017-Aberdeen*, pages 1–7. IEEE, 2017.

[9] A. Alvarez, A. Caffaz, A. Caiti, G. Casalino, E. Clerici, F. Giorgi, L. Gualdesi, and A. Turetta. Design and realization of a very low cost prototypal autonomous vehicle for coastal oceanographic missions. In *IFAC Proceedings Volumes*, volume 37, pages 471 – 476, 2004. IFAC Conference on Computer Applications in Marine Systems - CAMS 2004, Ancona, Italy, 7-9 July 2004.

[10] A. Alvarez, A. Caffaz, A. Caiti, G. Casalino, E. Clerici, F. Giorgi, L. Gualdesi, A. Turetta, and R. Viviani. Folaga: A very low cost autonomous underwater vehicle for coastal oceanography. In *IFAC Proceedings Volumes*, volume 38, pages 31 – 36, 2005. 16th IFAC World Congress.

[11] A. Alvarez, A. Caffaz, A. Caiti, G. Casalino, L. Gualdesi, A. Turetta, and R. Viviani. Fòlaga: A low-cost autonomous underwater vehicle combining glider and auv capabilities. *Ocean Engineering*, 36(1):24 – 38, 2009. Autonomous Underwater Vehicles.

[12] J. Alves, P. Oliveira, R. Oliveira, A. Pascoal, M. Rufino, L. Sebastiao, and C. Silvestre. Vehicle and mission control of the delfim autonomous surface craft. In *2006 14th Mediterranean Conference on Control and Automation*, pages 1–6, Ancona, Italy, June 2006.

[13] J. Alves, J. Potter, P. Guerrini, G. Zappa, and K. Lepage. The LOON in 2014: Test bed description. In *Proceedings of Underwater Communications and Networking Conference 2014 (UComms 2014)*, Sestri Levante, Italy, Sep 2014.

[14] J. Alves, J. Potter, G. Zappa, P. Guerrini, and R. Been. A testbed for collaborative development of underwater communications and networking. In *Proceedings of MILCOM 2012 - IEEE Military Communications Conference*, pages 1–8, Orlando, FL, USA, Oct 2012.

[15] G. Antonelli. *Underwater robots*. Springer Publishing Company, Incorporated, 3rd edition, 2013.

[16] A. Bahr, J. J Leonard, and M. F. Fallon. Cooperative localization for autonomous underwater vehicles. *The International Journal of Robotics Research*, 28(6):714–728, 2009.

[17] Y. Bar-Shalom, X R. Li, and T. Kirubarajan. *Estimation with applications to tracking and navigation: theory algorithms and software*. J. Wiley & Sons, 2004.

[18] Behzad Bayat, Naveena Crasta, Alessandro Crespi, António M. Pascoal, and Auke Ijspeert. Environmental monitoring using autonomous vehicles: a survey of recent searching techniques. *Current Opinion in Biotechnology*, 45:76 – 84, 2017.

[19] J. G Bellingham. Autonomous ocean sampling network-ii (aosn-ii): Integration and demonstration of observation and modeling.

[20] J. G. Bellingham, C. A. Goudey, T. R. Consi, J. W. Bales, D. K. Atwood, J. J. Leonard, and C. Chryssostomidis. A second generation survey auv. In *Proceedings of IEEE Symposium on Autonomous Underwater Vehicle Technology (AUV'94)*, pages 148–155, July 1994.

[21] J.G. Bellingham, Yanwu Zhang, J.E. Kerwin, J. Erikson, B. Hobson, B. Kieft, M. Godin, R. McEwen, T. Hoover, J. Paul, A. Hamilton, J. Franklin, and A. Banka. Efficient propulsion for the Tethys long-range autonomous underwater vehicle. In *2010 IEEE/OES Autonomous Underwater Vehicles (AUV)*, pages 1–7, September 2010.

[22] V. Bertram. Unmanned surface vehicles-a survey. *Skibsteknisk Selskab, Copenhagen, Denmark*, 1:1–14, 2008.

[23] A. N. Bishop, B. Fidan, B. D. O. Anderson, K. Dogancay, and P. N. Pathirana. Optimality analysis of sensor-target geometries in passive localization: Part 1 - bearing-only localization. In *2007 3rd International Conference on Intelligent Sensors, Sensor Networks and Information*, pages 7–12, Dec 2007.

[24] A. N. Bishop, B. Fidan, B. D.O. Anderson, K. Doğançay, and P. N. Pathirana. Optimality analysis of sensor-target localization geometries. *Automatica*, 46(3):479 – 492, 2010.

[25] C. M Bishop. *Pattern recognition and machine learning*. springer Cambridge, UK, 2006.

[26] D. Blidberg, S. Mupparapu, S. Chappell, R. Komerska, JC Jalbert, and R Nitzelm. The sauv ii (solar powered auv) test results 2004. In *Oceans 2005-Europe*, volume 1, pages 545–550. IEEE, 2005.

[27] D R Blidberg. The development of autonomous underwater vehicles (auv); a brief summary. In *IEEE International Conference on Robotics and Automation (ICRA)*, volume 4, May 2001.

[28] P. Blondel. *The handbook of sidescan sonar*. Springer Science & Business Media, 2009.

[29] Schmidt H. Bovio E., Tyce R. Autonomous underwater vehicle and ocean modelling networks. In *NATO Undersea Research Centre GOATS 2000 Conference Proceedings*, 2001.

[30] J. A. Bowker, N. C. Townsend, M. Tan, and R. A. Shenoi. Experimental study of a wave energy scavenging system onboard autonomous surface vessels (ASVs). In *MTS/IEEE OCEANS 2015-Genova*, pages 1–9, May 2015.

[31] T. Bozzo, A. Caffaz, A. Caiti, G. Casalino, E. Clerici, F. Giorgi, L. Gualdesi, A. Pellegrini, A. Turetta, and R. Viviani. A very low cost prototypal autonomous vehicle for harbour monitoring and surveillance. In *International Workshop on Underwater Robotics (IWUR 2005)*, November 2005.

[32] P. Braca, P. Willett, K. LePage, S. Marano, and V. Matta. Bayesian tracking in underwater wireless sensor networks with port-starboard ambiguity. *IEEE Transactions on Signal Processing*, 62(7):1864–1878, April 2014.

[33] J. Braga, R. Martins, C. Petrioli, R. Petroccia, and L. Picari. Cooperation and networking in an underwater network composed by heterogeneous assets. In *Proceedings of MTS/IEEE OCEANS 2016*, pages 1–9, Monterey, CA, USA, September, 19–23 2016.

[34] J. L Butler and C. H Sherman. *Transducers and arrays for underwater sound*. Springer, 2016.

[35] A. Caffaz, A. Caiti, V. Calabrò, G. Casalino, P. Guerrini, A. Maguer, A. Munafò, J.R. Potter, H. Tay, and A. Turetta. The enhanced folaga: A hybrid auv with modular payloads. *Further Advances in Unmanned Marine Vehicles*, pages 309–330, 2012.

[36] A. Caffaz, A. Caiti, G. Casalino, and A. Turetta. The hybrid glider/auv folaga. *IEEE Robotics Automation Magazine*, 17(1):31–44, March 2010.

[37] A. Caiti and V. Calabrò. Control-oriented modelling of a hybrid auv. In *Robotics and Automation (ICRA), 2010 IEEE International Conference on*, pages 5275–5280. IEEE, 2010.

[38] A. Caiti, V. Calabró, S. Grammatico, A. Munafó, and M. Stifani. Lagrangian modelling of an underwater wave glider. *Ship Technology Research*, 59(1):6–12, 2012.

[39] A. Caiti, V. Calabrò, G. Dini, A.L. Duca, and A. Munafò. Secure cooperation of autonomous mobile sensors using an underwater acoustic network. *Sensors*, 12(2):1967–1989, 2012.

[40] A. Caiti, V. Calabrò, S. Grammatico, A. Munafò, and S. Geluardi. Switching control of an underwater glider with independently controllable wings. In *9th IFAC Conference on Manoeuvring and Control of Marine Craft*, volume 45, pages 194 – 199, September 2012.

[41] A. Caiti, F. Di Corato, D. Fenucci, B. Allotta, R. Costanzi, N. Monni, L. Pugi, and A. Ridolfi. Experimental results with a mixed USBL/LBL system for AUV navigation. In *Proceedings of Underwater Communications and Networking Conference 2014 (UComms 2014)*, pages 1–4, Sestri Levante, Italy, Sept 2014.

[42] A. Caiti, R. Costanzi, D. Fenucci, V. Manzari, A. Caffaz, and M. Stifani. Wave module for hybrid oceanographic autonomous underwater vehicle – prototype experimental validation and characterisation. In *International Ship Control Systems Symposium (iSCSS)*, Glasgow, Scotland (UK), October 2018.

[43] T. Camp, J. Boleng, and V. Davies. A survey of mobility models for ad hoc network research. *Wireless Communications and Mobile Computing*, 2(5):483–502, 2002.

[44] G. Canepa, A. Munafò, M. Micheli, L. Morlando, and S. Murphy. Real-time continuous active sonar processing. In *OCEANS 2015-Genova*, pages 1–6. IEEE, 2015.

[45] L. Cavaleri and M. Sclavo. The calibration of wind and wave model data in the mediterranean sea. *Coastal Engineering*, 53(7):613 – 627, 2006.

[46] T Chance, A. Kleiner, and J Northcutt. The autonomous underwater vehicle (auv): A cost-effective alternative to deep-towed technology. *Integrated Coastal Zone Management*, 2(7):65–69, 01 2000.

[47] H. Chen, S. Zhang, M. Liu, and Q. Zhang. An artificial measurements-based adaptive filter for energy-efficient target tracking via underwater wireless sensor networks. *Sensors*, 17(5), 2017.

[48] A. S. Chhetri. *SENSOR SCHEDULING AND EFFICIENT ALGORITHM IMPLEMENTATION FOR*. PhD thesis, Citeseer, 2006.

[49] R.D. Christ and R. Wernli. *The ROV Manual: A User Guide for Remotely Operated Vehicles*. Elsevier Science, 2nd edition, 2013.

[50] A. T. Chwang and T. Y. Wu. Hydromechanics of low-reynolds-number flow. part 2. singularity method for stokes flows. *Journal of Fluid Mechanics*, 67(4):787–815, 1975.

[51] M. R. Clark, A. Rowden, T. Schlacher, A. W.s, M. Consalvey, K. Stocks, A. Rogers, T. O'Hara, M. White, T. Shank, et al. The ecology of seamounts: structure, function, and human impacts. *Annual Review of Marine Science*, 2:253–278, 2010.

[52] S. Coraluppi. Multistatic sonar localization. *IEEE Journal of Oceanic Engineering*, 31(4):964–974, 2006.

[53] R. Costanzi, D. Fenucci, V. Manzari, and A. Caiti. Bearing-only AUV tracking performance: The effect of uncertainty in underwater nodes position. In *Proceedings of MTS/IEEE OCEANS 2016*, pages 1–6, Monterey, CA, USA, Sept 2016.

[54] R. Costanzi, D. Fenucci, V. Manzari, and A. Caiti. Bearing-only AUV tracking performance: Unscented kalman filter estimation against uncertainty in underwater nodes position. In *Proceedings of 20th IFAC World Congress*, pages 13674 – 13679, Toulouse, France, July 2017.

[55] R. Costanzi, D. Fenucci, V. Manzari, M. Micheli, L. Morlando, D. Natale, M. Stifani, A. Tesei, and A. Caiti. At-sea nato operational experimentation with interoperable underwater assets using different robotic middlewares. In *Technology and Science for the Ships of the Future: Proceedings of NAV 2018: 19th International Conference on Ship & Maritime Research*, page 194. IOS Press, 2018.

[56] R. Costanzi, D.e Fenucci, V. Manzari, A. Caiti, and R. Petroccia. Towards an autonomous underwater vehicles test range: At-sea experimentation of bearing-only tracking algorithms. *Annual Reviews in Control*, 2018.

[57] R. Costanzi, N. Monni, A. Ridolfi, B. Allotta, and A. Caiti. On field experience on underwater acoustic localization through USBL modems. In *Proceedings of MTS/IEEE OCEANS 2017*, pages 1–5, Aberdeen, Scotland, June 2017.

[58] J. P Costas. Medium constraints on sonar design and performance. *IEEE TRANSACTIONS ON AEROSPACE AND ELECTRONIC SYSTEMS*, 11(5), 1975.

[59] H. Cox. Fundamentals of bistatic active sonar. In Y. T. Chan, editor, *Underwater Acoustic Data Processing*, pages 3–24. Springer Netherlands, Dordrecht, 1989.

[60] N. A. Cruz, B. M. Ferreira, A. C. Matos, C. Petrioli, R. Petroccia, and D. Spaccini. Implementation of an underwater acoustic network using multiple heterogeneous vehicles. In *Proceedings of MTS/IEEE OCEANS 2012*, pages 1–10, Hampton Roads, VA, USA, October, 14–19 2012.

[61] T. B Curtin, J. G Bellingham, J. Catipovic, and D. Webb. Autonomous oceanographic sampling networks. *Oceanography*, 6(3):86–94, 1993.

[62] S. J Davey, M. G Rutten, and B. Cheung. A comparison of detection performance for several track-before-detect algorithms. *EURASIP Journal on Advances in Signal Processing*, 2008:41, 2008.

[63] S. J. Davey, M. Wieneke, and H. Vu. Histogram-pmht unfettered. *IEEE Journal of Selected Topics in Signal Processing*, 7(3):435–447, June 2013.

[64] J. B. de Sousa, J. Pereira, J. Alves, M. Galocha, B. Pereira, C. Lourenço, and M. Portuguesa. Experiments in multi-vehicle operations: The rapid environmental picture atlantic exercise 2014. In *OCEANS 2015 - Genova*, pages 1–7, May 2015.

[65] K. DeMarco, M. E West, and T. R Collins. An implementation of ros on the yellowfin autonomous underwater vehicle (auv). In *OCEANS 2011*, pages 1–7. IEEE, 2011.

[66] O. Demigha, W. Hidouci, and T. Ahmed. On energy efficiency in collaborative target tracking in wireless sensor network: A review. *IEEE Communications Surveys & Tutorials*, 15(3):1210–1222, 2013.

[67] J. Denavit and R. S. Hartenberg. A kinematic notation for lower-pair mechanisms based on matrices. *Trans. of the ASME Journal of Applied Mechanics*, 22:215–221, 1955.

[68] V. Djapic and Đ. Nađ. Collaborative autonomous vehicle use in mine countermeasures. *Sea technology*, 51(10):19, 2010.

[69] S. E. Dosso. Bayesian localization of an unknown number of ocean acoustic sources. *The Journal of the Acoustical Society of America*, 133(5):3574–3574, 2013.

[70] K. Doğançay. On the bias of linear least squares algorithms for passive target localization. *Signal Processing*, 84(3):475 – 486, 2004.

[71] K. Doğançay and H. Hmam. Optimal angular sensor separation for AOA localization. *Signal Processing*, 88(5):1248 – 1260, 2008.

[72] C. C. Eriksen, T. J. Osse, R. D. Light, T. Wen, T. W. Lehman, P. L. Sabin, J. W. Ballard, and A. M. Chiodi. Seaglider: a long-range autonomous underwater vehicle for oceanographic research. *IEEE Journal of Oceanic Engineering*, 26(4):424–436, October 2001.

[73] M. Erol-Kantarci, H.T. Mouftah, and S. Oktug. A survey of architectures and localization techniques for underwater acoustic sensor networks. *IEEE Communications Surveys and Tutorials*, 13(3):487–502, 2011.

[74] J. S. Esteves, A. Carvalho, and C. Couto. Generalized geometric triangulation algorithm for mobile robot absolute self-localization. In *Industrial Electronics, 2003. ISIE'03. 2003 IEEE International Symposium on*, volume 1, pages 346–351. IEEE, 2003.

[75] T. E. Ewart. Observations from straight line isobaric runs of spurv. In *Joint Oceanography Assembly*. Edinburgh (UK), 1976.

[76] A. Farina. Target tracking with bearings – only measurements. *Signal Processing*, 78(1):61 – 78, 1999.

[77] D. Fenucci, A. Caffaz, R. Costanzi, E. Fontanesi, V. Manzari, L. Sani, M. Stifani, D. Tricarico, A. Turetta, and A. Caiti. Wave: A wave energy recovery module for long endurance gliders and auvs. In *OCEANS 2016 MTS/IEEE Monterey*, Sept 2016.

[78] G. Ferri, M. Cococcioni, and A. Alvarez. Mission planning and decision support for underwater glider networks: A sampling on-demand approach. *Sensors*, 16(1), 2016.

[79] G. Ferri, A. Munafò, R. Goldhahn, and K. LePage. A non-myopic, receding horizon control strategy for an auv to track an underwater target in a bistatic sonar scenario. In *Decision and Control (CDC), 2014 IEEE 53rd Annual Conference on*, pages 5352–5358. IEEE, 2014.

[80] G. Ferri, A. Munafò, R. Goldhahn, and K. LePage. Results from collab13 sea trial on tracking underwater targets with auvs in bistatic sonar scenarios. In *Oceans-St. J.'s, 2014*, pages 1–9. IEEE, 2014.

[81] G. Ferri, A. Munafò, R. Goldhahn, and K. D. LePage. Towards fully autonomous underwater vehicles in asw scenarios: An adaptive, data driven auv mission management layer. In *OCEANS 2015 - Genova*, pages 1–9, 2015.

[82] G. Ferri, A. Munafo, and K.D. LePage. An autonomous underwater vehicle data-driven control strategy for target tracking. *IEEE Journal of Oceanic Engineering*, 43(2):323–343, 2018.

[83] G. Ferri, A. Munafò, A. Tesei, P. Braca, F. Meyer, K. Pelekanakis, R. Petroccia, J. Alves, C. Strode, and K. LePage. Cooperative robotic networks for underwater surveillance: an overview. *IET Radar, Sonar & Navigation*, 11(12):1740–1761, 2017.

[84] T. I. Fossen. *Marine Control Systems: Guidance, Navigation and Control of Ships, Rigs and Underwater Vehicles*. MARINE CYBERNETICS, 2002.

[85] T. I. Fossen. *Handbook of marine craft hydrodynamics and motion control*. J. Wiley & Sons, 2011.

[86] L. Freitag, M. Grund, S. Singh, J. Partan, P. Koski, and K. Ball. The whoi micro-modem: an acoustic communications and navigation system for multiple platforms. In *Proceedings of OCEANS 2005 MTS/IEEE*, pages 1086–1092 Vol. 2, Sept 2005.

[87] J. Gebbie, M. Siderius, P. L. Nielsen, and J. Miller. Passive localization of noise-producing targets using a compact volumetric array. *The Journal of the Acoustical Society of America*, 136(1):80–89, 2014.

[88] R. Georgescu and P. Willett. The gm-cphd tracker applied to real and realistic multistatic sonar data sets. *IEEE Journal of Oceanic Engineering*, 37(2):220–235, April 2012.

[89] J. Georgy and A. Noureldin. Unconstrained underwater multi-target tracking in passive sonar systems using two-stage pf-based technique. *International Journal of Systems Science*, 45(3):439–455, 2014.

[90] S. Glenn, O. Schofield, J. Kohut, J. McDonnell, R. Ludescher, D. Seidel, D. Aragon, T. Haskins, E. Handel, C. Haldeman, et al. The trans-atlantic slocum glider expeditions: A catalyst for undergraduate participation in ocean science and technology. *Marine Technology Society Journal*, 45(1):52–67, 2011.

[91] R. Grasso, P. Braca, S. Fortunati, F. Gini, and M. S. Greco. Dynamic underwater glider network for environmental field estimation. *IEEE Transactions on Aerospace and Electronic Systems*, 52(1):379–395, February 2016.

[92] G. Griffiths, J. Jamieson, S. Mitchell, and K. Rutherford. Energy storage for long endurance AUVs. In *Advances in Technology for Underwater Vehicles, Conference Proceedings*, pages 8–16. The Institute of Marine Engineering, Science and Technology, March 2004.

[93] D. J Grimmett. Automatic identification of specular detections in multistatic sonar systems. In *OCEANS 2009, MTS/IEEE Biloxi-Marine Technology for Our Future: Global and Local Challenges*, pages 1–10. IEEE, 2009.

[94] P. E. Hagen, N Storkersen, B-E Marthinsen, G. Sten, and K. Vestgard. Military operations with hugin auvs: lessons learned and the way ahead. In *Oceans 2005-Europe*, volume 2, pages 810–813. IEEE, 2005.

[95] P. E. Hagen, N. J. Storkersen, and K. Vestgard. Hugin-use of uuv technology in marine applications. In *Oceans '99. MTS/IEEE. Riding the Crest into the 21st Century. Conference and Exhibition. Conference Proceedings (IEEE Cat. No.99CH37008)*, volume 2, pages 967–972 vol.2, Sept 1999.

[96] P.E. Hagen, N. Størkersen, B. Marthinsen, G. Sten, and K. Vestgård. Rapid environmental assessment with autonomous underwater vehicles — examples from hugin operations. *Journal of Marine Systems*, 69:137–145, 01 2008.

[97] G. Hagerman. Wave energy systems for recharging AUV energy supplies. In *Proceedings of the 2002 Workshop on Autonomous Underwater Vehicles*, pages 75–84, 2002.

[98] G. Han, H. Xu, T.Q. Duong, J. Jiang, and T. Hara. Localization algorithms of wireless sensor networks: A survey. *Telecommunication Systems*, 52(4):2419–2436, 2013.

[99] A J Haug. *Bayesian estimation and tracking: a practical guide*. J. Wiley & Sons, 2012.

[100] ML Hernandez, THIA Kirubarajan, and YAAKOV Bar-Shalom. Multisensor resource deployment using posterior cramér-rao bounds. *IEEE Transactions on Aerospace and Electronic Systems*, 40(2):399–416, 2004.

[101] O. Hlinka, F. Hlawatsch, and P. M. Djuric. Distributed particle filtering in agent networks: A survey, classification, and comparison. *IEEE Signal Processing Magazine*, 30(1):61–81, 2013.

[102] B. W. Hobson, R. S. McEwen, J. Erickson, T. Hoover, L. McBride, F. Shane, and J. G. Bellingham. The development and ocean testing of an AUV docking station for a 21" AUV. In *MTS/IEEE OCEANS 2007-Vancouver*, pages 1–6, September 2007.

[103] B. Hollings, C. B. Pattiaratchi, M. Woo, and C. E. Hanson. Sustained oceanographic observations around australia using autonomous ocean gliders. In *OCEANS'10 IEEE SYDNEY*, pages 1–4, May 2010.

[104] J. M. Hovem. Underwater acoustics: Propagation, devices and systems. *Journal of Electroceramics*, 19(4):339–347, 2007.

[105] B. Huang, T. Li, B.D.O. Anderson, and C. Yu. Performance limits in sensor localization. *Automatica*, 49(2):503–509, 2013.

[106] H. Huang. Autonomy levels for unmanned systems (alfus) framework volume i: Terminology version 2.0, 2004.

[107] Y. Huang, W. Liang, H. Yu, and Y. Xiao. Target tracking based on a distributed particle filter in underwater sensor networks. *Wireless Communications and Mobile Computing*, 8(8):1023–1033, 2008.

[108] D. T Hughes. Aspects of cardioid processing, 2000.

[109] TT Jeong. Particle phd filter multiple target tracking in sonar image. *IEEE Transactions on Aerospace and Electronic Systems*, 43(1), 2007.

[110] C. Jones, E. Creed, S. Glenn, J. Kerfoot, J. Kohut, C. Mudgal, and O. Schofield. Slocum gliders—a component of operational oceanography. In *Proc. 14th Int. Symp. on Unmanned Untethered Submersible Technology*, 2005.

[111] C. P. Jones. Slocum glider persistent oceanography. In *2012 IEEE/OES Autonomous Underwater Vehicles (AUV)*, pages 1–6, Sept 2012.

[112] S. J. Julier. The scaled unscented transformation. In *American Control Conference, 2002. Proceedings of the 2002*, volume 6, pages 4555–4559. IEEE, 2002.

[113] S. J. Julier and J. K. Uhlmann. New extension of the Kalman filter to nonlinear systems. In *Proceedings of Signal processing, sensor fusion, and target recognition VI*, volume 3068, pages 182–194, Orlando, FL, USA, 1997. International Society for Optics and Photonics.

[114] S. J. Julier and J. K. Uhlmann. Unscented filtering and nonlinear estimation. *Proceedings of the IEEE*, 92(3):401–422, Mar 2004.

[115] T. Kawasaki, T. Fukasawa, T. Noguchi, and M. Baino. Development of AUV "Marine Bird" with underwater docking and recharging system. In *The 3rd International Workshop on Scientific Use of Submarine Cables and Related Technologies*, pages 166–170, June 2003.

[116] S. M. Kay. *Fundamentals of Statistical Signal Processing: Estimation Theory*. Prentice-Hall, Inc., 1993.

[117] E. Kelasidi, P. Liljeback, K. Y. Pettersen, and J. T. Gravdahl. Innovation in underwater robots: biologically inspired swimming snake robots. *IEEE robotics & automation magazine*, 23(1):44–62, 2016.

[118] S. Kim, C. Laschi, and B. Trimmer. Soft robotics: a bioinspired evolution in robotics. *Trends in Biotechnology*, 31(5):287 – 294, 2013.

[119] S. Koteswara Rao. Algorithm for detection of manoeuvring targets in bearings-only passive target tracking. *IEE Proceedings: Radar, Sonar and Navigation*, 146(3):141–146, 1999.

[120] D. W. Krout, W. Kooiman, G. Okopal, and Evan Hanusa. Object tracking with imaging sonar. In *Information Fusion (FUSION), 2012 15th International Conference on*, pages 2400–2405. IEEE, 2012.

[121] D.V.A.N. Ravi Kumar, S. Koteswara Rao, and K. Padma Raju. A novel stochastic estimator using preprocessing technique for long range target tracking in heavy noise environment. *Optik - International Journal for Light and Electron Optics*, 127(10):4520 – 4530, 2016.

[122] D.V.A.N. Ravi Kumar, S. Koteswara Rao, and K. Padma Raju. A novel stochastic estimator using preprocessing technique for long range target tracking in heavy noise environment. *Optik*, 127(10):4520 – 4530, 2016.

[123] D.V.A.N.Ravi Kumar, S.Koteswara Rao, and K.Padma Raju. Integrated unscented kalman filter for underwater passive target tracking with towed array measurements. *Optik - International Journal for Light and Electron Optics*, 127(5):2840 – 2847, 2016.

[124] Y. Kuwata, M. T. Wolf, D. Zarzhitsky, and T. L. Huntsberger. Safe maritime autonomous navigation with COLREGS, using velocity obstacles. *IEEE Journal of Oceanic Engineering*, 39(1):110–119, Jan 2014.

[125] F. Lehmann. Recursive bayesian filtering for multitarget track-before-detect in passive radars. *IEEE Transactions on Aerospace and Electronic Systems*, 48(3):2458–2480, JULY 2012.

[126] N E Leonard, D A Paley, R E Davis, D. M Fratantoni, F Lekien, and F Zhang. Coordinated control of an underwater glider fleet in an adaptive ocean sampling field experiment in monterey bay. *Journal of Field Robotics*, 27(6):718–740, 2010.

[127] K. D. LePage, R. Goldhahn, J. Alves, C. Strode, P. Braca, G. Ferri, A. Munafò, M. Oddone, J. Sildam, F. Baralli, S. Biagini, G. Canepa, M. Colombo, V. Grandi, G. Grenon, M. Mazzi, M. Micheli, G. Parisi, P. Saia, A. Vermeij, and G. Zappa. Autonomous networked anti-submarine warfare research and development at cmre. In *OCEANS 2015 - Genova*, pages 1–6, May 2015.

[128] C. C. Leroy, S. P. Robinson, and M. J. Goldsmith. A new equation for the accurate calculation of sound speed in all oceans. *The Journal of the Acoustical Society of America*, 124(5):2774–2782, 2008.

[129] D. Lerro and Y. Bar-Shalom. Bias compensation for improved recursive bearings-only target state estimation. In *Proceedings of American Control Conference 1995*, volume 1, pages 648–652 vol.1, Seattle, WA, USA, Jun 1995.

[130] X. Li, J. Martínez, J. Rodríguez-Molina, and N. L. Martínez. A survey on intermediation architectures for underwater robotics. *Sensors*, 16(2), 2016.

[131] X. Li, P. Willett, M. Baum, and Y. Li. Pmht approach for underwater bearing-only multisensor-multitarget tracking in clutter. *IEEE Journal of Oceanic Engineering*, 41(4):831–839, Oct 2016.

[132] P. Liljebäck, Ø. Stavdahl, K. Y. Pettersen, and J. T. Gravdahl. Mamba - a waterproof snake robot with tactile sensing. In *2014 IEEE/RSJ International Conference on Intelligent Robots and Systems*, pages 294–301, Sept 2014.

[133] J S Liu and R Chen. Sequential monte carlo methods for dynamic systems. *Journal of the American statistical association*, 93(443):1032–1044, 1998.

[134] Z. Liu, Y. Zhang, X. Yu, and C. Yuan. Unmanned surface vehicles: An overview of developments and challenges. *Annual Reviews in Control*, 41:71–93, 2016.

[135] J. Lloret. Underwater sensor nodes and networks. *Sensors*, 13:11782–11796, 2013.

[136] Martin Ludvigsen and Asgeir J. Sørensen. Towards integrated autonomous underwater operations for ocean mapping and monitoring. *Annual Reviews in Control*, 42:145 – 157, 2016.

[137] J. Luo, Y. Han, and L. Fan. Underwater acoustic target tracking: A review. *Sensors*, 18(1):112, 2018.

[138] F. Mandić, I. Rendulić, N. Mišković, and Đ. Nađ. Underwater object tracking using sonar and usbl measurements. *Journal of Sensors*, 2016, 2016.

[139] J. E. Manley. Unmanned surface vehicles, 15 years of development. In *OCEANS 2008*, pages 1–4, Sept 2008.

[140] J. E. Manley and S. Willcox. The wave glider: A persistent platform for ocean science. In *OCEANS 2010 IEEE-Sydney*, pages 1–5. IEEE, 2010.

[141] M. Mansouri, O. Ilham, H. Snoussi, and C. Richard. Adaptive quantized target tracking in wireless sensor networks. *Wireless Networks*, 17(7):1625, Jul 2011.

[142] S. Martínez and F. Bullo. Optimal sensor placement and motion coordination for target tracking. *Automatica*, 42(4):661–668, apr 2006.

[143] C M McKinney. The early history of high frequency, short range, high resolution, active sonar. *Echoes*, 12(2):4–7, 2002.

[144] H. Medwin and C. S. Clay. *Fundamentals of acoustical oceanography*. Academic press, 1997.

[145] F. Meyer, P. Braca, P. Willett, and F. Hlawatsch. Tracking an unknown number of targets using multiple sensors: A belief propagation method. In *2016 19th International Conference on Information Fusion (FUSION)*, pages 719–726, July 2016.

[146] D. Moreno-Salinas, A. Pascoal, and J. Aranda. Optimal sensor placement for acoustic underwater target positioning with range-only measurements. *IEEE Journal of Oceanic Engineering*, 41(3):620–643, July 2016.

[147] D. Moreno-Salinas, A.M. Pascoal, and J. Aranda. Optimal sensor trajectories for mobile underwater target positioning with noisy range measurements. In *Proceeding of 19th IFAC World Congress*, volume 47, pages 5139 – 5144, Cape Town, South Africa, 2014.

[148] A. Motwani. A survey of uninhabited surface vehicles. *Marine and Industrial Dynamic Analysis, School of Marine Science and Engineering Plymouth University, Plymouth, Tech. Rep.*, 2012.

[149] L. Mozzone, P. Lorenzelli, A. Caiti, and S. Bongi. Acoustic localization of marine crafts with multistatic deployable sonar. *5th IFAC Conference on Manoeuvring and Control of Marine Craft (MCMC 2000), Aalborg, Denmark, 23-25 August 2000*, 33(21):111 – 116, 2000.

[150] A. Munafò and G. Ferri. An acoustic network navigation system. *Journal of Field Robotics*, 34(7):1332–1351, 2017.

[151] A. Munafò, T. Furfaro, G. Ferri, and J. Alves. Supporting auv localisation through next generation underwater acoustic networks: Results from the field. In *2016 IEEE/RSJ International Conference on Intelligent Robots and Systems (IROS)*, pages 1328–1333, Daejeon, South Korea, October, 9–14 2016.

[152] A. Munafò, E. Simetti, A. Turetta, A. Caiti, and G. Casalino. Autonomous underwater vehicle teams for adaptive ocean sampling: a data-driven approach. *Ocean Dynamics*, 61(11):1981–1994, Nov 2011.

[153] A. Munafo, J. Sliwka, and J. Alves. Dynamic placement of a constellation of surface buoys for enhanced underwater positioning. In *MTS/IEEE OCEANS 2015 - Genova: Discovering Sustainable Ocean Energy for a New World*, pages 1–6. Institute of Electrical and Electronics Engineers Inc., May 2015.

[154] C.P. Newswire. Autonomous underwater vehicle market. 2017. global forecast to 2023., 2017. Last time accessed: July 2018.

[155] Department of International Economic and Social Affairs. *A Guide to Ocean Thermal Energy Conversion for Developing Countries*. United Nations, 1984.

[156] The Remotely Operated Vehicles Committee of the Marine Technology Society (MTS ROV). ROV applications - military. Last time accessed: August 2018.

[157] Department of the Navy United States of America. *The Navy Unmanned Surface Vehicle (USV) Master Plan*. US Navy Program Executive Office Littoral and Mine Warfare (PEO-LMW), Washington DC, 2007.

[158] R. Olfati-Saber. Distributed kalman filtering for sensor networks. In *Decision and Control, 2007 46th IEEE Conference on*, pages 5492–5498. IEEE, 2007.

[159] Conference on Trade and Development. *Review of Maritime Transport 2018*. United Nations, 2018.

[160] M. Örnfelt. Best practice guide for unmanned maritime systems handling, operations, design and regulations.

[161] Y. Oshman and P. D.son. Optimization of observer trajectories for bearings-only target localization. *IEEE Transactions on Aerospace and Electronic Systems*, 35(3):892–902, 1999.

[162] R. Parasuraman, T. B Sheridan, and C. D Wickens. A model for types and levels of human interaction with automation. *IEEE Transactions on systems, man, and cybernetics-Part A: Systems and Humans*, 30(3):286–297, 2000.

[163] J. Partan, J. Kurose, and B. N. Levine. A survey of practical issues in underwater networks. *ACM SIGMOBILE Mobile Computing and Communications Review*, 11(4):23–33, 2007.

[164] A. Pascoal, P. Oliveira, C. Silvestre, A. Bjerrum, A. Ishoy, J. Pignon, G. Ayela, and C. Petzelt. Marius: an autonomous underwater vehicle for coastal oceanography. *IEEE Robotics Automation Magazine*, 4(4):46–59, Dec 1997.

[165] T. Pastore and V. Djapic. Improving autonomy and control of autonomous surface vehicles in port protection and mine countermeasure scenarios. *Journal of Field Robotics*, 27(6):903–914, 2010.

[166] L. Paull, S. Saeedi, M. Seto, and H. Li. AUV navigation and localization: A review. *IEEE Journal of Oceanic Engineering*, 39(1):131–149, Jan 2014.

[167] Y. N. Petillot, I. T Ruiz, and D. M Lane. Underwater vehicle obstacle avoidance and path planning using a multi-beam forward looking sonar. *IEEE Journal of Oceanic Engineering*, 26(2):240–251, 2001.

[168] R. Petroccia, J. Sliwka, A. Grati, V. Grandi, P. Guerrini, A. Munafò, M. Stipanov, J. Alves, and R. Been. Deployment of a Persistent Underwater Acoustic Sensor Network: The CommsNet17 Experience. In *Proceedings of MTS/IEEE OCEANS 2018*, Kobe, Japan, 2018.

[169] V. Pierlot and M. Van Droogenbroeck. A new three object triangulation algorithm for mobile robot positioning. *IEEE Transactions on Robotics*, 30(3):566–577, June 2014.

[170] N. Poostpasand and R. Javidan. An adaptive target tracking method for 3d underwater wireless sensor networks. *Wireless Networks*, pages 1–14, 2017.

[171] J. Potter, J. Alves, T. Furfaro, A. Vermeij, N. Jourden, D. Merani, G. Zappa, and A. Berni. Software defined open architecture modem development at cmre. In *2014 Underwater Communications and Networking (UComms)*, pages 1–4. IEEE, 2014.

[172] M. C. Potter, D. C Wiggert, and B. H. Ramadan. *Mechanics of fluids*. Nelson Education, 2016.

[173] GW Pulford. Taxonomy of multiple target tracking methods. *IEE Proceedings-Radar, Sonar and Navigation*, 152(5):291–304, 2005.

[174] Y. Qu, Z. Liu, and S. Sun. The research of underwater target tracking adaptive algorithm based on bearings and time-delay. In *2007 IEEE International Conference on Integration Technology*, pages 530–533, March 2007.

[175] H. Ramezani, H. Jamali-Rad, and G. Leus. Target localization and tracking for an isogradient sound speed profile. *IEEE Transactions on Signal Processing*, 61(6):1434–1446, March 2013.

[176] I. Rhee, J. Lee, J. Kim, E. Serpedin, and Y. Wu. Clock synchronization in wireless sensor networks: An overview. *Sensors*, 9(1):56–85, 2009.

[177] D. Ribas, P. Ridao, L. Magí, N. Palomeras, and M. Carreras. The girona 500, a multipurpose autonomous underwater vehicle. In *OCEANS 2011 IEEE - Spain*, pages 1–5, June 2011.

[178] P. Rigby, O. Pizarro, and S. B Williams. Towards geo-referenced auv navigation through fusion of usbl and dvl measurements. In *OCEANS 2006*, pages 1–6. IEEE, 2006.

[179] C. Robert and G. Casella. *Monte Carlo statistical methods*. Springer Science & Business Media, 2013.

[180] D. L Rudnick, R. E Davis, C. C Eriksen, D. M Fratantoni, and M. J. Perry. Underwater gliders for ocean research. *Marine Technology Society Journal*, 38(2):73–84, 2004.

[181] S. Sadhu, S. Mondal, M. Srinivasan, and T.K. Ghoshal. Sigma point Kalman filter for bearing only tracking. *Signal Processing*, 86(12):3769 – 3777, 2006. special section: Multimodal Human-Computer Interfaces.

[182] R. Salmon. Introduction to ocean waves, 2008.

[183] M. T Satterly, LCD Stubbs, MG D Gilbert, MCL Iler, and CKB Glen. Intelligence preparation of the battlespace-an airman's introduction. *Air Chronicles*, 26, 1999.

[184] C Schlenoff, E Prestes, PJ Sequeira Gonçalves, M Abel, Y Amirat, S Balakirsky, ME Barreto, JL Carbonera, A Chibani, SR Fiorini, et al. IEEE Standard Ontologies for Robotics and Automation. *IEEE Std 1872-2015*, pages 1–60, April 2015.

[185] HH Schloemer. Technology development of submarine sonar hull arrays. *Naval Undersea Warfare Center Division Newport, Technical Digest*, September 1999.

[186] S. Sendra, J. Lloret, J. M. Jimenez, and L. Parra. Underwater acoustic modems. *IEEE Sensors Journal*, 16(11):4063–4071, June 2016.

[187] L. F Shampine and M. W Reichelt. The matlab ode suite. *SIAM journal on scientific computing*, 18(1):1–22, 1997.

[188] X. Sheng, Yu-Hen Hu, and P. Ramanathan. Distributed particle filter with gmm approximation for multiple targets localization and tracking in wireless sensor network. In *Proceedings of the 4th international symposium on Information processing in sensor networks*, page 24. IEEE Press, 2005.

[189] J. Sherman, R. E. Davis, W. B. Owens, and J. Valdes. The autonomous underwater glider "Spray". *IEEE Journal of Oceanic Engineering*, 26(4):437–446, October 2001.

[190] H. Singh, J. G. Bellingham, F. Hover, S. Lemer, B. A. Moran, K. Von der Heydt, and D. Yoerger. Docking for an autonomous ocean sampling network. *IEEE Journal of Oceanic Engineering*, 26(4):498–514, October 2001.

[191] J. Sliwka, R. Petroccia, A. Munafò, and V. Djapic. Experimental evaluation of Net-LBL: An acoustic network-based navigation system. In *Proceedings of MTS/IEEE OCEANS 2017*, Aberdeen, Scotland, June 19–22 2017.

[192] É. L Souza, E. F Nakamura, and R. W Pazzi. Target tracking for sensor networks: A survey. *ACM Computing Surveys (CSUR)*, 49(2):30, 2016.

[193] R. G. Stansfield. Statistical theory of d.f. fixing. *Electrical Engineers - Part IIIA: Radiocommunication, Journal of the Institution of*, 94(15):762–770, March 1947.

[194] L. Steels and R. Brooks. *The artificial life route to artificial intelligence: Building embodied, situated agents*. Routledge, 2018.

[195] N. Stilinović, Đ. Nađ, and N. Mišković. Auv for diver assistance and safety—design and implementation. In *Oceans 2015-Genova*, pages 1–4. IEEE, 2015.

[196] M. Stojanovic. On the relationship between capacity and distance in an underwater acoustic communication channel. In *Proceedings of the 1st ACM International Workshop on Underwater Networks*, WUWNet '06, pages 41–47. ACM, 2006.

[197] R. Stokey, T. Austin, B. Allen, N. Forrester, E. Gifford, R. Goldsborough, G. Packard, M. Purcell, and C. von Alt. Very shallow water mine countermeasures using the remus auv: a practical approach yielding accurate results. In *OCEANS, 2001. MTS/IEEE Conference and Exhibition*, volume 1, pages 149–156. IEEE, 2001.

[198] H. Stommel. The slocum mission. *Oceanography*, 2(1):22–25, 1989.

[199] E. Stringa and C. S Regazzoni. Real-time video-shot detection for scene surveillance applications. *IEEE Transactions on Image Processing*, 9(1):69–79, 2000.

[200] C. Strode, B. Mourre, and M. Rixen. Decision support using the multistatic tactical planning aid (mstpa). *Ocean Dynamics*, 62(1):161–175, Jan 2012.

[201] A Tesei, R Been, D Williams, B Cardeira, D Galletti, D Cecchi, B Garau, and A Maguer. Passive acoustic surveillance of surface vessels using tridimensional array on an underwater glider. In *OCEANS 2015-Genova*, pages 1–8. IEEE, 2015.

[202] N. C. Townsend. Self-powered autonomous underwater vehicles: results from a gyroscopic energy scavenging prototype. *IET Renewable Power Generation*, April 2016.

[203] D. Ucinski. *Optimal measurement methods for distributed parameter system identification*. CRC Press, 2004.

[204] Rutgers University. The scarlet knight's trans-atlantic challenge. Last time accessed: August 2018.

[205] J. Vaganay, J. J. Leonard, and J. G. Bellingham. Outlier rejection for autonomous acoustic navigation. In *Proceedings of IEEE International Conference on Robotics and Automation*, volume 3, pages 2174–2181 vol.3, Minneapolis, MN, USA, Apr 1996.

[206] H L Van Trees. *Detection, estimation, and modulation theory, part I: detection, estimation, and linear modulation theory*. J. Wiley & Sons, 2004.

[207] N. Vedachalam, R. Ramesh, V. Bala Naga Jyothi, V. Doss Prakash, and G. A. Ramadass. Autonomous underwater vehicles - challenging developments and technological maturity towards strategic swarm robotics systems. *Marine Georesources & Geotechnology*, pages 1–14, Apr 2018.

[208] C. Von Alt. Autonomous underwater vehicles. In *Autonomous Underwater Lagrangian Platforms and Sensors Workshop*, 2003.

[209] C. Von Alt. Remus 100 transportable mine countermeasure package. In *Oceans 2003. Celebrating the Past ... Teaming Toward the Future (IEEE Cat. No.03CH37492)*, volume 4, pages 1925–1930, Sept 2003.

[210] P. Wadhams. The use of autonomous underwater vehicles to map the variability of under-ice topography. *Ocean Dynamics*, 62(3):439–447, Mar 2012.

[211] A D Waite and AD Waite. *Sonar for practising engineers*, volume 3. Wiley London, 2002.

[212] E. A. Wan and R. Van Der Merwe. The unscented Kalman filter for nonlinear estimation. In *Proceedings of the IEEE 2000 Adaptive Systems for Signal Processing, Communications, and Control Symposium*, pages 153–158, Lake Louise, Alberta, Canada, 2000.

[213] L. Wang. *A course in fuzzy systems*. Prentice-Hall press, USA, 1999.

[214] X. Wang, J. Shang, Z. Luo, L. Tang, X. Zhang, and J. Li. Reviews of power systems and environmental energy conversion for unmanned underwater vehicles. *Renewable and Sustainable Energy Reviews*, 16(4):1958–1970, May 2012.

[215] D. C. Webb, P. J. Simonetti, and C. P. Jones. Slocum: an underwater glider propelled by environmental energy. *IEEE Journal of Oceanic Engineering*, 26(4):447–452, Oct 2001.

[216] D. Westwood. Global auv fleet to increase 42% by 2018, 2014. Last time accessed: July 2018.

[217] S. Willcox, J. Manley, and S. Wiggins. The Wave Glider, an energy harvesting autonomous surface vessel. *Sea Technology*, 49:29–31, November 2009.

[218] RS Woolett. Power limitation of sonic transducers. *IEEE Trans. Sonics and Ultrasonics*, 15:218–229, 1968.

[219] R. B. Wynn, V. A.I. Huvenne, T. P. Le Bas, B. J. Murton, D. P. Connelly, B. J. Bett, H. A. Ruhl, K. J. Morris, J. Peakall, D. R. Parsons, E. J. Sumner, S. E. Darby, R. M. Dorrell, and J. E. Hunt. Autonomous underwater vehicles (auvs): Their past, present and future contributions to the advancement of marine geoscience. *Marine Geology*, 352:451 – 468, 2014. 50th Anniversary Special Issue.

[220] R. Yan, S. Pang, H. Sun, and Y. Pang. Development and missions of unmanned surface vehicle. *Journal of Marine Science and Application*, 9(4):451–457, Dec 2010.

[221] S. Yang and H. Li. Application of EKF and UKF in target tracking problem. In *Proceedings of 8th International Conference on Intelligent Human-Machine Systems and Cybernetics (IHMSC) 2016*, volume 01, pages 116–120, Hangzhou, China, Aug 2016.

[222] C. H. Yu, J. C. Lee, J. W. Choi, M.n Park, and D. J. Kang. Energy efficient distributed interacting multiple model filter in uwsns. In *Control, Automation and Systems (ICCAS), 2012 12th International Conference on*, pages 1093–1098. IEEE, 2012.

[223] C. H. Yu, K. H. Lee, J. W. Choi, and Y. B. Seo. Distributed single target tracking in underwater wireless sensor networks. In *SICE Annual Conference, 2008*, pages 1351–1356. IEEE, 2008.

[224] D. Yue. Marine hydrodynamics (13.021). MIT OpenCourseWare, 2005.

[225] J. Yuh and S. Negahdaripour. Report of the workshop on future research directions in underwater robotics, 1994.

[226] F. Zhang, G. Marani, R. N Smith, and H. Choi. Future trends in marine robotics [tc spotlight]. *IEEE Robotics & Automation Magazine*, 22(1):14–122, 2015.

[227] Q. Zhang, M. Liu, and S. Zhang. Node topology effect on target tracking based on uwsns using quantized measurements. *IEEE transactions on cybernetics*, 45(10):2323–2335, 2015.

[228] Q. Zhang, C. Zhang, M. Liu, and S. Zhang. Local node selection for target tracking based on underwater wireless sensor networks. *International Journal of Systems Science*, 46(16):2918–2927, 2015.

[229] S. Zhang, H. Chen, and M. Liu. Adaptive sensor scheduling for target tracking in underwater wireless sensor networks. In *Mechatronics and Control (ICMC), 2014 International Conference on*, pages 55–60. IEEE, 2014.

[230] S. Zhang, H. Chen, M. Liu, and Q. Zhang. Optimal quantization scheme for data-efficient target tracking via uwsns using quantized measurements. *Sensors*, 17(11):2565, 2017.